Fast-Ion Conducting Glass and Glass-Ceramics for the pH Sensor

By

Anuson Niyompan

Supervised by

Dr. Diane Holland

A thesis submitted in partial fulfilment of the requirements for the degree of Doctor of Philosophy in Physics

University of Warwick, Department of Physics

April 2002

Contents

List of Tables

List of Figures

List of abbreviations

BO	Bridging Oxygen
C_Q	Quadrupolar coupling constant
δ	Isotropic chemical shift
DTA	Differential Thermal Analysis
η	Quadrupolar asymmetric parameters
MAS NMR	Magic Angle Spinning Nuclear Magnetic Resonance
NASICON	Sodium superionic conductors
NASIGLAS	Sodium superionic conducting glass
NBO	Non-Bridging Oxygen
NMR	Nuclear Magnetic Resonance
SEM	Scanning Electron Microscopy
TEC	Thermal Expansion Coefficient
TMS	Tetramethylsilane
UDR	Universal Dynamics Response
XANES	X-ray Absorption Near Edge Structure
XRD	X-Ray Diffraction

Acknowledgements

I would like to thank my supervisor, Dr. Diane Holland, for the excellent supervision of this research. My special thanks go to; all the members of the NMR group at University of Warwick, all the technical staff who support the work, all the members of Glass-Ceramics group at University of Warwick, Dr M. Thomas and A. Beasley at University of Liverpool for their help in the Mössbauer spectroscopic study. I also thank Prof. M.D. Ingram and his colleagues at the University of Aberdeen for invaluable advice and help for ionic conductivity measurement.

I would like formally to thanks the University Affairs Department of the Royal Thai Government for the sponsorship and support. My sincere thanks go to all of my colleagues at Ubonratchathani University, Thailand, for the assistance. I also acknowledge all people who support me during my stay in the UK.

My deepest thanks are to my family, especially my parents for their love and support. Finally, my grateful thanks go to Miss Rungnapa Tipakontithikun for her understanding, support and inspiration.

Declaration

The work presented in this thesis was carried out at the Department of Physics, University of Warwick, under the supervision of Dr. Diane Holland. The results are the product of my own independent work, unless otherwise stated in the text. This research has not been submitted for any other degrees and some of this work has been published as:

A. Niyompan and D. Holland, *Journal of Non-Crystalline Solids* **293-295** (2001), 709.

It is anticipated that more of this work will be submitted for publication in the future.

Abstract

Fast-ion conducting glasses of the compositions $Na_{1+x}M_{2-x/3}Si_xP_{3-x}O_{12-2x/3}$ ($0 \leq x \leq 3$), where M = Zr, Ti, were studied to determine their structural arrangement, physical properties and ionic conductivity. Glass samples were prepared using the conventional melt-quench method in the melting temperature range, 1550 °C to 1650 °C. Glass products were characterised by XRD, DTA, dilatometry and density measurement. Solid state MAS NMR experiments of three accessible nuclei, ^{23}Na, ^{29}Si and ^{31}P were used to determine short-range order arrangement in the glasses.

XRD confirms the amorphicity of glasses for the compositions of x in range 0-3. Glass transition temperatures, T_g, TEC, and molar volume are controlled by glass composition. The MAS NMR results suggest that glass structure could be visualised as the silicate network modified by Na^+ and Zr^{4+} or Ti^{4+} and $[PO_4]$ tetrahedra link up with the remaining of these modifiers with no Si-O-P observed. The glass structures were also controlled by the compositions.

Using parameters determined by DTA, the corresponding glass-ceramics were produced by heat treatment for 4 hr. The composition containing ZrO_2 provided the fast-ion conducting crystalline phase at a small concentration. The major crystalline phase is $Na_2ZrSi_2O_7$. Glass-ceramics containing TiO_2 produce very small concentration of the crystallised phase. Ionic conductivity measurement was used to determine the electrical properties of glass and glass-ceramics. Glasses having high Na_2O content showed the higher ionic conductivity compared to the others.

CHAPTER 1

General

1.1 Introduction

The discovery of fast-ion conduction in ceramics oxides has stimulated considerable interest both in the conduction mechanisms and potential utilisation in batteries and related devices. Fast-ion conductors (FICs), which retain their high ionic conductivities over extended temperatures and chemical activities, may be used instead of liquid electrolytes in electrochemical devices. In several technological applications, development of electrochemical devices of the required performance requires the advantages of these solid ionic conductors. Traditional electrochemical sensors that contain a liquid electrolyte as the conduction path are limited to certain environments. Use of fast-ion conductors in the conduction layer of these sensors could overcome these practical limits. Oxide-solid solutions (e.g. ZrO_2-CaO, ZrO_2-MgO, ZrO_2-Y_2O_3) are by far the most commonly used in commercial applications, as in several type of gas sensors. However, many additional applications can be extended by means of other kinds of fast-ion conductors that are waiting to be exploited.

Recently, fast-ion conduction has also been found in many glass systems containing alkali, alkaline earth, or silver ions. Glassy FICs offer ease of fabrication into a variety of complex structures, which could result in significant advantage over the polycrystalline FICs. However, use of glass in electrochemical devices is not commercially widespread. To exploit glass and glass-ceramic FICs, better understanding of structure/performance relations is required.

The possibility of using fast-ion conducting glass in the electrolyte layer of a solid state pH probe is schematically demonstrated on the right of Fig. 1.01 comparing it with

the conventional pH probe (left). The main focus of this research is to study and develop materials for that electrolyte layer. This solid state probe is designed for high temperature measurement, which is up to 350 °C. There are two important properties, ionic conductivity and thermal expansion, that must be considered for choice of electrolyte material. The appropriate ionic conductivity should be 10^{-6}-10^{-3} S.cm^{-1}. Thermal expansion coefficient matching with the interface materials is required in order to avoid physical deformation. Since both requirements can be found in fast-ion conducting glasses therefore the investigation is carried out by present work.

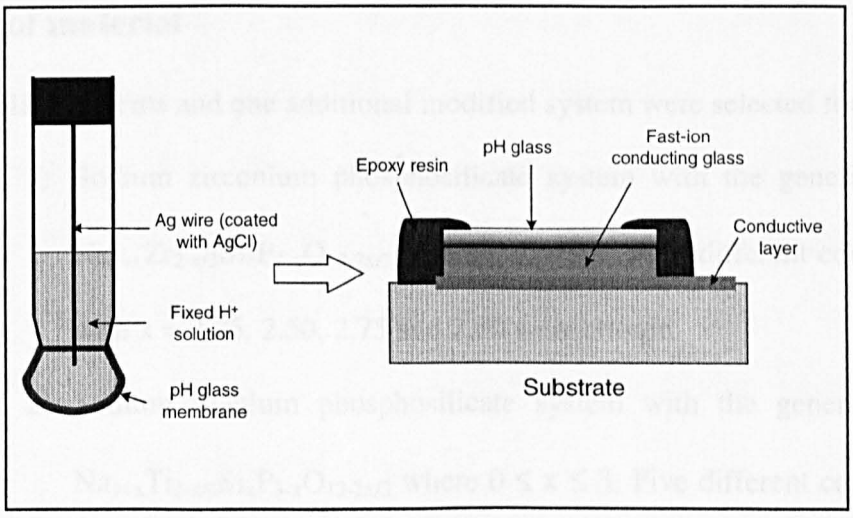

Figure 1.01 *Comparison between aconventional pH probe and the proposed solid state pH cell. Note: the diagram is not drawn to scale.*

1.2 Aims of the research

The main objectives of the following work is to prepare fast-ion conducting glasses and glass-ceramics from silicate based glass systems. An investigation has been made of the structural arrangement, physical properties and ionic conduction behaviour, which will aid the exploitation of fast-ion conducting glasses in the area of electrochemical application. Particular emphasis has been placed on structural related conductivity, which will be useful for construction of the electrochemical cell.

Sodium silicate based glasses play a most important role in this study because a large homogeneous glass body with high mobility of sodium ions can be obtained without devitrification. In the realistic sensor under consideration, a pH electrode, the electrolyte layer is needed to behave as a mixed electronic-ionic conductor. Therefore, modification of these sodium silicate based glasses to be mixed electronic-ionic conductors has also been attempted by adding Fe_2O_3 into the glass composition. This can supply conduction electrons via the Fe^{2+}/Fe^{3+} redox couple. The effect of such modification is studied.

1.3 Choice of material

Two glass systems and one additional modified system were selected for study:

1) Sodium zirconium phosphosilicate system with the general formula $Na_{1+x}Zr_{2-x/3}Si_xP_{3-x}O_{12-2x/3}$ where $0 \leq x \leq 3$. Four different compositions with x = 2.25, 2.50, 2.75 and 3.00 were chosen.
2) Sodium titanium phosphosilicate system with the general formula $Na_{1+x}Ti_{2-x/3}Si_xP_{3-x}O_{12-2x/3}$ where $0 \leq x \leq 3$. Five different compositions with x = 2.00, 2.25, 2.50, 2.75 and 3.00 were chosen.
3) The systems 1) and 2) with 1 mol% and 2 mol% Fe_2O_3 added.

1.4 Thesis plan

This thesis consists of 10 chapters. The brief details of chapters 2-10 are given below.

Chapter 2 describes the theoretical background of fast-ion conduction and a review of fast-ion conducting materials is also given.

Chapter 3 presents the theoretical background of glass and glass-ceramic materials containing basic discussions of glass formation, nucleation and ionic conduction.

Chapter 4 introduces the experimental techniques with some important theoretical background and the experimental details. X-ray diffraction (XRD), differential thermal analysis (DTA), dilatometry and density measurement are used in general glass characterisation. Solid state nuclear magnetic resonance (NMR) is essentially used for structural investigation. Combinations of XRD, NMR and scanning electron microscopy (SEM) are used for crystallisation study in glass-ceramics. Mössbauer spectroscopy is used to investigate the redox equilibrium of Fe^{n+} species in glasses. Ionic conductivity measurement is used to study the electrical properties of the materials.

Chapter 5 shows the results of glass characterisation in the $Na_{1+x}Zr_{2-x/3}Si_xP_{3-x}O_{12-2x/3}$ system with full discussion. A structural model is also proposed.

Chapter 6 is devoted to the characterisation of the $Na_{1+x}Ti_{2-x/3}Si_xP_{3-x}O_{12-2x/3}$ system. The proposed structural model is discussed and compared with the results in chapter 5.

Chapter 7 presents the results of the crystallisation study of the glass-ceramic samples produced by heat treatment of the parent glasses. Phase identification is conducted and reported along with the microstructure images.

Chapter 8 reports the results of Mössbauer spectroscopic studies. The redox equilibrium of Fe^{2+}/Fe^{3+} present in glass samples is also analysed.

Chapter 9 presents the results of ionic conductivity measurements for all relevant glass samples. The mechanism of sodium ion conduction in the silicate network is discussed.

Chapter 10 is the summary and overall conclusion of the present studies. Possible future work is also suggested.

CHAPTER 2

Fast-ion Conduction in Materials

2.1 Introduction

Solid ionic materials exhibiting high electrical conductivies, comparable with those of liquid electrolytes, are termed Fast-Ion Conductors (FICs), superionic conductors or solid electrolytes. Such high ionic conduction (or fast-ion conduction) can be due to transport of either cations or anions. In some cases, FIC materials are distinguished by their main mobile species. For example, the electrical conduction of *fluoride ion conductors* is mainly due to F^- ions, whereas Na^+ ions are the highly mobile species in *sodium ion conductors* and so on. These systems occur in 3 main classes of materials [1]: (i) crystalline compounds, (ii) glasses and (iii) polymers. In this chapter, only the first two classes will be described in detail. A review of crystalline fast-ion conductors is given, relating their structure and conductivity behaviour. In particular it will cover the sodium superionic conductors (NASICON) since the amorphous form of NASICON, a sodium superionic conducting glass or NASIGLAS, is the main focus of this study. The review commences with the basic theory of ionic conduction in materials.

2.2 Basic theory of fast-ion conduction

In a fast-ion conductor, point defects play an important role for ion migration. In general, solid ionic materials have a concentration of ionic defects much higher than the concentration of electronic defects [2]. The conductivity in ionic materials can be strongly dependent on temperature and on structure. However, in the superionic conductors, there are clear pathways for ions to migrate. The concentration of available sites for ions to

occupy is greater than that of the mobile ions. The ionic transport results from ionic defects hopping into adjacent available sites under the influence of an applied electric field and it is expressed as the conductivity [3]

$$\sigma_i = C_i(Ze)\mu_i \qquad 2.1$$

Where μ_i is the ionic mobility, C_i is the concentration of ionic defects or conducting ions per unit volume and Ze is the charge on ion charge carriers. The ionic conductivity (σ_i) is usually dependent on temperature and it can be expressed in the form of an Arrhenius relationship:

$$\sigma_i = \sigma_0.\exp(-E_a/kT) \qquad 2.2$$

Where σ_0 is the pre-exponential term, E_a is the activation energy for ion hopping, k is the Boltzmann constant and T is the absolute temperature. In some cases, the pre-exponential term (σ_0) is significantly temperature dependent and the Arrhenius relation becomes

$$\sigma_i = (\sigma_0/T)\exp(-E_a/kT)$$

or
$$\sigma_i T = \sigma_0\exp(-E_a/kT) \qquad 2.3$$

Generally, the equation of mobility of an ion can be given as [4]

$$\mu_i = (Ze/kT).\lambda_d^2.\nu_0.\gamma.\exp(-\Delta G_m/kT) \qquad 2.4$$

where λ_d is the jump distance, ν_0 is the jump attempt frequency, γ is the geometric factor, ΔG_m is the Gibbs free energy, k is the Boltzmann constant and T is the absolute temperature. If we define V_0 as the concentration of vacancies and N_0 as the number of cation sites per unit volume and substitute them into Eq. 2.1, then, from Eq. 2.4, the expression for ionic conductivity can be written as

$$\sigma_i = [V_0N_0(Ze)^2/kT].).\lambda_d^2.\nu_0.\gamma.\exp(-\Delta S_m/k).\exp[-\Delta H_m/kT] \qquad 2.5$$

or
$$\sigma_i = A_i\exp[-\Delta H_m/kT] \qquad 2.6$$

where ΔH_m is the enthalpy of ion migration and ΔS_m is approximately constant with T. The plotting of σ_i or $\sigma_i T$ versus reciprocal temperature should provide a straight line whose slope gives the enthalpy for ion migration. However, the Arrhenius plot is frequently observed to change slope towards lower activation energy with increasing temperature. This reflects the complex association between enthalpy of ion migration and the concentration of vacancies.

The conductivity is also related to the diffusion coefficient (D_i) of ions following the Nernst-Einstein relationship;

$$\sigma_i = [C_i(Ze)^2/kT]\, D_i \qquad 2.7$$

To compare the conductivity and the diffusion, the correlation factor *F* is often used and it is defined as the ratio of isotopic diffusion D^* and D_i as the following equation

$$F = D^*/D_i = C_i(Ze)^2/\sigma_i\, kT \qquad 2.8$$

The correlation factor F is usually between 0.5 and 1.0, depending on the transport mechanism, and it is often termed the Haven ratio, H_R [5].

2.3 Fast-ion conductors

Typically a fast-ionic conductor has the following characteristics [6]

1. the crystal bond is ionic;
2. electrical conductivity is high (i.e. > 10^{-6} $S.cm^{-1}$)
3. principal charge carriers are ions, which means that the ionic transference number (t_{ion}) is almost equal to 1 (here t_{ion} refers to the fractional contribution of the ionic conductivity to the total conductivity);
4. the electronic conductivity is small; generally materials with electronic transference number (t_e) less than 10^{-4} are considered satisfactory fast-ionic conductors.

There is a large, growing family of ionic solids in which certain ions exhibit high ionic conductivity at ambient temperature. There is huge interest in the science and technology of fast-ionic conductors in view of their potential use as electrodes or electrolyte materials in electrochemical energy conversion devices [6,7].

In order for a solid to show fast-ionic conduction, it must satisfy the following criteria: [8]

1. it must have a high concentration of potential charge carriers,
2. a high concentration of vacancies or interstitial sites,
3. a low activation energy for ion hopping.

A lot of materials can be fabricated with structures corresponding to the characteristics listed above. Crystal and chemical considerations can be applied to identify structures that meet the first two criteria, but prediction of activation energy is not so easy.

In 1914, fast-ion conduction was discovered in certain silver compounds by Tubant and Lorentz. These workers found that the conductivity of α-AgI just below the melting point was actually more than 20% greater than the conductivity of molten AgI. Since then, several Ag^+ fast-ion conductors have been identified in stoichiometric compounds such as $RbAg_4I_5$, AgSI and $AgAl_{11}O_{17}$ [9]. Also, a numbers of non-stoichiometric compounds have been identified as fast-ion conductors. For example: β-alumina ($Na_{1+x}Al_{11}O_{17+x/2}$) [10,11], calcia-stabilized zirconia ($Zr_{1-x}Ca_xO_{2-x}$) [12] and Li_xTiS_2 [9]. Fast-ion conduction has also been found in a number of glasses containing Li^+, Na^+ or Ag^+ [13].

Depending on crystal structure, fast-ion conduction can occur in one, two or three dimensions. A good example of conduction in one-dimension is $LiAlSiO_4$ (β-eucryptite), which has a hexagonal structure with lithium ions found in channels parallel to the c-axis.

Two-dimensional conductors usually have a layer structure, a typical example being β-alumina whose local structure is built up from spinel block layers which leave a plane between the layers to be a pathway for mobile species (i.e Na^+). Three-dimensional conduction is found in Li_3NaS_2 as well as in the complex structures consisting of interlocking polyhedra, such as $Na_3Zr_2Si_2O_{12}$ or Sodium Superionic Conductor (NASICON). Analogous lithium ion conductors (LISICON) based on solid solutions of Li_2ZnGeO_4 and Li_4GeO_4 are also known [14,15].

The mechanism of ionic transport in the fast-ionic conductor materials is generally considered as via a sublattice in which the movement of the mobile ion in fast-ionic conduction states is like that in liquid electrolyte [9]. Accordingly, it is also well known as the ***molten sublattice model.*** This model was first proposed by Strock [16], on the basis of structural and thermodynamic data for AgI. In most FICs, the entropy of the phase transition to the fast-ion conduction states is larger than the entropy of melting.

In some cases, electronic conduction can take place simultaneously with ionic conduction if there are sufficient electronic charge carriers, this material is called a *mixed ionic-electronic conductor* [8].

2.4 Sodium superionic conductors (NASICON)

The NASICON material was synthesised first by Hong in 1976 [17] and is described by the general formula $Na_{1+x}Zr_2Si_xP_{3-x}O_{12}$. The NASICON compound can be considered as a solid solution of $NaZr_2(PO_4)_3$ and $Na_4Zr_2(SiO_4)_3$. At 300 °C, the highest conductivity of NASICON was found for a composition of $x \approx 2$ ($Na_3Zr_2Si_2PO_{12}$) which is competitive with the best β″-alumina. The greater advantage of NASICON is the 3D-conduction path compared to only 2D-conduction for β″-alumina. In recent years

NASICON has been dominant in the area of new solid electrolyte study. It is expected to be the new substitute electrolyte in battery technology.

The structure of NASICON can be classified as a framework (skeleton) structure as proposed by Goodenough and co-workers in 1976 [18]. It can be considered as substitution of silicate tetrahedra (SiO_4) by phosphate tetrahedra (PO_4) going from $Na_4Zr_2(SiO_4)_3$ solid to $NaZr_2(PO_4)_3$ solid. The hexagonal framework of $NaZr_2(PO_4)_3$ has three-dimensionally linked interstitial sites (Fig. 2.01).

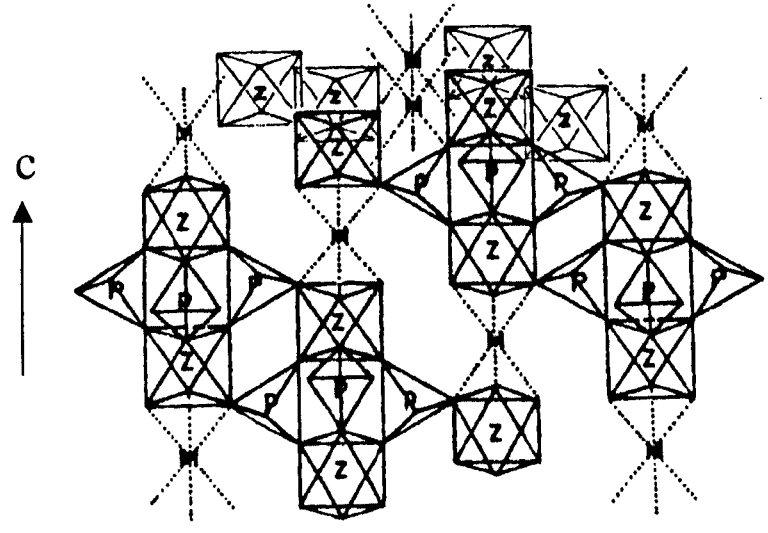

Figure 2.01. *Structure of $NaZr_2(PO_4)_3$ [7].*

Along the c-axis, the vacant trigonal-prismatic sites (p), the octahedral Zr^{4+} sites (Z), and the octahedral sites available to Na^+ ions (M) are ordered as Z-p-Z-M-Z. For each filled M site, there are three empty M_0 sites forming hcp layers perpendicular to the c- axis. Diffusion paths and single particle potentials of Na^+ ion in NASICON have been studied [19].

However, inhomogeneity of NASICON was the main concern in its improvement because the low solubility of ZrO_2 caused it to appear as a second phase [20]. Therefore, compositions $Na_{1+x}Zr_{2-x/3}Si_xP_{3-x}O_{12-2x/3}$ ($0 \leq x \leq 3$) have been proposed, also known as ZrO_2-deficient compositions. For a typical range of $1.55 \leq x \leq 3$, this system exhibits monoclinic symmetry and the end member associated with $x = 3.0$ ($Na_4ZrSi_3O_{10}$) has shown the highest conductivity, i.e. 4×10^{-3} $\Omega^{-1}.cm^{-1}$ at 300 °C [21]. Unfortunately, the presence of free ZrO_2 in sintered compounds places restrictions on the effectiveness of this composition. Furthermore, non-existence of the composition $Na_4ZrSi_3O_{10}$ was reported [22], by the means of X-ray analysis. It was proposed that this composition was actually a composite material consisting of $Na_4Zr_2(SiO_4)_3$ and a glassy phase ($Na_4Si_3O_8$), rather than the stoichiometric compound $Na_4ZrSi_3O_{10}$. Clearfield et al. [23] and Boilot et al. [24] confirmed co-existence of a glassy phase in this particular composition.

Besides the original NASICON, Na_2O-ZrO_2-SiO_2-P_2O_5 system, several other ternary or quaternary systems have also been derived, related to the NASICON framework structure. Typical examples of materials derived from NASICON are shown with their ionic conductivities in Table 2.01.

Analogous to NASICON type materials, the lithium superionic conductors or LISICON type FICS have also been widely studied. The best example of a LISICON compound is presented by the $Li_{2+2x}Zn_{1-x}GeO_4$ ($0 \leq x \leq 1$) system [25-27]. There are also many other LISICON related systems with ZnO being replaced by other transition metal oxides and GeO_2 being replaced by MO_2 or M_2O_5 type oxides [28-30].

It can seen that both NASICON and LISICON can be prepared from a variety of compositions, leading to greater advantage of these two fast-ion conducting conductors. It also extends the area of solid electrolyte study and probably generates more possible applications.

Table 2.01 *Examples of materials analogous to NASICON, with their ionic conductivities at indicated temperature.*

Composition	Conductivity ($S.cm^{-1}$)	References
$Na_3Sc_2P_3O_{12}$	2.70×10^{-2} (300 °C)	[31]
$Na_{3.36}Zr_{1.92}Mg_{0.08}Si_{2.2}P_{0.8}O_{12}$	1.84×10^{-1} (300 °C)	[32]
$Na_{2.8}Zr_{1.7}Nd_{0.3}Si_{1.5}P_{1.5}O_{12}$	5.30×10^{-2} (300 °C)	[33]
$Na_{1.5}Nb_{0.3}Zr_{1.5}(PO_4)_3$	1.30×10^{-5} (200 °C)	[34]
$Na_{2.8}Al_{0.6}Hf_{1.4}Si_{1.2}P_{1.8}O_{12}$	1.22×10^{-2} (350 °C)	[35]
$Na_5YSi_4O_{12}$*	4.30×10^{-2} (300 °C)	[36]
$Na_{3.9}Y_{0.6}P_{0.3}Si_{2.7}O_9$*	6.60×10^{-4} (RT)	[37]

*Note: RT = room temperature, * = glass-ceramic composition.*

2.5 Sodium superionic conducting glass (NASIGLAS)

From the search for new solid electrolytes, not only crystalline materials have been developed, but also glassy forms have been encountered. This is because many glass compositions also fulfil the criteria of good ionically-conducting materials. Ionic conduction in glasses is commonly found in compositions containing alkali ions or Ag^+. By using the conventional melt quench method, the glassy form of ZrO_2-deficient NASICON ($Na_{1+x}Zr_{2-x/3}Si_xP_{3-x}O_{12-2x/3}$, $0 \leq x \leq 3$) was prepared first by Susman et al. in 1983 [38] and afterwards the name NASIGLAS was applied. In the NASIGLAS composition, SiO_2 and P_2O_5 are glass formers while ZrO_2 and Na_2O are the modifiers. The NASIGLAS samples were proved to be fast-ion conductors [38] and the Na^+ conductivity was of the order of 10^{-4} $S.cm^{-1}$ at 300 °C.

High Na^+ conductivity was also found in NASIGLAS prepared using the sol-gel technique [39,40], though the conductivity was slightly lower than that obtained from

melt quenched samples. All glassy phases in this system show a lower ionic conductivity compared with the polycrystalline counterpart. However, the lower conductivity of NASIGLAS is offset by the advantage of preparing the fast-ion conductors in glassy form compared with preparing by the conventional ceramic route. For example, glasses lack grain boundaries, have isotropic properties, and good mechanical strength. Furthermore, glass can be prepared from a variety of compositions and, also, lead themselves to high volume production and economy.

Practically, the objective of studying fast-ion conducting materials is largely concerned with electrochemical applications where there is a compromise between fabrication, physical properties and ionic conductivity [41]. NASIGLAS might be useful for this optimisation, leading to ease of fabrication and ease of preparing the electrochemical cell assembly. NASIGLAS has not been as widely subject to such electrochemical application as the analogous NASICON, but some applications need the advantage of a glassy phase. Use of NASIGLAS might be extended if there were greater understanding of its structure.

There were few studies of the structure of NASIGLAS, until Ennas and co-workers [42] used x-ray diffraction to study one end member, i.e. x = 3.0 or $Na_4ZrSi_3O_{10}$. According to this study, NASIGLAS was proposed to consist of a framework of tetrahedral [SiO_4] units and octahedral [ZrO_6] units linked together with Na^+ occupying sites adjacent to non-bridging oxygen. In could be said that the NASIGLAS structure is related to the corresponding crystalline phase which possesses a monoclinic lattice type.

The study of fast-ionic conducting materials, especially in the vitreous state, requires employment of many techniques. For the structural study, x-ray diffraction, neutron diffraction and solid state-nuclear magnetic resonance are involved, and electrical measurements are useful for the study of conduction behaviour. Thermal behaviour is

also investigated using thermal analysis. To find the appropriate applications for FIC glasses requires a through understanding of the structural role of the different components, related to conductivity and other relevant physical properties.

References

[1] Mahan, G.D. and Roth, W.L. (Ed.) *Superionic Conductors*. New York: Plenum Press, 1976.

[2] Badwal, S.P.S. *"Ceramics Superionic Conductors" in: Materials Science and Technology* **11**. Ed. M V. Swain. Berlin: VCH, 1994.

[3] Subbaroa, E.C. *Solid Electrolyte and Their Applications*. New York: Plenum Press, 1980.

[4] Kilner, J.A., and Steele, B.C.H. *Nonstoichiometric Oxides*. Ed. O.T. Sorensen. New York: Academic Press, 1981.

[5] Haven, Y. *Solid Electrolyte; General principles, characterisation, materials, applications*. Eds. Hagenmuller, P. and W. Van Gool. New York; Academic Press, 1978.

[6] Chandra, S. *Superionic Solid*. Amsterdam: North Holland, 1981.

[7] Goodenough, J.B. *Proceeding of Royal Society London*. **A393** (1984), 215.

[8] Rao, C.N.R. and Gopalakrishnan, J. *New Directions in Solid State Chemistry*. 2nd ed. Cambridge: Cambridge University Press, 1986.

[9] Van Gool, W. *Annual Review of Materials Science*. **4** (1974), 311.

[10] Devries, R.C., Roth, W.L., *Journal of the American Ceramics Society*. **52** (1969), 364.

[11] Kummer, J.T., *Progress in Solid State Chemistry*. **7** (1972), 141.

[12] Maskalick, N.J. and Sun, C.C., *Journal of Electrochemical Society*. **118** (1971), 1386.

[13] Hughes, K. and Isard, J.O., *"Ionic Transport in Glasses" in: Physics of Electrolytes, Vol. 1*. J. Hladik (ed.). London: Academic Press, 1972.

[14] Bruce, P.G. and West, A.R. *Journal of Solid State Chemistry*. **44** (1982), 354.

[15] Mazumdar, D., Bose, D. N. and Mukherjee, M.L. *Solid State Ionics*. **14** (1984), 143.

[16] Strock, L. W. *Z. Physical Chemistry*. **B31** (1936), 132.

[17] Hong, H. Y-P. *Materials Research Bulletin*. **11** (1976), 173.

[18] Goodenough, Hong, H. Y-P., and Kafalas J.A. *Materials Research Bulletin*. **11**, (1976), 220.

[19] Kohlor, H. and Schulg, H. *Materials Research Bulletin*. **20** (1985), 1461.

[20] Von Alpen, U., Bell, M.F., and Hofer, H.H. *Solid State Ionics*. **3-4** (1981), 215.

[21] Von Alpen, U., Bell, M.F., and Hofer, H.H. *Solid State Ionics*. **7** (1982), 345.

[22] Barth, S., Feltz, A., and Jager, C. *Solid State Ionics*. **26** (1988), 189.

[23] Clearfield, A. Subramanian, M.A., Rudolf, P.R. and Moini, A. *Solid State Ionics*. **18&19** (1986), 13.

[24] Boilot, J.P. Colomban, Ph. and Collin, G. *Solid State Ionics* **28-30** (1988), 403.

[25] Abrahams, I., Bruce, P.G., West, A.R. and David, I.F., *Journal of Solid State Chemistry*. **75** (1988), 390.

[26] Bruce, P.G., Abrahams, I. and West, A.R., *Solid State Ionics*. **40/41** (1990), 293.

[27] Bruce, P.G. and Abrahams, I., *Journal of Solid State Chemistry*. **95** (1991), 74.

[28] Bose, D.N., Parthasarathy, G., Mazumdar, D. and Gopal, E.S.R. *Physical Review Letters.* **53** (1984), 1368.
[29] Ivanov-Schitz, A.K. and Sigaryov, S.E., *Solid State Ionics.* **27** (1988), 89.
[30] Sumathipala, H.H., Dissanayake, M.A.K.L. and West, A.R. *Journal Electrochemical Society.* **142**, no. 7 (1995), 2138.
[31] Boelm, L., Delbecq, C.J., Hutchinson, E., and Susman, S. *Solid State Ionics.* **5** (1981), 311.
[32] Krok, F. *Solid State Ionics.* **24** (1987), 21.
[33] Wang, W., Wang, S., Rao, L., Lu, Z., and Yi, X. *Solid State Ionics.* **28-30** (1988), 424.
[34] Veríssimo, C., Garrido, F., Alves, O.L., Calle, P., Martínez-Juárez, A., Glesias, J.E., and Rojo, J.M. *Solid State Ionics.* **100** (1997), 127.
[35] Wang, W. and Liu, X *Solid State Ionics.* **89** (1996), 165.
[36] Yamashita, K., Noriji, T., Umegaki, T., and Kanazawa, T. *Solid State Ionics.* **40/41** (1990), 48.
[37] Cho, T., Yamashita, K., Matsuda, M., and Umegaki, T. *Materials Research Bulletin.* **29** no.6 (1994), 595.
[38] Susman, S., Delbecq, C.J., and McMillan, J.A. *Solid State Ionics.* **9&10** (1983), 667.
[39] Boilot, J.P. and Colomban, Ph. *Journal of Material Science Letters.* **4** (1985), 22.
[40] Boilot, J.P. and Colomban, Ph. *Solid State Ionics.* **18&19** (1986), 974.
[41] Hunter, C.C., and Ingram, M.D. *Solid State Ionics.* **14** (1984), 31.
[42] Ennas, G., Musinu, A., Piccaluga, G., Pinna G., and Magini, M. *Chemical Physics Letters.* **141** no.1, 2 (1987), 143.

Chapter 3

Glasses and Glass-Ceramics

3.1 Definition of glass

Physically, glass is an amorphous material or non-crystalline solid. Its formation can be distinguished from other materials. Generally, the glassy state can be produced from a variety of inorganic oxides, but there are four main glass-forming oxides, SiO_2, B_2O_3, GeO_2, and P_2O_5. These oxides are from elements of intermediate electronegativity and, as a result, bonding is usually a mixture of ionic and covalent. From combinations of the main four glass-forming oxides with one or more other oxides, many compositions can be derived.

Several definitions have been given for glass. Firstly, the definition of glass in terms of its preparation says that *glass is an inorganic product of fusion, which has been cooled to a rigid condition without crystallisation.* This definition has several drawbacks. The restriction is implied that glass should be prepared from the cooling of a glass melt, although glass can be prepared by the sol-gel method and metallic glasses have been also prepared by either rapid melt quenching or melt spinning methods. Consequently, Roy [1] gave a new definition of glass based on the structure and thermal behaviour; *glass is a solid which has short-range order but lacks long-range molecular order.* However, this in itself is not a sufficient definition. Stevels has drawn attention to the subjective nature of the definition of glasses by referring to the Deborah number [2], which is given as the ratio of relaxation time to observation time. For a material to be regarded as solid, which a glass must be by definition; *the Deborah number must be greater than 1.* Even though glass does not have a unique definition, every glass found to date shows two common

characteristics [3]. First, no glass has a long-range ordered, periodic atomic arrangement. Second, every glass exhibits the time-dependent behaviour known as glass transformation behaviour. This behaviour occurs over a temperature range known as the glass transformation region. Thus, glass can be defined as *an amorphous solid, completely lacking in long range ordered, periodic atomic structure and exhibiting a region of glass transformation behaviour.* In other words, it can be said that any materials, inorganic, organic, or metallic, formed by any technique, which exhibits glass transformation behaviour, is a glass.

3.2 Glass formation

Several properties of glass are related to its preparation route. In conventional glass production, glass can be formed by melting of raw materials (i.e. a mixture of component oxides) and cooling to obtain the solid glass without crystallisation. The temperature dependence of several properties of crystalline solids and glasses are compared schematically in Fig. 3.01. Typical crystalline solids will normally crystallise on cooling through their melting point, with an abrupt and significant drop in the specific volume and configuration entropy (Fig. 3.01a and 3.01b). However the changes in these properties for glasses are more gradual, and there are no abrupt changes at the melting point, but rather the properties follow the liquid line down to a temperature where the slope of the specific volume or entropy versus temperature curve is markedly decreased [4]. The point at which the break in slope occurs is known as the glass transition temperature (T_g) and denotes the temperature at which a glass-forming liquid transforms from a rubbery, soft plastic state to a rigid, brittle, glassy state. In other words, the temperature at which a supercooled liquid becomes a glass, i.e. a rigid amorphous body, is known as the glass transition temperature. In the range between the glass transition and

melting temperatures, the material is usually referred to as a supercooled liquid or undercooled liquid [5].

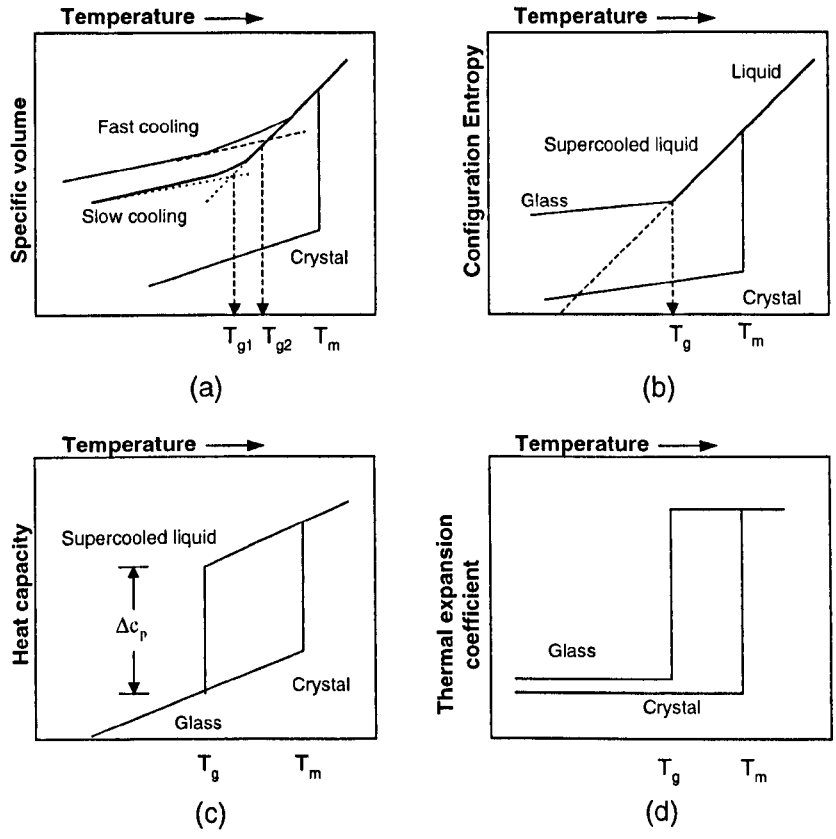

Figure 3.01. *Relation between some properties of glass and temperature during cooled through glass transition T_g: (a) Specific volume, (b) configuration entropy, (c) heat capacity and (d) thermal expansion [6].*

In thermodynamic terms, at the glass transition temperature, the entropy S and specific volume V_s are continuous, whereas the thermal expansion coefficient α and heat capacity c_p, are discontinuous. The events at T_g are complex because T_g is a function of the cooling rate [7], as can be seen from experiments. The transition temperature T_g shifts to lower temperatures when the cooling rate is decreased. This means that the atoms have more time to rearrange themselves and a denser glass is formed. Therefore, T_g is not a thermodynamic quantity, but rather a kinetic one. Furthermore, the viscosity of a glass at T_g is large, of the order of 10^{15} Pa.s, which in turn implies that atomic mobility is

definitely low. It follows that, if the timescale of the experiments is smaller than the average time for an atom to move, then that atom will not contribute to the property being measured and, for all practical purposes, the glass transition would appear as a relatively abrupt phenomenon, as observed.

3.3 Kinetics of crystallisation and glass transformation

In order for glass to form, the rate of crystallisation of the undercooled liquid must be sufficiently slow that it does not occur during cooling. Crystallisation of an undercooled liquid is a two-stage process involving (a) the formation of crystal nuclei followed by (b) their subsequent growth. A kinetic condition for glass formation is that the rate of nucleation and/or the rate of crystal growth should be relatively slow [8]. In some undercooled liquids, nucleation can take place easily because plenty of nucleation sites are available. The rate of crystallisation is then largely controlled by the rate of growth, which varies with temperature in a manner shown in Fig. 3.02. The rate is zero at the melting point, increases to a maximum at a certain degree of undercooling and then falls to zero again at still lower temperatures. At temperatures close to the melting point T_m, crystals and liquid have similar free energy. There is no driving force for any change to occur, therefore, the net rate of crystallisation of a liquid is essentially zero. At temperatures below T_m, the free energy of the crystal is less than that of the liquid. Assuming the entropy of fusion, ΔS_m, to be independent of temperature, the difference in free energy between liquid and crystal is given by [9]

$$\Delta G = \Delta H - T\Delta S_m \qquad 3.1$$

However at T_m;

$$\Delta G = \Delta H_m - T\Delta S_m = 0$$

Hence $\Delta H_m = T_m \Delta S_m$, then

$$\Delta G = \Delta S_m(T_m - T) \quad \text{for } T < T_m \qquad 3.2$$

The increase in rate of crystallisation below T_m therefore corresponds to an increasing difference in free energy between crystals and liquid, hence, it is associated with a greater driving force for crystallisation. At lower temperature, especially for glass-forming liquids, an additional factor, the viscosity of undercooled liquid, becomes increasingly important. With increasing viscosity, the diffusion of atoms or ions through the liquid to the surface of the growing crystal becomes increasingly difficult and the rate of crystallisation tends to decrease accordingly. With decreasing temperature, there are therefore two competing effects. The increased difference in free energy between crystals and liquid favour crystallisation whereas the increased viscosity of the undercooled liquid reduces the tendency to crystallisation. The peak in the rate of crystallisation corresponds to the situation where these two competing effects have equal weight. On the high temperature side, it is the difference in free energy between crystal and liquid that predominates.

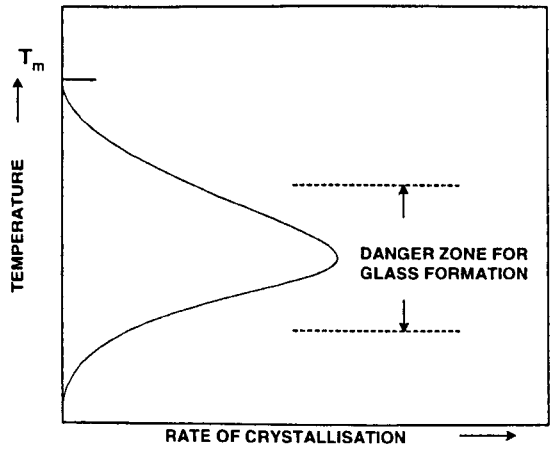

Figure 3.02. *Dependence of rate of crystallisation of an undercooled liquid on temperature [10].*

In considering the crystallisation of undercooled liquids and their ability to form a glass, there is a "danger zone" for glass formation that corresponds to the maximum in the

crystallisation rate. If it is possible to undercool a liquid through this danger zone, it should be relatively safe from subsequent crystallisation or devitrification and form a kinetically stable glass.

The above discussion refers to the kinetics of crystal growth and assumes that nucleation has either already taken place or is relatively easy. Two nucleation mechanisms heterogeneous and homogeneous may be distinguished. If heterogeneous nuclei, such as foreign particles, are not present in the undercooled liquid, spontaneous homogeneous nucleation may occur. This situation will take place throughout the bulk of the liquid without the necessity of artificial nucleation sites (see section 3.5.2).

3.4 The structure of glasses

In discussing the structure of glasses, the vitreous state of simple oxides forms the basic example, especially vitreous silica. Structural study of the vitreous state can be carried out more easily for a one component system. However, other glass forming systems can be also prepared such as metal, alloy and organic polymer glasses. Therefore, several descriptions of glass structure have been developed. In 1926, Goldschmidt's Rule was presented which noted that, in simple glass-forming oxides, the glass-forming ability and the radius ratio of cation to anion were correlated [11]. Glass forming ability was associated with a ratio of 0.2-0.4. In 1932, Zachariasen [12] used the basic idea of Goldschmidt to extend his model for glass structure. He commented on the glass-forming ability of oxides by considering the relation between metal atoms and oxygen atoms. From the conclusions of his observations, Zachariasen presented his rules of glass structure, known as the ***random network model***. The rules can be used to determine glass formers and define their structures from the knowledge of crystalline oxide structures. Zachariasen's rules can be detailed as;

1. No oxygen atom may be linked to more than two metal atoms.
2. The metal atom must have a low co-ordination number.
3. The $M\text{-}O_x$ polyhedra share corners with each other, never edges or faces
4. For glasses with 3-D structures, at least three corners of a polyhedron must be shared.

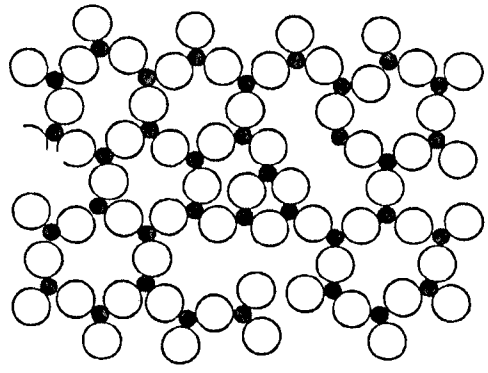

Figure 3.03. *Schematic 2-D structure of pure glass former as described by the random network model of Zachariasen, the open circles are oxygen atoms and the small filled circles are silicon atoms [3].*

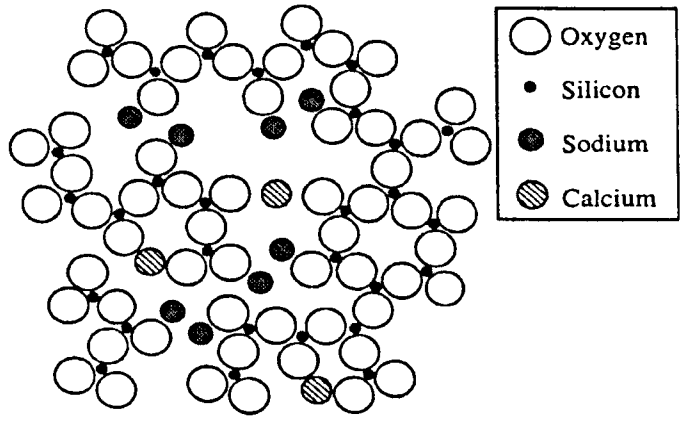

Figure 3.04. *Schematic 2-D drawing of the structure of soda-lime-silicate glass [3].*

A restriction of the random network model of Zachariasen is that oxygen atoms have to form a simple polyhedral (e.g. tetrahedral) arrangement around the metal atom. The 2-D picture of this model is shown in Fig. 3.03, which is the structural model of a pure glass former. In the binary system (complex glasses), Zachariasen modified his model to describe the system of glass-forming oxide mixed with non–glass-forming oxide, by saying that; (a) an oxide glass is formed if the sample contains a high percentage of cations surrounded by oxygen tetrahedra or triangles, (b) the tetrahedra or triangles only share corners, (c) some but not all oxygen atoms are linked to two network cations, i.e. there are bridging oxygens (BO) and non-bridging oxygens (NBO). This is illustrated in Fig. 3.04.

Lebedev presented the crystallite hypothesis of glass structure in 1921, according to which glasses are considered as agglomerates of sub microscopic crystallites. The consequence of this hypothesis would be that glasses are multiphase and micro-heterogeneous in their structure. However, it could not explain the diffraction of x-rays by glasses. In other work on glass structure, Warren [13] developed the theory of x-ray diffraction of amorphous materials and his work strongly supported the random network model of Zachariasen. Subsequently, other suggestions were given, for example, the theories of Porai-Koshits [14], Huggins, Sun and Silverman [15], and the discrete ions concept [16].

The theory of Porai-Koshits (1958) was based mainly on x-ray diffraction studies of binary silicate glasses between silica and the metasilicate composition which he proposed were inhomogeneous. The constitution of the glass was suggested to consist of various regions; (I) vitreous silica, (II) Na_2SiO_3 and (III) an intermediate chemically disordered phase which bonded together (I) and (II). The conclusion of this theory gave support to the crystallite hypothesis. However, this theory is unable to explain the abrupt

variation of properties (i.e. partial molar volume, thermal expansion and viscosity) at 10-20 mole% of metal oxide. The theory of Huggins, Sun, and Silverman (1943) suggested that the basic structural units of the binary glasses are analogous to those found in crystalline silicates, which can be infinite sheets (micas), infinite chains (pyroxenes), rings (wollastonite) or small silicon-oxygen ions (thortveitite), depending on the composition. The discrete ions concept was established by Bockris and co-workers. They postulated the presence of discrete ions such as $Si_6O_{15}^{6-}$ and $Si_8O_{20}^{8-}$ in the melt, probably at concentrations of metal oxide up to 40 mol%. All theories give good explanation of their respective individual experimental results but no single direct experimental method can provide complete information on glass structure.

In the present day, several complementary experimental methods are used for the study of glass structure, hence, greater understanding of glass structure can be achieved. Unfortunately, most modern techniques; neutron diffraction, Raman spectroscopy, Infrared spectroscopy (IR), electron spin resonance (ESR), nuclear magnetic resonance (NMR), extended x-ray absorption fine structure (EXAFS) etc., are best suited for examining only the local structure about an ion, with some extension to the intermediate range of order [3]. In consequence, they are not capable of application to materials where the properties are controlled by microstructure rather than short to intermediate range order. However, from those modern techniques, magic angle sample spinning- nuclear magnetic resonance (MAS-NMR) seems to be the most powerful technique for the study of glass structure, since MAS-NMR can directly determine the relation between the observed nucleus and its surrounding ions or atoms. As a result, the co-ordination of an observed nucleus can be analysed. Moreover, MAS-NMR can provide directly the arrangement and number of bridging and non-bridging oxygens in complex glass systems. In general, MAS-NMR should not be used alone to investigate the structure of glass. It is

better to combine it with other investigation techniques, to obtain complementary information on the structure of glasses.

The main objective of structural study to the glasses is to understand the relation between structure and their properties. The most successful structural derivations are from the oxide glasses those are influenced by the *random network model.* The simple approach of the model describes glass structure as a network of glass former units (tetrahedron or octahedron) modified by modifier cations at the NBO sites. The tetrahedron units are commonly denoted by Q^n notation, where n indicates number of BO. Q^n species have different local environment where MAS NMR technique can probe these differences. The best examples are the structure of binary alkali silicate glasses which Q^n species are well determined by MAS NMR. Using MAS NMR is also applicable to the complex silicate glass systems that contain several types of structural units. Alkali borosilicate glass is probably the best example that MAS NMR gives the best determination of coordinate transformation between borate species. In addition, NMR results also show that PbO do not behave as a simple modifier in lead silicate glass. There is a network linkage between Pb^{2+} ions via bridging oxygen. However, it should pointed out that no single structure exists for any given glass composition. The proposed model is always an idealised structure, which can vary with varying composition. Thus, the best model should provide the best explanation for all observations from both spectral and properties studies. Thus, any proposed glass structure should be based on all available evidences rather than a single set of data.

3.5 Glass-ceramics

3.5.1 General description

Glass-ceramics are crystalline materials formed by controlled devitrification of glass. Glass is melted, fabricated to shape, and then converted to a ceramic by a heat treatment

process. A typical temperature versus time cycle for the processing of a glass-ceramic is shown in Fig. 3.05, and it requires four steps;

1. Mixing and melting. All raw materials are mixed with the nucleation agents, such as TiO_2 or ZrO_2, and are melted.
2. Forming. Glass-ceramics can be formed using conventional glass forming methods such as spinning, rolling, blowing, or casting. The cooling rate during the forming process, however, has to be rapid enough to avoid crystallisation or growth.
3. Nucleation. After shaping is completed, the glass body is heated to a temperature high enough to obtain a very large nucleation rate. The efficiency of nucleation is the important factor for success of the process.
4. Growth. Following nucleation, the temperature is increased to the level where growth of crystallites occurs readily. And then, after a certain time of growing, the desired microstructure is achieved. Finally, it is cooled at a selected slow rate.

3.5.2 Homogeneous and Heterogeneous Nucleation

When a homogeneous viscous liquid is cooled below the equilibrium solubility point of its most insoluble species, it enters a metastable zone. In this range of temperature, nuclei do not form at a detectable rate but crystals can easily grow. Below this temperature zone, nuclei may spontaneously and uniformly form. On further cooling, the liquid reaches a high viscosity that restrains both of the formation and growth of nuclei [17]. This type of nucleation is termed *homogeneous nucleation.* On other hand, nuclei may not form spontaneously in the bulk but form in preference at an interface or on the surface of foreign nuclei or impurities, this is termed *heterogeneous nucleation.*

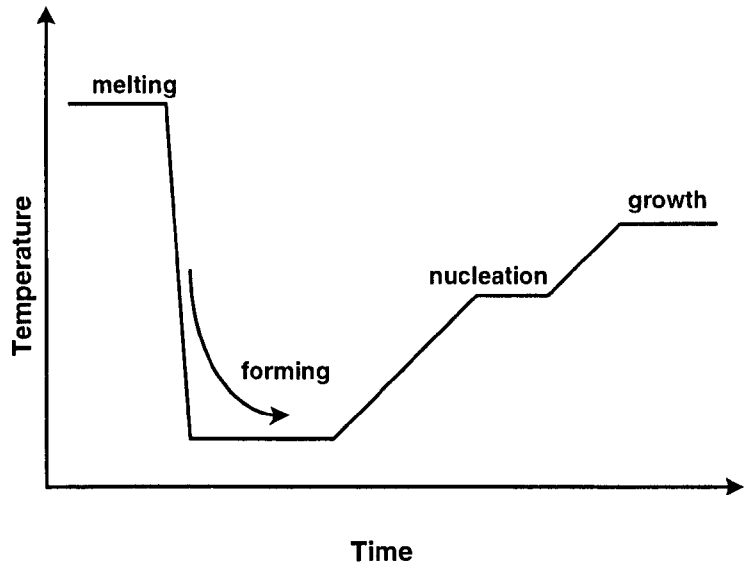

Figure 3.05 *Typical temperature versus time for the heat treatment process of glass-ceramic.*

Typical representation of both homogeneous nucleation and growth rates as a function of temperature for a typical undercooled liquid are shown in Fig. 3.06. The nucleation rate can be expressed as [18]

$$I = A\exp\left(\frac{-\Delta G^{*}+Q}{kT}\right) \qquad 3.3$$

Where I is the homogeneous nucleation rate, A is a constant approximately equal to NkT/h (N is Avogadro's number, k is Boltzmann's constant, T is absolute temperature, and h is Planck's constant), ΔG^{*} is the maximum free energy change at the critical radius of a spherical nucleus (activation barrier for nucleus formation), and Q is the activation energy for short-range diffusion of atoms or molecules across the interface. The crystal growth rate U is given by

$$U = fRT\left[1-\exp\left(\frac{\Delta G}{RT}\right)\right].3\pi N a_0^2 \eta \qquad 3.4$$

Where U is the rate of crystal growth, f is the fraction of total number of sites available for growth, ΔG is the bulk free energy of crystallisation, R is the gas constant, a_0 is the

interatomic interaction, and η is the viscosity of the liquid. Most glass-forming liquids, when supercooled, do not crystallise according to the simple laws of homogeneous nucleation.

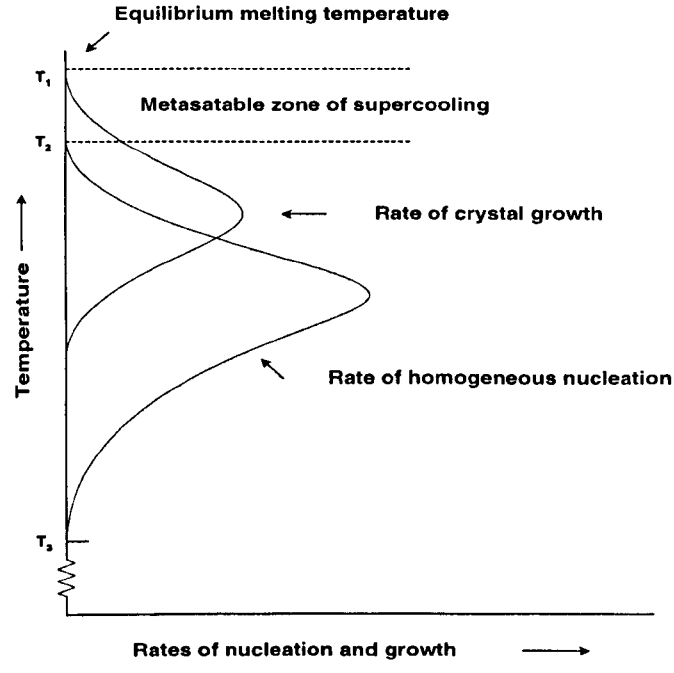

Figure 3.06. *The variation of nucleation rate and growth rate on cooling.*

Heterogeneous nucleation is more important for forming glass-ceramics. Generally, the *nucleating agent* is introduced into a glass composition to produce heterogeneous nuclei. It may be a metal, titanate, zirconate or other species. The nucleating agent will promote phase separation in a glass melt. By cooling the melt or re-heating glass to the temperature at which nucleation takes place, the structural incompatibility of the dispersed phase with the host glass causes it to precipitate as tiny crystalline nuclei and subsequently nucleate the primary crystalline phase. Following heat treatment at higher temperature to promote crystallisation, the polycrystalline microstructure is obtained.

3.5.3 The properties of glass-ceramics

The most important advantage of glass-ceramics over conventional sintered ceramics is the ease of the processing. This is because viscous sintering is much easier

and faster than solid state sintering. Usually the presence of the crystalline phase results in much higher deformation temperatures than the corresponding glasses of the same composition. For example, many oxides have T_g values of 400 to 450 °C and soften readily at temperatures above 600 °C. A glass-ceramic of the same composition, however, can retain its mechanical integrity and rigidity to temperatures as high as 1000 to 1200 °C [6]. In addition, the strength and toughness of glass-ceramics are usually higher than those of glasses and composition modification can be used for controlling thermal expansion coefficients [19]. In many applications, such as the joining of glass-ceramics with metal or ceramics, it is very important to match the thermal expansion coefficients to avoid the generation of thermal stresses.

3.6 Ionic transport in glasses

3.6.1 Introduction

In normal circumstances, all commercial glasses are good insulators at room temperature. The mobility of charge carrier is relatively low throughout the glass network. Therefore, early electrical studies of glasses were turned into a study of resistivity rather than conductivity. Nowadays, glasses possessing high ionic conductivity can be produced in a wide range of compositions containing good charge carriers [20]. Ionic conduction can be found in oxide glass compositions containing alkali, alkaline earth or silver ions, while, electronic conduction can be found in semi-conducting glasses. There are two groups of semi-conducting glasses, one based on the chalcogen elements (S, Se and Te) and the other on compositions containing high percentages of one or more of the transition metal oxides (especially V_2O_5, MoO_3 and WO_3) [21]. Nevertheless, some glass compositions can show both ionic and electronic conduction simultaneously. In this

section, a model for the mechanism of ionic conduction in glasses is described with regard to compositions.

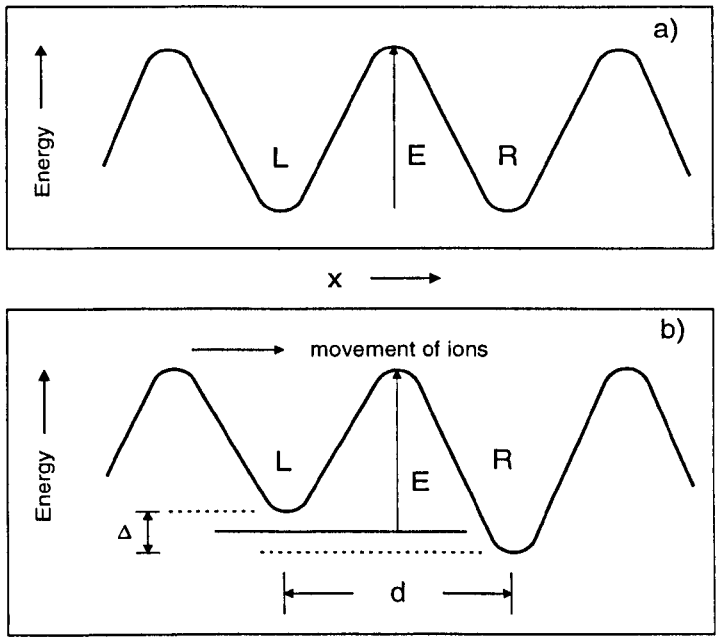

Figure 3.07. *Schematic diagram of energy barriers, a) no applied field, b) applying field ξ. Note that $\Delta = \xi ed$.*

3.6.2 A simple model of ionic conduction

The conduction of charge in most oxide glasses is due to the movement of ions and those ions require some energy to overcome the attraction force which holds them at one position. The consequence is the temperature dependence of ionic conduction. Thus, a simple model must deal with the effect of temperature and ion concentration. Since the ionic conduction of glasses is comparable to the conduction of crystalline solid electrolytes such as NaCl, then, the model can be simplified by using the ionic conduction mechanism of a cation in the periodic potential of the lattice of ionic crystal. Fig. 3.07a shows a schematic representation of the variation with position of the energy of a cation as it moves along one direction in a crystal. For a cation to be able to move, an adjacent vacant site must be available for it to move into. In the case of no applied field, the ion

can jump from site L to R (Fig. 3.07a) or vice versa by gaining energy from a vibration process. At temperature T, the probability of a jump is proportional to $exp(-E/kT)$ [22], where k is the Boltzmann constant and E is the activation energy of an ion to jump between sites. If the ion is vibrating about its equilibrium position at frequency ν, the number of jumps per second will equal $\nu.exp(-E/kT)$. Over a period of time, the number of jumps in backward and forward directions are the same, hence, there is no net current flow through material.

If an electric field ξ is applied, the effect will be a tilting of the energy diagram (Fig.3.07b). Since the net work done in moving a univalent ion against the applied field ξ is ξed where e is the electric charge and d is the distance between adjacent sites, it follows that bottom of one energy well must be much higher than the one to immediately its right. The energy barrier on the left of each well has been increased by $\xi ed/2$ and that on the right has been decreased by the same amount. Consequently, the frequency of jumps to the right will be increased and that to the left decreased. The net number of jumps per second, W, made by each ion in the direction of the field can be given by

$$W = \nu.\exp[-(E-\xi ed/2)/kT] - \nu.\exp[-(E+\xi ed/2)/kT]$$

$$= \nu.\exp(-E/kT).[\exp(\xi ed/2kT) - \exp(-\xi ed/2kT)] \qquad 3.5$$

The current density J is equal to $nedW$, where n is the ion concentration. Since the value of ξed is very small compared to kT, the term in square brackets can be expressed, using a Taylor series, as approximately $\xi ed/kT$. Then J can be expressed as

$$J = (ne^2 \nu \xi d^2/kT).\exp(-E/kT) \qquad 3.6$$

Since $J = \sigma\xi$, The electrical conductivity is readily shown to be

$$\sigma = (ne^2 \nu d^2/kT).\exp(-E/kT) \qquad 3.7$$

By taking logarithms, we obtain the simple expression

$$\ln \sigma = A - B/T \qquad 3.8$$

where $A = ln(ne^2 vd^2/kT)$ and $B = E/k$. Both A and B are constants for particular materials. Eq. 3.8 can be written inversely as $ln\rho = a + b/T$, where ρ is the resistivity, a and b are arbitrary constants, and this is the well-known *Rasch-Hinrichsen law of electrical resistivity of glass* [23]. It was discovered many years ago and used successfully to determine the experimental resistivity response of many glass compositions.

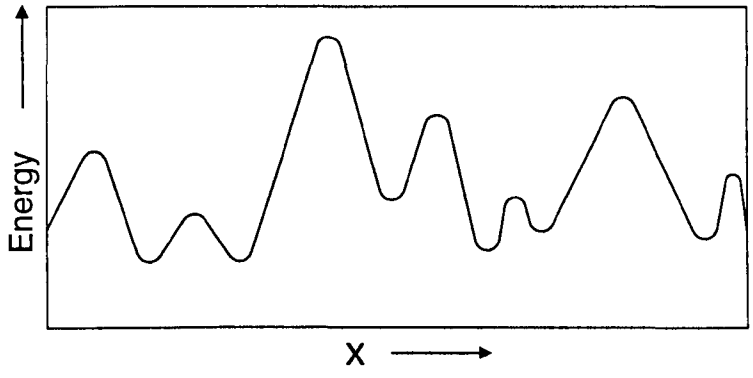

Figure 3.08. *Schematic diagram showing the distribution of energy barriers which may exist in a glass.*

In fact, the structure of glass is presented as a random network. Thus, the potential energy diagram must be more complicated than that in Fig. 3.07. It may be represented as the random distribution of potential energy wells as in Fig. 3.08. Finally, it should be pointed out that the activation energy E found from glass is the average quantity [24], i.e. apparent activation energy, rather than an absolute value as found from crystalline materials.

3.6.3 Effect of glass composition

In binary alkali silicate systems, the conductivity increases monotonically with increasing alkali content. At low alkali content (less than 10 mol%), there are some considerable discrepancies of conductivity. This may be due to a consequence of the

difficulty of making a sufficiently homogenous samples [25]. Although the conductivity increases with increasing alkali content, it is not simply proportional to the increasing number of alkali ions per unit volume of the glasses. For example, increasing alkali content from 15 to 45 mol% raises the conductivity by approximately two orders of magnitude. Reduction in the activation energy of the alkali ion occurs as its concentration is increased, and this causes the significant increase of the conductivity. Conductivity decreases when cation size increases but there is no simple relationship between activation energy and cation size [26].

The introduction of alkaline earth oxide component into the binary alkali silicate glasses has a remarkable effect on decreasing the conductivity of alkali ions. This effect was demonstrated in composition $20Na_2O.20RO.60SiO_2$ (R = Be, Mg, Ca, Sr and Ba) and can be described simply as the blocking effect, since these divalent ions occupy similar sites in the glass structure. Since the blocking effect directly relates to the size of the third ions, the larger the ion the higher the blocking effect and so the lower the conductivity of the alkali ion [27].

The effect of various network-forming oxides on the conduction mechanism of alkali ions can be described by the examples of sodium and lithium boro-silicate glasses. During substitution of B_2O_3 for SiO_2 in a series of glasses with constant alkali content, it was found that the activation energy of alkali ions increased linearly with B_2O_3 content over the whole range of substitution [25] despite the fact that $[BO_4]^-$ groups formed at low B_2O_3 content and changed to $[BO_3]$ groups at higher B_2O_3 content. For compositions of fixed mole fraction of B_2O_3 and SiO_2, the activation energy decreased with increasing alkali content.

The introduction of intermediate oxides has other effects on the activation energy of alkali ion. In the system $Na_2O.xAl_2O_3.2(4-x)SiO_2$, the activation energy goes through a

minimum at x = 1.0. The increase of Al^{3+} content decreases the number of non-bridging oxygens as it enters the silicate network and affects the coordination shell of Na^+ forming $[AlO_4]^-Na^+$. When x exceeds 1.0, Al^{3+} enters a modifier position and occupies hexagonal sites, such that the number of non-bridging oxygens increases again. As a result, the activation energy of Na^+ has a minimum value [28].

It may be concluded that any change in composition which alters the mobility of alkali ions or modifies non-bridging oxygen number can affect the conductivity of the alkali ion.

References

[1] Roy, R. *Journal of Non-Crystalline Solids.* **3** (1970), 33.
[2] Stevels, J.M. *Journal of Non-Crystalline Solids.* **6** (1971), 307.
[3] Shelby, J. E. *Introduction to Glass Science and Technology.* Cambridge: The Royal Society of Chemistry, 1997.
[4] Elliott, S.R., *Physics of Amorphous Materials*; London: Longman, 1983.
[5] Mackenzie, J.D. *Modern Aspects of The Vitreous State.* London: Butterworths, 1960.
[6] Barsoum, M. W. *Fundamentals of Ceramics.* Singapore: Mcgraw-Hill, 1997.
[7] Pye, L.D., Stevens, H.J., and LaCourse, W.C., (Eds). *Introduction to Glass Science.* New York: Plenum Press, 1972.
[8] Vogel, W. *Glass Chemistry.* Berlin: Springer-Verlag, 1994.
[9] Barry, T.I. *"Oxide Glasses" in; Inorganic Chemistry Series Two, Vol. 10 (Solid State Chemistry).* Ed. I.E.J. Roberts. London; Butherworths, 1975.
[10] West, A. R. *Solid State Chemistry and its Applications.* Trowbridge, Wiltshire: John Wiley & Sons, 1995.
[11] Gutzzow, I., Schmelzer, J. *The Vitreous State.* Berlin: Springer-Verlag, 1995.
[12] Zachariasen, W.H. *Journal of American Chemical Society.* **54** (1932), 3841.
[13] Warren, B.E. *Journal of Applied Physics.* **8** (1937), 645.
[14] Porai-Koshits, E.A., *The Structure of Glass.* New York: Consultants Bureau Inc, 1958.
[15] Huggins, M.L., Sun, K.H., and Silverman, A. *Journal of American Ceramics Society.* **26** (1943), 393.
[16] Bockris, J. O´ M., Mackenzie, J.D., and Kitchener, J.A. *Transaction of Faraday Society.* **51** (1955), 1734.
[17] Beall, G. H. and Duke, D.A. *"Glass-ceramic Technology" in: Glass Science and Technology* **1**. London: Academic Press, 1983.
[18] McMillan, P.W. *Glas-Ceramics.* London: Academic Press, 1979.
[19] McMillan, P.W. *Glas-Ceramics.* London: Academic Press, 1964.
[20] Ravaine, D. and Souquet, J.L. *"Ionic Conductive Glasses" in: Solid Electrolytes; general principles, characterization, materials, applications.* Eds. P. Hagenmuller and W. Van Gool. New York: Academic Press, 1978.

[21] Rawson, H. *Properties and Applications of Glass.* Amsterdam: Elsevier Scientific Publishing Company, 1980.
[22] Kittel, C. *Introduction to Solid State Physics.* 7th ed. New York: John Wiley & Sons, Inc., 1996.
[23] Hench, L.L. and West. J.K. *Principles of Electronic Ceramics.* Singapore: John Wiley & Son, 1990.
[24] Ingram, M.D. *"Electrical Properties of Glasses" in: Materials Science and Technology; A Comprehensive Treatment,* **9**. Ed. J. Zrzycki. Weinheim: VCH, 1991.
[25] Otto, K. *Physics and Chemistry of Glasses,* **7** (1966), 29.
[26] Charles, R.J. *Journal of the American Ceramics Society.* **49** (1966), 55.
[27] Hughes, K and Isard, J.O. *"Ionic Transport in Glasses" in: Physics of Electrolyte.* Ed. J. Hladik. London: Academic Press, 1972.
[28] Isard, J.O. *Journal of the Society of Glass Technology.* **43** (1959), 133T.

Chapter 4

Experimental Techniques; Theory and practice

4.1 Glass preparation

4.1.1 Compositions

The glass compositions to be studied were selected from the NASIGLAS system, with general formula $Na_{1+x}Zr_{2-x/3}Si_xP_{3-x}O_{12-2x/3}$. Five glass compositions, x = 2.00, 2.25, 2.50, 2.75 and 3.00, were chosen within the glass forming region of the ternary Na_2O-ZrO_2-SiO_2 system. For comparison, a second series was obtained by replacing ZrO_2 by TiO_2 to give the general formula $Na_{1+x}Ti_{2-3/x}Si_xP_{3-x}O_{12-2x/3}$, and exploit the comparatively larger glass forming region in the ternary system Na_2O-TiO_2-SiO_2. The nominal compositions of these glass samples are detailed in Table 4.01 and Fig 4.01 shows the ternary plot of the selected glass compositions. Hereafter, the prefixes G and NTS are used to differentiate the original NASIGLAS composition and TiO_2 substituted composition, respectively. The aim of producing these two series of glass composition was to study the glass forming ability of both series as well as to compare their properties, especially their electrical properties which is the main theme of this research. In applications, it is not only the electrical conductivity parameter which has practical significance but others physical properties, e.g. thermal expansion, density and mechanical strength, must also be optimised. Therefore, a vital point of this study is to obtain as much useful information as possible and to develop a possibly better understanding of these two glass series.

The main charge transport mode of NASIGLAS is ionic conduction, with Na^+ serving as the mobile species. In order to induce electronic conduction or to produce a mixed electronic/ionic conducting glass, some Fe_2O_3 dopant was introduced into the

NASIGLAS composition. Here, both glass series were doped with either 1 or 2 mol% of Fe_2O_3. Doping with these small amount of Fe_2O_3 is based on the assumption that it is uniformly distributed throughout the glass network and does not significantly affect thermal and mechanical properties.

4.1.2 Preparation procedures

The glass preparation process employed the conventional melt quenching method. High purity Na_2CO_3, ZrO_2, SiO_2 and Na_2HPO_4 were selected to be the starting materials for preparing the NASIGLAS system. Na_2CO_3 and Na_2HPO_4 were used as sources of Na_2O and P_2O_5. For the NTS glass samples, Na_3PO_4 was used as the source of P_2O_5 instead of Na_2HPO_4 and TiO_2 was substituted for ZrO_2. Before weighing, Na_2CO_3 was ground to a finer powder to eliminate the effect of starting material particle size. For a 50 g glass batch, all starting materials were accurately weighed to yield the desired stoichiometries in Table 4.01 and 4.02, and tumble mixed for several hours. The glass batch was melted in a Pt/Rh crucible, heated at about 10° C/min to 1600°C and held for 2 hours before raising to 1650°C at 8 °C/min, and keeping the temperature steady at 1650°C for approximately 40 minutes. Then the molten glass was quenched into cold de-ionised water. The glass frit produced was dried at 100°C in an oven for 8 hours. After that, the glass frit was re-melted, following exactly the same heating programme as the first melt. Next, the molten glass was cast into a steel mould and it was immediately annealed at the appropriate temperature identified from differential thermal analysis (DTA). The annealing took place for 2 hours, followed by cooling down at an arbitrary slow rate to room temperature. Finally, a thick block sample was obtained. Thin samples were also made, using the sample melting procedure, but finished by splat-quenching on a copper plate cooled by liquid nitrogen.

Table 4.01 *Mol% of component oxides in the nominal compositions of glass samples produced in this work;* $Na_{1+x}M_{2-x/3}Si_xP_{3-x}O_{12-x/3}$ *where M = Zr, Ti.*

X	Composition	Mol% of component oxides			
		Na_2O	MO_2	SiO_2	P_2O_5
3.00	$Na_4MSi_3O_{10}$	33.33	16.66	50.00	-
2.75	$Na_{3.75}M_{1.08}Si_{2.75}P_{0.250}O_{10.17}$	32.10	18.54	47.21	2.15
2.50	$Na_{3.50}M_{1.17}Si_{2.50}P_{0.50}O_{10.33}$	30.92	20.49	44.17	4.42
2.25	$Na_{3.25}M_{1.25}Si_{2.25}P_{0.75}O_{10.50}$	29.54	22.73	40.91	6.82
2.00	$Na_{3.00}M_{1.33}Si_{2.00}PO_{10.66}$	28.12	25.00	37.50	9.38

Note: *Only the first four compositions are selected for producing NASIGLAS samples.*

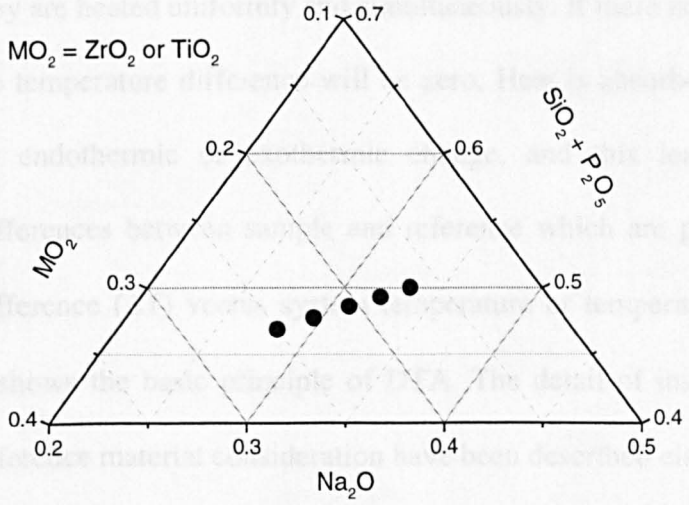

Figure 4.01 *Ternary plot of the selected glass compositions prepared in this work. Note that the graph is plotted in scale of mole fraction network formers (SiO_2+ P_2O_5), network modifiers (Na_2O) and network "intermediates" (ZrO_2 or TiO_2)*

4.2 Thermal techniques

4.2.1 Differential Thermal Analysis (DTA)

4.2.1.1 DTA theory

Thermal Analysis is an important technique for investigation of a material. There are many techniques which comprise thermal analysis; for example Thermogravimetry (TG), Differential Thermal Analysis (DTA), Differential Scanning Calorimetry (DSC)

and Thermo-mechanical Analysis (TMA). The principle of DTA is the detection of heat transfer related to changes in Gibbs' free energy in the sample during heating; such as oxidation, glass transformation, crystallisation, melting or decomposition which produce a change in temperature. The transformation from initial phase to final phase in a material means that, due to their different value of Gibbs free energy, heat is either evolved or absorbed. This evolution or absorption of the heat can be measured directly and used to investigate the kinetics of glass transformation, crystallisation or devitrification and glass melting,

DTA involves measuring the temperature difference between a sample and an inert reference as they are heated uniformly and simultaneously. If there is no transformation in the sample, the temperature difference will be zero. Heat is absorbed or evolved by the sample during endothermic or exothermic change, and this leads to characteristic temperature differences between sample and reference which are plotted as a graph of temperature difference (ΔT) versus system temperature or temperature of the reference (T). Fig. 4.02 shows the basic principle of DTA. The detail of instrumentation, design method, and reference material consideration have been described elsewhere [1,2].

Even though the basic principles of DTA are not complicated, in practice, it should be recognised that it is a comparative not an absolute method. To obtain good data requires control of equipment and sample. The position of the heating block with respect to the furnace, the position of sample wells in the heating block, the position of the thermocouples, the shape of crucibles, are all important. Sample parameters such as sample size, sample particle size and sample packing can affect the shape and position of the DTA curves. Also thermal conductivity of the sample and sample holder and the heating rate are important. Explanation of the effect of these parameters and their control can be found elsewhere [3].

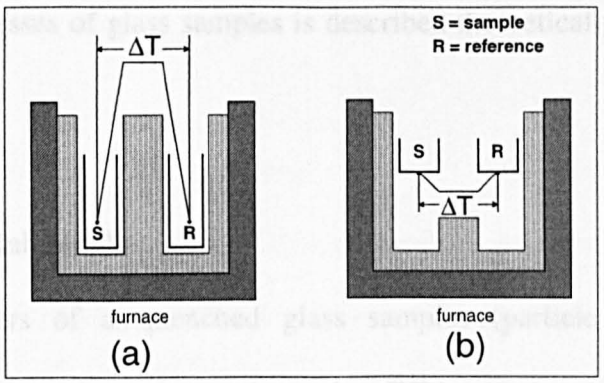

Figure 4.02. *Two possible arrangements of DTA apparatus; (a) Classical arrangement and (b) Calorimetric DTA or heat-flux DSC.*

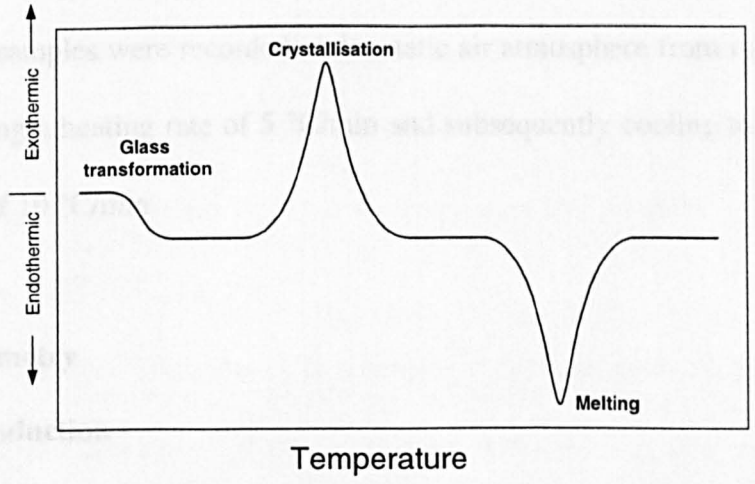

Figure 4.03. *A schematic DTA curve of glass characterisation.*

DTA characterisation of glasses is extensive. Detailed discussions of both the theoretical and practical aspects of the technique have been reported in the literature [4-6], and the application of DTA in the study of glasses has been reviewed [7]. In Fig 4.03, there are three thermal events related to behaviour of glass; (i) crystallisation, (ii) melting, and (iii) glass transformation. When glass transforms from rigid glass to a supercooled liquid, the glass transformation temperature is represented by a shift of baseline; crystallisation in a glass sample is related to the exothermic peak and melting is related to

the endothermic peak. The method of studying the kinetics of glass transformation and crystallisation processes of glass samples is described theoretically as well as practically in ref. [8].

4.2.1.2 Experimental details

Fine powders of as-quenched glass samples (particle size ~38 μm) were investigated about their thermal response using DTA technique. The ***Stanton Redcroft DTA 673-4*** module was employed as the main instrument with platinum crucibles. Fine powder of silica (SiO_2) and alumina (Al_2O_3) were selected to be the reference substances. The mass of both sample and reference substances were set to be 120 mg. The DTA data of the glass samples were recorded under static air atmosphere from room temperature to 1500 °C using a heating rate of 5 °C/min and subsequently cooling to room temperature with a rate of 10 °C/min.

4.2.2 Dilatometry

4.2.2.1 Introduction

Dilatometry is widely used for the measurement of the thermal expansion coefficient (TEC) of several classes of materials. The basic principle of dilatometry is the measurement of the increase in length of a rod shaped sample on increasing the temperature. Experimentally, micron resolution allows the TEC to be determined to better than 1%. However, in order to determine the thermal expansion coefficient correctly, calibration of the equipment with a standard material is needed. During this work, a standard commercial Pt rod was used as a reference. Most values of TEC are reported over a specific temperature range, therefore care must be taken when comparing experimental values. The units should also be carefully compared since several have been

in common usage. For example, glass scientists have frequently used units of 10^{-7} K^{-1} in reporting TEC values of glasses.

4.2.2.2 Basic theory of thermal expansion

When a material experiences constant heating, the atoms in that material are excited and produce anharmonic vibrations, as a result of which there is an increase of interatomic distance or bond angle and hence the expansion of the whole substance [9]. The thermodynamic coefficient of thermal expansion, β, is defined as a rate of change in volume V, with temperature [10]. This can be expressed as

$$\beta = 1/V.(\partial V/\partial T)_P \qquad 4.1$$

where V is a function of the absolute temperature T, at constant pressure, P. Determining β, a 3 dimensional quantity, is practically not straightforward. Alternatively, the linear thermal expansion coefficient, α, is taken into account and it is defined as

$$\alpha_x = 1/X.(\partial X/\partial T)_p \qquad 4.2$$

where the length X is a function of temperature at constant pressure. From Eq. 4.1, β can be also expressed as a sum of three coefficients as $\beta = \alpha_x + \alpha_y + \alpha_z$ where α_x, α_y and α_z are the coefficients of expansion along the x, y and z axes, respectively. For isotropic materials such as glasses, the relation $\alpha_x = \alpha_y = \alpha_z$ holds, therefore, the relation between β and α can be reduced to

$$\beta = 3\alpha_x \qquad 4.3$$

However, α itself can be temperature dependent. In general, materials expand linearly only over a particular temperature range. Therefore, the reported value of α is normally specified by temperature range.

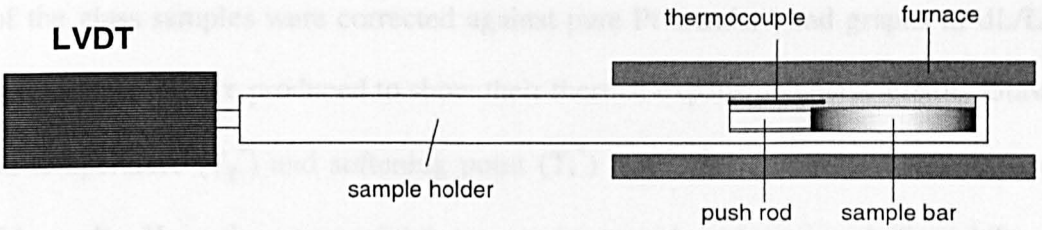

Figure 4.04. *Schematic diagram of dilatometer (Netzsch 402E).*

4.2.2.3 Methods of measurement

In this work, measurements were performed using the commercial dilatometer, Netzsch 402E. Its schematic diagram is shown in Fig. 4.04. During measurement, the bar shaped sample is placed in the alumina sample holder with one face of the sample in contact with the alumina push rod, whose other end is in contact with the core of a linear variable differential transducer or LVDT. The main component of an LVDT is an inductance coil, which is capable of detecting very small movements of the core when the push rod moves in either positive or negative direction. To obtain high accuracy experimental values, a low heating rate is applied, normally in the range 2-3 °C/min. The temperature of sample is determined by placing a thermocouple close to, but not touching, the sample.

4.2.2.4 Experimental details

Bar shaped samples of dimension approximately 5mm × 5mm × 25 mm were used for dilatometric measurement. All samples were obtained from cutting bulk glass specimens which had been annealed at around 50 °C below T_g for 3 hours. The dilatometric measurements were performed in a temperature range from room temperature up to 900 °C with a heating rate of 2 °C/min and under air atmosphere. Experimentally, the dilatometric acquisition range did not exceed the temperature of softening point at which viscous flow was detectable. The thermal expansion coefficients

(TEC) of the glass samples were corrected against pure Pt standard and graphs of dL/L_0 versus temperature T were produced to show their thermal expansion characteristic. Glass transition temperature (T_g^*) and softening point (T_s^*) were also determined to compare with DTA results. Here, the superscript * was used to avoid confusion with T_g and T_s of the DTA data.

4.3 Nuclear Magnetic Resonance (NMR)

4.3.1 Basic NMR

Like the electron, nuclei have an intrinsic angular momentum, or spin, which is characterised by a spin quantum number I. The magnitude of the spin angular momentum is given by $S = \hbar\sqrt{(I(I+1)}$, and the orientation of the spin angular momentum is restricted by the condition $S_z = m\hbar$; where m is an integer or half integer and the allowed values of m range between –I and +I at integer intervals. Associated with the intrinsic spin angular momentum is an intrinsic magnetic moment μ, which is expressed as

$$\vec{\mu} = \gamma\hbar\vec{I} = g\vec{\mu}_N \qquad 4.4$$

where γ is known as the "gyromagnetic ratio" and g is the nuclear g factor. The quantization laws of angular momentum predict the presence of 2I+1 states. On application of an external magnetic field of magnitude B_0 to the nuclei, the degeneracy of all possible states is removed, due to the Zeeman interaction between the nuclear magnetic moment and the external field. The energy of this interaction is

$$E = -\vec{\mu}.\vec{B}_0 \qquad 4.5$$

If the alignment of the external field is in the z- direction, the allowed energy levels of the states are then

$$E_m = -\gamma S_z B = -\gamma m\hbar B \qquad 4.6$$

Here B is the magnetic field experienced by the nuclei, it comprises the external field B_0 and internal components B_{int} (i.e. $B_{int} << B_0$), which arise from internal interaction of the nuclei with their surrounding environments; Thus, $\vec{B} = \vec{B}_0 + \vec{B}_{int}$, and separation between Zeeman energy levels is

$$\Delta E = \gamma \hbar B$$

For the example of spin I =3/2, the Zeeman energy levels are shown in Fig. 4.05.

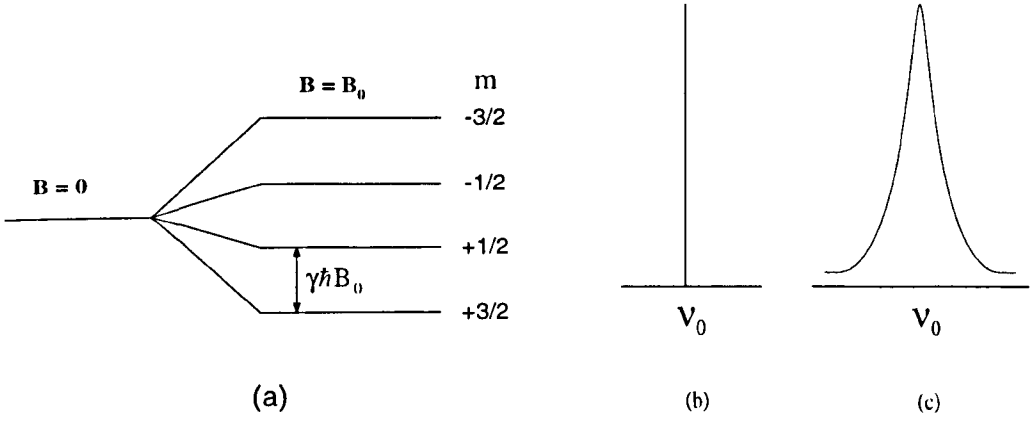

Figure 4.05. *Characteristics of the Zeeman interaction (a) Zeeman energy levels, (b) Spectrum line at the resonance frequency ν_0 and (c) broadened line shape of spectrum.*

Since the internal field (B_{int}) is initially related to the structure of the material, its evaluation is of major interest in nuclear magnetic resonance spectroscopy.

Electromagnetic radiation of radio frequency is applied, and the transition between the Zeeman energy levels is induced from the energy absorption [11]. Thus the resonance frequency (ν_0) associated with the energy difference between states is

$$\Delta E = h\upsilon_0 = \gamma \hbar B, \quad \upsilon_0 = \gamma \frac{B}{2\pi} \qquad 4.7$$

The resulting NMR absorption spectrum is a single sharp peak at ν_0.

In general, B_{int} arises from the combined effect of three physically distinct interaction mechanisms; (1) magnetic dipole-dipole coupling, (2) magnetic shielding and (3) electric quadrupole coupling (for spin I> ½). These interactions play an important role

in determining the resonance frequency and line shape of the NMR spectrum. The following sections detail the effect of each interaction on the NMR spectrum.

4.3.2 Magnetic dipole-dipole interaction

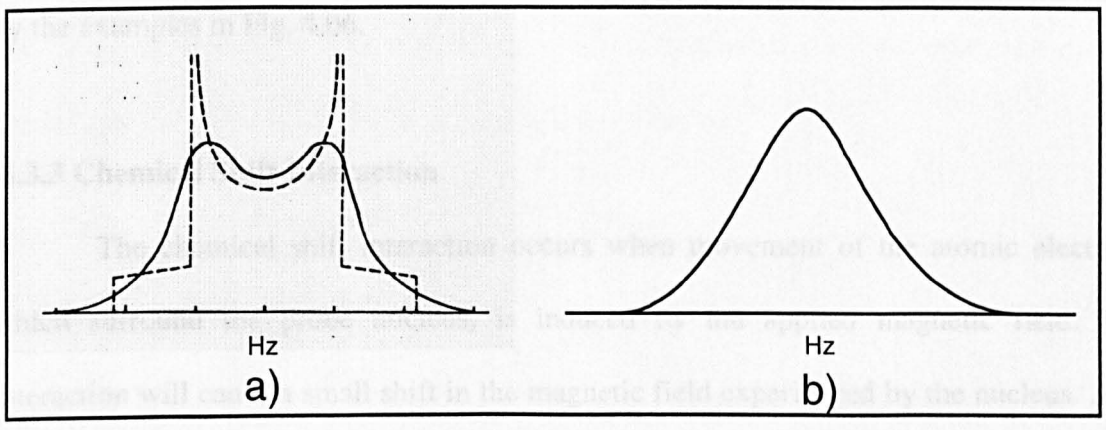

Figure 4.06 *NMR spectral lineshape effected by the dipole-dipole interaction, a) for two-spin system (dotted curve is of isolated pair of nuclei and solid curve shows the powder pattern) and b) for many-spin system.*

The dipole-dipole interaction represents the effect of neighbouring nuclear magnetic moments on the observed nucleus. The effect on the NMR line shape produces overall broadening (Fig 4.05c). The line width is dependent on the magnitudes of the magnetic moments, and their internuclear separation (r). The dipolar contribution to the full width at half maximum (FWHM) of the NMR line broadening (φ), can be calculated by using Van Vleck's method of moments. Hence, it gives

$$\varphi = 2.36\sqrt{M_2^I} \qquad 4.8$$

where M_2^I is the *second moment* for a nuclear spin in the presence of like spins (I) and unlike spins (S). It has been shown that for polycrystalline materials and glassy samples, the second moment can be given as [12]

$$M_2^I = \Delta_{II} + \Delta_{IS} \qquad 4.9$$

$$\Delta_{II} = \frac{3}{5}\gamma_I^4\hbar^2.I(I+1)\sum\frac{1}{r_{ij}^6}$$
$$\Delta_{IS} = \frac{4}{15}\gamma_I^2\gamma_S^2\hbar^2.S(S+1)\sum\frac{1}{r_{ik}^6} \qquad 4.10$$

where r_{ij} and r_{ik} are the internuclear distance r from probed nucleus to homonucleus and heteronucleus, respectively. The effect of this interaction on the NMR line shape is shown by the examples in Fig. 4.06.

4.3.3 Chemical Shift Interaction

The chemical shift interaction occurs when movement of the atomic electrons which surround the probe nucleus, is induced by the applied magnetic field. The interaction will cause a small shift in the magnetic field experienced by the nucleus. As a result, the resonance frequency ν_0 is influenced. The change of ν_0 is termed "Chemical shift" and it is measured in parts per millions (ppm). Such influences comprise, (a) diamagnetic shielding by closed electronic shells, (b) paramagnetic deshielding by the angular momenta of admixed excited electronic states, (c) shielding or deshielding effects from rapidly fluctuating paramagnetic electron spins, and (d) shielding or deshielding effects due to conduction electrons at the Fermi edge ("Knight shift") [13]. The energy of interaction can be expressed as the coupling of the spin vector $\vec{I}$ with the magnetic field $\vec{B}$ via the chemical shift tensor (σ);

$$E_{CS} = \gamma(h/2\pi).\vec{I}.\sigma.\vec{B} \qquad 4.11$$

Then the observed spectral frequency becomes

$$\nu = \nu_0(1-\sigma_{zz}) \qquad 4.12$$

Where ν_0 is the resonance frequency of the bare nucleus and σ_{zz} is the component of the shift tensor along the direction of the external magnetic field. In the principal axis system

(x,y,z), the diagonal components of the chemical shift tensor are denoted as σ_1, σ_2, and σ_3 respectively. If the NMR lineshape is dominated by the chemical shift anisotropy, the NMR frequency depends on the polar and azimuthal angles θ and ϕ of the chemical shift principal axis system relative to the direction of the magnetic field (Fig. 4.07), that is

$$\nu = \nu_0(1-\sigma_{iso}-\sigma_{ax}(3\cos^2\theta-1)-\sigma_{aniso}(\sin^2\theta\cos 2\phi) \qquad 4.13$$

Where σ_{iso} = isotropic chemical shift, σ_{ax} = axially symmetric chemical shift, and σ_{aniso} = anisotropic chemical shift. These parameters are given by

$$\begin{aligned} \sigma_{iso} &= \frac{1}{3}(\sigma_1+\sigma_2+\sigma_3) \\ \sigma_{ax} &= \frac{1}{6}(2\sigma_3-\sigma_1+\sigma_2) \\ \sigma_{aniso} &= \frac{1}{2}(\sigma_2-\sigma_1) \end{aligned} \qquad 4.14$$

The frequency ν depends on θ and ϕ. These give the NMR spectrum of the glassy sample or powdered polycrystalline sample as the envelope of responses of all θ and ϕ values. Representative powder patterns are shown in Fig 4.07. The three components of the chemical shift are selected so that $\sigma_{11} \leq \sigma_{22} \leq \sigma_{33}$ and the asymmetry parameter is denoted by η where $\eta = (\sigma_{22} - \sigma_{11})/(\sigma_{33} - \sigma)$ [14]. Thus for axial symmetry $\sigma_{22} = \sigma_{11}$ and $\eta = 0$ and for lower symmetry η will range between 0 and 1.

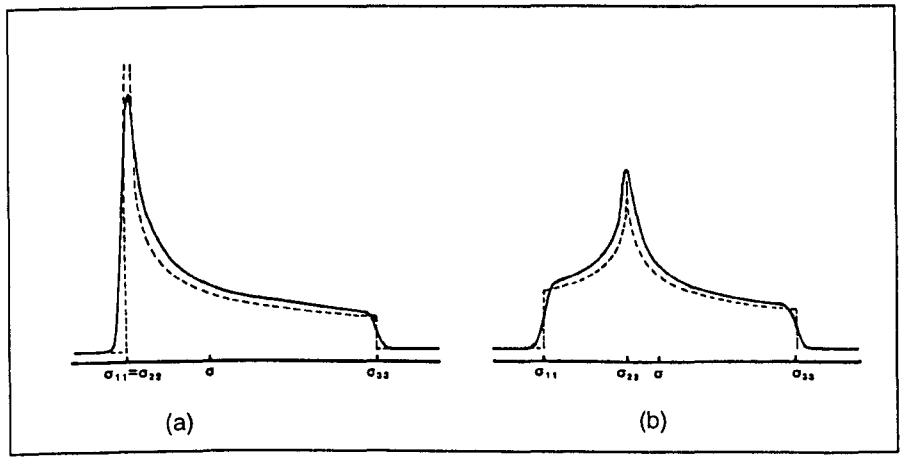

Figure 4.07. *The NMR lineshape (powder pattern) showing the influence of chemical shift, (a) axial site symmetry, (b) lower site symmetry (After Dupree and Holland, 1988).*

To determine the structure of a material, the resonance frequency of a particular nucleus is normally reported in terms of the chemical shift, δ, relative to the resonance of an experimentally useful standard reference substance, whose structure is clearly known [15]. Hence

$$\delta = (\nu_{sample}-\nu_{reference})/\nu_{reference} \times 10^6 \text{ ppm} \qquad 4.15$$

4.3.4 Nuclear electric quadrupole interaction

The nuclear electric quadrupole interaction is described as the interaction of a non-spherically symmetric nuclear charge distribution ("nuclear electric quadrupole tensor") with the electric field gradient (EFG). The EFG is generated by asymmetric electron distributions in molecules or lattice sites. The nuclear electric quadrupole interaction occurs in nuclei of spin 1 or more and is denoted as eQ. The energy levels of the nucleus depend on the orientation of the charge distribution with respect to the principal axes of the EFG [13]. EFG is not generated by closed shell of electrons but by bonding electrons and it decreases as r^{-3}. Thus, quadrupolar interaction is highly sensitive to configuration of chemical bonding and atomic arrangements. If we treat the quadrupole interaction as a first-order perturbation to the Zeeman energy levels, the frequency corresponding to the energy of transitions from m to m-1 will be

$$\nu_{m\to m-1} = \nu_0 - \nu_Q \frac{(m-1/2)}{2}[3\cos^2\theta - 1 - \eta\sin^2\theta\cos 2\phi] \qquad 4.15$$

where

$$\nu_Q = \frac{3Q_{cc}}{2I(2I-1)} \quad \text{and} \quad Q_{cc} = \frac{eQV_{zz}}{h} \qquad 4.16$$

Q_{cc} is the quadrupole coupling constant. The asymmetry parameter η is used to determine the departure of the EFG from cylindrical symmetry and it is given by

$$\eta = \frac{V_{xx}-V_{yy}}{V_{zz}} \quad ;0\le\eta\le 1 \qquad 4.17$$

where V_{xx}, V_{yy}, and V_{zz} are the diagonal components of the EFG tensor expressed in this principal axis system. The polar angles θ and ϕ are the orientations of the magnetic field with respect to the principal axis system of the EFG tensor. In a glass or polycrystalline sample, all orientations of the principal axis system will occur and give a powder pattern to the NMR spectrum lineshape.

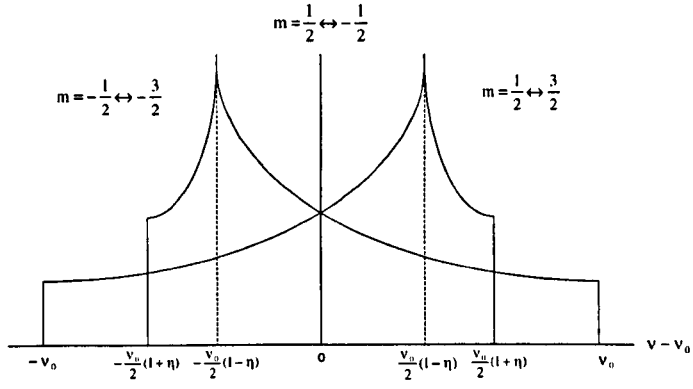

Figure 4.08. *First-order quadrupole powder pattern for a system of spin 3/2 nuclei. The central transition is not affected [12].*

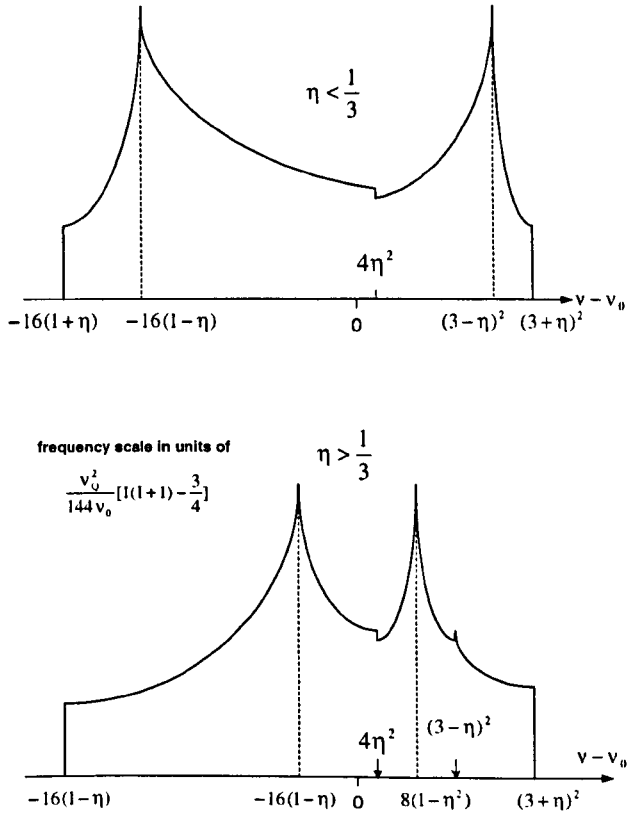

Figure 4.09. *Second-order quadrupole powder pattern for the central transition of a half-integral nuclear spin. They are shown in case of η less than and more than 1/3 [12].*

The magnitude of external magnetic field has no influence on the NMR spectrum due to a first-order quadrupole effect. For the example of a spin 3/2 nucleus, the powder pattern is shown by Fig. 4.08. However, the dominant interaction is a second-order quadrupole effect which is expressed by Eq. 4.18 and the contribution to the spectral lineshape are shown in Fig. 4.09.

$$\nu_{m\rightarrow m-1}{}^{2nd} = (-\nu_q^2/16\nu_0)(a-3/4)(1-\cos^2\theta)(9\cos^2\theta-1) \qquad 4.18$$

where a = I(I+1).

Then parameters Q_{cc} and η can be determined from NMR line shape. When the strength of the quadrupole interaction is large, second order effects in the NMR spectrum for a glass or polycrystalline powder produce a broadening that varies inversely with the magnitude of the external field [16]. The central transition (m=1/2 $\leftrightarrow$m= -1/2), is broadened by an amount that depends on η and Q_{cc} (Fig. 4.09).

4.3.5 Experimental techniques of NMR

There are two basic techniques in NMR; continuous wave and pulse spectroscopy. They are employed to excite the nuclear magnetization with radio frequency (RF). The subsequent response of the spin system is measured by detecting the absorbed energy. There are advantages and disadvantages in each method, depending on the width of the NMR line and type of information sought.

- Pulsed NMR

In pulsed NMR spectroscopy the entire frequency range of interest is irradiated simultaneously by a short intense RF pulse (1-10 μs length and 100-1000 Watt power). For a pulse length of t_p, with angular frequency γB_1, the local magnetisation of sample will be rotated from its equilibrium position along the z-axis by the angle

$$\theta_p = \gamma B_1 t_p \qquad 4.19$$

And will precess about the z-axis, as seen in Fig. 4.10. If the rotating frame precesses about the z-axis, the magnetisation will be stationary. The component of $\bar{M}$ in the xy plane will induce a signal in a receiver coil, known as free induction. Experimentally, a short pulse is applied to tip the magnetization from equilibrium into the plane perpendicular to the direction of the magnetic field, this pulse is called the "90° pulse". The principle is illustrated with vector diagrams in Fig. 4.11. Immediately following the pulse, spin-spin interaction (characterised by the time constant T_2) causes dephasing of the spins and reduces the magnitude of $\bar{M}$. The other phenomenon is spin-lattice relaxation which returns the magnetisation vector toward equilibrium, diminishing the free induction. The time of spin –lattice relaxation has been denoted as T_1. The decaying signal is termed the free induction decay (FID) and it is characterised by a time constant T_2^* (the apparent T_2) [13]. It is inversely related to the line width of the absorption spectrum as shown in figure 4.12. The T_2^* is approximated as

$$\frac{1}{T_2^*} \approx \frac{1}{2T_1} + \frac{1}{T_2} + \gamma \delta B_0 \qquad 4.20$$

In the case of a solid sample, $T_1 >> T_2$; hence the T_2 term dominates the decay rate. The last term in the Eq. 4.20 represents broadening due to field inhomogeneity of extent δB_0.

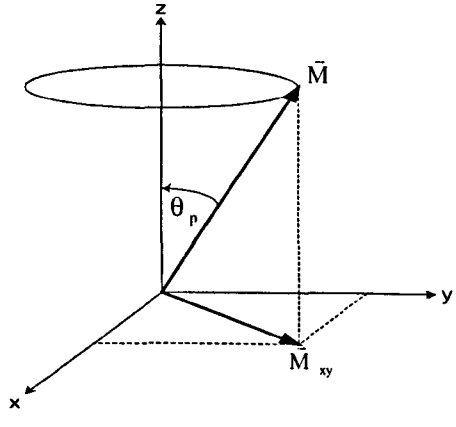

Figure 4.10. *A pulse of length t_p rotates the magnetisation vector from its equilibrium position by an angle θ_p.*

The frequency range of observation or spectral width, SW, is inversely proportional to the pulse length, (t_p); shorter pulse lengths allow irradiation of a broader frequency range. Pulse lengths are typically of the order of a microsecond. The delay time is a most important parameter in the experiment, because the spin system requires sufficient time to relax to its equilibrium [12]. If the delay time is not long enough, the acquired signal will be very weak but it should not be very long, otherwise one experiment will require a extensive acquisition time. For quantitative applications, the delay time must exceed 5 times the longest spin-relaxation time present in the sample.

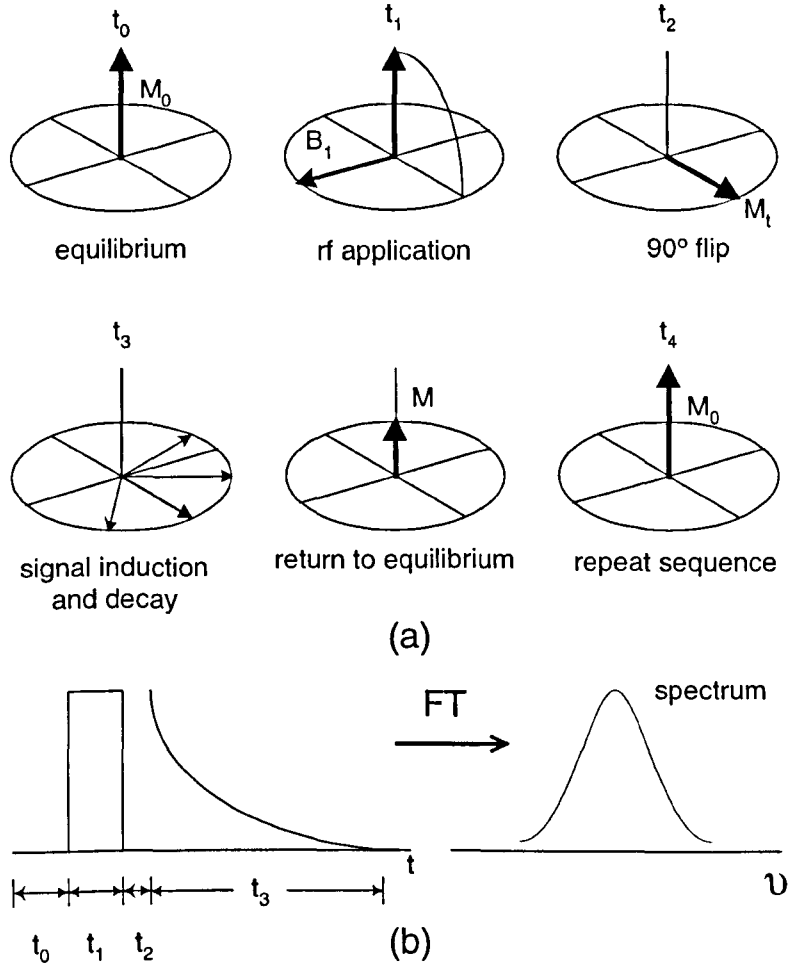

Figure 4.11 *(a) Detection of NMR signals by pulsed spectroscopy, shown in a rotating frame associated with magnetic field B_0 in the z-direction at various stages of the experiment: t_0 -spin system with magnetization at equilibrium (M_0), in other words, time t_0 is the delay time of the pulse sequence, t_1 (pulse length) -irradiation of the rf field B_1 orthogonal to the magnetization direction tips the magnetization, t_2 – the system after a 90°pulse resulting in transverse magnetization M_t, t_3 –off-resonance precession and free induction decay in the signal acquisition period following the pulse, t_4 -return to spin equilibrium due to spin-lattice relaxation. (b) Timing diagram of the experiment followed by Fourier transformation.*

- Magic-Angle Spinning NMR (MAS-NMR)

The broadening of the line shape is critical in resolving the different nucleus sites. Dipolar, chemical shift, and first-order quadrupolar interaction can contribute to the broadening, and they contain terms that have an angular dependence of $1\text{-}3\cos^2\theta$ where θ is the angle between the internuclear vector and the external magnetic field. Then, if θ = 54.74°, the relative terms will be zero and narrowing of the NMR line shape will result [17]. In the MAS-NMR technique; the sample is placed in a rotor and the axis of the rotor is oriented at an angle of θ = 54.74° with respect to the external field. In that orientation, the sample is spun at constant frequency (normally of the order of kHz). Therefore, any internuclear vector will be averaged along the rotation axis of a rotor (Fig.4.13). To narrow the line effectively, the rate of rotation must exceed the line width, otherwise the transverse magnetisation decays faster than the time it takes to complete one revolution.

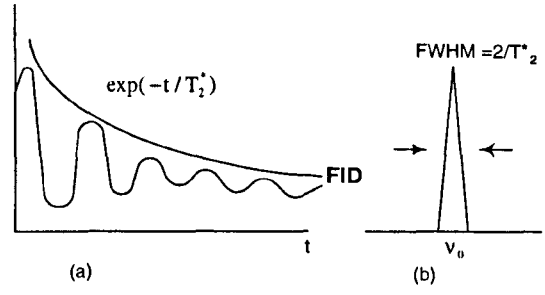

Figure 4.12. *(a) FID decay and (b) The FWHM value associated with* T_2^*

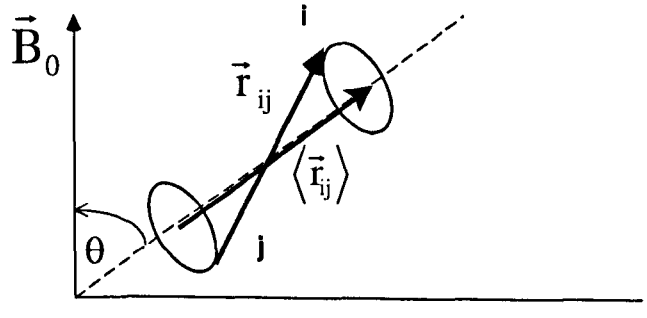

Figure 4.13. *Orientation of the spin axis of the sample.*

4.3.6 Experimental details

4.3.6.1 Introduction

Two spectrometers were employed in the solid state NMR measurements, a BRUKER MSL 300 and a CMX 360 with magnetic field strengths 7.05 T and 8.45 T respectively. The related resonance frequencies of three particular nuclei, ^{23}Na, ^{29}Si and ^{31}P, are detailed in Table 4.02.

Table 4.02 *Resonance frequency of ^{23}Na, ^{29}Si and ^{31}P in two different magnetic fields.*

Nuclei	Resonance frequency of nuclei (MHz)	
	7.05 T	8.45 T
^{23}Na	79.38	95.26
^{29}Si	59.63	71.58
^{31}P	121.50	145.78

4.3.6.2 ^{29}Si MAS NMR

The ^{29}Si MAS NMR spectra were recorded from fine powder of as-quenched samples contained paramagnetic impurity (i.e. doping with 0.1 mol% of Fe_2O_3 to reduce the relaxation time of ^{29}Si nuclei) using both spectrometers. The ^{29}Si chemical shifts were referenced to TMS (tetramethylsilane). The experimental parameters for each sample group are summarised in Table 4.03a.

Table 4.03a *Experimental details of ^{29}Si MAS NMR.*

Sample	Pulse width (μs)	Pulse delay time (s)	Sample spinning speed (kHz)
NASIGLAS	2	30	3.7
NTS glass	2	30	10.0
Glass ceramics	2	20	4.2

4.3.6.3 ^{31}P MAS NMR

^{31}P MAS NMR spectra were acquired using the spectrometer CMX 360. Fine powder of as-quenched and heat treated glass samples (no paramagnetic impurity) were used to fill a zirconia rotor of 4 mm diameter. The ^{31}P chemical shifts were referenced to the shift of finely powdered $NH_4H_2PO_4$ which possess $\delta^{31}P \approx -0.9$ ppm with respect to H_3PO_4. The experimental parameters are summarised in Table 4.03b

Table 4.03b *Experimental parameters of ^{31}P MAS NMR experiments.*

Sample	Pulse width (μs)	Pulse delay (s)	Sample spinning speed (kHz)
NASIGLAS	2	10	10
NTG glass	2	60	6, 10
Glass ceramics	2	30	10

4.3.6.4 ^{23}Na MAS NMR

^{23}Na MAS NMR spectra were recorded using the CMX360 spectrometer. A zirconia rotor of 4 mm diameter was used. The ^{23}Na chemical shifts were referenced to the shift of NaCl solution. The experimental parameters are summarised in Table 4.03c.

Table 4.03c *Experimental parameters of ^{31}P MAS NMR experiments*

Sample	Pulse width (μs)	Pulse delay (s)	Sample spinning speed (kHz)
NASIGLAS	2	2	10
NTG glass	2	1	10
Glass ceramics	2	1	10

4.4 Crystallisation studies

4.4.1 X-ray diffraction (XRD)

4.4.1.1 Theory

X-rays are a form of electromagnetic radiation that have high energies and short wavelengths, of the order of the atomic spacing for solids. When a beam of x-rays

impinges on a solid material, a part of this beam will be scattered in all directions by the electrons associated with each atom or ion that lies within the beam's path. Diffraction occurs when x-rays scattering from an object interfere constructively and destructively with each other. The intensity pattern of diffracted x-rays will correspond to the arrangement of planes of atoms in an object. Therefore, the diffraction pattern will be different for each solid structure and depend on space group and site occupancy. W.L. Bragg was the first to show that the scattering process which leads to diffraction can be equally visualised as if the x-rays were "reflecting" from the planes defined by Miller indices hkl (Fig 4.14). The condition of diffraction is given by Bragg's law [18],

$$2d_{hkl}\sin\theta = n\lambda \qquad 4.21$$

where d_{hkl} is the distance between planes which correspond to an interatomic spacing, θ is the diffracted angle, λ is the wavelength of the x-rays and n is the order of diffraction

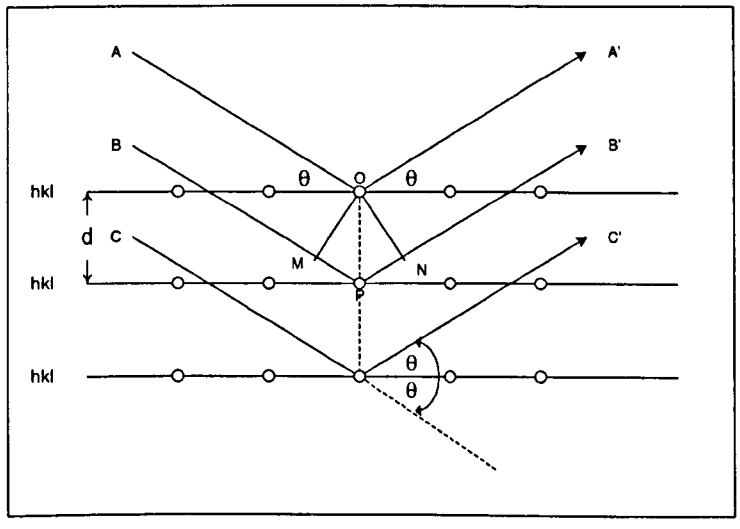

Figure 4.14. *Diffraction of x-rays from the planes of atoms. The miller indices hkl is used to specify the order of atomic planes.*

There are three standard methods of x-ray diffraction: (a) the Laue method, involving a stationary single crystal, (b) the rotating crystal method, (c) the powder method, involving a polycrystalline sample. X-ray powder diffractometers are commonly

used for identification of crystal structure, analysis, etc.; for accurate determination of cell dimensions, the Guinier focussing camera is often employed. Generally, schematic representation of powder pattern of XRD is a plot of intensity versus 2θ or d-spacing values.

Solid materials can occur in two structural forms, crystalline and amorphous. A periodic arrangement in the array of atoms can be found in the polycrystalline substance, however a random arrangement is found in amorphous material. The long range order of atoms in crystalline materials gives a powder pattern of sharp peaks. The angles of diffraction yield inter-planar separations. The powder pattern of the amorphous state gives just a broad peak [19]. For this reason, although determination of the structure of crystalline materials can be done directly from x-ray diffraction, other techniques also need to be applied to identify the structure of amorphous solids. The intensity of diffraction from an amorphous material, as a function of angle, can be transformed to obtain the Radial Distribution Function (RDF). This function can be used to determine the average interatomic distance and also provides the co-ordination number of the observed atoms by estimation [20]. Even so, the RDF only gives information on short-range order.

4.4.1.2 Experimental details

All samples subjected to XRD measurement were ground to fine powder. Monochromatic CuKα_1 radiation was employed and the XRD data were obtained over 2θ range from 5° to 75° with scanning rate of 0.02° a second.

4.4.2 Scanning Electron Microscopy (SEM)

4.4.2.1 General

In SEM, the electron beam is used to produce the image of the specimen under examination. During operation, an electron beam is scanned on the specimen by starting

from the top left corner of the area, pixel by pixel, until the whole area has been scanned. When the specimen is being irradiated by the electron beam, a variety of electron and photon emissions are produced. The chosen signal is collected, detected, amplified and used to modulate the brightness on the cathode ray tube (CRT) display. If the dimension of area needed to scan a specimen is M × M in size, and the displaying area of CRT is N × N in size, variations in signal from the specimen will be mapped onto the CRT as variations in brightness with a linear magnifications of N/M. Then, the magnification can be simply adjusted by varying the dimensions of the area scanned on the specimen.

The main components of an SEM are electron column and display unit. The electron column is operated in vacuum. The electron beam is generated by an electron gun of which two types are currently used; thermionic electron gun and field emission electron gun. Typically, the electron gun is operated over a voltage range 0 to 30 keV. The specimen is maintained at earth potential. To get the best resolution, the electron beam must have high brightness or energy and its diameter has to be small [21]. Also, any unintentionally generated noise should be as low as possible.

Sample preparation for the SEM is ideally no prior treatment needed. In practice, it is desirable to ensure that surfaces to be examined are free from all form of defect and contamination. For the rigid solid, a well smoothly polished surface is required to eliminate unwanted effects. But one has to ensure that polishing does not produce microstructural or chemical change in the specimen. If the specimen is not a good electrical conductor, it is often provided with some conductivity by coating the surface of interest with a thin metal layer (typically 3 to 10 nm of gold) and electrically grounding this [22].

4.4.2.2 The image modes of the SEM

The interaction between electrons and a specimen produces several emissions (Fig. 4.15), all of which are potentially useful for imaging. Each corresponding signal carries different information about the specimen. From the interaction, two types of electrons will be scattered. *Backscattered electrons* are scattered back in the opposite direction for the primary electrons with only a small of energy loss. Some electrons will be scattered many times within the specimen before escaping from the specimen surface, and they lose a considerable amount of their energy. There are termed *Secondary electrons.* The energy of backscattered electrons is higher and closest to that of the primary beam. But backscattered electrons are not usually as numerous as secondary electron. Therefore, secondary electrons seem to be the most popular choice of interaction with which to form an image [23].

The other interaction which can be used to form an image is that between the primary electron beam and the electrons in the valence band in semiconductor type specimen. This interaction creates an electron-hole pair in the specimen which drift in opposite directions under external bias. The movement of electron and hole will generate the *specimen current* [23], which carries local information on the semiconductor specimen. These three commonly used imaging modes are summarised in Table 4.05 along with the information obtained as well as the associated resolution [23].

4.4.2.3 Experimental details

The samples subjected to microstructure investigation were glass ceramic samples which had been heat treated at appropriate temperatures and times. Bulk glass ceramic samples were cross sectioned, mounted and polished, followed by carbon coating. During image acquisition, both backscattered and secondary electron modes were used with an

accelerating voltage 20 kV. Energy dispersive X-ray spectrometry (EDX) was also performed.

Table 4.04 *The three commonly used imaging modes in SEM together with resolution attainable [24].*

Mode	Information	Typical resolution (nm)	High resolution (nm)
Backscattered electrons	Topographic, Crystallographic, Composition	10	3
Secondary	Topographic	10	3
	Voltage	100	50
	Magnetic and Electric field	500	100
Absorbed specimen current	Topographic	50	20
	Composition		

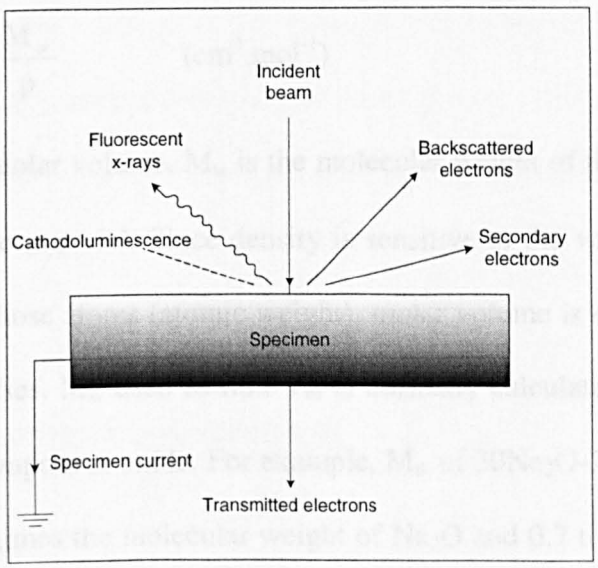

Figure 4.15. *Imaging modes available from the variety of emissions produced from a specimen when illuminated by an electron beam.*

4.5 Density measurement

4.5.1 Theory

Generally, the density of a material is defined as the mass of substance per unit volume, or

$$\rho = \frac{m}{V} \quad g.cm^{-3} \qquad 4.22$$

where ρ is the density, m is the mass and V is the volume of sample. We can get a true density value from direct calculation if the sample is free from bubbles, voids or other defects. If, however, the sample contains bubbles or some defects, especially in the case of glass samples, the calculated density will be less than that of the true density and is termed the "apparent density". In some cases, the apparent density might be higher than the true density when particles of non-melted batches are present, or crystals form during cooling of the glass melt.

The molar volume is defined as the volume occupied by one mole of a material and is obtained by dividing the molecular weight of a material by its density;

$$V_m = \frac{M_w}{\rho} \quad (cm^3.mol^{-1}) \qquad 4.23$$

where V_m is the molar volume, M_w is the molecular weight of the substance, and ρ is the true density of the material. Since density is sensitive to the volume occupied by atoms and the mass of those atoms (atomic weight), molar volume is often used to compare the behaviour of glasses. M_w used to find V_m is normally calculated from the mole fraction formula of the component oxide. For example, M_w of $30Na_2O$-$70SiO_2$ glass can be found by summing 0.3 times the molecular weight of Na_2O and 0.7 times the molecular weight of SiO_2 [25].

Density can be calculated from sample volume from accurately measured dimensions if the geometry is simple. Otherwise, the liquid displacement or Archimedes

method is employed. The sample is weighed both in air and when suspended in a liquid of knows density at the temperature of the experiment. The difference in weight equals the weight of displaced liquid. If W_a is the weight of sample in air and W_s is weight of sample when suspended in a liquid, then the density of the sample can be found through Eq. 4.24

$$\rho_x = \rho_l \cdot \left(\frac{W_a}{W_a - W_s}\right) \qquad 4.24$$

Where ρ_l is the density of the displaced liquid at the temperature of the experiment which is generally room temperature. The choice of the immersion liquid is based on convenience and the chemical durability of the sample. Water is usually employed, but kerosene or an alcohol, are also often used for samples which react with water.

4.5.2 Experimental details

Well-defined samples were selected and weighed both in air and as submerged in pure water at room temperature. Then the density values were evaluated using Eq. 4.24. The experiments were repeated several times to ensure the minimum error generated by the porous nature of glass samples. Silicate based glasses can absorb and react with water over a period of time. Hence, the weight was checked for stability over the experimental time scale, e.g. 2-10 min.

4.6 Ionic conductivity measurement

4.6.1 Introduction

The ionic conductivity of solid materials can be determined using direct current (dc) or alternating current (ac) techniques or both. To obtain highly accurate conductivity

data, the dc technique requires very sensitive apparatus to measure the very small currents which are normally used. The ac technique is more complicated but has advantages. The ac technique will be described in detail since it has been used in this work. First, the basic theory will be explained briefly to clarify all formalisms corresponding with the experimental parameters. Details of the analysis method are also given as well as a description of instrumentation.

4.6.2 AC theory

Applying a time dependent sinusoidal form voltage, $\mathbf{V} = V_0\exp(j\omega t)$ to an electrical circuit, will generate the same form of current that is $\mathbf{I} = I_0\exp(j\omega t + j\phi)$, where ω and ϕ are the frequency and phase difference between **V** and **I**, respectively. By Ohm's law, the impedance **Z** (complex resistance) is defined and written in the form of a complex quantity as

$$\mathbf{Z} = \mathbf{V/I} = Z_0\exp(-j\phi) = Z' - jZ'' \qquad 4.25$$

The inverse of Z is termed the complex admittance, **Y**, as

$$\mathbf{Y} = 1/\mathbf{Z} = \frac{Z' + jZ''}{Z'^2 + Z''^2} = Y' + jY'' \qquad 4.26$$

The other two formalisms are defined as parameters of dielectric materials; the complex permittivity, ε, and its inverse, the electric modulus, **M**. They can be expressed as

$$\varepsilon = \mathbf{Y}/j\omega\varepsilon_0, \qquad \mathbf{M} = \varepsilon^{-1} = j\omega\varepsilon_0.\mathbf{Z} \qquad 4.27$$

Typically, **M** is useful for determining electrical relaxation phenomena of vitreous ionic conductors [26]. All these four parameters, i.e. **Z**, **Y**, ε and **M**, are interrelated.

4.6.3 Methods of determining ionic conductivity

The ionic conductivity to be determined is the dc conductivity σ_{dc}, which is a function of temperature as described in the proceeding chapter. Practically, σ_{dc} can be determined from two analytical methods; (i) using conductivity spectra and (ii) complex plane impedance (admittance) analysis. The conductivity spectrum is the plot of frequency dependent conductivity (σ_{ac}) versus frequency on a log-log scale. The characteristic of the conductivity spectra has been claimed to be a "***Universal Dielectric Response***" or UDR of ionic materials proposed by Jonscher [27]. The general mathematical form of σ_{ac} according to UDR behaviour approximately follows a "*power law*" expressed as combination of two terms,

$$\sigma_{ac}(\omega) = \sigma(0) + A\omega^{s} \qquad 4.28$$

Here, $\sigma(0)$ is the σ_{dc} (i.e. the low-frequency conductivity), A is the thermal activated parameter and the exponent s lies in range $0<s<1$ [28, 29].

For many glasses, the conductivity spectrum can be represented schematically as in Fig. 4.16. The response by the glass specimen to a sinusoidal signal can be separated into three regions associated with individual frequency ranges. Region I is attributed to the "*electrode polarisation effect*" at low frequencies (long time migration). As temperature increases, this effect becomes more important. At intermediate frequencies (region II, long-range ion migration), the frequency independent conductivity appears as a plateau, which is clearly attributed to σ_{dc} [30]. Steady increase of σ_{ac} with increasing frequency can be found in region III (short-range ion migration), associated with the second term in Eq. 4.28. This increase in σ_{ac} is due to the higher probability of ion jumps at the higher frequency [31].

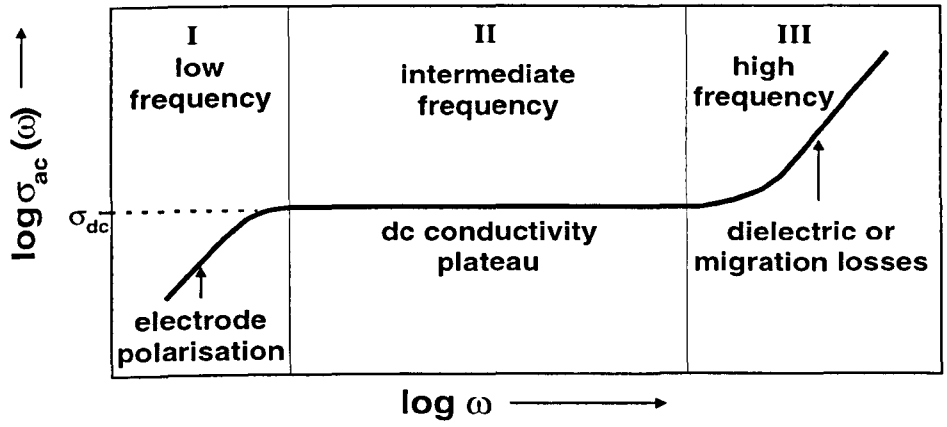

Figure 4.16. *Schematic representation of conductivity spectrum obtained from ionically conducting glasses.*

To determine σ_{dc} of glass from a conductivity spectrum as in Fig 4.16, one needs to use a least-squares fitting method on Eq. 4.28. The drawback to this method is the dispersion of ac conductivity in the low frequency region, where electrode polarisation occurs, which diminishes the accuracy of the σ_{dc} value obtained.

The complex plane impedance or CPI method can overcome the difficulty raising from electrode polarisation at the interface between bulk glasses and their electrodes, because this effect can be separated from an analytical range obtained from the bulk glass response [32]. The impedance reponse of glasses can be represented by that of a simple equivalent circuit containing resistance and capacitance. Therefore, by plotting the imaginary part (Z″) against the real part (Z′) of the impedance on the complex plane, the resistance R of the bulk sample can be found directly from the intercept of the graph on the Z′ axis. Then σ_{dc} can be calculated from the relation, $R = (1/\sigma).d/A$, where d and A are the thickness and electrode surface area of the sample respectively.

It shoud be noted that choice of electrode material is of considerable importance in an ionic conductivity measurement. For glass samples, three inert metal electrodes, e.g Au, Pt and Ag, are frequently used in the form of paste or coating. Other metals may also used for a specific investigations. There are two types of electrode materials, *blocking*

and non-blocking electrodes. A blocking electrode does not permit the migration of charge across the electrode/glass interface. It may be considered as having an infinite resistance. A typical example of a blocking electrode is Pt in contact with sodium silicate glass. In contrast, a non-blocking electrode allows the transfer of charge across the aforementioned interface. Ideally, the contact resistance at the interface should be zero. In reality, perfect non-blocking electrodes are not available but contact between a Na-Hg amalgam and β-alumina may represent a good example of this electrode type.

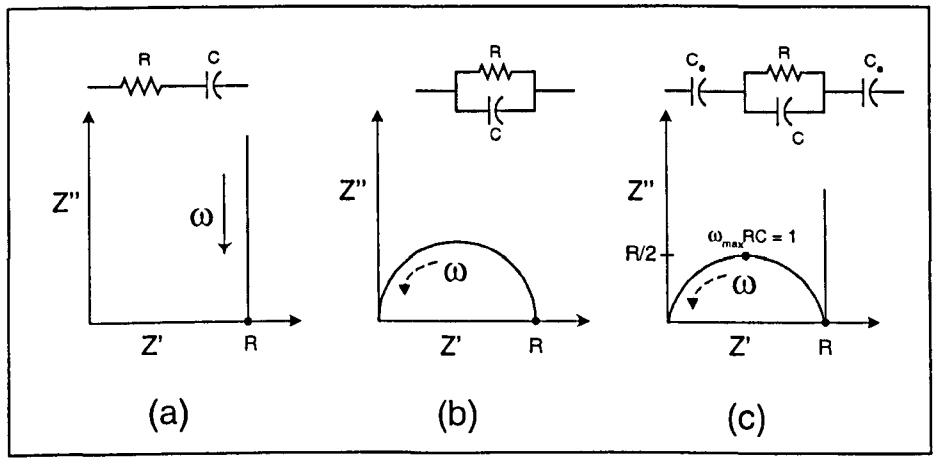

Figure 4.17. *Complex plane impedance plots for a combination of a resistor, R, and capacitor, C, (a) in series and (b) in parallel, (c) the possible equivalent circuit and complex plane impedance plots for a real ionically conducting glass with a blocking electrode, C_e is the electrode capacitance.*

The CPI plots of two simple equivalent circiuts, i.e. the combination of resistor R and capacitor C in series and parallel, are illustrated in Fig 4.17a and 4.17b. The magnitude of the complex impedance **Z** is the combination of resistance *R* and capacitive resistance X_c. *R* is independent of frequency because the voltage across a resistor is always in phase with the current passing through, i.e. $\phi = 0$. However, the voltage across a capacitor lags behind the current by 90°, i.e. $\phi = \pi/2$, which means X_c is frequency

dependent and defined as $X_c = (\omega C)^{-1}$. Thus, the CPI plots for the series combination gives a vertical straight line, i.e. *the electrode spike*, and intercept Z′ axis at *R*, and it gives a semicircle for the parallel combination. Here, ω_{max} is the frequency at which $R = (\omega C)^{-1}$. The complex impedance response of a real ionic material is rather more complex, especially where the material can exhibit several possible conduction mechanisms. The CPI may show two or more semicircles and the electrode spike may not be a straight line but rather a partial semicircle. For a glass containing only one mobile species connected to a blocking electrode, the CPI plots may be obtained as shown in Fig 4.17c, with the equivalent circuit shown above.

4.6.4 Instrumentation

The features of the ionic conductivity measurement jig are shown essentially in Fig. 4.18. The jig consists of a supporting structure and electrical connections. The supporting structure is a stainless steel skeleton covered by glass sleeving. The sample is held under pressure between high purity silica glass discs and the electrical contact to the sample is made via connections consisting of; (1) gold foils in contact with both sample electrodes (2) platinum leads connected to the gold foils and a BNC cable, one end of which goes to the data acquisition unit. The platinum leads have to be shielded in silica glass tubes to eliminate stray capacitance. The thermocouple is inserted close to the sample to monitor its temperature (with error of ± 2 °C). The commercial *HP 4925 Low Frequency Impedance Analyser* module is used to acquire the impedance data and send it for storage in a personal computer (PC).

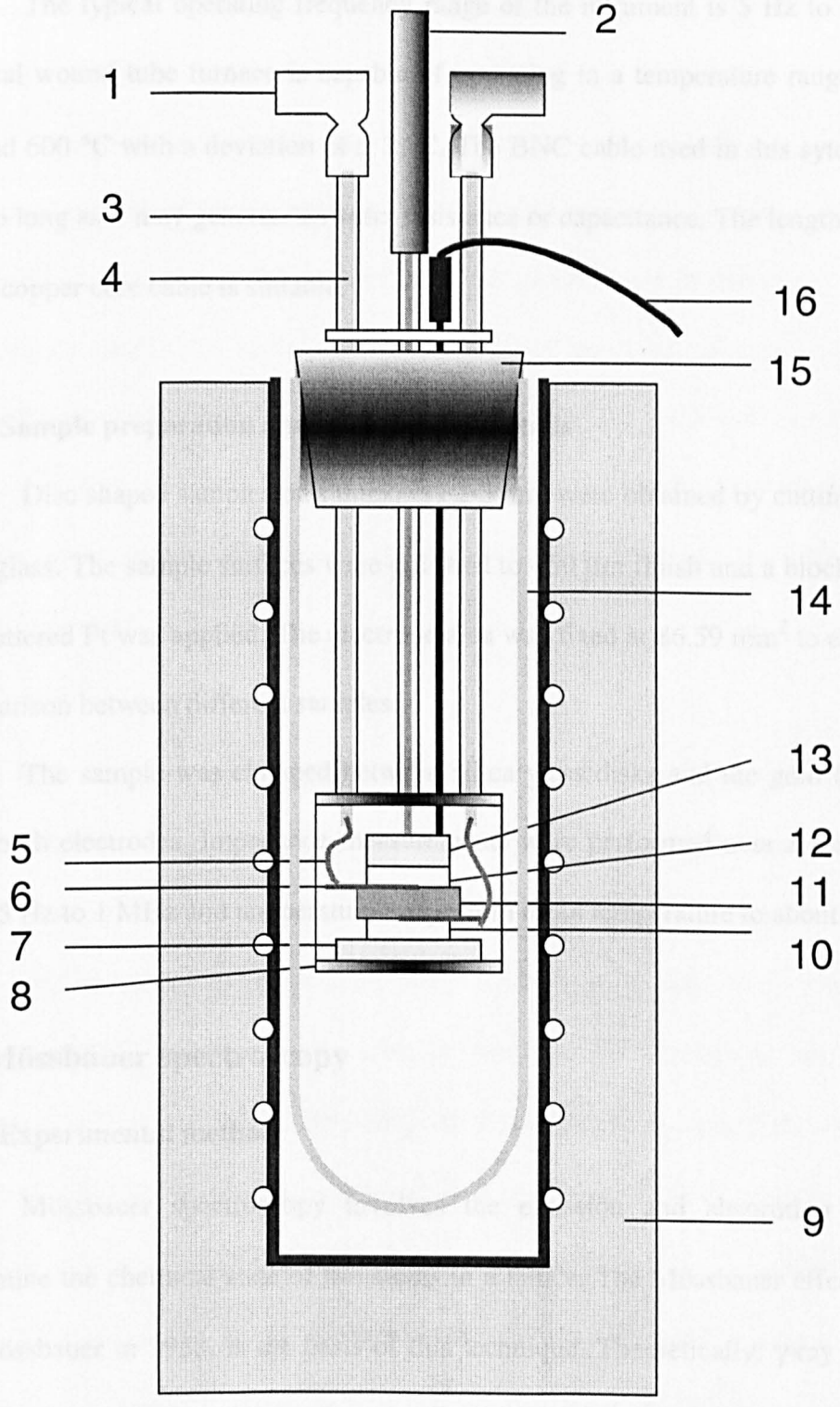

Figure 4.18. *Cross section view of the conductivity jig and details of arrangement: 1. BNC head, 2. Spring loaded plunger, 3. Stainless steel skeleton, 4. Silica glass tube fit inside stainless steel rod, 5. Pt lead, 6. gold foil, 7. & 13. Ceramic discs, 8. Sample support part, 9. Wound tube furnace, 10. & 12. Silica glass discs, 11. Sample disc, 14. Glass sleeve, 15. Rubber bung and 16. R-type thermocouple.*

The typical operating frequency range of the intrument is 5 Hz to 13 MHz. The vertical wound tube furnace is capable of operating in a temperature range of 25 °C to around 600 °C with a deviation of ± 2 °C. The BNC cable used in this sytem should not be too long as it may generate an extra resistance or capacitance. The length of 1 metre of 50 Ω copper core cable is suitable.

4.6.5 Sample preparation and experimental details

Disc shaped samples of a thickness 2-3 mm were obtained by cutting an annealed bulk glass. The sample surfaces were polished to ~50 μm finish and a blocking electrode of sputtered Pt was applied. The electrode area was fixed at 86.59 mm^2 to ensure the best comparison between different samples.

The sample was clamped between silica glass disks and the gold foil connected with both electrodes. Impedance measurements were performed over a frequency range from 5 Hz to 1 MHz and temperature range from room temperature to about 300 °C.

4.7 Mössbauer spectroscopy

4.7.1 Experimental method

Mössbauer spectroscopy involves the emission and absorption of γ-rays to determine the chemical state of the atoms in a lattice. The Mössbauer effect, discovered by Mössbauer in 1958, is the basis of this technique. Theoretically, γ-ray absorption or emission by isolated nuclei causes a recoil process, but if the nuclei are bound in a solid matrix, the recoil energy can be very small compared to the excitation energy of lattice vibration, then no recoil takes place. Hence, the resonance condition can occur. The most common isotope used in the Mössbauer spectroscopy is ^{57}Fe and the transition from the

3/2 excited state to the ground state (1/2) produces a γ-ray with a specific energy of 14.4 keV [23].

Mössbauer spectroscopy requires an emitter (source) and an absorber (sample) that contain the identical isotope, e.g. ^{57}Fe. The sample is placed between the source and a detector. The energy gap between excited and ground state of the nuclei in the source must match that in the sample for resonance but the effect of chemical environment makes it necessary to scan over a range of energies to obtain a Mössbauer spectrum. This is achieved by exploiting the Doppler shift of energy in a source or sample moving at a velocity, v, (the most common method is moving source). Hence, the energy change ΔE can be expressed as

$$\Delta E = \pm E_{\gamma}.v/c \qquad 4.29$$

where E_{γ} is the energy of the γ-ray (14.4 keV) and c is the velocity of light (3×10^8 m/s). The appropriate range of the velocity, the spectrum of ΔE can be produced. Since ΔE is not an absolute value but reflects the difference of the environment around nuclei in the emitter and the absorber, the reported data is normally referenced to the energy change of the same nuclei in a reference substance. In the case of ^{57}Fe isotope, an iron foil is used as a reference. The shift of ΔE from that of the reference is termed the *isomer shift* or *chemical shift* [33]. Before measurement, the calibration has to be made at the stationary emission of γ-ray to correct the energy matching between source and sample.

Conventionally, the information from a Mössbauer study is presented as a plot of γ-ray intensity versus velocity or ΔE. The resonant peak of each transition state can be determined accurately by Gaussian or Lorentzian fitting function. However, in some cases, quadrupole effects cause splitting of the energy level giving rise to split peaks. The presence of a magnetic field can also split the energy levels of the nucleus hence further

complicating the Mössbauer spectrum. Mössbauer spectroscopy has the great advantage of being able to distinguish the valence states of ions contained in glass the network.

4.7.2 Experimental details

All spectra were produced by Dr M. Thomas and Angela Beasley at the University of Liverpool. Glass samples contain Fe_2O_3 were crushed to fine powder, mixed with BN and packed into a plastic holder. Mössbauer spectra were recorded at room temperature (293 K) using ~50 mCi sources of ^{57}Co in a rhodium matrix. The isomer shift was referenced to the centre of the α-iron foil spectrum at zero velocity. Source movement was modulated by a triangular waveform. Several scans were made to obtain best resolution. Isomer shift, Quadrupole splitting and spectrum area were determined by Gaussian fit.

4.8 Summary

Once the glass samples are prepared, they are checked for amorphicity using XRD; densities are determined from the Archimedes method; DTA is used to determine T_g, T_x and T_c of the glass sample; and thermal expansion coefficients are obtained from the Dilatometry technique. Short-range order in the local structure of glass samples is investigated using solid state MAS NMR. The ionic conductivities of the bulk glass samples are essentially measured to study the conduction role of Na^+ both in the original glass composition and in Fe_2O_3 doped-glass samples. Further information on the state of Fe atoms in the glass is obtained using Mössbauer spectroscopy. Finally, SEM is used to determine the phase composition and microstructure of glass-ceramics produced by controlled crystallisation.

References

[1] Brown, M.E. *Introduction to Thermal Analysis; Technique and Applications.* Cambridge: University Press, 1988.

[2] Wunderlich, B. *Thermal Analysis.* New York: Academic Press, 1990.

[3] Christeian, G.D. and O' Reilly, J.E. *Instrumental Analysis.* 2nd ed. New York: Allyn and Bacon Inc., 1981.

[4] Chen, S.K. and Liu, H.S. *Journal of Materials Science.* **29** (1994), 2921.

[5] Donald, I.W. *Journal of Materials Science.* **30** (1995), 904.

[6] Mishima, N. Ota, R., Wakasagi, T. and Fukunaga, J. *Journal of Non-Crystalline Solids.* **197** (1996), 19.

[7] McMillan, P.W. *Glass-ceramics.* London: Academic Press, 1979.

[8] Susman, S., Delbeccq, C.J. and McMillan, J.A. *Solid State Ionics.* **9&10** (1983), 667.

[9] Paul, A. *Chemistry of Glasses.* New York: Chapman and Hall, 1982.

[10] Rawson, H. *Properties and Applications of Glass.* Amsterdam: Elsevier Science Publishing Inc., 1980.

[11] Blatt, F.J. *Modern Physics.* London: McGraw-Hill, 1992.

[12] Emerson, J.F. and Bray, P.J. *"NMR Analysis of Glass Structure" in; Experimental Techniques of Glass Science.* Eds. C.J. Simmons and O.H. El-Bayoumi. Westerville, Ohio: The American Ceramic Society, 1993.

[13] Eckert, H. *Progress in Nuclear Magnetic Resonance Spectroscopy.* **24** (1992), 159.

[14] Dupree, R. and Holland, D. *"NMR; a new spectroscopic technique for structure determination in glasses and ceramics" in; Glass and Glass-Ceramics.* Ed. M. Lewis. London, Chapman & Hall, 1988.

[15] Kirkpatrick, R. J. *Reviews in mineralogy.* **18** (1988), 341.

[16] Ailion, D.C. and Ohlsen, D. *"Magnetic Resonance Methods for Studying Defect Structure in Solids" in; Methods of Experimental Physics, 21.* Eds. J.N. Mundy (et al.). London: Academic Press, 1983.

[17] Virlet, J. *"Line Narrowing Methods in Solids" in; Encyclopedia of Nuclear Magnetic Resonance.* Ed. D.M. Gran. Chichester: Wiley, 1996.

[18] Hammond, C. *The Basics of Crystallography and Diffraction.* Oxford: Oxford University Press, 1997.

[19] Blakemore, J.S. *Solid State Physics.* 2nd ed. Cambridge: Cambridge University Press, 1995.

[20] Suryaharayana, C. and Norton, M.G. *X-Ray Diffraction; A practical approach.* New York: Plenum Press, 1998.

[21] Goodhew,, P.J. and Humphreys, F.J. *Electron Microscopy and Analysis.* 2nd ed. London: Taylor & Francis, 1997.

[22] Joy, D.C. *"Scanning Electron Microscopy" in; Materials Science and Technology: A comprehensive treatment, 2A; Charactersization of Materials, Part I.* Ed. E. Lifsh. Weinhiem: VCH, 1992.

[23] Flewitt, P.E.J. and Wild, R.K. *Physical methods for Materials Characterisation.* Bristol: IOP Publishing Ltd., 1994.

[24] Flewitt, P.E.J. and Wild, R.K. *Microstructural Characterisation of Materials and Alloys.* London: Institute of Metals, 1985.

[25] Shelby, J.E. *Introduction to Glass Science and Technology.* Cambridge: The Royal Society of Chemistry, 1997.

[26] Macedo, P.B., Moynihan, C.T. and Bose, R. Physics and Chemistry of Glasses. **13**, no.6 (1972), 171.

[27] Jonscher, A.K. *Nature*. **267** (1977), 673.
[28] Lee, W.K., Lim, B.S., Liu, J.F. and Nowick, A.S. *Solid State Ionics*. **53-56** (1992), 831.
[29] Hsieh, C.H. and Jain, H. *Journal of Non-Crystalline Solids*. **203** (1996), 293.
[30] Malcolm, D.I. *"Electrical Properties of Glasses" in; Materials Science and Technology: A comprehensive Treatment, 9*. Ed. J. Zarzycki. Wienheim: VCH, 1991.
[31] Dyre, J.C. *Journal of Applies Physics*. **64**, no. 5 (1988), 2456.
[32] Jain, H. *"Measurement of Electrical Conductivity of Glasses" in; Experimental Techniques of Glass Science*. Eds. C.J. Simmons and O.H. El-Bayoumi. Westerville, Ohio: The American Ceramics Society, 1993.
[33] Joseph, I and Pye, L.D. *Mössbauer Spectroscopy in Glasses in; Experiemental Techniques of Glass Science*. Eds. C.J. Simmons and O.H. El-Bayoumi. Westerville, Ohio: The American Ceramic Society, 1993.

CHAPTER 5

Na_2O-ZrO_2-SiO_2-P_2O_5 Glass System

5.1 Glass preparation and glass product

The selected glass compositions and starting materials were described in chapter 4. To study glass of the Na_2O-ZrO_2-SiO_2-P_2O_5 system, four compositions were chosen from the glass forming region. The NASIGLAS samples were prepared using the melt-quench method, in which the glass batch was melted at 1600 °C for 2 hours followed by 1650 °C for 40 minutes. The homogeneous glass melt was quenched and two forms of glass sample were produced: (i) glass sheet obtained from quenching on a copper plate cooled by liquid nitrogen and (ii) a bulk specimen approximately 25 mm × 45 mm × 15 mm in size which was subsequently annealed at 50°C below T_g for 3 hours. Some of the glass sheet sample was ground to powder of particle size smaller than 38 μm and used for DTA and NMR study. Further samples of powder were heat treated at the temperature at which crystallisation took place (identified from DTA) to study the crystallisation behaviour. The bulk glass specimen was cut into rods of dimension 5 mm × 5mm × 25 mm for measuring the thermal expansion coefficient and discs of 15 mm in diameter and 3 mm thick which were used for ionic conductivity measurement (chapter 9).

Mass balance was checked for each glass melt. From the starting materials, e.g. Na_2CO_3, Na_2HPO_4, ZrO_2, and SiO_2, the first two substances decompose during melting to release CO_2 gas and H_2O (vapour) respectively as shown in the following equations

$$Na_2CO_3 \rightarrow Na_2O + CO_2\,(g) \qquad 5.1$$

$$2Na_2HPO_4 \rightarrow Na_4P_2O_7 + H_2O(g) \qquad 5.2$$

A general equation can be written to express the reaction of components and evaluate the theoretical quantity of released gases as follows:

$$\left(\frac{3x-5}{2}\right)Na_2CO_3+\left(2-\frac{x}{3}\right)ZrO_2+x.SiO_2+(3-x).Na_2HPO_4 \Rightarrow Na_{1+x}Zr_{2-x/3}Si_xP_{3-x}O_{12-2x/3} + \left(\frac{3x-5}{2}\right)CO_2+\left(\frac{3-x}{2}\right)H_2O \quad 5.3$$

Eq. 5.3 is useful for observing the completion of reaction and release of gas by detecting weight lost from the glass product. The observed weight is also useful for estimating loss of Na_2O content because this volatile oxide can be evaporated out easily at the extremely high melting temperature being used throughout this work (1600 °C).

Table 5.01 shows the nominal glass compositions of NASIGLAS in mol% and their observed excess weight loss in percent with respect to the final mass. It can be seen that the loss of 3 or 4%, may be assigned to loss of Na_2O and P_2O_5 content combined with accidental loss during casting. However, the observation of weight loss is a rough method for detecting perfection of glass product. Chemical analysis would provide more information relating the glass batch and glass product compositions and completion of reaction during melting.

Table 5.01 *Nominal compositions of NASIGLAS ($Na_{1+x}Zr_{2-3/x}Si_xP_{3-x}O_{12-2x/3}$) with their given name and weight lost, δW.*

x	Sample name	Nominal compositions (mol%)				δW (%)
		Na_2O	ZrO_2	SiO_2	P_2O_5	
3.00	G1	33.33	16.66	50.00	-	1.4
2.75	G2	32.10	18.54	47.21	2.15	3.6
2.50	G3	30.92	20.49	44.17	4.42	4.2
2.25	G4	29.54	22.73	40.91	6.82	4.8

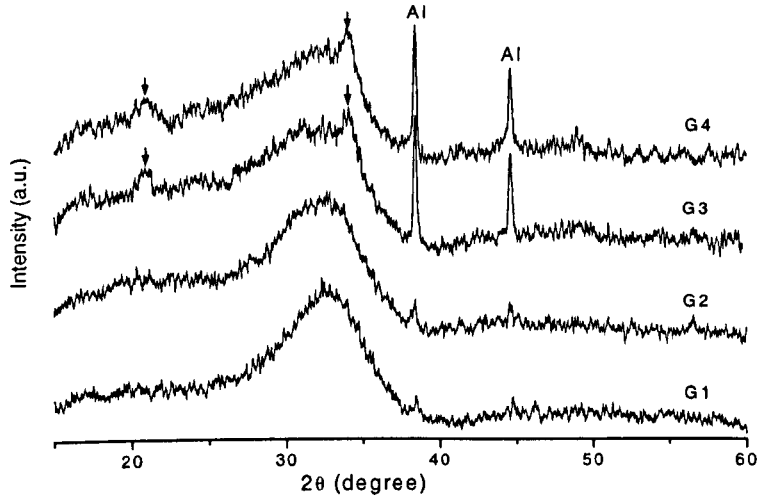

Figure 5.01. *XRD graph of NASIGLAS samples. The arrows indicate the presence of crystalline $ZrSiO_4$. The diffracted signal from the Al sample holder provided 2 sharp peaks at ~38° and ~45°.*

5.2 Results and discussion

5.2.1 Introduction

All the glass samples of the NASIGLAS compositions were transparent but trace amounts of crystalline $ZrSiO_4$ were present for x = 2.50 and 2.25 (identified by XRD). This result may indicate the solubility limit of ZrO_2 since its content was as high as 22 mol% for x = 2.25, Otherwise, no defects were observed in the as-quenched glass samples.

5.2.2 XRD

The XRD powder patterns of NASIGLAS are shown in Fig.5.01. The patterns from G1 and G2 show the characteristic glass trace with no sharp peaks from crystalline material. The main amorphous hump narrows on going from G4 to G3, G2 and G1 respectively. There are, however, small peaks at $2\theta = 20.8°$ (d-spacing = 2.1709 Å) and 34.0° (d-spacing = 1.3786 Å) in the XRD powder patterns of G3 and G4 (indicated by the

arrows) suggesting some crystalline phase in these samples. These peaks may be from crystalline $ZrSiO_4$ (JCPDF no. 6-266).

5.2.3 DTA

The DTA curves of the powdered as-quenched, glass samples are shown in Figures 5.02 and 5.03 which represent the heating and cooling traces respectively. The inflection point is attributed to the glass transition temperature, T_g, and the exothermic peaks are attributed to the crystallisation process. During crystallisation, T_x is denoted as the onset temperature and T_c is the temperature where the crystallisation peaks go through a maximum. T_g, T_x and T_c values are summarised in Table 5.02 along with the difference between T_x and T_g. From Fig. 5.02, it can be seen that the glass transformation region of the NASIGLAS composition is in the range 650 °C to 730 °C with large differences in behaviour between samples G1, G2 and G3, G4. Lower transition temperatures of 652 °C and 658 °C are observed for G1 and G2 respectively but G3 and G4 have transition temperatures of 705 °C and 728 °C, respectively. These results suggest that increase of ZrO_2 and decrease of Na_2O content tend to increase the T_g. All DTA curves show the inflection just before crystallisation peak which is due to the sintering event. This is the consequence of viscous flow during which glass powder undergoes sintering, forming a denser body and leads to change of heat transfer coefficient between sample and crucible. Two well-resolved exothermic peaks occur for G1 and G2, whilst only one peak is observed for G3 and G4. The crystallisation peaks of G1 and G2 are similar but much sharper for G2 and shifted to higher temperature. In addition, the first crystallisation peak of G2 seems to have a high temperature shoulder but its low peak area makes it difficult to resolve. This indicates complex crystallisation in samples G1 and G2. The single crystallisation peaks of G3 and G4 are located at approximately the same temperature,

suggesting that the same crystalline phase has grown in both samples. A detailed study on the crystallisation using heat treatment and XRD provided more evidence about the crystalline phases formed and this is detailed separately in the chapter 7.

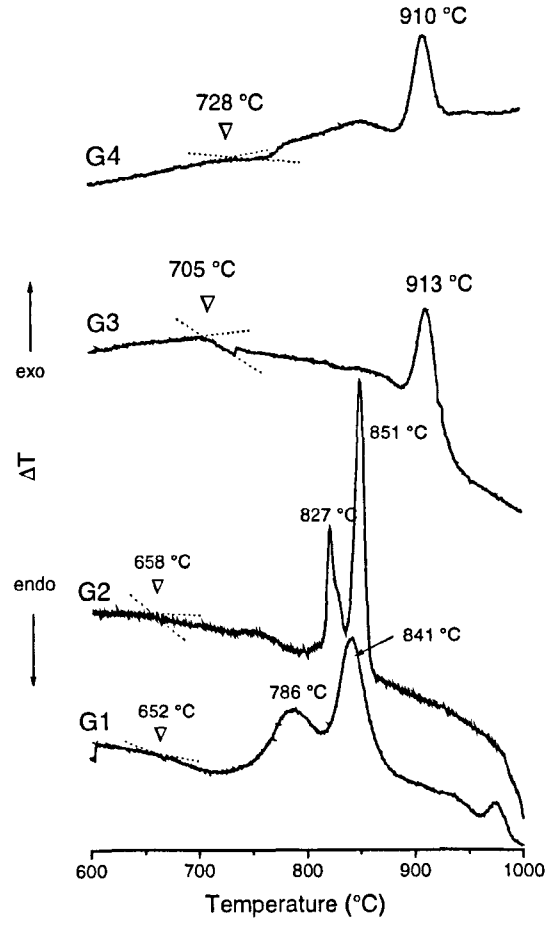

Figure 5.02. *DTA curves of NASIGLAS during heating at constant rate of 5 °C/min, ∇ indicates glass transition temperatures (T_g).*

Table 5.02 *Glass transition (T_g) and crystallisation (T_c) temperatures of NASIGLAS.*

Sample	T_g (°C)	T_x (±5 °C)	T_c (±3 °C)	T_x-T_g (°C)
G1	652 ± 10	751	786, 841	99 ± 10
G2	675 ± 8	800	827, 851	125 ± 8
G3	705 ± 5	890	913	185 ± 5
G4	728 ± 5	885	910	157 ± 5

During cooling of a glass melt (Fig. 5.03), the sample should show a peak corresponding to crystallisation, and this can be observed in the DTA cooling traces of

G3 and G4 at 1076 and 1090 °C, respectively. No devitrification was observed in the samples G1 and G2 although these had been taken above their liquidus temperatures. Phase transitions of SiO_2 polymorphs, from the quartz reference, are also observed in the DTA traces. The β-α quartz transition shows as an endothermic peak at 573 °C (exothermic in reference crucible), while transition of α–β tridymite occurred at around 230 °C. The tridymite is formed by the reconstructive quartz ↔ tridymite transition at 867 °C and since the transition is slow, it is not reversed on cooling. Thus the α–β transition of tridymite can then be observed at 230 °C.

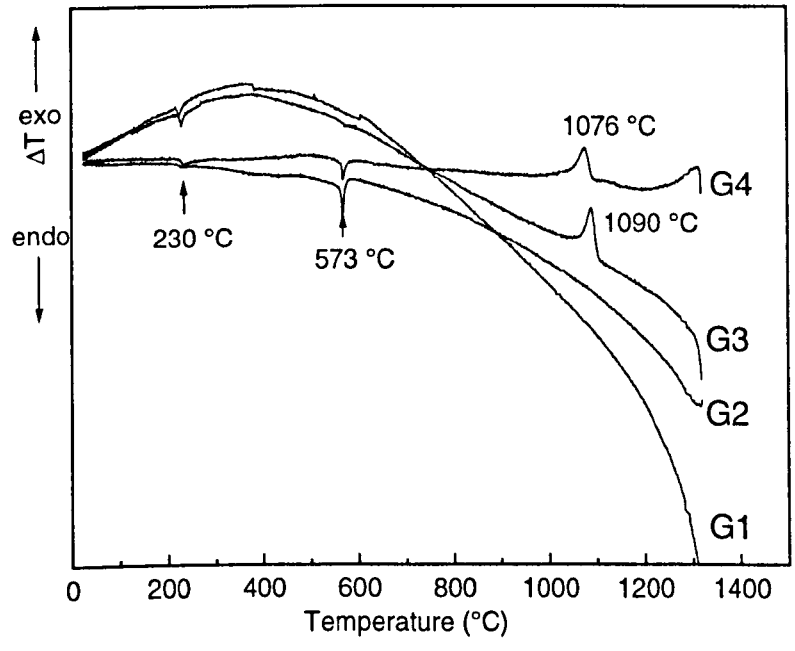

Figure 5.03. *DTA curves of NASIGLAS during cooling at constant rate of 10 °C/min. The transitions of silica polymorphs are indicated by the arrows.*

The T_x-T_g parameter has been used to determine the glass stability in many glass systems [1-3]. In Table 5.02, there is no systematic relation between T_x-T_g values and glass compositions, it is highest for G3 (185 °C) and lowest for G1 (99 °C). This parameter is strongly dependent on the assignment of T_g. The complex crystallisation

behaviour of glass in the present study also confuses the assignment of T_x. Thus, use of T_x-T_g as the indicator of glass stability may not be applicable for NASIGLAS.

Glass characteristics are clearly controlled by their composition. The transition temperature T_g is associated with the strength of the glass network. Adding $[PO_4]$ tetrahedra to the glass network at the same time as Na_2O is being reduced (in G2, G3 and G4) leads to repolymerization of the silicate network as can be observed from the ^{29}Si MAS spectra (5.2.6.1). Although we know how Na^+ and $[PO_4]$ units enter the silicate network, the role of Zr^{4+} in the network is difficult to derive from the available information because it can enter either the modifier or glass-former site [4]. If the latter, then increasing ZrO_2 should increase the viscosity of glass owing to the increase in number of bridging oxygens per silicon atom [5]. Also, higher ZrO_2 content in glass contributes a more densely packed structure with a higher T_g [6]. Thus, increase of T_g with P_2O_5 and ZrO_2 content is clearly observed in NASIGLAS. It is not clear whether P_2O_5 or ZrO_2 content has the stronger influence on the strength of the silicate network.

Crystallisation in glass is generally controlled by the nucleating agent. In the compositions studied, introduction of P_2O_5 alters the course of devitrification, as we can see by the sharper crystallisation peaks in G2 compared to G1. The same result was also discovered in these compositions by Susman et al. [7] where differences in activation enthalpy and entropy of the crystallisation process between these two compositions were observed. The influence on crystallisation of added P_2O_5 was also observed in the ternary Li_2O-ZrO_2-SiO_2 glass system [8]. Three crystalline phases were formed in this system, $Li_2Si_2O_5$, $ZrSiO_4$ and tridymite and adding P_2O_5 delayed the growth rate of $Li_2Si_2O_5$ but markedly enhanced crystallisation of $ZrSiO_4$ and tridymite. P_2O_5 may also play the same role in NASIGLAS which gives rise to complex crystallisation.

5.2.4 Density

Table 5.03 *Density, ρ_x and molar volume, V_m of NASIGLAS comparing between as-quenched and annealed samples.*

Sample	As-quenched		Annealed	
	ρ_x ($\pm$ 0.005 g/cm^3)	V_m ($\pm$ 0.5cm^3)	ρ_x ($\pm$ 0.005 g/cm^3)	V_m ($\pm$ 0.5cm^3)
G1	2.950	24.1	2.956	24.1
G2	2.911	25.4	2.915	25.4
G3	2.904	26.6	2.906	26.6
G4	2.890	27.8	2.890	27.8

The densities (ρ_x) and related molar volumes (V_m) of all NASIGLAS samples are shown in Table 5.03 and plotted as a function of x in Fig 5.04. As the x value decreases, the densities also decrease and the molar volumes increase. The larger atomic size and coordination number of the Zr atom cause an expansion of the silicate network, resulting in lower density and larger molar volume despite the larger atomic mass of Zr. The density of G1 (2.950 g.cm^{-3}) is slightly higher than the 2.869 g.cm^{-3}, reported by Ennas et al. [9]. This difference may be due to using a different casting method. Practically, casting on a copper plate should produce a denser sample compared to casting in cold water as in ref. [9]. The as-quenched and annealed densities agree within experimental error.

The density of glass depends on the fraction of the volume occupied by structural units that link together as a vitreous network and the unoccupied volume or free volume [10]. Addition of species that enter interstices in the glass network will increase the density by reducing free volume [11], but on adding ZrO_2, the free volume of the vitreous network is increased as observed by the decrease of density. This result indicates that Zr^{4+} do not fill the interstitial sites left by the withdrawn Na^+. When [ZrO_6] octahedra and [PO_4] tetrahedra are inserted into the network, these excess structural units compensate the withdrawn [SiO_4] tetrahedra, and result in the expansion of the vitreous network.

Filling free volume with the modifer (Na^+) is a key mechanism of controlling glass density. The relation between alkali content and glass density has been also reported in binary alkali-silicate glass [12]. Furthermore, workers have reported the relationship between the density of binary silicate glasses and their microstructural arrangement [12-16], mostly using mathematical methods to evaluate the density of particular structural units. For example, the Q^4 species would be assigned a lower density compared to Q^3 which has one alkali ion associated with it. Knowing the density of individual structural units, and finding their proportions in a glass from NMR or Raman spectroscopy, these authors were able to calculate the density of a glass. Remarkably good agreement between experiment and calculation were obtained. Here, it would be unreliable to use a density model as these glass contains several structural units. This means that many assumptions have to be involved. Therefore, only the compositional dependence of density is discussed in the present work.

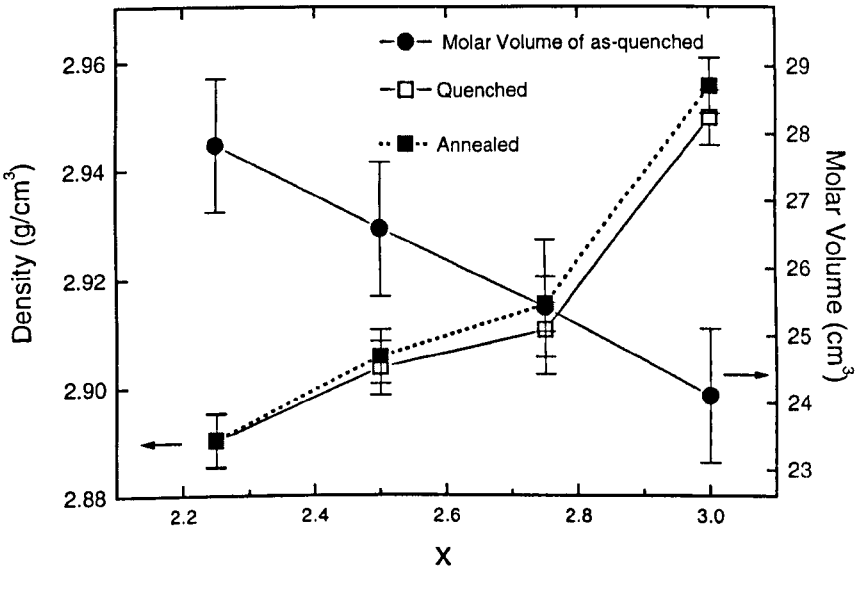

Figure 5.04. *The bulk density of NASIGLAS as a function of x value, comparing as-quenched and annealed samples. The molar volume of as-quenched samples is also shown.*

5.2.5 Thermal expansion

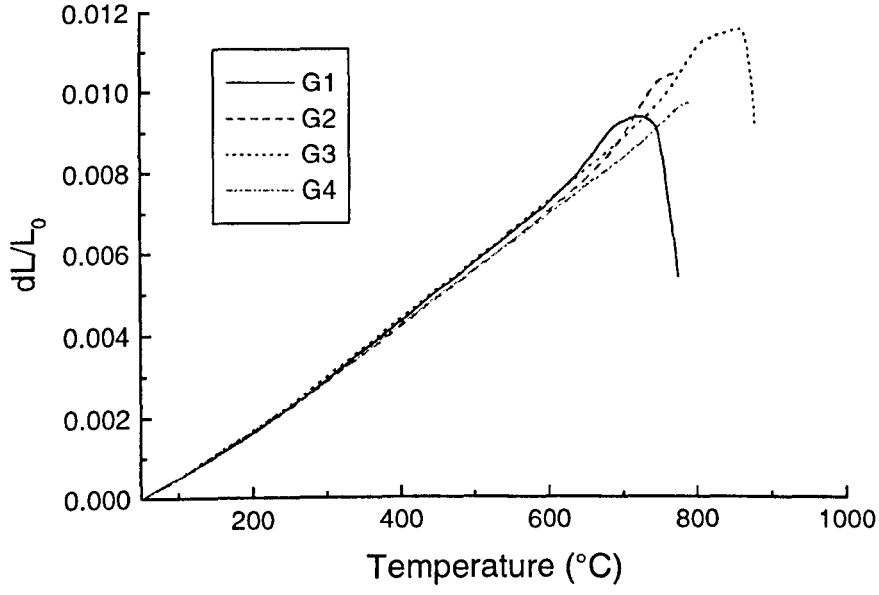

Figure 5.05. *Thermal expansion characteristic curves of NASIGLAS.*

The dilatometric curves of annealed G samples are shown in Fig. 5.05. In Table 5.04, the thermal expansion coefficients (TEC) calculated from these curves are summarised over three different temperature ranges, from 50 °C to 100, 300 and 500 °C respectively. Also, the dilatometric transitions, T_g^*, and softening points, T_s^* (differentiated by the * from DTA values), are included in Table 5.4 to compare with the results which have been determined previously by DTA. It can be seen that all glass samples exhibit similar expansion characteristics. T_g^* exhibit the same trend as the DTA results. The highest T_s^* is observed for G3. The values from TCE are lower than those from DTA because of the dead load applied by the dilatometer push-rod. The TEC values also have a maximum at G3. From these results, we cannot derive a simple empirical relation between composition and TEC data as has been reported in another glass system

[17]. However, the TEC values of G samples are approximately constant with composition and within experimental error.

Table 5.04 *Results of dilatometric measurement of NASIGLAS. The TEC values are shown with three indicated temperature ranges. The apparent glass transition temperatures, T_g^* and the dilatometric softening points, T_s^* are also included.*

Sample	TEC, α (×10^{-6}/°C) (± 0.05)			T_g^* (°C)	T_s^* (±3 °C)
	$\alpha_{50\text{-}100}$	$\alpha_{50\text{-}300}$	$\alpha_{50\text{-}500}$		
G1	9.82	11.61	12.83	612 ±3	776
G2	9.75	11.47	12.41	664 ±3	770
G3	9.87	11.94	12.93	729 ±5	880
G4	9.72	11.55	12.43	735 ±5	794

5.2.6 MAS NMR

5.2.6.1 ^{31}P MAS

5.2.6.1.1 Results

In Fig 5.06, The ^{31}P spectrum of G2 shows four distinct resonances (α, β, χ and ε) which, on fitting to Gaussian lineshapes, yield isotropic chemical shifts 15.2 ppm, 7.8 ppm, 2.1 ppm and –3.3 ppm. The small peak at –0.8 ppm with narrow linewidth of 2.1 ppm is believed to be due to a crystalline impurity. On increasing P_2O_5 content in G3 and G4, there are slight changes in chemical shift of peaks α, β and ε and considerable shifts to higher shielding for peak χ. For G4, another peak appears at -8.9 ppm. These results indicate that there are contributions from five different phosphate species in NASIGLAS. The isotropic chemical shifts, linewidths and the relative peak areas are summarised in Table 5.5a and 5.5b. With increasing mol% P_2O_5 and decreasing $[Na_2O]/[ZrO_2]$ molar ratio, the integrated areas of peak χ and ε increase. For G3, the peak area goes through a maximum for peak α (~15 ppm) and a minimum for peak β (~7 ppm). This may imply non-systematic interaction between the phosphate unit and the next nearest atom in this sample.

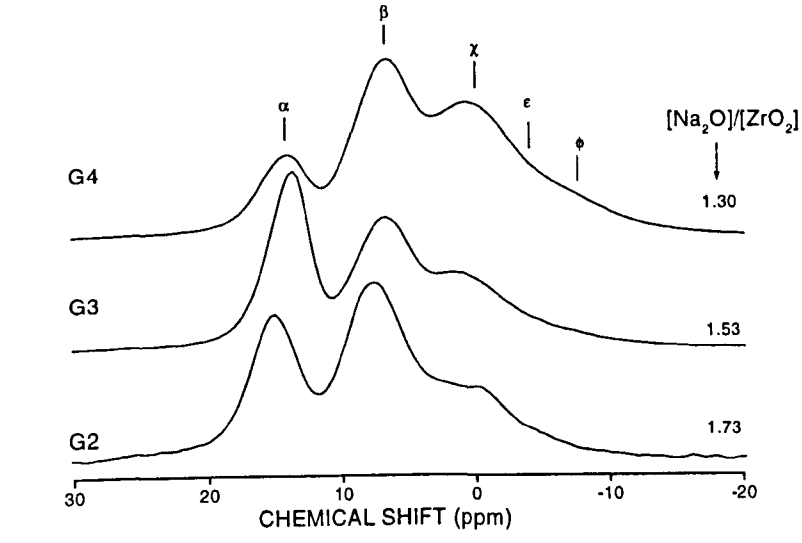

a)

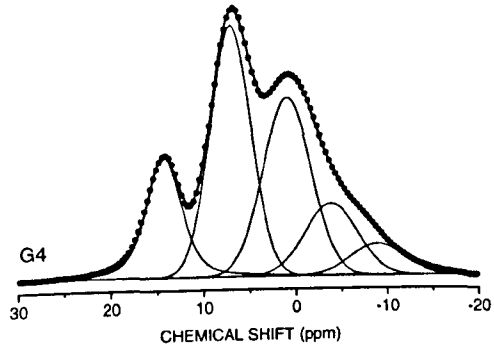

b)

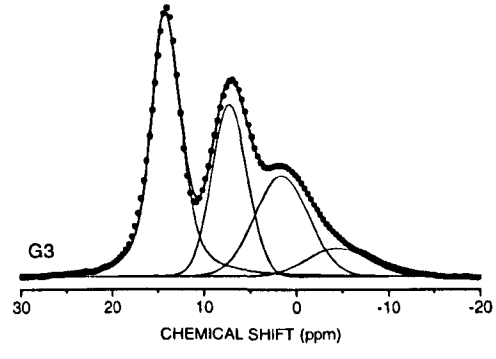

c)

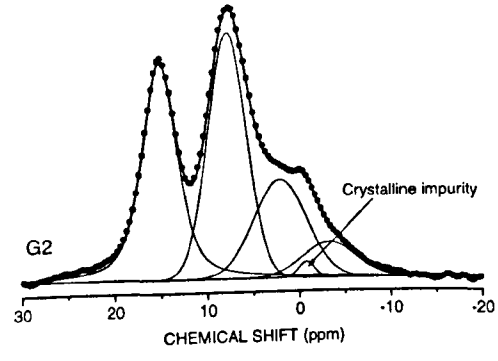

d)

Figure 5.06. *a) ^{31}P MAS NMR spectra of NASIGLAS, referenced to crystalline $NH_4H_2PO_4$. The spinning rate of 10 kHz shifts the spinning sidebands outside the chemical shift range shown. b), c) and d) show Gaussian fitting for ^{31}P spectra, dots are the experimental data and solid lines are the simulation curves. The spectra show five possible phosphate species ($\alpha, \beta, \chi, \varepsilon$, and ϕ) present in NASIGLAS. For peak assignment, see text.*

Table 5.05a *Chemical shift (δ), linewidth (W) of phosphate species present in NASIGLAS.*

Sample	$P(Q^0)_{Na}$ - α		$P(Q^0)_{Na,Zr}$ -β		$P(Q^1)_{Na}$ -χ		$P(Q^0)_{Na,2Zr}$ -ε		$P(Q^1)_{Na,Zr}$ -ϕ	
	δ ±0.5 (ppm)	W ±0.5 (ppm)	δ ±0.5 (ppm)	W ±0.5 (ppm)	δ ±0.5 (ppm)	W ±0.5 (ppm)	δ ±0.5 (ppm)	W ±0.5 (ppm)	δ ±0.5 (ppm)	W ±0.5 (ppm)
G2	15.2	4.5	7.8	4.9	2.1	6.8	-3.3	6.8	-	-
G3	14.0	3.8	7.1	4.5	1.5	6.9	-4.5	7.8	-	-
G4	14.3	4.5	7.0	5.2	0.9	6.1	-3.9	6.7	-8.9	6.8

Table 5.05b *Relative peak area (A) of phosphate species.*

Sample	Relative peak area of phosphate species (±3.0 %)				
	$P(Q^0)_{Na}$ -α	$P(Q^0)_{Na,Zr}$ -β	$P(Q^1)_{Na}$ -χ	$P(Q^0)_{Na,2Zr}$ -ε	$P(Q^1)_{Na,Zr}$ -ϕ
G2	35	37	20	7.	-
G3	41	27	24	8	-
G4	17	35	30	13	5

5.2.6.1.2 $P(Q^n)$ assignments

The spectra shown in Fig. 5.06 were fitted using the Gaussian model in the Winfit programme [18]. The first three peaks (α, β, and χ) are well-resolved from each other, which leads to good optimisation and small error during fitting. However, the last two peaks (ε and ϕ) have greater associated uncertainty since they appear as shoulders on peak χ. However, all peak parameters can be determined successfully and are reported in Tables 5.05a and 5.05b. The phosphate species are described by $P(Q^n)_{j,k}$ where n is the number of bridging oxygens, j and k are the types of atom bonded to the phosphate species. The assignments of the peaks are discussed below.

The peaks at 15 ppm and 2 ppm, i.e. peaks α and β can be assigned as $P(Q^0)_{Na}$, -orthophosphate species and $P(Q^1)_{Na}$, -pyrophosphate species as their isotropic chemical shifts are close to those reported for crystalline Na_3PO_4 (13 ppm) and $Na_4P_2O_7$ (2 ppm) [19-21]. The subscript $_{Na}$ is added to indicate that all three non-bridging oxygens of these two species are bonded to Na^+. This assignment is consistent with previous reports for incorporation of phosphate species in alkali silicate glasses doped with P_2O_5 by Dupree and co-workers [22,23]. Formation of $P(Q^0)_{Na}$ and $P(Q^1)_{Na}$ in Na_2O-SiO_2-P_2O_5 glasses was also confirmed by a XANES study [24]. Incorporation of phosphate species in a silicate network to form these same species was also observed in the Na_2O-Al_2O_3-SiO_2: P_2O_5 system [25]. In binary alkaline earth silicate glass contained 2 wt% P_2O_5, the scavenging of M^{2+} by phosphate was also observed but only $P(Q^0)$ species were found with ^{31}P resonance peaks in the range 0.4 ppm to 3.9 ppm depending on type of alkaline earth ion [26]. It may be concluded that $P(Q^0)_{Na}$ and $P(Q^1)_{Na}$ species are present in several silicate glass systems. The modifier scavenging behaviour of phosphate species is therefore well established and confirmed by the present study on the Na_2O-ZrO_2-SiO_5-P_2O_5 system.

The remaining peaks at 7 ppm, –3 ppm and –8 ppm (peaks β, ε and ϕ) show variation with composition. The relative areas of these peaks increase with increasing P_2O_5 content and with decreasing $[Na_2O]/[ZrO_2]$ molar ratio, i.e from 1.73, 1.53 to 1.30. These results suggest that the association of phosphate species with both Na^+ and Zr^{4+} may be responsible for peaks β, ε and ϕ. The effect of replacing Na by Zr in bonding with $[PO_4]$ tetrahedra can be considered in terms of its effect on the chemical shift of the phosphate species. If one Na attached to $P(Q^0)_{Na}$ is replaced by a higher valency ion, for example Ca^{2+}, the higher electronegativity of the Ca^{2+} leads to a higher shielding environment for the ^{31}P nucleus and its chemical shift moves towards more negative

values. This effect has been observed in the Na_2O-CaO-SiO_2-P_2O_5 system [27,28]. In the current study, replacement of Na^+ by Zr^{4+} should produce the same effect. From the data in Table 5.06a, the chemical shift and linewidth of peak β are almost constant, only peak area changes with increasing P_2O_5 content and with decreasing $[Na_2O]/[ZrO_2]$ molar ratio. Thus, the peak at 7 ppm may be assigned as $P(Q^0)_{Na,Zr}$ -an orthophosphate unit bonded to two Na^+ and one Zr^{4+}. The effect of replacing one of the Na in $P(Q^0)$ units by Zr is clearly seen as the resonance of $P(Q^0)$ moves from 15 ppm for $P(Q^0)_{Na}$ to 7 ppm for $P(Q^0)_{Na,Zr}$. The consistency of this assignment is supported by the nearly constant chemical shift of the peak, with only peak area changing with composition. However, other possibilities must be considered (i) formation of $P(Q^0)_{Zr}$, i.e. all three non-bridging oxygens bonded to Zr, (ii) formation of Si-O-P bonds or $P(Q^0)_{Si}$. To answer this question, we shall consider the chemical bonding characteristic of orthophosphate species. In crystalline $Na_2Zr(PO_4)_3$ (NASICON), phosphorus occupies an orthophosphate site with all non-bridging oxygen bonded to Zr. This produces $\delta(^{31}P)$ at –25 ppm [29]. Since no resonance peak is observed close to –25 ppm, $P(Q^0)_{Zr}$ is not present in this glass. $P(Q^0)_{Zr}$ would also be expected to destabilise the glass which would readily transform to the crystalline state. No silicon orthophosphate compound is found, only silicon pyrophosphate (SiP_2O_7) and the Si-O-P bonds are found to have significantly more negative ^{31}P chemical shift, <-32 ppm [30]. Raman studies of sodium silicate glasses with low phosphate contents also revealed no links between $[SiO_4]$ and $[PO_4]$ units [31]. Hence, $P(Q^0)_{Si}$ is not expected to exist in NASIGLAS.

The peaks at –3 ppm and –8 ppm are more difficult to assign as these are not well-resolved. $P(Q^2)_{Na}$ is not expected to be present since the normal chemical shift range for this species is from –15 ppm to – 30 ppm in binary sodium phosphate glasses [32]. Thus, these two peaks could be either $P(Q^0)$ or $P(Q^1)$ species. The formation of $P(Q^1)_{Si}$ or

SiP_2O_7 like species and $P(Q^1)_{Zr}$ or ZrP_2O_7 like species can be excluded since they should give $\delta(^{31}P)$ at –49 ppm and –39 ppm, respectively [19,30], and no such resonances were observed. Therefore, the same method used to identify $P(Q^0)_{Na,Zr}$ species may also be applied to these peaks. Two possible environments could be proposed (i) further replacement of Na by Zr in $P(Q^0)_{Na,Zr}$ to give $P(Q^0)_{Na,2Zr}$ species, i.e. $P(Q^0)$ species with one Na and two Zr bonding to the non-bridging oxygens, (ii) replacement of Na by Zr in $P(Q^1)_{Na}$ to produce $P(Q^1)_{Na,Zr}$ species.

A ^{31}P MAS NMR investigation of the environments of phosphate species in the sodium aluminosilicate glass system suggested that when Na^+ in $P(Q^0)_{Na}$ is replaced by Al^{3+}, $P(Q^0)_{Na,Al}$ and $P(Q^0)_{Na,2Al}$ are formed with chemical shifts at 7 ppm and –5 ppm, respectively [25]. The same results were also confirmed by Schaller and co-worker [33] using the TRAPDOR NMR technique. Analogously, further replacement of Na^+ in $P(Q^0)_{Na,Zr}$ by Zr^{4+} to form $P(Q^0)_{Na,2Zr}$ should also give a chemical shift close to that found for $P(Q^0)_{Na,2Al}$. Thus, the resonance at –3 ppm may be assigned as $P(Q^0)_{Na,2Zr}$. This assignment is consistent with increasing concentration of $P(Q^0)_{Na,2Zr}$ when the Na_2O/ZrO_2 molar ratio is decreased.

Considering the chemical shifts of $P(Q^1)_{Na}$ (2 ppm) and of $P(Q^1)_{Zr}$ in crystalline ZrP_2O_7 (-39 ppm), the effect of replacement one of Na^+ by Zr^{4+} in $P(Q^1)_{Na}$ and formation of $P(Q^1)_{Na,Zr}$ should give a chemical shift at around –11 ppm. Thus, peak ϕ with a chemical shift at –8 ppm may be assigned as $P(Q^1)_{Na,Zr}$. This assignment is in accordance with increase of this peak when the mol% of P_2O_5 increases.

The assignment of these five ^{31}P resonances are consistent with many previous reports on both glassy and crystalline materials. Fig. 5.07 gives a summary of the chemical shifts and assignments in the present study compared to chemical shift data reported for several glass systems and crystalline compounds.

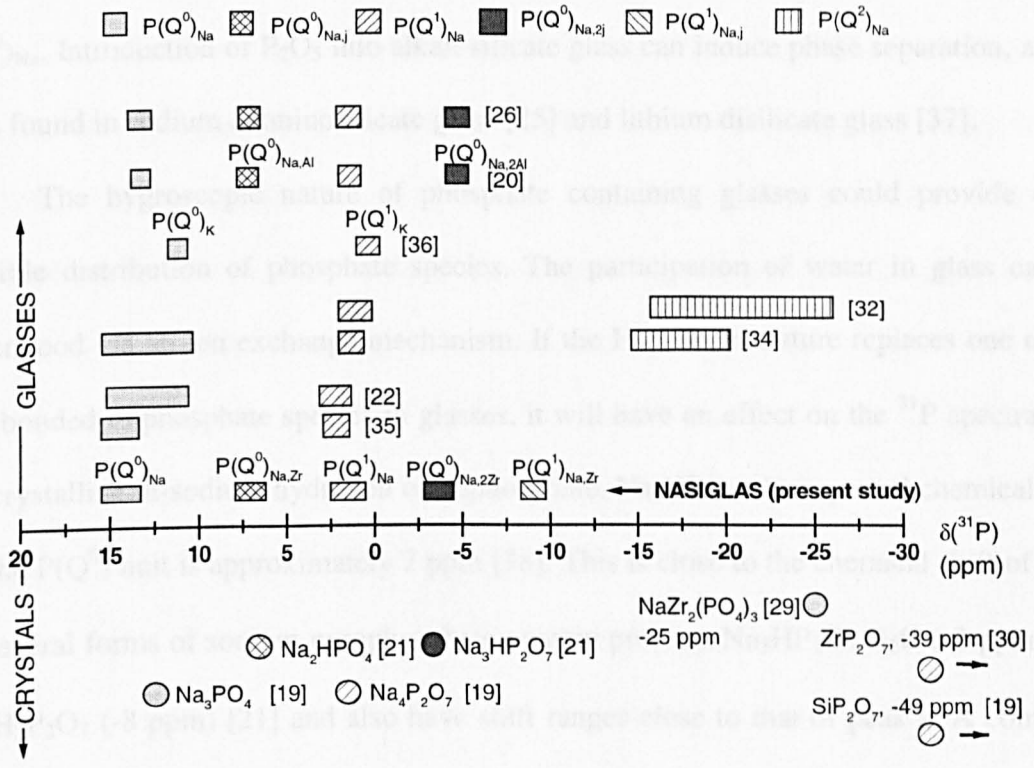

Figure 5.07 *Chemical shift range for typical phosphate species present in various glass systems: $xNa_2O.(1-x)Al_2O_3.2SiO_2.yP_2O_5$ [20], Na_2O-CaO-SiO_2 + 6 mol% P_2O_5 [22], $xNa_2O.(1-x)Al_2O_3.2SiO_2$ + 4 mol% P_2O_5 [26] $x(Na_2O+H_2O).(1-x)P_2O_5$ [30], $R_2O.2SiO_2$: P_2O_5 [34], $Na_2O.2SiO_2$:P_2O_5 [35], $19K_2O.76SiO_2.5P_2O_5$ [36] and in crystalline phosphates.*

5.2.6.1.3 Distribution of $P(Q^n)$

There is a discrepancy in the $P(Q^0)_{Na}$ peak intensity for the G3 sample (41.23%). This should be a value lying between 34% (G2) and 16% (G4) if there were a systematic change in the distribution of all five phosphate species. A possible explanation may be given by considering the acid-base reaction between orthophosphate and pyrophosphate units which can be expressed as [28]

$$2PO_4^{3-} \Leftrightarrow P_2O_7^{4-} + O^{2-} \quad \text{or} \quad 2P(Q^0)_{Na} \Leftrightarrow P(Q^1)_{Na} + O^{2-}$$

This reaction should go to the right with decreasing $[Na_2O]/[P_2O_5]$ molar ratio but this is not the case in G3. The excess concentration of $P(Q^0)_{Na}$ in G3 may be due to phase separation forming a Na_3PO_4-like environment in which phosphate species are present as $P(Q^0)_{Na}$. Introduction of P_2O_5 into alkali silicate glass can induce phase separation, as has been found in sodium aluminosilicate glass [25] and lithium disilicate glass [37].

The hygroscopic nature of phosphate containing glasses could provide other possible distribution of phosphate species. The participation of water in glass can be understood via an ion exchange mechanism. If the H^+ from moisture replaces one of the Na^+ bonded to phosphate species in glasses, it will have an effect on the ^{31}P spectra. For the crystalline di-sodium hydrogen orthophosphate, Na_2HPO_4, the reported chemical shift for the $P(Q^0)$ unit is approximately 7 ppm [38]. This is close to the chemical shift of peak β. Several forms of sodium pyrophosphate contain protons, $Na_3HP_2O_7.H_2O$ (-2 ppm) and $Na_2H_2P_2O_7$ (-8 ppm) [21] and also have shift ranges close to that of peak ε. A complete answer cannot be produced by means of ^{31}P MAS NMR alone. Other information should be gathered using ^1H MAS NMR.

5.2.6.2 ^{29}Si MAS

5.2.6.2.1 Results

^{29}Si MAS spectra are shown graphically in Fig. 5.08. The spectra are displayed over a small chemical shift range to emphasise the differences in their lineshape. Commonly, the SiO_4 structural units are represented by using the symbol $Si(Q^n)$, where n is the number of bridging oxygens, and the ^{29}Si MAS spectra can be interpreted in terms of the distribution of $Si(Q^n)$. This can be done using Gaussian fitting and Fig 5.10 shows the fitting results. The ^{29}Si MAS NMR spectra can be characterised by two Gaussian components whose peak parameters are summarised in Table 5.06. Fig 5.08 shows that

the centre of gravity of the spectra is in the range -83.5 ppm (G1) to -89.1 ppm (G4). This suggests that there is a mixture of $Si(Q^2)$-$Si(Q^3)$ by comparison with binary sodium silicate, i.e. –76 ppm for $Si(Q^2)$ and –90 ppm for $Si(Q^3)$ [39,40]. However, the role of ZrO_2 should also be considered. In NASICON ($Na_{1+x}Zr_2(SiO_4)_x(PO_4)_{3-x}$, $0 \leq x \leq 3$), the reported ^{29}Si chemical shift is in the range –87 ppm to –95 ppm when x is varied from 3 to 1 [29]. This is in accordance with Zr^{4+} being present in an octahedral site or as $[ZrO_6]^{2-}$ structural units. The chemical shifts observed here suggest that $[ZrO_6]^{2-}$ units are also found in the ZrO_2 deficient compositions of NASIGLAS.

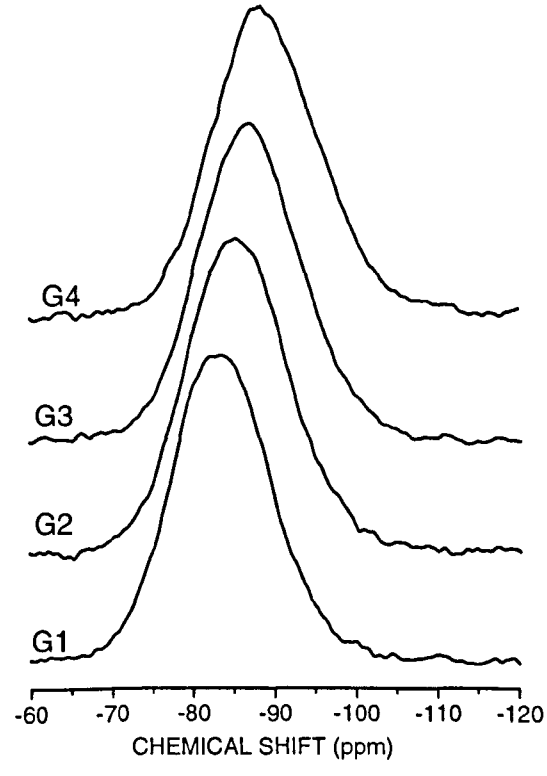

Figure 5.08 *^{29}Si MAS NMR spectra of NASIGLAS acquired on the BRUKER MSL 300 spectrometer at spinning rate of 3.7 kHz. A small chemical shift range has been used to emphasise the differences in the spectral lineshape and the spinning sidebands are therefore not shown.*

5.2.6.1.2 Spectral analysis and Si(Q^n) assignment

The assignment of the ^{29}Si MAS NMR spectra must start with the simplest system, G1, with stoichiometric composition $2Na_2O.ZrO_2.3SiO_2$. It should be assumed that Zr^{4+} are distributed uniformly throughout the glass network and all Na^+ associate with Si(Q^n) species. The possibility of Zr^{4+} having four coordination and being present as $[ZrO_4]$ units can be excluded since the existence of $[ZrO_4]$ units in a glass has not been reported. For example, the X-ray absorption spectroscopic study of high-zirconia borosilicate glasses suggested that Zr environments are typically octahedral [41]. This indicates a difference between Zr^{4+} and Ti^{4+} since Ti^{4+} can be found as $[TiO_4]$ in a glass. In sodium titanium silicate glasses, Hanada and Soga [42] reported that $[TiO_{6/2}]^{2-}$ is found at small TiO_2 contents and $[TiO_{4/2}]^0$ is found at higher TiO_2 contents. A Zr coordination study in some amorphous and crystalline silicates using X-ray absorption spectroscopy suggested that Zr occupy octahedral sites at low ZrO_2 concentrations (below 5 wt%) [41]. Structural studies in many crystalline materials of the Na_2O-ZrO_2-SiO_2 system, employing multiple techniques, also suggested that Zr^{4+} prefer to occupy only octahedral sites with the exception of the mineral zircon ($ZrSiO_4$) [34,35,43]. Thus, our assignment is also based on the assumption that Zr^{4+} is in octahedral sites. This is discussed below.

If all Zr^{4+} were present as $[ZrO_6]^{2-}$ units in G1, this would require charge compensation from two Na^+. The remaining Na_2O would provide a number of non-bridging oxygens per silicate tetrahedron $[SiO_4]$ (NBO/Si) equal to $33.3/50 \approx 0.67$. However, this corresponds to mixed Si(Q^3)-Si(Q^4) species which is not consistent with the observed chemical shift range.

If all Zr^{4+} enter the silicate network as modifier, the NBO/Si ratio is given by

$$\text{NBO/Si} = (2\times\text{mol\% of } Na_2O + 4\times\text{mol\% of } ZrO_2)/\text{mol\% of } SiO_2$$

$$= 133.46/50 \approx 2.67$$

This corresponds to mixed $Si(Q^1)$-$Si(Q^2)$ in G1 and is the most probable assignment of $Si(Q^n)$ species. The observed chemical shift range is also consistent with the reported chemical shifts of crystalline phases in the Na_2O-ZrO_2-SiO_2 system, e.g. $Na_2ZrSi_2O_7$ – $Si(Q^1)$, -86.7 ppm & -88.9 ppm, $Na_4ZrSi_4O_{11}$ – $Si(Q^2)$, -96.2 ppm & -98.2 ppm, $Na_2ZrSi_3O_9.2H_2O$ - $Si(Q^2)$, -96.0 ppm. Thus, G1 is believed to contain mixed $Si(Q^1)$ and $Si(Q^2)$ in the concentration ratio 2:1.

The assignment is based on the assumption that Zr^{4+} is effectively found in the octahedral environment even though Zr^{4+} exhibits a modifying role. This can be understood if four of the coordinated oxygens are the non-bridging oxygens and the other two are bridging oxygens from $Si(Q^n)$. The possible structural unit is illustrated in Fig. 5.09. Dotted lines indicate indirect bonding between Zr^{4+} and the bridging oxygens of nearby $Si(Q^n)$ groups.

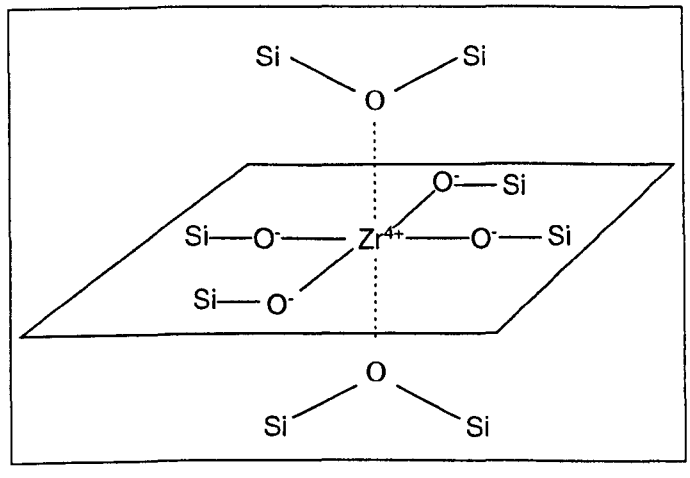

Figure 5.09 *Possible linkage between $Si(Q^n)$ groups and Zr^{4+} proposed for G1 ($2Na_2O.ZrO2.3SiO_2$) where O and O^- are bridging and non-bridging oxygens, respectively.*

If 66.6 mole of $Na^+$and 16.7 mole of Zr^{4+} modify the network built up from 50 mole of SiO_2, these will produce 66.8 Zr-O-Si bonds and 66.6 Na-O-Si bonds. Thus, the most possible distribution should be at least three $Si(Q^n)$ species as

16.7 mol - $SiO(ONa)_2(OZr)$ $\equiv Si(Q^1)_{Na,Zr}$

16.7 mol - $SiO(ONa)(OZr)_2$ $\equiv Si(Q^1)_{Na,2Zr}$

16.7 mol - $SiO_2(ONa)(OZr)$ $\equiv Si(Q^2)_{Na,Zr}$

This distribution is consistent with the observed chemical shift range and gives $Si(Q^1)/Si(Q^2)$ ratio = 2:1. It should be noted that $[Si(Q^1)] = [Si(Q^1)_{Na,Zr} + Si(Q^1)_{Na,2Zr}]$. Presence of other $Si(Q^n)$ species is not possible; $Si(Q^1)_{Na}$ should show a peak in the range –66 ppm to –68 ppm as in binary sodium silicate glasses [36,43], $Si(Q^1)_{3Zr}$ and $Si(Q^2)_{2Zr}$ would initiate segregation.

In G2, G3 and G4, replacement of some $[SiO_4]$ tetrahedra by $[PO_4]$ tetrahedra results in change of NBO/Si. Thus, NBO/Si of G2, G3 and G4 can be evaluated using the results of ^{31}P MAS NMR (Table 5.05b). The cation charge (Na^+, Zr^{4+}) being removed from the silicate network by $P(Q^0)$ and $P(Q^1)$ species is +3 and +2, respectively. From the general formula of NASIGLAS ($Na_{1+x}Zr_{2-x/3}Si_xP_{3-x}O_{12-2x/3}$) and the concentration fraction of $P(Q^0)$ and $P(Q^1)$ reported in Table 5.5b, the general expression of NBO/Si can be given as

$$\begin{aligned} NBO/Si &= [(1+x) + 4.(2-x/3) - (3C_1 + 2C_2).(3-x)]/x \\ &= [(9-x/3) - (3C_1 + 2C_2).(3-x)]/x \end{aligned} \quad 5.4$$

where C_1 and C_2 are the fraction of $P(Q^0)$ and $P(Q^1)$, respectively, and defined as

$$C_1 = [P(Q^0)_{Na} + P(Q^0)_{Na,Zr} + P(Q^0)_{Na,2Zr}]/P \quad 5.5$$

$$C_2 = [P(Q^1)_{Na} + P(Q^1)_{Na,Zr}]/P \quad 5.6$$

$$P = [P(Q^0)_{Na} + P(Q^0)_{Na,Zr} + P(Q^0)_{Na,2Zr} + P(Q^1)_{Na} + P(Q^1)_{Na,Zr}] \quad 5.7$$

The $[Si(Q^1)]/[Si(Q^2)]$ ratio can also be calculated using the relation below

$$3.[Si(Q^1)] + 2.[Si(Q^2)] = NBO/Si \times mol\%\ SiO_2 \quad 5.8$$

$$[Si(Q^1)] + [Si(Q^2)] = mol\%\ SiO_2 \quad 5.9$$

Hence, $[Si(Q^1)]/[Si(Q^2)] = (NBO/Si - 2)/(3 - NBO/Si)$ 5.10

where NBO/Si < 3. The results of the calculations are summarised in Table 5.06a.

Table 5.06a *Calculated NBO/Si for G2,G3 and G4, and predicted $[Si(Q^1)]/[Si(Q^2)]$ ratio.*

Sample	X	C_1	C_2	Calculated NBO/Si	Predicted $[Si(Q^1)]/[Si(Q^2)]$
G2	2.75	0.80	0.20	2.68	2.13
G3	2.50	0.76	0.24	2.71	2.45
G4	2.25	0.65	0.35	2.79	3.76

Note: C_1 and C_2 are determined using data in Table 5.05b

Table 5.06b *^{29}Si chemical shift, δ, linewidth ,W, and relative peak area, A, of $Si(Q^n)_{i,j}$ species determined by Gaussian fit for ^{29}Si MAS NMR spectra of NASIGLAS.*

Sample	$Si(Q^1)_{Na,Zr}$			$Si(Q^1)_{Na,2Zr}$			$Si(Q^2)_{Na,Zr}$			Q^1/Q^2
	δ ± 0.5 ppm	W ± 0.5 ppm	A ± 2.0 %	δ ± 0.5 ppm	W ± 0.5 ppm	A ± 2.0 %	δ ± 0.5 ppm	W ± 0.5 ppm	A ± 2.0 %	
G1	-78.8	8.7	34	-84.4	8.5	34	-88.2	11.6	32	2.1
G2	-79.9	8.8	24	-85.7	9.0	44	-90.5	11.8	32	2.1
G3	-80.0	8.7	15	-86.9	9.4	56	-92.2	12.6	29	2.5
G4	-80.7	8.9	8	-88.1	10.2	67	-95.5	11.4	25	3.0

Note: $Q^1/Q^2 = [Si(Q^1)_{Na,Zr} + Si(Q^1)_{Na,2Zr}]/[Si(Q^2)_{Na,Zr}]$

It can be seen that the NBO/Si are actually increased in G2, G3 and G4 since the reduction in Na_2O and increase in P_2O_5 are effectively offset by increase in ZrO_2. Increasing $Si(Q^1)$ concentration is due to replacement of Na^+ by the higher valency Zr^{4+} which can create more NBO. This is the implication of the $Si(Q^1)_{Na,Zr} \rightarrow Si(Q^1)_{Na,2Zr}$ transformation.

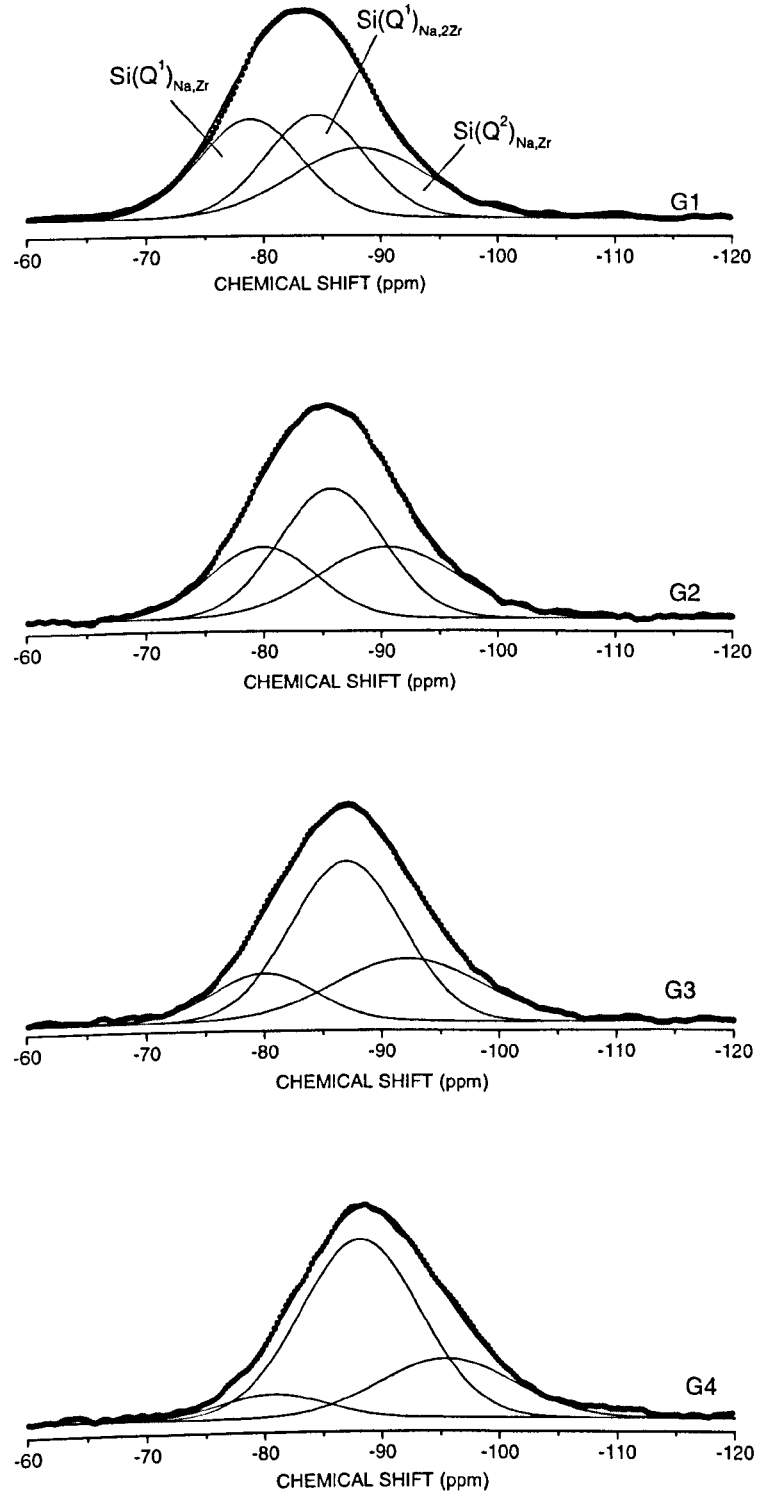

Figure 5.10 *Deconvolution of ^{29}Si MAS NMR spectra of NASIGLAS. Dots are the experimental data, solid lines are the simulation curves.*

5.2.6.2.3 $Si(Q^n)$ distribution

Table 5.6b shows the results of Gaussian fitting for ^{29}Si MAS NMR spectra which is illustrated by Fig. 5.10. The constraints applied to chemical shift and linewidth: I) peak positions are separated by minimum ~4 ppm, II) linewidth is in the range 7 ppm to 20 ppm. It can be seen that the spectrum of G1 is well determined by three Gaussian peaks with relative area ratio approximately 1:1:1. There is a good agreement between the proposed model and the experimental result. This confirms that G1 contains three silicate species, $Si(Q^1)_{Na,Zr}$, $Si(Q^1)_{Na,2Zr}$ and $Si(Q^2)_{Na,Zr}$, in equal concentrations with chemical shifts –78.8 ppm, -84.4 ppm and –88.2 ppm, respectively. Introduction of P_2O_5 and decrease of Na_2O/ZrO_2 ratio in G2, G3 and G4, result in a small shift for $Si(Q^1)_{Na,Zr}$ (-78.8 ppm to –80.7 ppm) and larger shift for $Si(Q^1)_{Na,2Zr}$ and $Si(Q^2)_{Na,Zr}$, i.e. from –84.4 ppm to –88.1 ppm and from –88.2 ppm to –95.5 ppm. These results suggest that association of $Si(Q^n)$ species with Zr^{4+} shifts the ^{29}Si resonance toward lower frequency compared to association with Na^+. However, $[PO_4]$ units may be also responsible for this low frequency shift by indirect influence. The linewidth of $Si(Q^1)_{Na,Zr}$ is almost constant at 8.8 ppm. Larger variations of linewidth are observed for $Si(Q^1)_{Na,2Zr}$ and $Si(Q^2)_{Na,Zr}$ which are in the range 8.5 ppm–10.2 ppm and 11.4 ppm-12.6 ppm, respectively. The effect of decrease in the Na_2O/ZrO_2 ratio is observed as replacement of Na^+ by Zr^{4+} which increase the $Si(Q^1)_{Na,2Zr}$ concentration via the $Si(Q^1)_{Na,Zr} \rightarrow Si(Q^1)_{Na,2Zr}$ transformation. There is also good agreement between calculation (Table 5.6a) and the observed $Si(Q^1)/Si(Q^2)$ ratio (Table 5.6b). However, a large discrepancy is observed for G4. Calculation suggests the $Si(Q^1)/Si(Q^2)$ ratio = 3.76 but the experimental result is only 3.0 indicating less formation of $Si(Q^1)_{Na,2Zr}$. This is the consequence of the solubility limit of ZrO_2 and the observation of a trace amount of crystalline $ZrSiO_4$ by XRD. Thus the actual ZrO_2 content is less than nominal and less Zr^{4+} ions are available to form $Si(Q^1)_{Na,2Zr}$.

The ^{29}Si MAS NMR results indicate that removal of Na^+ and Zr^{4+} from the silicate network to form phosphate complexes (known as the scavenging effect [22]) does not produce the expected decrease of NBO/Si because, although Na^+ removal is complete Zr^{4+} are still bound to $[SiO_4]$ whilst at least one octahedral corner links to $[PO_4]$. Replacement of Na^+ by Zr^{4+} is responsible for an increase of NBO/Si with decreasing x. The absence of repolymerisation of the silicate network seems to conflict with the trend of increased T_g with decreasing x, implying a strengthened network. The influence of Zr-O-Si bonds may be the answer and this was discussed in section 5.2.3. However, the results of ^{31}P MAS NMR and ^{29}Si MAS NMR confirms that scavenging of Na^+ from the silicate network does occur. This seems to be a common effect for silicate based glasses on addition of P_2O_5.

5.2.6.3 ^{23}Na MAS

The MAS spectra of ^{23}Na are shown in Fig. 5.11 and the spectral parameters are summarised in Table 5.07. In most cases, only a single peak (central transition) is observed and the peak maximum lies in the chemical shift range from –5 ppm to approximately –19 ppm. The additional sharp features in the spectrum from G1 are probably ionic Na^+ from fingerprints. The spectrum from sample G3 is obviously very different in shape being Lorentzian rather than Gaussian (or quadrupolar). Its line width is twice that of the other samples and the chemical shift is about –5 ppm, very different from the –19 ppm and –16 ppm observed for the other three samples. This spectrum is reproducible for different samples of G3 from both the same and different melt preparations. The Lorentzian lineshape of the ^{23}Na resonance from this particular sample indicates that the width is dominated by T_2 (the spin-spin relaxation time, which is inversely proportional to spectrum linewidth) rather than dipolar interactions [46]. The implication of this result is that Na^+ ions are undergoing very different motion in sample

G3 than in the other compositions. Dynamically, the Na^+ can migrate more rapidly in the situation of high Na^+ concentration. Thus, if micro phase separation is really occurring in G3 to give a phase with composition close to Na_3PO_4, the Na^+ would certainly possess higher mobility in this phase. This means that higher Na^+ concentration can be found and contribute to a higher conductive state. It could resemble the highly conducting Na^+ in crystalline Na_3PO_4 (high temperature phase) [47]. High temperature ^{23}Na NMR investigation of crystalline Na_3PO_4 (low temperature phase) showed that the chemical shift of ^{23}Na is close to 0 ppm and characterised by a Lorentzian lineshape [48]. This is very similar to the ^{23}Na MAS NMR spectrum of G3. It strongly supports the idea that G3 contains phase separation with one phase have a composition close to Na_3PO_4. This observation is also consistent with the excess $P(Q^0)_{Na}$ concentration determined from ^{31}P MAS NMR spectra of G3 as discussed above. However, it should be noted that no crystalline Na_3PO_4 is present.

Table 5.07 *Spectral parameters of ^{23}Na MAS spectra.*

Sample	Chemical shift (±0.5 ppm)	Linewidth (±0.5 ppm)
G1	-16.4	43.1
G2	-19.1	40.6
G3	-5.8	88.4
G4	-16.5	35.9

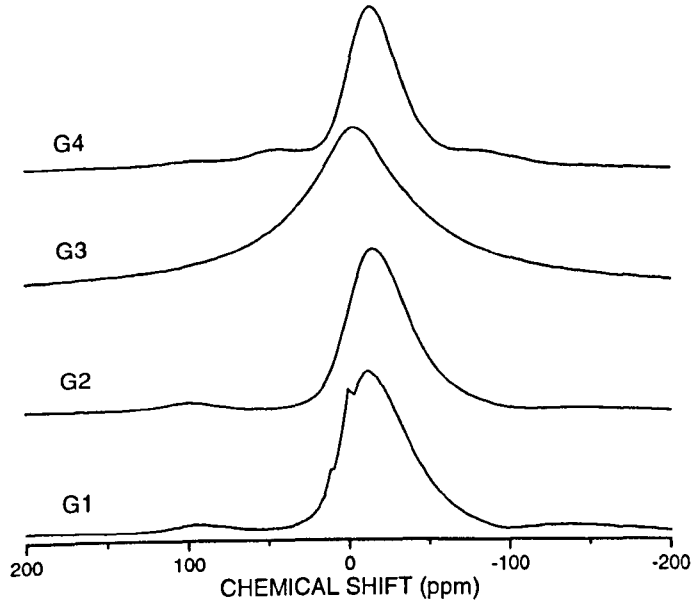

Figure 5.11 *^{23}Na MAS NMR spectra of NASIGLAS acquired at field strength 8.45 T with resonance frequency 95.26 MHz and spinning speed 10 kHz.*

5.3 Conclusions

It is possible to prepare fast-ion conducting glass samples corresponding to the Zr-deficient composition or NASIGLAS, $Na_{1+x}Zr_{2-x/3}Si_xP_{3-x}O_{12-2x/3}$, where $0 \leq x \leq 3$. To obtain high quality glass, silica rich compositions were selected which lie in the range of $2 \leq x \leq 3$. Four glass samples were prepared from compositions of x = 2.25, 2.50, 2.75 and 3.00 designated as G4, G3, G2 and G1 respectively. The glass forming ability of this system improves with increasing SiO_2 content. From the DTA study of as-quenched glass samples, it is found that the glass transition regions are shifted to higher temperature corresponding to higher strength of the silicate network. This strengthening is the effect of (i) removal of Na^+ from the silicate network by P_2O_5 content and (ii) forming more densely packed structure with increasing ZrO_2 mol%. When the mol% of ZrO_2 reaches its solubility limit, trace amounts of crystalline $ZrSiO_4$ can be observed from G3 and G4.

The crystallisation process occurs as two distinctive features in the DTA, two crystallisation peaks for G1 and G2, and one crystallisation peak for G3 and G4. The higher temperature crystallisation peaks of G1 and G2 are located in the same range but differ by ~60 °C from those peaks of G3 and G4. It indicates that the crystallisation of fast-ion conducting glasses in this system is complex. This will be detailed in chapter 7.

The ^{31}P MAS NMR results show formation of five different phosphate species, $P(Q^0)_{Na}$, $P(Q^0)_{Na,Zr}$, $P(Q^1)_{Na}$ and $P(Q^0)_{Na,2Zr}$ and $P(Q^1)_{Na,Zr}$, by removing Na^+ from the silicate network and also progressively linking to $[ZrO_6]$ units. The possible transformation of phosphate species may be described as $P(Q^0)_{Na} \rightarrow P(Q^0)_{Na,Zr} \rightarrow P(Q^0)_{Na,2Zr}$ and $P(Q^1)_{Na} \rightarrow P(Q^1)_{Na,Zr}$ when Na_2O/ZrO_2 decreases and mol% P_2O_5 increases. However, excess concentration of $P(Q^0)_{Na}$ was found in G3. This is believed to be due to occurrence of phase separation giving a phase with composition close to Na_3PO_4. The information from ^{23}Na MAS spectra also suggests possible phase separation in G3, as its possesses Lorenzian rather Gaussian lineshape. However, direct observation of phase separated would require TEM or SAXS/SAM.

The ^{29}Si MAS NMR study suggests that G1 contains three different silicate species; $Si(Q^1)_{Na,Zr}$, $Si(Q^1)_{Na,2Zr}$ and $Si(Q^2)_{Na,Zr}$ with a concentration ratio 1:1:1. The spectral lineshape shows that these three $Si(Q^n)_{i,j}$ species are also present in G2, G3 and G4. Using results of ^{31}P MAS NMR, we can calculate the NBO/Si and $Si(Q^1)/Si(Q^2)$ ratios. From the results of Gaussian fit, good agreements between the predicted and the experimental ratios were found. The NBO/Si and $Si(Q^1)/Si(Q^2)$ ratios increase with decrease in x. This is believed due to the replacement of Na^+ by Zr^{4+} with a higher valency which can create more NBO. Further evidence was given by increase of $Si(Q^1)_{Na,2Zr}$ which is the indication of formation of $Si(Q^1)_{Na,2Zr}$ from $Si(Q^1)_{Na,Zr}$. An additional consequence was the decrease in $Si(Q^2)_{Na,Zr}$.

References

[1] Cooper, E.I. and Angell, C.A. *Journal of Non-Crystalline Solids*. **56** (1983), 75.

[2] Drexhage, M.G., El-Bayoumi, O.H., Lipson, H., Moynihan, C.T., Bruce, A.J., Lucas, J. and Fonteneau, G. *Journal of Non-Crystalline Solids*. **56** (1983), 51.

[3] Bansal, N.P., Bruce, A.J., Doremus, R.H. and Moynihan, C.T. *Journal of Non-Crystalline Solids*. **70** (1985), 379.

[4] Kingerly, W.D., Bowen, H.K. and Uhlmann, D.R. *Introduction to Ceramics*. New York: John Wiley and Sons, 1960.

[5] Hoffman, L.C., Kupinski, T.A., Thakur. R.L. and Weyl, W.A. *Journal of Society of Glass Technology*. **36** (1952), 196.

[6] Navaes de Oliveira, A.P., Corradi, A.B. Barbieri, L., Leonelli, C. and Manfredini, T. *Thermochimica Acta*. **286** (1996), 375.

[7] Susman, S. Delbecq, C.J. and McMillan, J.A. *Solid State Ionics*. **9&10** (1983), 667.

[8] Navaes de Oliveira, A.P and Manfredini, T., *Journal of Materials Science*. **36** (2001), 2581.

[9] Ennas, G. Musinu, A., Piccaluga, G., Pinna, G. and Magini, M. *Chemical Physics Letters*. **141**, no.1, 2 (1987), 143.

[10] *Engineer materials handbook Vol. 4; Ceramics and glasses*. Cleveland, Ohio: ASM International, 1991.

[11] Novaes de Oliveira, A.P., Leonelli, C., Manfredini, T., Pellacani, G.C., Ramis, G., Trombetta, M. and Busca, G. *Physics and Chemistry of Glasses*. **39**, no. 4 (1998), 213.

[12] Doweidar, H. *Journal of Non-Crystalline Solids*. **194** (1996), 155.

[13] Greaves, G.N., Smith, W., Giulotto, E. and Pantos, E. *Journal of Non-Crystalline Solids*. **222** (1997), 13.

[14] Tischebdorf, B., Ma, C., Hammersten, E., Venhuizen, P. Peters, M., Affatigato, M. and Feller, S. *Journal of Non-Crystalline Solids*. **239** (1998), 197.

[15] Doweidar, H. *Journal of Non-Crystalline Solids*. **249** (1999), 194.

[16] Doweidar, H., Feller, S., Affatigato, M., Tischendorf, B., Ma, C. and Hamarsten, E. *Physics and Chemistry of Glasses*. **40** no.6 (1999), 339.

[17] Larsen, P.H., Poulsen, F.W. and Berg, R.W. *Journal of Non-Crystalline Solids*. **244** (1999), 16.

[18] Massiot, D., Thiele, H., and Germanus, A., *"WinFit - a Windows-based program for lineshape analysis " Bruker Report*. **140**, (1994), 43.

[19] Mudrakovskii, I.L., Shmachkova, V.P. and Kotsarenko, N.S., *Journal of Physics and Chemistry of Solids*. **47**, no. 4 (1986), 335.

[20] Duncan, T.M., and Douglass, D.C., *Chemical Physics*. **87** (1984), 339.

[21] Griffiths, L., Root, A., Harris, R.K., Packer, K.J., Chippendale, A.M. and Tromans, F.R., *Journal of Chemical Society, Dalton transaction*. (1986), 2247.

[22] Dupree, R. and Holland, D. *"NMR: a new spectroscopic technique for structure determination in glasses and ceramics" in: Glass and Glass-ceramics*. Ed. M. Lewis. London: Chapman & Hall, 1988.

[23] Dupree, R., Holland, D. and Mortuza, M.G. *Physics and Chemistry of Glasses*. **29** (1988), 18.

[24] Li, D., Fleet, M.E. Bancroft, G.M., Kasrai, M., and Pan, Y., *Journal of Non-Crystalline Solids*. **188** (1995), 181.

[25] Toplis, M.J.and Schaller, T. *Journal of Non-Crystalline Solids*. **224** (1998), 57.

[26] Yang, W.H. and Kirkpatrick, R.J., *Journal of American Ceramics Society*. **69**, no. 10 (1986), C222.
[27] Lockyer, M.W.G., Holland, D. and Dupree, R. *Journal of Non-Crystalline Solids*. **188** (1995), 207.
[28] Grussaute, H., Montagne, L., Palavit, G., and Bernard, J.L., *Journal of Non-Crystalline Solids*. **263&264** (2000), 312.
[29] Jäger, C., Scheler, G., Sternberg, U., Barth, S., and Feltz, A., *Chemical Physics Letters*. **147**, no. 1 (1988), 49.
[30] Mudrakovskii, I.L., Mastikhin, V.M., Shmachkova, V.P., and Kotsarenko, N.S., *Chemical Physics Letters*. **120** (1985), 424.
[31] Nelson, C., and Tallant, D.R., *Physics and Chemistry of Glasses*. **25**, no. 2 (1984), 31.
[32] Brown, R.K., Kirkpatrick, R.J. and Turner, G.L. *Journal of Non-Crystalline Solid*. **116** (1990), 39.
[33] Schaller, T., Rong, C., Toplis, M.J. and Cho, H., *Journal of Non-Crystalline Solids*. **248** (1999), 19.
[34] Bortun, A.I., Bortun, L.N. and Clearfield, A., *Chemistry of Materials*. **9** (1997), 1854.
[35] Ferreira, P., Ferriera, A., Rocha, J. and Soares, M.R., *Chemistry of Materials*. **13** (2001), 355.
[36] Dupree, R., Holland, D. and Mortuza, M.G. *Nature*. **328** (1987), 416.
[37] Iqbal, Y., Lee, W.E., Holland, D. and James, P.F. *Journal of Materials Science*. **34** (1999), 4399.
[38] Turner, G.L., Smith, K.A., Kirkpatrick, R.J. and Oldfield, E., *Journal of Magnetic Resonance*. **70** (1986), 408.
[39] Grimmer, A.R., Mägni, M. Hähnert. M., Stade, H., Samoson, A., Wieker. W. and Lippmaa, E., *Physics and Chemistry of Glasses*. **25**, no. 4 (1984), 105.
[40] Dupree, R., Holland, D., McMillan, P.W. and Pettifer, R.F. *Journal of Non-Crystalline Solids*. **68** (1984), 399.
[41] McKeown, D.A., Muller, I.S., Buechele, A.C. and Pegg, I.L., *Journal of Non-Crystalline Solids*. **258** (1999), 98.
[42] Hanada, T. and Soga, S., *Journal of Non-Crystalline Solids*. **38-39** (1980), 105
[43] Lin, Z., Rocha, J., Ferriera, P., Thursfield, A., Agger, J.R., and Anderson, M.W., *Journal of Physical Chemistry B*. **103** (1999), 957.
[44] Maekawa, H., Maekawa, T., Kawamura, K. and Yokokawa, T., *Journal of Non-Crystalline Solids*. **127** (1991), 53.
[45] Lockyer, M.W.G., Holland, D. and Dupree, R. *Physics and Chemistry of Glasses*. **36**, no.1 (1995), 22.
[46] Forsyth, M., Smith, M.E., Meakin, P. and MacFarlane, D.R. *Journal of Polymer Science*. **B32** (1994), 2077.
[47] Witschas, M. and Eckert, H. *Journal of Physical Chemistry A*. **103** (1999), 10764.
[48] Witschas, M. and Eckert, H., Freiheit, H., Putnis, A., Korus, G. and Jansen, M., *Journal of Physical Chemistry A*. **105** (2001), 6808.

CHAPTER 6

Na_2O-TiO_2-SiO_2-P_2O_5 Glass System

6.1 Introduction

TiO_2 is used as a nucleating agent in glass-ceramics processing since it can shorten the induction period of crystalline nuclei and increases their growth rate. In this work, TiO_2 was used as an intermediate oxide for preparing fast-ion conducting glass related to the NASIGLAS composition. The aim of using TiO_2 is to enhance the ease of glass formation with respect to the original NASIGLAS composition which contained ZrO_2 as the intermediate oxide (Ch. 5). In glasses, the difference in ionic field strength of cations can be used to classify the glass forming ability of the oxide of those ions. The higher field strength gives the higher glass forming ability [1]. Ionic field strength is defined as a ratio of valency of cation to the square of its ionic radius. Typically, Ti^{4+} has an ionic field strength of 8.7 which is higher than the 6.3 of Zr^{4+}, this leads to the higher glass forming ability of TiO_2 [1].

TiO_2 also induces phase separation and increases hardness and toughness in glasses[2, 3]. The important feature of Ti ions in compounds is the possibility of multiple coordination states, these are Ti^{IV} , Ti^{V} and Ti^{VI}. Ti^{VI} is common in crystalline materials [4]. In glasses, the coordination number of Ti ions can be changed from 4 to 6 depending on concentration and glass systems. For sodium titanium silicate glasses, Hanada and Soga [4] suggested that Ti^{4+} occupy octahedral sites at low TiO_2 and change to lower coordination sites when the TiO_2/SiO_2 ratio increases toward one. Mysen and Neuville [5] suggested Ti^{4+} is only found in tetrahedral coordination. This indicates that Ti^{4+}can adopt different roles in glass networks depending on its concentration and the overall glass compositions.

In this chapter, the results of using TiO_2 in NASIGLAS compositions on structural arrangement and related properties will be reported. These new glass compositions, $Na_{1+x}Ti_{2-x/3}Si_xP_{3-x}O_{12-2x/3}$, are referred to as NTS glasses. The same experimental procedures as used for investigation of NASIGLAS were repeated for the NTS glasses.

6.2 Glass preparation

Details of glass preparation have been given in Chapter 4. Five glass compositions were selected from the general formula $Na_{1+x}Ti_{2-x/3}Si_xP_{3-x}O_{12-2x/3}$ with x = 3.00, 2.75, 2.50, 2.25 and 2.00. Sample names and the nominal mol% are summarised in Table 6.01 along with the excess weight loss during melting. The chemical reaction of constituent oxides can be presented as

$$(2x-4).Na_2CO_3 + (2-x/3).TiO_2 + x.SiO_2 + (3-x)Na_3PO_4 \rightarrow Na_{1+x}Ti_{2-x/3}Si_xP_{3-x}O_{12-2x/3} + (2x-4).CO_2\,(g) \quad 6.1$$

Table 6.01 *Nominal compositions of NTS glasses ($Na_{1+x}Ti_{2-x/3}Si_xP_{3-x}O_{12-2x/3}$) with weight lost in melting, δW.*

x	Sample name	Nominal compositions (mol%)				δW (%)
		Na_2O	TiO_2	SiO_2	P_2O_5	
3.00	NTS1	33.33	16.66	50.00	-	1.7
2.75	NTS2	32.10	18.54	47.21	2.15	3.0
2.50	NTS3	30.92	20.49	44.17	4.42	2.2
2.25	NTS4	29.54	22.73	40.91	6.82	4.9
2.00	NTS5	28.12	25.00	37.50	9.38	5.0

From this equation, it can be seen that only CO_2 gas is being released during melting of the glass batch. Thus, observing mass balance between glass batch and glass product can

determine the loss of Na_2O and P_2O_5 components. The observed weight loss (Table 6.01) increased with decreasing Na_2O and SiO_2 contents. The highest loss of 5% was found in NTS5 (x=2.00). This level of loss may alter the proportion of structural units presented in glass samples. However, some loss is also mechanical, during handling, and therefore the loss has been neglected when discussing structural arrangement and physical properties.

6.3 Glass characterisation

6.3.1 XRD

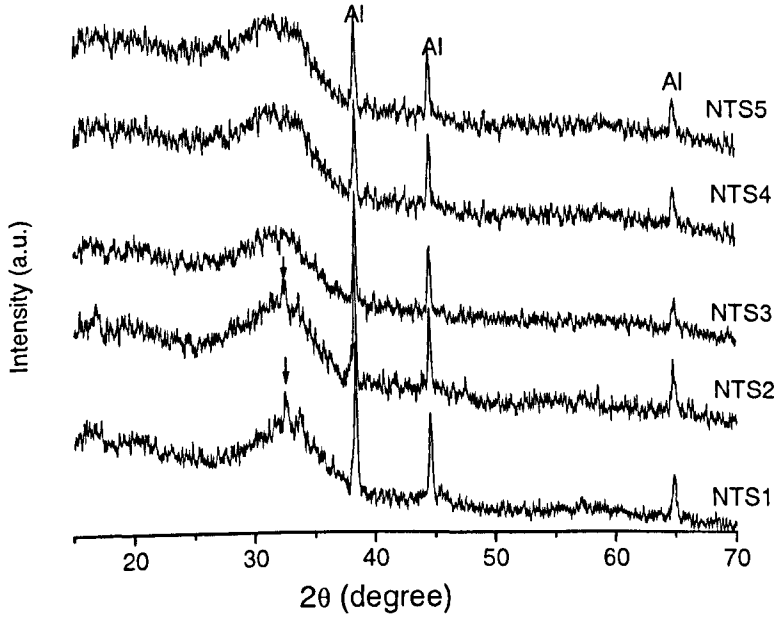

Figure 6.01 *XRD traces of NTS samples. The arrows indicate possible presence of crystalline phases. The diffracted signal from the Al sample holder provided 3 sharp peaks at ~38°, ~45° and ~65°.*

The XRD powder patterns of NTS glasses are shown in Fig. 6.01. These XRD results confirm the amorphous character of NTS glasses. Three sharp peaks at 2θ ~ 38°, 44° and 65° are assigned to the aluminium sample holder. However, an unidentified peak

is present in the patterns of NTS1 and NTS2 at 2θ ~ 33° (d-spacing = 1.4154 Å). Although those peaks are clearly visible, with only one peak for each pattern, it is insufficient to identify the crystalline phase. Nevertheless, it should be noted that the most common role of TiO_2 found in several titanosilicate glasses is to form a heterogeneous glass at high TiO_2 concentration (above 20 mol% TiO_2). In some cases, cryptocrystalline anatase can be found in that heterogenous glass [6]. Thus, the composition of NTS glass may readily provide sufficient TiO_2 to form titanate complexes, which may associate with sodium ions or phosphate units.

6.3.2 DTA

The DTA measurements for NTS glasses were performed using two different reference substances, SiO_2 and Al_2O_3. The DTA heating traces measured using SiO_2 are shown in Fig. 6.02. Two deflections, due to glass transition and softening point, are observed for all NTS glass samples. Unfortunately, the glass transitions regions are in the range of the α–β quartz transition, resulting in some details of the DTA curves being lost. However, with care, glass transition, T_g and softening point, T_s can be determined and these are summarised in Table 6.02a. It can be seen that the crystallisation peaks become more pronounced on going from NTS1 to NTS5. These results indicate the effect of TiO_2 and P_2O_5 on the crystallisation behaviour of glass samples.

Results from the measurements using Al_2O_3 as the reference substance (Fig. 6.03) show clearer details over the glass transition range. The parameters obtained from this measurement are summarised in Table 6.02b to illustrate the reproducibility of these data. It can be seen that T_g, T_s, T_x and T_c determined from these two experiments show the same trends within the experimental error.

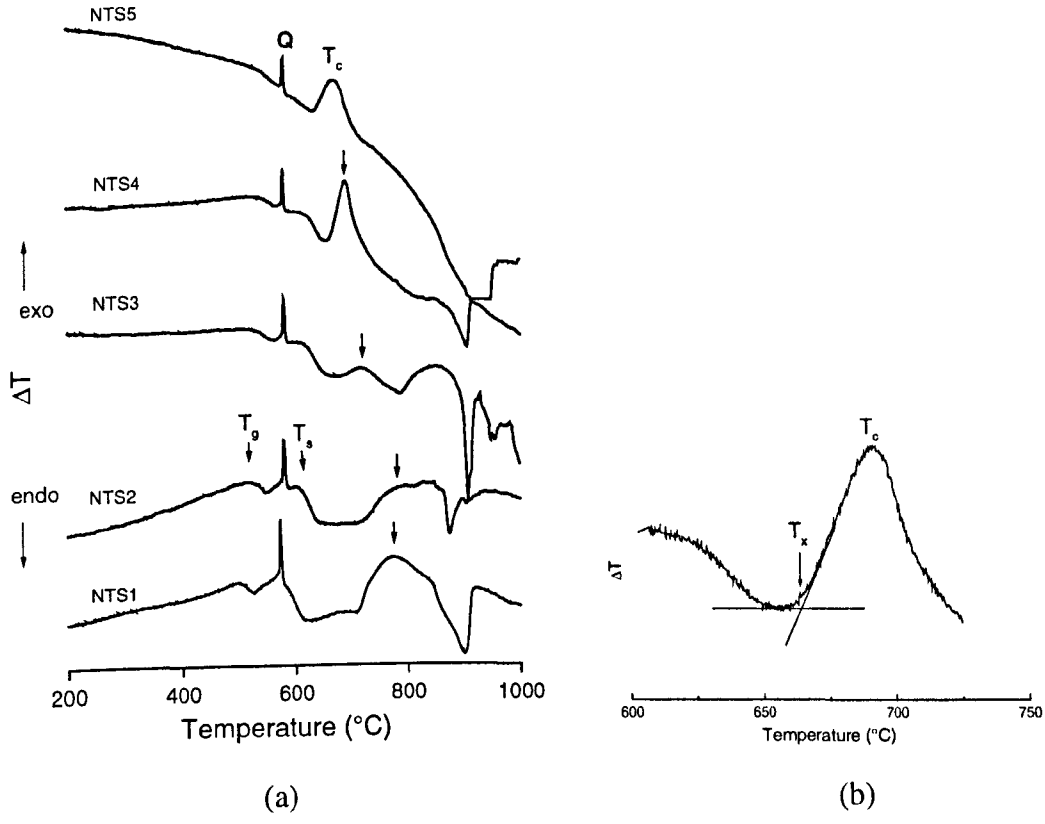

Figure 6.02 (a) *DTA traces of NTS samples obtained using SiO_2 as the reference substance. T_g, T_s and T_c are the glass transition, softening and the crystallisation temperatures, respectively. Q denotes the endothermic peak of the α–β quartz transition, (b) method of determining T_x.*

In Fig. 6.05, plotting averaged T_g and T_s versus Na_2O:SiO_2+P_2O_5 ratio shows that T_g increases continuously but T_s go through a broad maximum. From Table 6.02a and 6.02b, it can be also seen that T_x and T_c exhibit the same tendency as T_s. The crystallisation peaks from the NTS samples become better resolved with decreasing x value, i.e. with increasing mol% of TiO_2 and P_2O_5. It is known that TiO_2 and P_2O_5 can promote heterogeneous nuclei during forming a glass from the melt and those nuclei are readily grown when subjected to subsequent heat treatment. Thus, the relation between the mol% of both oxides and the degree of crystallinity are clearly shown by Figs. 6.02 and 6.03. The effect of TiO_2 and P_2O_5 contents on crystallisation of silicate glasses has

been widely reported [7, 8, 9] However, it should be noted that other factors also affect crystallisation. These include glass stability and viscosity of glass melt.

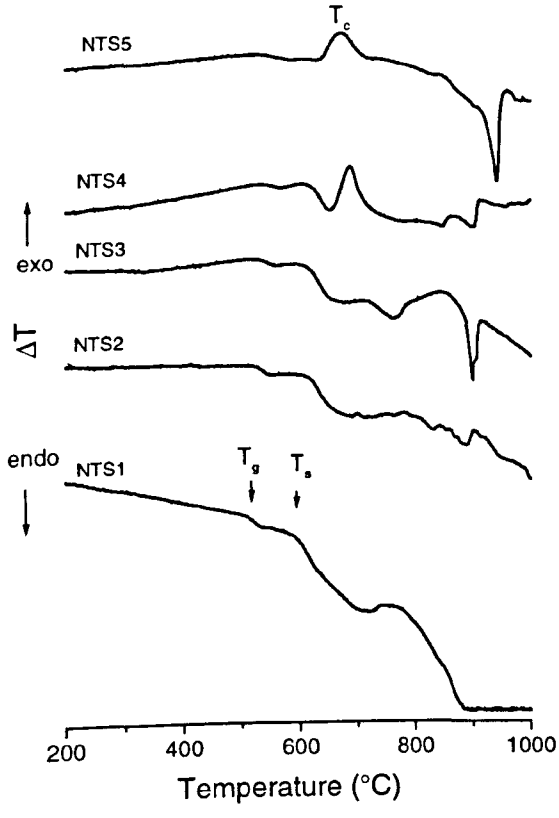

Figure 6.03 *DTA traces of NTS samples obtained from using Al_2O_3 as the reference substance. The symbols T_g, T_s and T_c indicate the glass transition range, softening point and the crystallisation temperature, respectively.*

The liquidus temperatures (endothermic transitions due to melting of glass samples) are clearly seen as peaks in the temperature range 900-1000 °C with the measurement using SiO_2 reference. In contrast, the measurement using Al_2O_3 provided clear endothermic peaks for only two samples, NTS3 and NTS5. Here, it can be seen that the melting range of NTS glass samples is lower than those of NASIGLAS whose melting range is above 1200 °C.

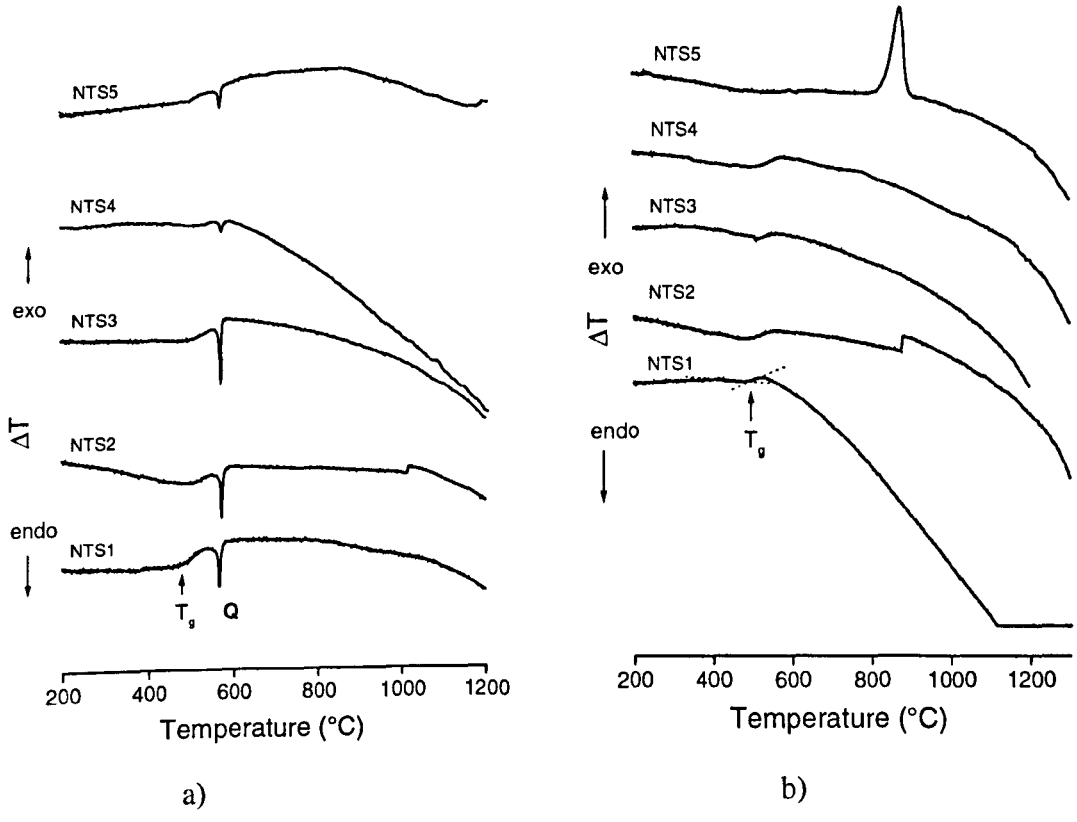

Figure 6.04 *DTA cooling traces of NTS glasses, a) quartz (SiO_2) and b) alumina (Al_2O_3) as the reference substances. T_g and Q represent the glass transition temperature and transition of quartz, respectively.*

Table 6.02a *Glass transition, T_g, softening point, T_s, crystallisation onset temperature, T_x, and crystallisation peak position, T_c, of NTS glasses using SiO_2 as the reference substance.*

Sample	T_g (±3 °C)	T_s (±3 °C)	T_x (±3 °C)	T_c (±3 °C)	T_x-T_g (±3 °C)
NTS1	502	~575	712	775	211
NTS2	521	613	722	795	201
NTS3	528	619	688	710	160
NTS4	535	618	661	690	126
NTS5	538	606	639	669	101

Table 6.02b *DTA results of NTS glasses as using Al_2O_3 as the reference.*

Sample	T_g (±3 °C)	T_s (±3 °C)	T_x (±3 °C)	T_c (±3 °C)	T_x-T_g (±3 °C)
NTS1	509	582	716	772	207
NTS2	522	611	620	790	198
NTS3	525	614	686	~715	161
NTS4	528	615	656	686	128
NTS5	533	604	638	671	105

During cooling of the glass melts from approximately 1500 °C, a crystallisation peak is observed at 880 °C in the trace of NTS5 when using Al_2O_3 reference (Fig. 6.4). The abrupt change at approximately 1000 °C observed in both DTA traces of NTS2 is believed to be due to equipment fluctuation. After cooling to below 600 °C, single glass transitions are clearly seen for all glass samples and for both measurements.

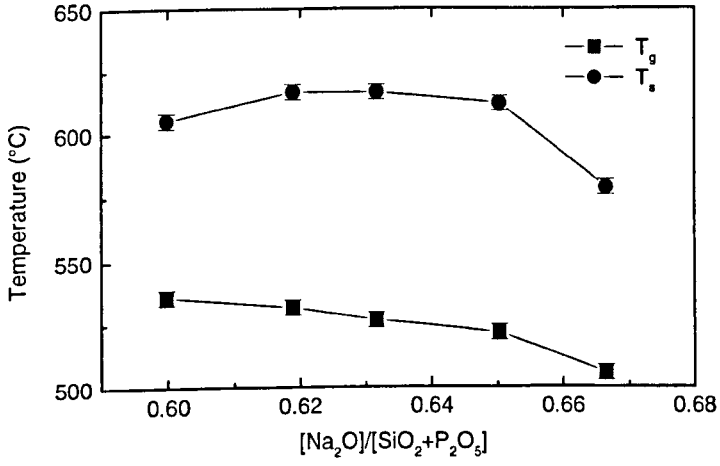

Figure 6.05 *Averaged transition temperature, T_g, and softening temperature, T_s, of NTS glasses as a function of $[Na_2O]/[SiO_2+P_2O_5]$ ratio.*

For NTS glasses, increasing T_g with replacement of $[SiO_4]$ tetrahedra by $[PO_4]$ tetrahedra is clearly seen, as was observed for the NASIGLAS compositions. Removal of Na^+ from the silicate network by $[PO_4]$ units can increase the average number of bridging oxygen per $[SiO_4]$ units leading to higher cross-linking of the network and higher T_g. Increasing T_g is also the consequence of decreasing the molar ratio of modifier oxide (Na_2O) per glass-former oxides ($SiO_2+P_2O_5$). The lower transition temperature observed for NTS glasses, compared to NASIGLAS compositions, reflects the less refractory nature of TiO_2. The reason for the different tends of T_g and T_s with composition is not clear. It should be noted that both terms are the function of thermal history, e.g. cooling

rate. T_s normally indicates the point at which there is a rapid change in viscosity and the start of viscous flow. Consequently, structural rearrangement takes place in this temperature range. The observed T_s of NTS glasses may reflect how such rearrangements depend on the different proportions of structural units. It can be seen that increasing the TiO_2/Na_2O ratio from 0.50 in NTS1 to 0.53 in NTS3 tends to increase T_s, but further increase in this ratio in NTS4 and NTS5 results in decrease of T_s. This may suggest that NTS4 and NTS5 are structurally different from the other glasses. The TiO_2/Na_2O ratio may also affect the crystallisation behaviour. In the Na_2O-TiO_2-SiO_2 system, TiO_2 crystallises as rutile or possibly anatase when the TiO_2/Na_2O ratio exceeds 1 and in the form of silicate complexes when TiO_2/Na_2O is less than 1 [10]. The TiO_2/Na_2O ratio may also be responsible for the crystallisation behaviour of NTS glasses and this will be described in more detail in chapter 7.

6.3.3 Density

The measured densities of NTS glasses are shown as a function of x in Fig. 6.06 and summarised in Table 6.03. There is no systematic relation between densities and glass compositions. This suggests that the density of these glasses is sensitive to type and mass of ions which are added to the silicate network [11]. Although, density change varies seemingly erratically with x, molar volume decreases in a near linear fashion. Molar volume is a much better indicator of systematic structural change since it is not influenced by atomic mass. Increase of molar volume with decreasing x is probably the result of expansion of the silicate network due to increase of TiO_2 and P_2O_5.

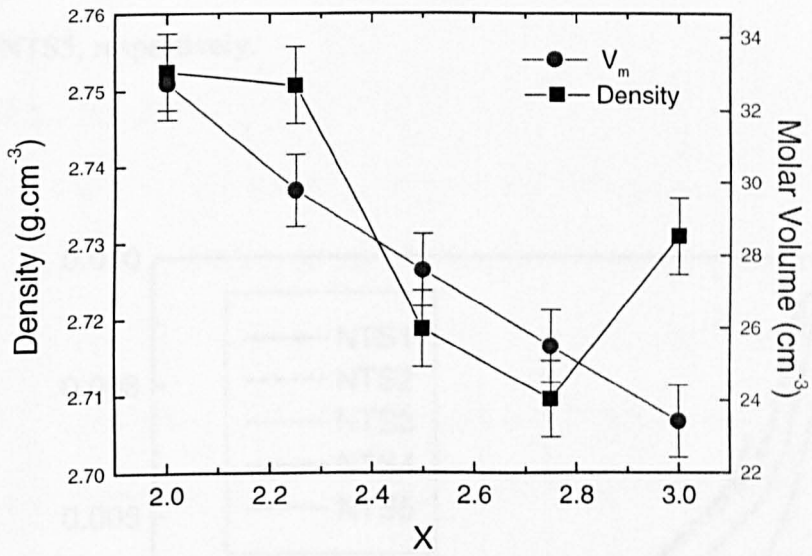

Figure 6.06 *Density and Molar Volume of NTS samples as a function of X.*

Table 6.03 *Density, ρ_x, and molar volume, V_m, of NTS glasses.*

Sample	ρ_x (±0.005 g/cm^3)	V_m (± 1.00 cm^3)
NTS1	2.731	23.4
NTS2	2.710	25.5
NTS3	2.719	27.6
NTS4	2.751	29.8
NTS5	2.753	32.8

6.3.4 Thermal expansion

The dilatometric curves from the annealed NTS samples are shown in Fig. 6.07 and TEC values are summarised over three temperature ranges in Table 6.04. To compare with DTA results, the dilatometric transitions, T_g^*, and the softening temperatures, T_s^*, are also included. Single T_g values are found from NTS1, NTS2 and NTS3 whereas double T_g events are clearly seen in the curves of both NTS4 and NTS5. This result suggests occurrence of phase separation. The transition at the lower

temperature is from the less viscous phase. These are at 348 °C for NTS4 and at 390 °C for NTS5, respectively.

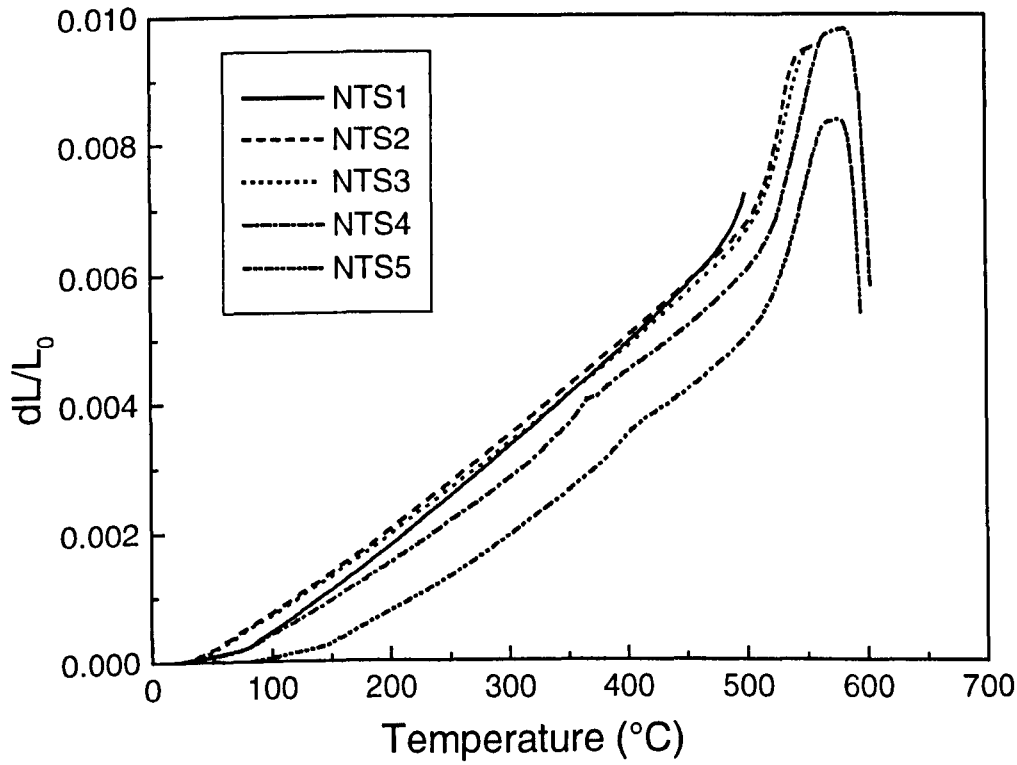

Figure 6.07 *Expansion characteristic of NTS glasses at the heating rate of 2 °C/min.*

Table 6.04 *Results of dilatometric measurement of NTS glasses. T_g^* and T_s^* are the dilatometric glass transition and the softening point, respectively.*

Sample	TEC, α, $\times 10^{-6}$/°C (±0.05)			T_g^* (±3 °C)	T_s^* (±3 °C)
	$\alpha_{50\text{-}100}$	$\alpha_{50\text{-}200}$	$\alpha_{50\text{-}500}$		
NTS1	7.12	2.59	2.16	487	515
NTS2	11.29	12.30	13.17	514	552
NTS3	11.08	12.04	12.83	516	560
NTS4	6.74	9.67	10.93	522	568
NTS5	1.05	5.10	7.71	524	570

6.3.5 MAS NMR

6.3.5.1 ^{31}P MAS

6.3.5.1.1 Results

The ^{31}P MAS NMR spectra from the NTS glass samples are shown in Fig. 6.08. Gaussian fitting shows four possible components, peaks α, β, χ and δ (Fig. 6.09) and the spectral parameters obtained from fitting are summarised in Table 6.05. In the spectra of NTS2, (containing 2.15 mol% of P_2O_5), three distinctive resonance peaks (α, β and χ) are clearly observed at chemical shifts of approximately 15.9, 10.7 and 4.5 ppm. As P_2O_5 is increased to 6.82 mol% in NTS4, another resonance peak (ε) appears at ~ -3 ppm. The first resonance, at ~15 ppm, disappears in composition NTS5 (9.38 mol% of P_2O_5). All resonance peaks show a negative shift (shift toward higher frequency) with decreasing $[Na_2O+TiO_2]/[P_2O_5]$ molar ratio. With increasing P_2O_5 content, the relative areas increase for peak α, decrease for peak ε, are almost constant for peak β and go through a maximum at composition NTS3 for peak χ. The spinning sidebands appear as broad humps at ~ 60 and ~ -40 ppm (not shown in Figure 6.08).

6.3.5.1.2 $P(Q^n)$ Assignment

The deconvolution results of ^{31}P MAS spectra have shown that there are four possible components in the spectra which indicate contributions from four possible phosphate species present in NTS glasses. In chapter 5, it has been shown that phosphate species prefer to associate with Na^+ and the $[ZrO_6]$ units. Thus, the same association should also be observed here in the NTS glasses. First of all, we assume that the coordination number of Ti^{4+} remains as 6. Then we can assign the ^{31}P resonance in similar fashion as in chapter 5.

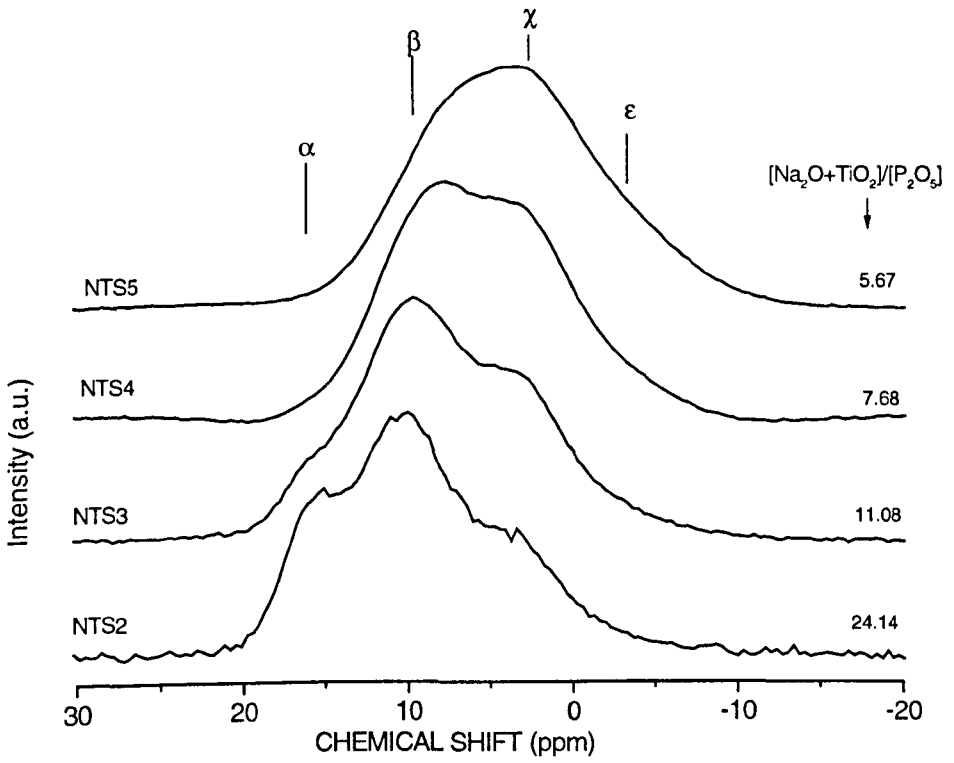

Figure 6.08 *^{31}P MAS NMR spectra of NTS samples.*

The ^{31}P resonances at ~15 ppm (peak α) and ~2 ppm (peak χ) can be simply assigned as $P(Q^0)_{Na}$ and $P(Q^1)_{Na}$ species, respectively, because their chemical shifts are close to the reported data for crystalline Na_3PO_4 (13 ppm) and $Na_4P_2O_7$ (2.9 ppm) [12,13]. These results are also consistent with the reported chemical shift of $Na_2O.2SiO_2$ glasses containing low concentration of P_2O_5 by Dupree and Holland [14]. The chemical shift of the $P(Q^1)_{Na}$ species is also consistent with the reported chemical shift (1.8 ppm) of the sodium phosphate glasses [15].

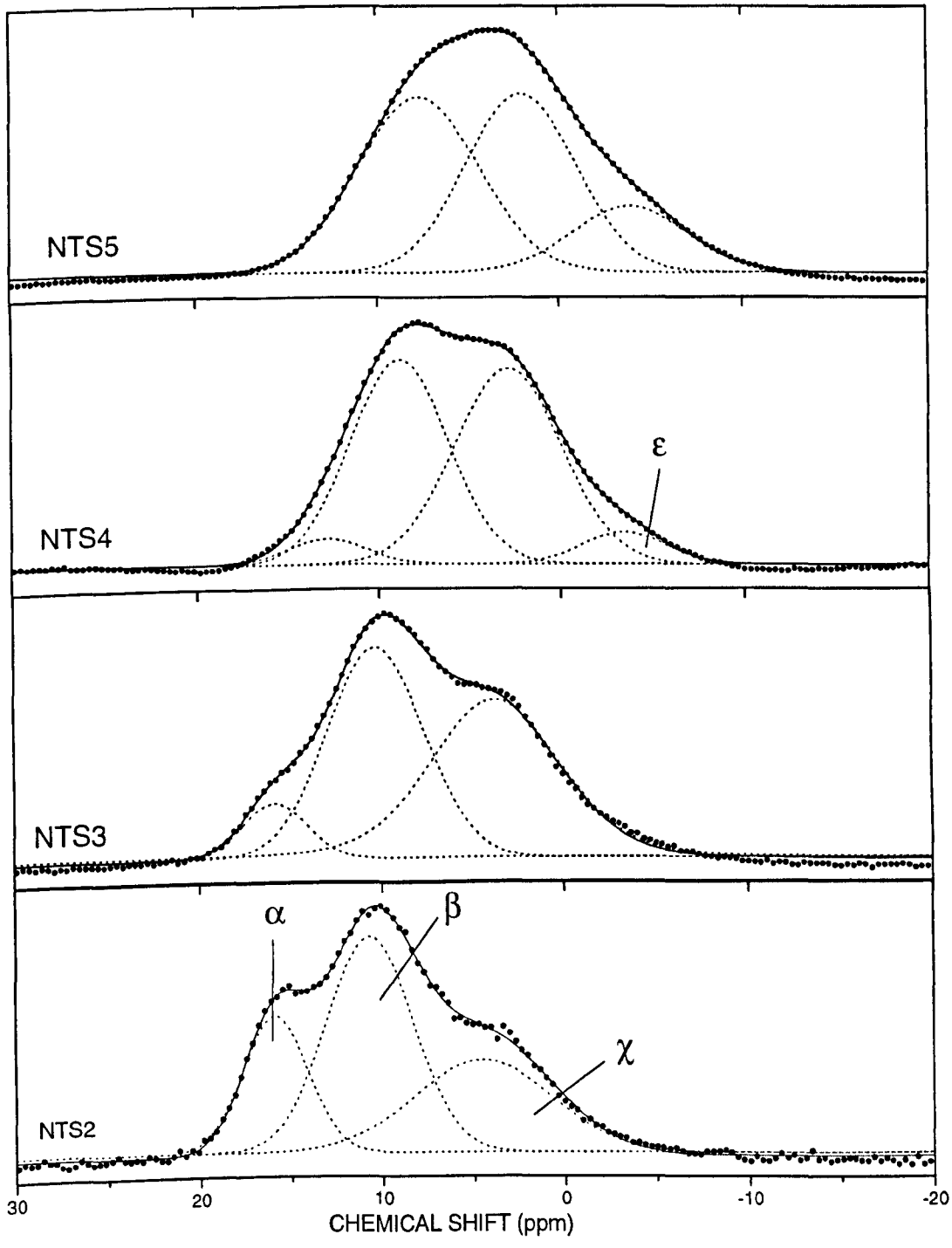

Figure 6.09 *Gaussian fits of ^{31}P spectra of NTS glasses, ● -experimental data, solid and dot lines are the simulation curves and the component peaks, respectively.*

Table 6.05 *Spectral parameters of ^{31}P MAS spectra of NTS glasses. $P(Q^n)_{i,j}$ represent the $[PO_4]$ tetrahedral species.*

Sample	$P(Q^0)_{Na}$			$P(Q^0)_{Na,Ti}$			$P(Q^1)_{Na}$			$P(Q^0)_{Na,2Ti}$		
	δ ± 0.5 Ppm	W ± 0.5 ppm	A ± 3 %	δ ± 0.5 Ppm	W ± 0.5 ppm	A ± 3 %	δ ± 0.5 ppm	W ± 0.5 ppm	A ± 3 %	δ ± 0.5 Ppm	W ± 0.5 ppm	A ± 3 %
NTS2	15.9	4.2	21	10.7	5.6	42	4.5	8.8	37	-	-	-
NTS3	15.9	4.1	8	10.3	6.2	45	3.7	8.3	47	-	-	-
NTS4	12.8	5.1	4	8.8	6.3	44	2.9	7.0	46	-3.5	5.3	6
NTS5	-	-	-	7.7	7.8	44	2.1	7.1	41	-3.9	7.4	15

The ^{31}P resonance at ~10 ppm can be assigned as $P(Q^0)_{Na,Ti}$, the subscript indicating that one of the Na^+ in $P(Q^0)_{Na}$ species is replaced by Ti^{4+}. This assignment is consistent with the previously reported shift range of $P(Q^0)$ species having mixed bonding to Na^+ and Ti^{4+} in the Na_2O-TiO_2-P_2O_5-SiO_2 system [16]. In sodium alumino-silicate glass containing P_2O_5, mixed bonding of phosphate species was also observed, and $P(Q^0)$ species that bond to two Na^+ and one Al^{3+} have a chemical shift at 7 ppm [17,18], this is lower than the 10 ppm of $P(Q^0)_{Na,Ti}$ observed here. The lower shielding environment of $P(Q^0)_{Na,Ti}$ species may be due to the effect of the higher electronegativity of the titanium atom (1.6) compared to aluminium (1.5). In chapter 5, the $P(Q^0)_{Na,Zr}$ species were seen to also have a chemical shift at 7 ppm which is due to the lower electronegativity of the zirconium atom (1.5), comparable to that of Al.

The ^{31}P resonance at –3 ppm (peak ε) may be assigned as $P(Q^1)_{Na,2Ti}$ analogous to $P(Q^0)_{Na,2Zr}$ of the Na_2O-ZrO_2-SiO_2-P_2O_5 system or NASIGLAS (ch. 5). This assignment is in accordance with the similar environments of Zr^{4+} and Ti^{4+} in glasses. Also, $P(Q^0)_{Na,2Zr}$ and $P(Q^0)_{Na,2Ti}$ occur at –3 ppm in both NASIGLAS and NTS glasses. The assignment is also consistent with the reported chemical shift of $P(Q^0)_{Na,2Al}$ as Al has the same electronegativity value as Zr. $P(Q^1)_{Na,Ti}$ should give a peak at around –6 ppm, which is between the 2 ppm of $P(Q^1)_{Na}$ (crystalline $Na_4P_2O_7$) and the –30.8 ppm of $P(Q^1)_{Ti}$

(titanium phosphate) [19]. Thus, $P(Q^1)_{Na,Ti}$ is not present in NTS glasses because no peak at –6 ppm is observed. A Double Quantum ^{31}P MAS NMR investigation of sodium titanophosphate glasses reported existence of the $P(Q^1)_{Na,Ti}$ species with a shift at -8.4 ppm [20]. In NTS glasses, $[TiO_6]$ octahedra are assumed to incorporate in the silicate network in a modifier role bonding with both $[SiO_4]$ and $[PO_4]$ tetrahedral units. The effective electron density of titanium atoms in a Si-O-Ti-O-P bond should be different from the pure Ti-O-P bonds in sodium titanophosphate and this may be responsible for the difference in shift reported in this study compared to those of referenced data. The effect of the higher electronegativity of the titanium atom compared to the sodium atom is also in the movement towards higher shielding when the TiO_2/Na_2O ratio is increased.

6.3.5.1.3 $P(Q^n)$ distribution

Phosphate units in NTS glasses exist as $P(Q^0)$ and $P(Q^1)$ with different next nearest neighbours generating four different species. The populations of phosphate species are clearly controlled by the $[PO_4]$ concentration. Fig. 6.10 shows the distribution of each species against mol% of P_2O_5. With increasing phosphate content, some $P(Q^0)$ transforms to $P(Q^1)$ and increases polymerisation of the phosphate linkage. The $P(Q^0)_{Na}$ concentration decreases when Na^+ is replaced by Ti^{4+}. The concentration of $P(Q^0)_{Na,Ti}$ is constant, within experimental error, with changing composition. This may indicate that this species is the most stable form of association of phosphate units with Na^+ and Ti^{4+}.

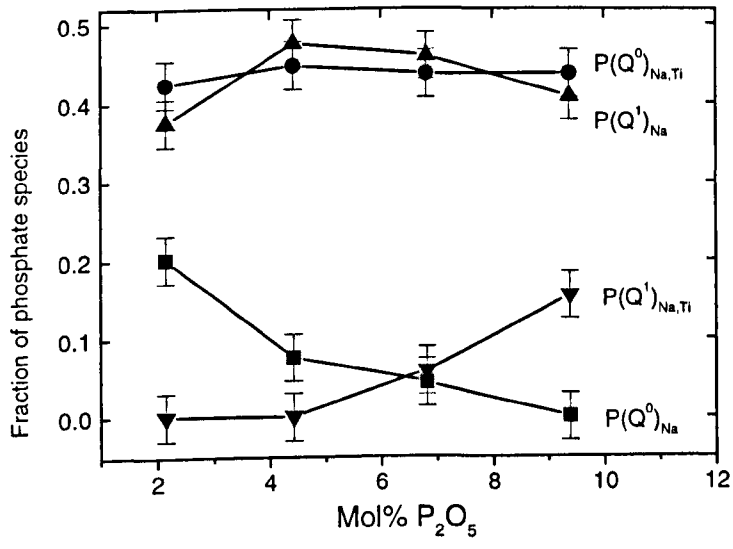

Figure 6.10 *Distribution of phosphate spcies in NTS glasses.*

6.3.5.2 ^{29}Si MAS

6.3.5.2.1 Results

Fig. 6.11 shows the ^{29}Si MAS NMR spectra of the NTS glass samples. Modification of the spectral lineshape with composition change can be observed as an increase in spectral linewidth with decreasing x. The centre of gravity of the ^{29}Si resonance moves from ~ -84.0 ppm in NTS1 to ~ -94.0 ppm in NTS5. This is a shift to higher shielding on replacement of SiO_2 by P_2O_5. In binary alkali silicate glasses with added P_2O_5 [21], this shift to higher shielding of the ^{29}Si resonance is also observed and, is due to removal of alkali ions from the silicate network by the [PO_4] tetrahedra. The same behaviour of [PO_4] tetrahedra was also observed in alkali ternary silicate glasses [16,17]. The observed ^{29}Si chemical shifts of the NTS samples are more negative than those of NASIGLAS reported in the previous chapter. This is due to the difference in electronegativity of Ti (1.6) and Zr (1.5).

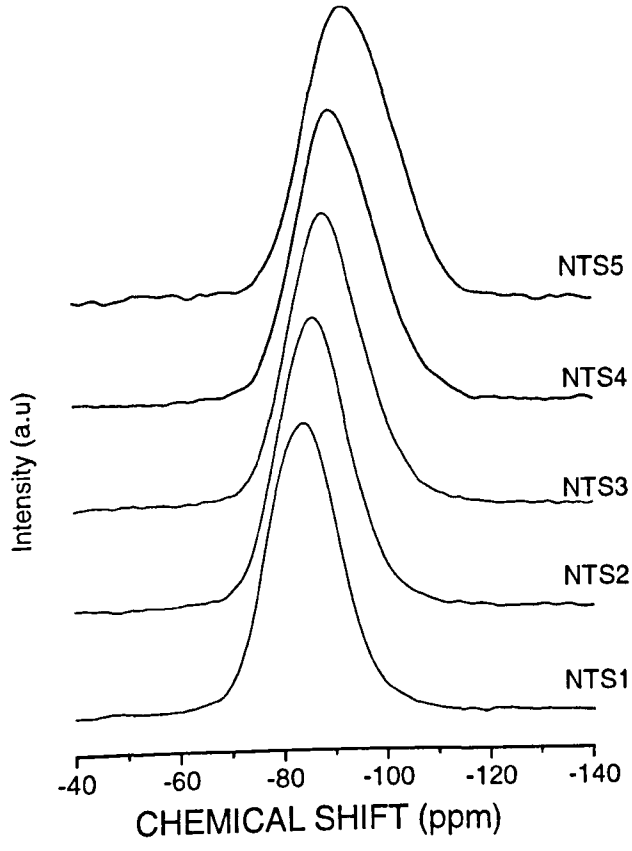

Figure 6.11 *^{29}Si MAS NMR spectra of NTS samples. To emphasise the spectral lineshape the spinning sidebands are therefore not shown.*

6.3.5.2.2 Spectral analysis and Si(Q^n) assignments

The ^{29}Si MAS NMR spectra of NTS glasses are similar to those of NASIGLAS (chapter 5). Thus, analogous spectral analysis and Si(Q^n) assignments may be made using the same fitting constraints. Here, the assignments will also start from NTS1 with the simplest composition, $2Na_2O.TiO_2.3SiO_2$. In NASIGLAS, the role of Zr^{4+} was the main consideration because it can enter modifier or former sites. It has been proposed that Zr^{4+} should enter only modifier sites with effective coordination number 6 (octahedral coordinated sites). For Ti^{4+}, the consideration may be more complicated because the coordination number of Ti^{4+} can be 4, 5 or 6 (i.e. Ti^{IV}, Ti^{V} or Ti^{VI}) depending on composition and Ti^{4+} concentration.

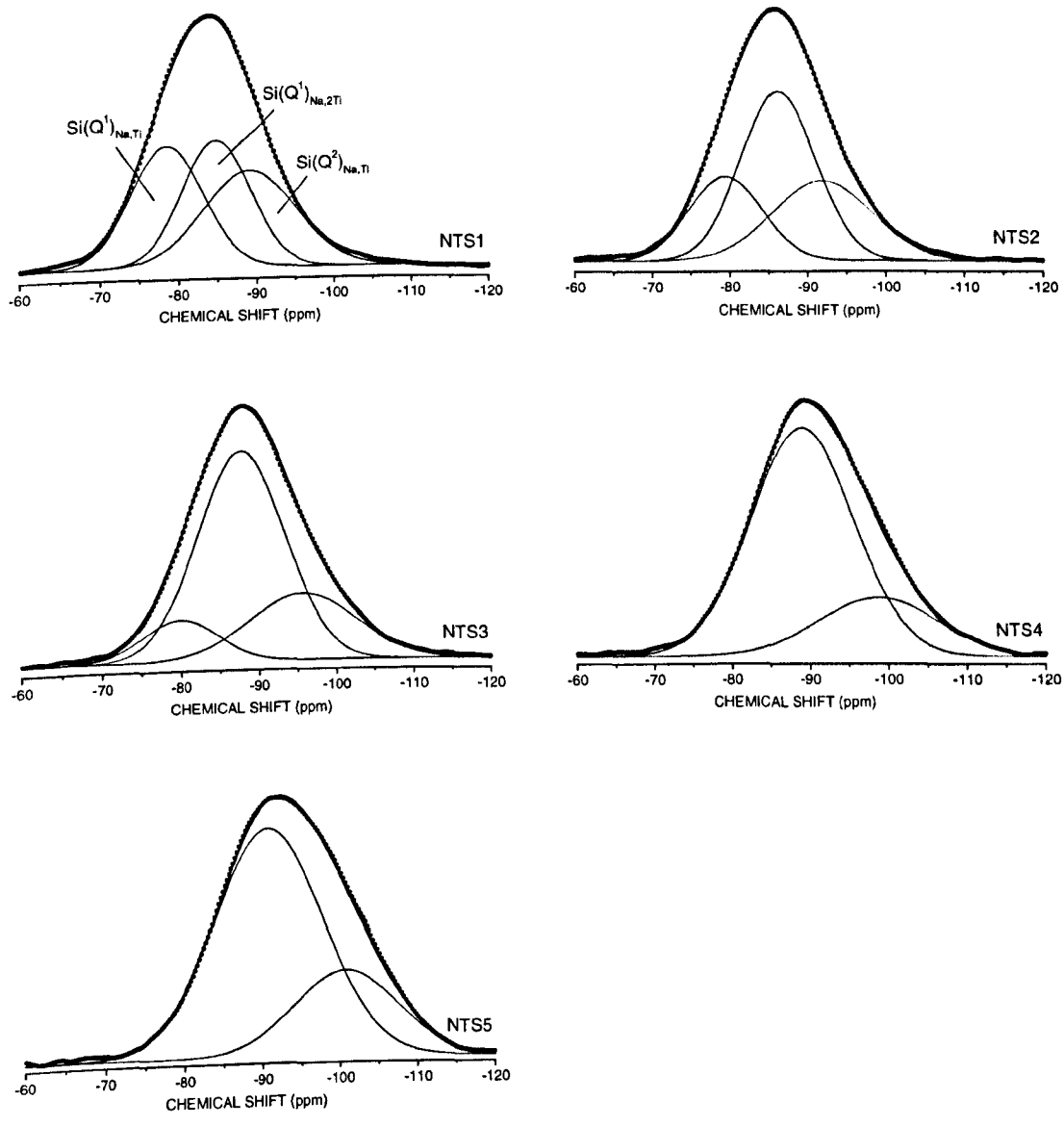

Figure 6.12 *Deconvolution of ^{29}Si MAS NMR spectra of NTS glasses, dots are the experimental data, solid lines are the simulation curves.*

Farges and co-workers [22] used XAFS to study the environment of Ti in several silicate compounds and glasses and suggested that Ti^{V} is the dominant species in some alkali titanosilicate and alkaline earth titanosilicate compounds. This group of workers also suggested the dominance of Ti^{V} in silicate glasses and melts [23]. In an EXAFS study, Ti^{IV} was found in amorphous silica-titania prepared using the sol-gel method [24]. The presence of Ti^{IV} in melts and glasses of the system $Na_2Si_2O_5$-$Na_2Ti_2O_5$ was also

confirmed by Raman and Ti^{4+} was suggested to substitute for Si^{4+} having a network former role.

Since the present results are obtained from ^{29}Si MAS NMR, assignment will be based on information from previous ^{29}Si MAS NMR studies of titanium containing silicate materials. This can be found in the work of Labouriau and co-workers [25], in which the ^{29}Si chemical shifts of some sodium titanosilicate compounds were predicted for Ti present as Ti^{VI}. There were reports of $Si(Q^n)$ species with their predicted chemical shifts, -87.6 ppm for $Si(Q^2)$ in $Na_2Ti_2Si_2O_9$ (lorenzenite) and –95.8 ppm for $Si(Q^3)$ in $Na_2TiOSi_4O_{10}$ (narsasukite) [25]. These two compounds have a structural framework formed from linkage of $[SiO_4]$ and $[TiO_6]$, with no association of Na^+ with $[SiO_4]$, which is different from Na^+ in titanosilicate glasses. The ^{29}Si chemical shift range with Ti present as Ti^{VI} was suggested to be from –90 ppm to –110 ppm; at –107.4 ppm for Ti^V; and in the range from –110 ppm to –116 ppm for Ti^{IV} [26]. From the observed ^{29}Si chemical shift range of NTS glasses, Ti^{4+} should also occupy a six coordinated site and the $Si(Q^n)$ species should have an association with both Ti^{4+} and Na^+.

If Ti^{4+} behaves as a network intermediate in a perfect $[TiO_6]$ unit, it will need local charge compensation from two Na^+. This would leave approximately 16.7 mol% of Na_2O to associate with 50 mol% of SiO_2 giving NBO/Si = 0.67 which equates to $Si(Q^3)$+$Si(Q^4)$, inconsistent with the observed shifts. It must be a mixed species state as found in NASIGLAS. Since we are assuming that Ti^{4+} environments have to be of octahedral coordination, therefore, the only possible role of Ti^{4+} is that of network modifier as proposed for Zr^{4+} in Chapter 5. Therefore, mixed $Si(Q^1)$-$Si(Q^2)$ is the most probable assignment for NTS1. This assignment is also consistent with the ^{29}Si chemical shift range observed here. Since the ^{29}Si MAS NMR data from NTS glasses are similar to those of NASIGLAS, NTS1 should also contains three species which are assigned as

$Si(Q^1)_{Na,Ti}$, $Si(Q^1)_{Na,2Ti}$ and $Si(Q^2)_{Na,Ti}$, with concentration ratio 1:1:1. The ^{31}P MAS NMR spectra of these two glass systems are also similar, thus, the other four NTS glass samples should also behave like G2, G3 and G4, in which $Si(Q^1)/Si(Q^2)$ ratio increase with decrease x.

To predict the $Si(Q^1)/Si(Q^2)$ ratio for NTS glasses, the calculation is made using the same expression as shown in Ch.5. Table 6.06a shows the results of this calculation. It can be seen that the $Si(Q^1)/Si(Q^2)$ ratio in NTS glasses increases more rapidly than in NASIGLAS. Gaussian fitting was performed to determine the spectral parameters for $Si(Q^n)_{i,j}$ species using the constraints described in chapter 5. The fitting results are shown in Fig. 6.12 and the spectral parameters are reported in Table 6.05. It can be seen that the spectrum of NTS1 is well characterised by three Gaussian peaks with almost equal relative area which can be assigned as $Si(Q^1)_{Na,Ti}$, $Si(Q^1)_{Na,2Ti}$, and $Si(Q^2)_{Na,Ti}$. This result confirms the consistency of our assignment. For NTS2 and NTS3, the $Si(Q^1)_{Na,Ti} \rightarrow Si(Q^1)_{Na,2Ti}$ transformation is observed as found in NASIGLAS. The peak corresponding to $Si(Q^1)_{Na,Ti}$ is not detected in spectra of NTS4 and NTS5, only two peaks for $Si(Q^1)_{Na,2Ti}$ and $Si(Q^2)_{Na,Ti}$ are observed. This may be due to Na^+ being less available to associate with $Si(Q^n)$ species.

Table 6.06a *Calculation of NBO/Si and $Si(Q^1)/Si(Q^2)$ ratios of NTS glasses.*

Sample	x	C_1	C_2	Calculated NBO/Si	Predicted $[Si(Q^1)]/[Si(Q^2)]$
NTS1	3.00	0	0	2.67	2.00
NTS2	2.75	0.62	0.38	2.70	2.35
NTS3	2.50	0.53	0.47	2.76	3.18
NTS4	2.25	0.50	0.50	2.83	5.00
NTS5	2.00	0.45	0.55	2.94	16.14

Note: NBO/Si and $Si(Q^1)/Si(Q^2)$ are calculated using Equations 5.4 and 5.10, respectively. C_1 and C_2 are the fraction of $P(Q^0)$ and $P(Q^1)$, respectively.

Table 6.06b *Deconvolution of the ^{29}Si MAS NMR spectra and assignment; δ = chemical shift, W = linewidth and A = relative area.*

Sample	$Si(Q^1)_{Na,Ti}$			$Si(Q^1)_{Na,2Ti}$			$Si(Q^2)_{Na,Ti}$			Q^1/Q^2
	δ ± 0.5 ppm	W ± 0.5 ppm	A ± 2.0 %	δ ± 0.5 ppm	W ± 0.5 ppm	A ± 2.0 %	δ ± 0.5 ppm	W ± 0.5 ppm	A ± 2.0 %	
NTS1	-78.6	9.2	33	-84.9	8.8	33	-89.2	11.9	34	2.0
NTS2	-79.5	9.4	23	-86.3	9.6	48	-91.9	12.6	30	2.4
NTS3	-80.0	9.5	11	-87.8	11.5	64	-95.7	13.8	25	3.0
NTS4	-	-	-	-89.0	13.2	77	-98.7	15.0	23	3.4
NTS5	-	-	-	-90.9	13.9	74	-100.8	13.26	26	2.8

This assignment is in accordance with the ^{29}Si chemical shifts reported for crystalline sodium titanosilicates. From the ^{29}Si MAS NMR study of the synthetic mineral Penkvilksite, with ideal formula $Na_4Ti_2Si_8O_{22}.5H_2O$, it was suggested that there are $Si(Q^2)_{2Ti}$ and $Si(Q^3)_{Ti}$ species (i.e. all non-bridging oxygens of $Si(Q^n)$ species associated with Ti^{4+} in the octahedral environment) present in this composition with chemical shifts of –95.7 ppm and –100 ppm, respectively [27]. It is clearly seen that the reported chemical shift range in Table 6.6b for $Si(Q^2)_{Na,Ti}$ of NTS glass compositions is consistent with that of ref. [27].

6.3.5.2.3 $Si(Q^n)$ distribution

The chemical shift and linewidth of $Si(Q^1)_{Na,Ti}$ are constant within the experimental error. The concentration of this species decreases dramatically when Na^+ is replaced by Ti^{4+} such that $Si(Q^1)_{Na,Ti}$ is not present in NTS4 and NTS5. This is because removal of Na^+ from the silicate network by phosphate species leads to a lower Na^+ concentration in the silicate network insufficient to form $Si(Q^1)_{Na,Ti}$. For $Si(Q^1)_{Na,2Ti}$,, the

chemical shift range is from – 84.9 ppm to –90.9 ppm and linewidth 8.8 ppm to 13.9 ppm. The concentration of $Si(Q^1)_{Na,2Ti}$ increases from 33.0% in NTS1 to about 73.6% in NTS5. This may indicates $Si(Q^1)_{Na,Ti} \rightarrow Si(Q^1)_{Na,2Ti}$ transformation. The chemical shift of $Si(Q^2)_{Na,Ti}$ changes over a wider range from –89.2 ppm to –100.8 ppm and the linewidth is in the range 11.9 ppm to 15.0 ppm. The concentration of $Si(Q^2)_{Na,Ti}$ decreases with x.

Tables 6.06a and 6.06b show good agreement between calculation and the experimental results of $Si(Q^1)/Si(Q^2)$ ratio for three samples, NTS1, NTS2 and NTS3. For NTS4 and NTS5, there are large deviations from calculation which predict much lower $Si(Q^2)_{Na,Ti}$ then actually observed. These results suggest that there is a different structural arrangement in these two samples with possible change in role of Ti^{4+} to that of intermediate which effectively reduces the NBO/Si and produce an increase in $Si(Q^2)_{Na,Ti}$ in NTS5. Thus the distribution of $Si(Q^n)$ species is dependent on the behaviour of Ti^{4+}. However, we can see that there are similar distributions of $Si(Q^n)$ species in the NASIGLAS and NTS glasses where $Si(Q^1)_{Na,2j}$ (j = Zr or Ti) species dominate.

6.3.5.3 ^{23}Na MAS

The ^{23}Na MAS spectra of NTS samples are shown in Fig. 6.13 and their peak positions and linewidths are summarised in Table 6.07. These ^{23}Na MAS NMR spectra are very similar for all glass samples giving a single resonance with linewidth in the range 30 ppm to 40 ppm. The spectral lineshape shows only the resonance from the central transition with no quadrupolar broadening. The large width of these spectra is due to the large electric field gradient experienced by the sodium ion, as revealed by the tail which extends out to approximately –100 ppm.

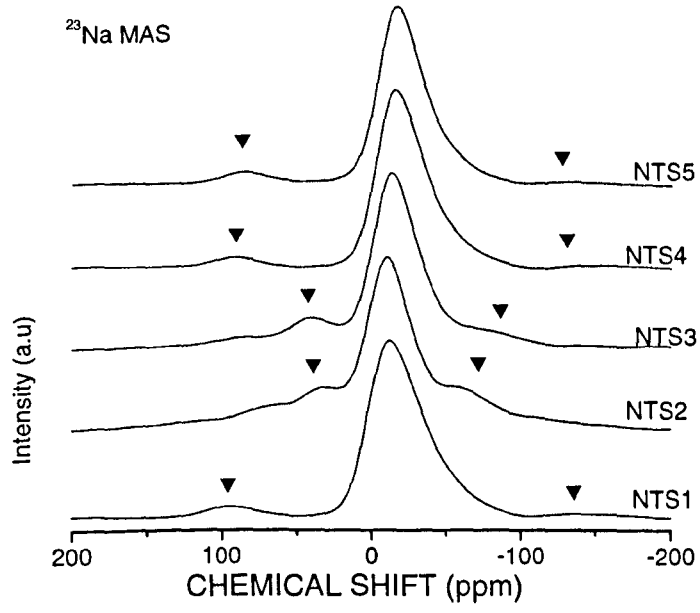

Figure 6.13 *^{23}Na MAS NMR spectra of NTS glasses, ▼ indicates spinning sidebands*

Table 6.07 *Isotropic chemical shift and linewidth of ^{23}Na MAS NMR spectra of NTS glasses.*

Sample	Chemical shift (±0.5 ppm)	Linewidth (±0.5 ppm)
NTS1	-16.9	39.9
NTS2	-11.4	31.7
NTS3	-15.5	33.0
NTS4	-20.1	35.2
NTS5	-20.5	34.1

In sodium silicate glasses, the ^{23}Na resonance has an increasingly negative shift with decreasing mol% of Na_2O [28]. This means that the population densities of Na^+ ions affect their own shielding environment, the lower density is the higher shielding situation.

In NTS glass samples, Na^+ may be present as two distinctive sites; Na1 in Si-O^-.Na^+ site and Na2 in P-O^-.Na^+ site. For NTS1, only Na1 is present and will be randomly distributed throughout the silicate network, giving a chemical shift at −16.9 ppm. With decreasing Na^+ content and introduction of $[PO_4]$ units in NTS2, this shift moves to −11.4 ppm which probably suggests a higher population density of Na2 associated with $P(Q^0)_{Na}$ and $P(Q^1)_{Na}$ species. Further decrease of Na^+ content from NTS3 to NTS5, lowers the population density of both Na1 and Na2 leading to a more negative shift. These results may be consistent with decrease in $P(Q^0)_{Na}$ and $P(Q^1)_{Na}$ concentration as the composition changes from NTS2 toward NTS5.

6.3.5.4 General discussion on glass structure

The structure of glasses in the system Na_2O-TiO_2-SiO_2-P_2O_5 may be visualised as a network of silicate units linked to $[TiO_6]$ octahedra units and Na^+ combined with phosphate species associated with $[TiO_6]$ and some Na^+. There is no evidence of interconnection between silicate units and phosphate units from results of both ^{29}Si and ^{31}P MAS NMR. This differs from the XANES study of Na_2O-SiO_2-P_2O_5 system where interconnection between silicate units and phosphate units was found [29]. In a variety of titanium containing glasses, Ti^{4+} has been reported to exist in both modifier and former roles depending on its concentration. The coordination number of Ti^{4+} has also been found to change from octahedrally (6) to tetrahedrally coordinated (4) if its role changes. However, the boundary of Ti^{4+} concentration for changing role from modifier to network former is not clear. It is dependent on glass composition and technique of investigation. For example, Ti^{4+} has been found to act as a network former when $TiO_2 < 8.3$ mol% and substitutes for Si^{4+} [30]. Si^{4+} substitution by Ti^{4+} was also reported for sodium titanium silicate glasses studied by means of x-ray emission spectroscopy [4]. In CaO-TiO_2-SiO_2

glasses system, a Raman study revealed a changing role for Ti^{4+} [31,32]. There was no indication of Ti^{4+} being found in tetrahedral sites for Li_2O-TiO_2-SiO_2 [3] and Na_2O-TiO_2-P_2O_5 glasses [27], where it incorporates in the glass network as a modifier in octahedral sites, $[TiO_6]$.

Thus, we may be able to draw a rough conclusion that the incorporation of Ti^{4+} in sodium silicate glasses is only as $[TiO_6]$ octrahedra when phosphate units are added. However, this situation is only true when the TiO_2/Na_2O ratio is less than 1 as in the NTS glasses. On increasing this ratio beyond 1, the excess Ti^{4+} may exist in a different way. Since information from ^{49}Ti MAS NMR is hard to obtain on glasses, it limits a clear picture of $[TiO_6]$ octahedra connectivities. The ^{29}Si MAS NMR spectra in Fig. 6.11 are also not well resolved leading to uncertain assignment of the type of modifier connected to the silicate units. The broad lineshape of the ^{23}Na MAS NMR spectra in Fig. 6.13 gives no clear distinction between Na1 and Na2 sites as found in crystalline NASICON [33]. The great majority of structural information is from the ^{31}P MAS NMR spectra where four distinctive phosphate species are clearly seen, leading to unambiguous assignment of the short-range order arrangement in NTS glasses. The remaining question is about the phosphate units themselves. In the compositions of the present study, every chemical component is changed simultaneously making it difficult to see trends in the arrangement between phosphate units.

6.4 Conclusion

$Na_{1+x}Ti_{2-x/3}Si_xP_{3-x}O_{12-2x/3}$ (NTS glasses), can be prepared via the conventional melt quench route with a greater glass forming region compared to the original compositions containing ZrO_2. Mass balance between glass batch and glass product reveals as much as 5 wt% loss during melting. This is thought to be due mostly to some mechanical plus loss

of Na_2O and P_2O_5. The XRD powder patterns of NTS glasses suggest all samples are crystal free. DTA results show increase of T_g with replacement of $[SiO_4]$ by $[PO_4]$ units. These results are consistent with observations from ^{29}Si MAS NMR which shows an increase of the average number of bridging oxygens per $[SiO_4]$. Crystallisation in NTS glasses seems to be influenced by TiO_2 and P_2O_5 content. Further investigation of crystallisation in these particular samples will be given in the following chapter. The liquidus temperatures of NTS glasses are observed at below 1000 °C, lower than those of NASIGLAS samples.

The molar volume of NTS glasses increases systematically with decrease x. The larger atomic mass of titanium is thought to be the influential factor for controlling density. Increasing $[TiO_6]$ concentration results in decrease of thermal expansion coefficient of NTS glasses.

The structure of NTS glasses may be described as a 3-dimensional silicate network linked to $[TiO_6]$ units with $[PO_4]$ tetrahedra sharing the corners of the $[TiO_6]$ units. Na^+ prefers to associate with the phosphate species. The formation of phosphate species results in a negative shift of the ^{29}Si MAS NMR spectra which is due to removal of Na^+ from $[SiO_4]$ tetrahedra. Phosphate units with Na^+ and Ti^{4+} produce four different species; $P(Q^0)_{Na}$, $P(Q^1)_{Na}$, $P(Q^0)_{Na,Ti}$, and $P(Q^0)_{Na,2Ti}$ respectively. Distributions of phosphate species are probably controlled by the concentration of $[PO_4]$ units and the TiO_2/Na_2O molar ratio. Three silicate species, $Si(Q^1)_{Na,Ti}$, $Si(Q^1)_{Na,2Ti}$ and $Si(Q^2)_{Na,Ti}$, are expected to be present in NTS1, NTS2 and NTS3 but only the latter two species present in NTS4 and NTS5. The distribution of $Si(Q^n)$ species is controlled by the Na_2O/TiO_2 ratio and the $Si(Q^1)_{Na,Ti} \rightarrow Si(Q^1)_{Na,2Ti}$ transformation is found with decrease of this ratio. The observed NBO/Si and $Si(Q^1)/Si(Q^2)$ are in good agreement with the calculation for three samples, NTS1, NTS2 and NTS3, but there is no agreement for NTS4 and NTS5.

Change in the structural role of Ti^{4+} is thought to be responsible for the disagreement observed for NTS4 and NTS5. However, the results of the ^{31}P, ^{29}Si and ^{23}Na MAS NMR studies show the same trends in structural arrangement comparing NASIGLAS and NTS glasses.

The ^{23}Na MAS NMR spectra lineshape observed in NTS glass system are similar for all samples, obtaining a single resonance due to the central transition of ^{23}Na nuclei with chemical shift range from –11 ppm to –20 ppm. Large linewidth of the spectra is thought to be due to the large electric field gradient experienced by ^{23}Na.

In future work, new composition design may be required to establish clearer relations between structural arrangement and the relevant properties. This could be done by fixing TiO_2/Na_2O molar ratio and varying SiO_2/P_2O_5 molar ratio or vice versa. Thus, the exact involvement of Ti^{4+} and $[PO_4]$ units in the silicate network may be more clearly observed. Using other spectroscopic techniques, such as Raman spectroscopy, to investigate the environment of Ti^{4+} is desirable. In order to obtain greater understanding of association of phosphate species with Na^+, advanced NMR experimental methods may also be employed, for example; cross polarisation $^{23}Na \rightarrow {}^{31}P$ MAS technique (CP MAS) and 2D-^{31}P MAS NMR. Participation of Na^+ in two distinctive sites may be resolved by using a higher field NMR spectrometer.

References

[1] McMillan, P.W., *Glass-ceramics*. London: Academic Press, 1964.

[2] Labarbe, P.D., Lin, J.S. and Osborn, E.F., *Physics and Chemistry of Glasses*. **29** (1988), 91.

[3] Villegas, M.A., De Pablos, A. and Fernández Navarro, J.M., *Journal of Materials Science*. **30** (1995), 995.

[4] Hanada, T. and Soga, N. *Journal of Non-Crystalline Solids*. **38&39** (1980), 105.

[5] Mysen, B. and Neuville, D., *Geochimica et Cosmochimica Acta*. **59**, no. 2 (1995), 325.

[6] Henderson, G.S. and Fleet, M.E., *Journal of Non-Crystalline Solids.* **211** (1997), 214.
[7] Duan, R.G., Liang, K.M. and Gu, S.R., *Journal of the European Ceramics Society.* **18** (1998), 1729.
[8] Iqbal, Y., Lee, W.E., Holland, D. and James, P.F., *Journal of Materials Science.* **34** (1999), 4399.
[9] Novaes De Oliveira, A.P. and Manfredini, T., *Journal of Materials Science.* **36** (2001), 2581.
[10] Volf, M.B., *Chemical Approach to Glass (Glass Science and Technology 7).* Amsterdam: Elsevier, 1984.
[11] *Engineer materials handbook Vol. 4; Ceramics and glasses.* Cleveland, Ohio: ASM International, 1991.
[12] Mudrakovskii, I.L., Shmachkova, V.P. and Kotsarenko, N.S., *Journal of Physics and Chemistry of Solids.* **47**, no. 4 (1986), 335.
[13] Griffiths, L., Root, A., Harris, R.K., Packer, K.J., Chippendale, A.M. and Tromans, F.R., *Journal of Chemical Society, Dalton transaction.* (1986), 2247.
[14] Dupree, R. and Holland, D. *"NMR: a new spectroscopic technique for structure determination in glasses and ceramics" in: Glass and Glass-ceramics.* Ed. M. Lewis. London: Chapman & Hall, 1988.
[15] Prabakar, S., Wenslow, R.M. and Muellere, K.T., *Journal of Non-Crystalline Solids.* **263&264** (2000), 82.
[16] Grussaute, H., Montagne, L., Palavit, G., and Bernard, J.L., *Journal of Non-Crystalline Solids.* **263&264** (2000), 312.
[17] Toplis, M.J. and Schaller, T. *Journal of Non-Crystalline Solids.* **224** (1998), 57.
[18] Schaller, T., Rong, C., Toplis, M.J. and Cho, H., *Journal of Non-Crystalline Solids.* **248** (1999), 19.
[19] Brow, R.K., Tallant, D.R., Warren, W.L., McIntyre, A. and Day, D.E., *Physics and Chemistry of Glasses.* **38** (1997), 300.
[20] Montagne, L., Palavit, G., Shaim, A., Et-Tabirou, M., Hartmann, P. and Jager, C., *Journal of Non-Crystalline Solids.* **293-295** (2001), 719.
[21] Dupree, R., Holland, D. and Mortuza, M.G. *Physics and Chemistry of Glasses.* **29** (1988), 18.
[22] Farges, F., Brown, G.E. and Rehr, J.J., *Geochimica et Cosmochimica Acta.* **60**, no. 16 (1996), 3023.
[23] Farges, F., Brown, G.E., Navrotsky, A., Gan, H. and Rehr, J.J., *Geochimica et Cosmochimica Acta.* **60**, no. 16 (1996), 3039.
[24] Anderson, R., Mountjoy, G., Smith, M.E. and Newport. R.J., *Journal of Non-Crystalline Solids.* **223-234** (1998), 72.
[25] Labouriau, A., Higley, T.J. and Earl, W.L., *Journal of Physical Chemistry B.* **102** (1998), 2897.
[26] Liu. Y., Du, H., Xiao, F-S., Zhu, G. and Pang, W., *Chemistry of Materials.* **12** (2000), 665.
[27] Lin, Z., Rocha, J., Brandão, P., Ferreira, A., Esculcas, A.P., Pedrosa de Jesus, J.D., Philippou, A. and Anderson, M.W., *Journal of Physical Chemistry B.* **101** (1997), 7114.
[28] Dupree, R., Holland, D., McMillan, P.W. and Pettifer, R.F., *Journal of Non-Crystalline Solids.* **68** (1984), 399.
[29] Li, D., Fleet, M.E., Bancroft, G.M., Kasrai, M. and Pan, Y., *Journal of Non-Crystalline Solids.* **188** (1995), 181.
[30] Evans, D.L., *Journal of The American Ceramics Society.* **53** (1970), 418.

[31] Villegas, M.A., De Pablos, A. and Fernández Navarro, J.M., *Glass Technology*. **35** (1994), 276.
[32] Alberto, H.V. and Ayres de Campos, N., *Physics and Chemistry of Glasses*. **36** (1995), 114.
[33] Jäger, C., Barth, S. and Feltz, A., *Chemical Physics Letters*. **154**, no.1 (1989), 45.

CHAPTER 7

Glass-ceramics

7.1 Introduction

Glass-ceramic materials whose major crystalline phases are fast-ion conductors can themselves also exhibit fast-ion conduction. The fast-ion conducting phases can only be crystallised from the appropriate glass compositions. The Na_2O-Re_2O_3-P_2O_5-SiO_2 glass systems (Re = rare earth) give the $Na_5ReSi_4O_{12}$ fast-ion conductor phase when subjected to heat treatment at 900 °C -1050 °C [1]. Ease of fabrication and high volume production are the advantages of fast-ion conducting glass-ceramics. Optimum physical properties may also be achieved by controlling the conditions of heat treatment. Thus, preparing fast-ion conductors in a glass-ceramic form may solve some of the problems found in the conventional ceramic sintering route.

Fast-ion conduction in NASICON compositions has stimulated many workers to study these materials, in an attempt to develop solid electrolytes for electrochemical cells. Yamashita and co-workers [2-5] prepared glass-ceramics from the NASICON related compositions, $Na_{3+3x-y}Y_{1-x}P_ySi_{3-y}O_9$. They have shown that $Na_5YSi_4O_{12}$ can be crystallised from this glass composition with greater stability compared to that obtained from solid state sintering. However, there have not been many studies on glass-ceramics from the original NASICON compositions. If the most fast-ion conducting phase found to date, could be crystallised from the appropriate parent glass, this would create much interest in the production method.

In this work, the crystallisation behaviour of NASIGLAS, has been studied using, DTA, XRD, solid state NMR and SEM. DTA was used to find the appropriate temperature for crystallisation to take place; XRD was used to identify the crystalline

phases formed in the glass-ceramic product. Solid state NMR was used as an extension of XRD, which is less successful at identifying low concentration phases; and SEM was used to produce the microstructure images. Density measurement was also carried out. In addition to the NASIGLAS composition, the TiO_2 substituted compositions or NTS glasses (chapter 6) were also subjected to the crystallisation investigation.

7.2 Crystallisation of NASIGLAS

7.2.1 Introduction

NASIGLAS has the general formula $Na_{1+x}Zr_{2-x/3}Si_xP_{3-x}O_{12-2x/3}$ where x ranges from 1 to 3. Four glass compositions were prepared (x = 2.25, 2.50 2.75 and 3.00) and these have been detailed in chapter 5. The DTA results suggested that these glasses crystallise in the temperature range from 750 °C to about 920 °C. Six glass-ceramic samples were prepared from both powder and bulk parent glasses by heat treatment in an electric furnace. The nucleation and crystallisation temperatures were chosen approximately from T_x and T_c in Table 5.2, respectively. A heating rate of 5 °C/min, nucleation time of 0.5 hr, and crystallisation time of 4 hr were applied. Then samples were cooled down to room temperature at a rate of 5 °C/min. The final glass-ceramic samples were crushed to fine powder and identified by XRD and NMR. Bulk glass-ceramic samples were subjected to density measurement and cross-sectioned for investigation by SEM.

7.2.2 XRD

Figure 7.01 shows the XRD powder pattern of six bulk glass-ceramic samples. The assigned name and crystalline phases formed in these samples are reported in Table 7.01 along with the density. Four crystalline phases, $Na_2ZrSi_2O_7$, $Na_4ZrSi_3O_{10}$, $Na_{2.5}Zr_2Si_{1.5}P_{1.5}O_{12}$ and Na_2SiO_3 can be identified. All samples contain $Na_2ZrSi_2O_7$ (i.e.

$Na_2O.ZrO_2.2SiO_3$ –the mineral parakeldysite) as a major phase. $Na_4ZrSi_3O_{10}$, a fast-ion conductor phase, can be found in Gcn1a. $Na_{2.5}Zr_2Si_{1.5}P_{1.5}O_{12}$, found in Gcn4, belongs to the NASICON family, $Na_{1+x}Zr_2Si_xP_{3-x}O_{12}$, with x = 1.5. Sodium metasilicate Na_2SiO_3 is formed only in Gcn1a and Gcn1b and, in Gcn2a, Gcn2b and Gcn3, there is a phase which could not be identified because of its very low intensity.

The $Na_2ZrSi_2O_7$ phase is identified from the JCPDS file no. 39-209. This phase has a triclinic crystal symmetry (space group P-1) with cell parameters, a = 6.629 Å, b= 8.814 Å and c = 5.434 Å. The structure of $Na_2ZrSi_2O_7$ consists of double-tetrahedra $Si_2O_7^{6-}$ coupled with isolated [ZrO_6] octahedra and Na atoms in eight-coordination occupying holes in the three-dimensional network [6]. $Na_2ZrSi_2O_7$ was reported to have high stability (up to 1200 °C) [6]. This may explain it being a dominant phase in the crystallisation of NASIGLAS. Susman et al. [7] also reported $Na_2ZrSi_2O_7$ as a major phase. There is no report that $Na_2ZrSi_2O_7$ is a fast-ion conductor. The dominance of $Na_2ZrSi_2O_7$ could indicate that the crystal phase formed by heat treatment of NASIGLAS prefers a Si/Zr ratio of 2:1.

Table 7.01 *Treatment temperature, density and crystalline phase formed in glass-ceramic samples derived from NASIGLAS.*

X	Parent glass*	Glass-ceramics	Heat treatment temperature (°C)	Density (g/cm^3) ± 0.005	Crystalline phases
3.00	G1	Gc1a	786	2.997	$Na_2ZrSi_2O_7$, Na_2SiO_3
		Gc1b	841	3.000	$Na_2ZrSi_2O_7$, Na_2SiO_3, $Na_4ZrSi_3O_{10}$
2.75	G2	Gc2a	827	3.014	$Na_2ZrSi_2O_7$ + Un
		Gc2b	851	3.009	$Na_2ZrSi_2O_7$ + Un
2.50	G3	Gc3	913	2.966	$Na_2ZrSi_2O_7$ + Un
2.25	G4	Gc4	910	2.885	$Na_2ZrSi_2O_7$, $Na_{2.5}Zr_2Si_{1.5}P_{1.5}O_{12}$

Note: Un = unidentified by XRD
** See Table 5.1 (Chapter 5) for parent glass compositions*

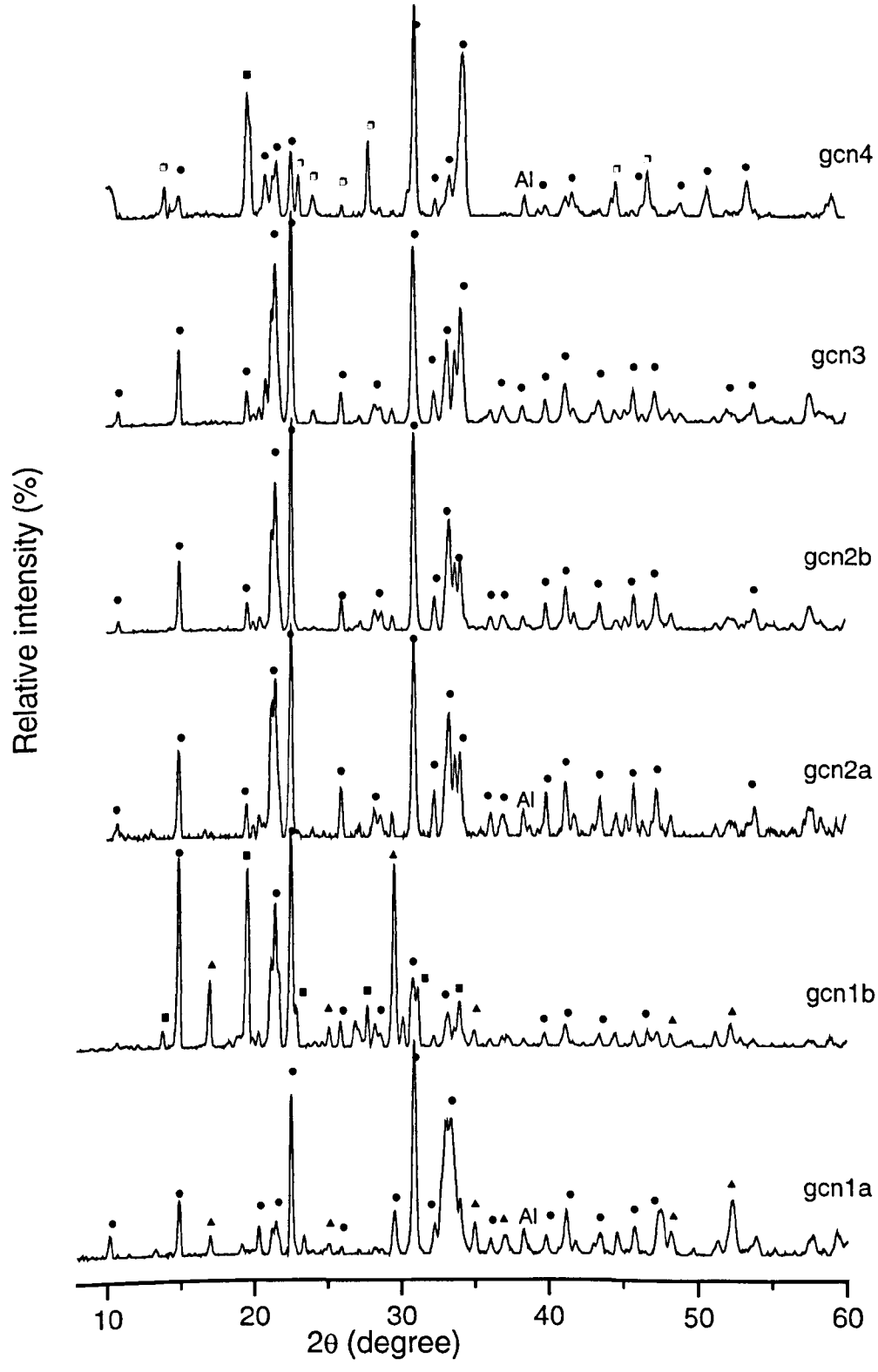

Figure 7.01 *XRD powder pattern of glass-ceramics derived form NASIGLAS after subtracting of glassy background. Five powder patterns are identified,* ● = $Na_2ZrSi_2O_7$ *(JCPDS no. 39-0209),* ▲ = Na_2SiO_3 *(JCPDS no.16-0818),* ■ = $Na_4ZrSi_3O_{10}$ *(JCPDS no. 37-0405) and* ❐ = $Na_{2.5}Zr_2Si_{1.5}P_{1.5}O_{12}$ *(JCPDS no. 47-0515).*

It can be seen that $Na_4ZrSi_3O_{10}$ ($2Na_2O.ZrO_2.3SiO_2$) can be crystallised in Gcn1b and reflects the composition of its parent glass. Polycrystalline, monoclinic, $Na_4ZrSi_3O_{10}$ was synthesised first by Von Alpen and co-workers [8]. The reported ionic conductivity was 4×10^{-3} $S.cm^{-1}$ at 300 °C. According to the evidence of XRD, DTA and solid state NMR studies, Barth et al. [9] suggested that this crystalline phase is actually a mixture of dispersed $Na_4Zr_2(SiO_4)_3$ crystal (NASICON) and a glassy phase which probably shows a composition as $Na_4Si_3O_8$. However, the present results have shown that the $Na_4ZrSi_3O_{10}$ phase can be formed by crystallisation of a glass of this composition. This result is also consistent with the observation of Bortun et al. [10]. They attempted to prepare hydrous sodium zirconium silicates using hydrothermal synthesis and found that $Na_4ZrSi_3O_{10}$ formed in co-existence with other hydrous phases. In Gcn1b, the presence of $Na_4ZrSi_3O_{10}$ may promote good ionic conduction. It can be seen that the intensity ratio of $Na_2ZrSi_2O_7$ and $Na_4ZrSi_3O_{10}$ is close to 1:1.

The crystal $Na_{2.5}Zr_2Si_{1.5}P_{1.5}O_{12}$ formed in Gcn4 is also a fast-ion conductor. The structure has been suggested to have rhombohedral symmetry with reported unit cell parameters a = 8.9904 Å and b = 22.901 Å [11]. This phase has an excellent ionic conductivity, as high as 10^{-2} $S.cm^{-1}$ at 300 °C [11-14]. Formation of this phase requires sufficient P_2O_5 content- a ratio Si/P =1 is preferable.

Crystalline Na_2SiO_3 ($Na_2O.SiO_2$) is only found in the compositions with no P_2O_5 content, i.e. Gcn1a and Gcn1b. Na_2SiO_3 has orthorhombic symmetry and the structure consists of silicate tetrahedra chains linked by Na^+ [15]. In binary sodium silicate glasses, Na_2SiO_3 can be crystallised easily from a wide range of composition and temperature, especially with some ZrO_2 additive [16,17]-similar to lithium silicate glasses [18]. Formation of crystals having composition R_2O/SiO_2 ratio close to 1:1 (R is alkali or alkaline earth) seems to be common even from a complex glass composition [19].

7.2.3 NMR

7.2.3.1 ^{29}Si MAS NMR

The ^{29}Si MAS NMR spectra of glass-ceramic samples are shown in Fig 7.02a and the fitted spectra are shown in Fig. 7.02b. The spectral parameters of the crystalline phases are summarised in Table 7.02a, while those of the residual glasses are summarised in Table 7.02b. Two sharp resonances, at approximately –86.0 ppm and –88.5 ppm, are from $Na_2ZrSi_2O_7$ and both peaks have linewidth around 2.0 ppm. The changes in chemical shift and line width of these peaks when the composition of parent glasses change are within the experimental error and these two peaks have a concentration ratio close to 1:1. The resonance from the sodium metasilicate crystal phase (Na_2SiO_3) has a chemical shift at around –76.4 ppm with linewidth in the range 2.2 ppm to 3.7 ppm. There is a decrease of Na_2SiO_3 concentration from 11% in Gcn1a to about 3% in Gcn1b. This may be the effect of the higher treatment temperature of Gcn1b, which is closer to the melting point of this phase. $Na_4ZrSi_3O_{10}$ and $Na_{2.5}Zr_2Si_{1.5}P_{1.5}O_{12}$ give ^{29}Si resonances at –93.1 ppm and –99.9, respectively. These two phases have linewidth of 3.0 ppm. In all samples, the residual glass is evidenced by a broad peak (dotted line in Fig. 7.02b) at the chemical shift –86.3 ppm with linewidth approximately 10 ppm. In Gcn3 and Gcn4, another broad resonance is present at –100.0 ppm with width in the range 10.6 ppm to 13.6 ppm. With decreasing SiO_2 content, a shift to lower frequency is observed for both peaks. According to data from binary sodium silicate glasses (Grimmer et al. [20]), the resonances at –86.3 ppm and at –100.0 ppm can be assigned as Si(Q^3) and Si(Q^4), respectively. The concentrations of the residual glass vary non-systematically with change of parent glass compositions.

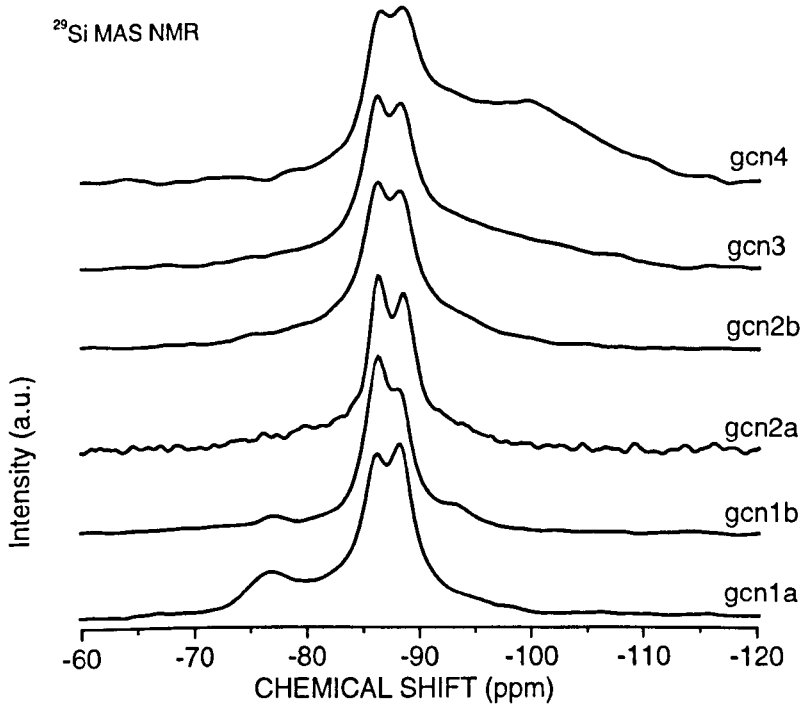

Figure 7.02a *^{29}Si MAS NMR spectra of glass-ceramic samples derived from NASIGLAS.*

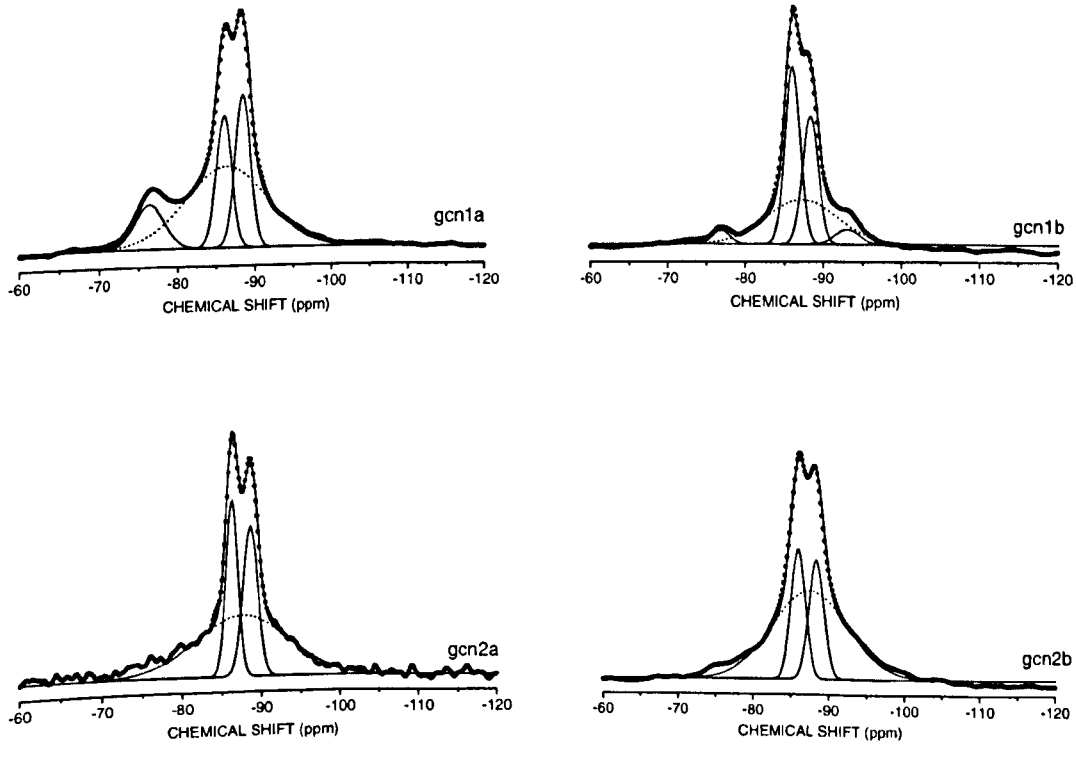

Figure 7.02b *Best fit of ^{29}Si MAS NMR spectra of glass-ceramics, dots are the experimental data, solid lines are the simulation curves and dotted lines are the peaks corresponding to the residual glass.*

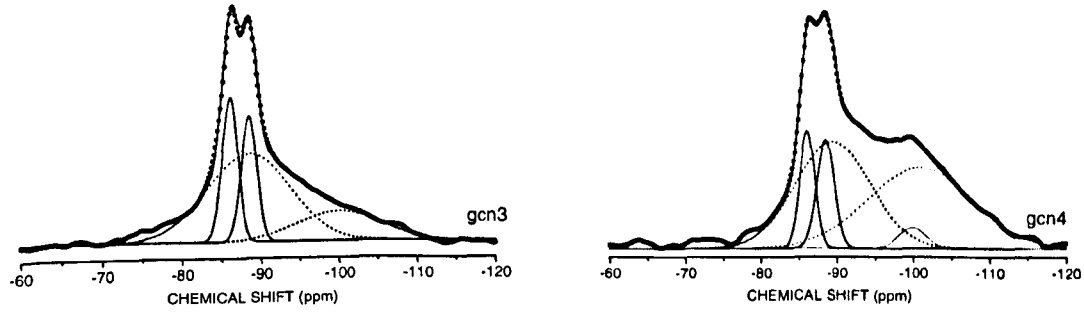

Figure 7.02b *(continued)*

Table 7.02a *Deconvolution of ^{29}Si MAS NMR spectra of glass-ceramics derived from NASIGLAS, δ = chemical shift, W = width and A = relative area.*

Sample	$Na_2ZrSi_2O_7$			Na_2SiO_3			NC		
	δ ±0.5 ppm	W ±0.5 ppm	A ±3.0 %	δ ±0.5 ppm	W ±0.5 ppm	A ±3.0 %	δ ±0.5 ppm	W ±0.5 ppm	A ±3.0 %
Gcn1a	-85.9	2.0	16.6	-76.4	3.7	10.5	-	-	-
	-88.6	*2.0*	*19.2*						
Gcn1b	-86.0	1.9	32.0	-76.8	2.2	2.8	-93.1	3.0	4.0
	-88.3	*2.0*	*23.6*						
Gcn2a	-86.2	1.5	21.0	-	-	-	-	-	-
	-88.5	*1.9*	*22.0*						
Gcn2b	-86.0	1.9	18.0	-	-	-	-	-	-
	-88.4	*2.0*	*17.4*						
Gcn3	-86.0	2.0	16.1	-	-	-	-	-	-
	-88.4	*2.0*	*14.1*						
Gcn4	-86.1	2.0	8.6	-	-	-	-99.9	3.1	2.7
	-88.6	*2.0*	*9.2*						
Literature	-86.7			-76.8					
	-88.9								

Note: *NC = $Na_4ZrSi_3O_{10}$ for Gcn1b, NC = $Na_{2.5}Zr_{2Si1.5}P_{1.5}O_{12}$ for Gcn4*

Table 7.02b *spectral parameters of residual glass.*

Sample	$Si(Q^3)$			$Si(Q^4)$		
	δ (±0.5 ppm)	W (±0.5 ppm)	A (±3.0 %)	δ (±0.5 ppm)	W (±0.5 ppm)	
Gcn1a	-86.3	10.5	53.7			
Gcn1b	-87.2	9.1	37.6			
Gcn2a	-87.6	11.8	57.0			
Gcn2b	-87.5	10.0	64.6			
Gcn3	-88.4	10.5	52.1	-100.0	10.6	17.7
Gcn4	-89.5	9.8	38.7	-100.9	13.6	40.8

All crystalline silicates formed in the glass-ceramic samples have significantly different chemical shifts, resulting in clearly resolved ^{29}Si MAS NMR spectra. Peak assignments are therefore unambiguous. Two sharp peaks at -86.0 ppm and -88.5 ppm are assigned as the two $Si(Q^1)$ species of $Na_2ZrSi_2O_7$ phase. The natural parakeldyshite mineral, $Na_2ZrSi_2O_7$ has two inequivalent $Si(Q^1)$ sites at –86.7 ppm and –88.9 ppm [21]. The observed concentration ratio of these two species, i.e. 1:1, is also consistent with the report in the literature.

There is no direct report of chemical shift data for the $Si(Q^n)$ species in $Na_4ZrSi_3O_{10}$. As discussed above, it was considered to be a mixed phase between $Na_4Zr_2(SiO_4)_3$ and glassy $2Na_2O.3SiO_2$ by Barth et al. [9]. These workers reported that $Na_4Zr_2(SiO_4)_3$ has a ^{29}Si chemical shift at –87.1 ppm and glassy $2Na_2O.3SiO_2$ has two resonances at –79.0 ppm and –88.6 ppm which are assigned as $Si(Q^2)$ and $Si(Q^3)$, respectively. However, the XRD result of Gcn1b shows strong evidence of $Na_4ZrSi_3O_{10}$ existence. From the ^{29}Si MAS NMR spectrum of Gcn1b, a sharp resonance is observed at –93.1 ppm as a shoulder on the main peaks of parakeldyshite. Two independent ^{29}Si MAS NMR studies of $Na_4Zr_2(SiO_4)_3$ also reported evidence of a sharp peak due to $Si(Q^0)$ at –87.5 ppm [22] and -86.6 ppm [23], respectively. Since both $Na_4ZrSi_3O_{10}$ and $Na_4Zr_2(SiO_4)_3$ compounds have a monoclinic crystal symmetry, Si may occupy similar crystallograpic sites in these two compound and show approximately the same chemical shift. In fact, preparing crystalline $Na_4Zr_2(SiO_4)_3$ compound can yield a second glassy phase [24] (described in Chapter 2). It should be noted that there is a significant difference between reference powder patterns of these two compounds and the powder pattern of Gcn1b is consistent only with the $Na_4ZrSi_3O_{10}$ phase. Thus, it may be concluded that $Na_4ZrSi_3O_{10}$ is formed in Gcn1b and gives a ^{29}Si resonance at –93.1 ppm with a relative concentration of 4%. The resonance due to the Na_2SiO_3 phase in Gcn1a

and Gcn1b is clearly resolved from the others. The observed shift is approximately –76.4 ppm. $Si(Q^n)$ species of Na_2SiO_3 can be assigned as $Si(Q^2)$ as suggested by its composition. This result is in accordance with the reported shift for Na_2SiO_3 crystal, -76.8 ppm [20] and for glass of composition $Na_2O.SiO_2$, –79 ppm [25].

In Gcn4, the crystalline phase $Na_{2.5}Zr_2Si_{1.5}P_{1.5}O_{12}$ gives a ^{29}Si resonance at approximately –99.9 ppm. This observed shift is significantly different from the report of Jäger et al. [22] which suggested that the compound $Na_{1+x}Zr_2Si_xP_{3-x}O_{12}$ with x = 1.5 shows a chemical shift around –93 ppm. This difference is not clear. However, evidence for existence of this phase should be found in the ^{31}P MAS NMR study (following section). The structural arrangement of this phase consists of a framework of $[ZrO_6]$ octahedra linked by $[SiO_4]$ and $[PO_4]$ tetrahedra with Na^+ occupying two distinctive interstitial sites [11]. Thus the silicate species may be assigned as $Si(Q^0)$. The chemical shift of $Si(Q^0)$ of $Na_{2.5}Zr_2Si_{1.5}P_{1.5}O_{12}$ is more negative than those of $Na_4Zr_2Si_3O_{12}$ (-88 ppm). This may be due to the presence of $[PO_4]$ tetrahedra which have greater preference to connect with $[ZrO_6]$ tetrahedra resulting in a higher shielding environment for $Si(Q^0)$ species.

The spectra of residual glasses from Gcn1 (a&b) and Gcn2 (a&b), are consistent with most silicate species being present as $Si(Q^3)$. These results suggest that the residual glass has a composition close to $0.45Na_2O.0.55SiO_3$ [25]. In Gcn3 and Gcn4, the concentration of $Si(Q^3)$ is considerably increased, from 18% to 41% indicating increased polymerisation of the silicate network of the residual glass. This may be due to introduction of $[PO_4]$ into the glass composition and removal of Na^+ from the silicate network to form phosphate complexes. This behaviour was described in Chapter 5. The phosphate complexes do not participate in the glass network. If these complexes were

crystallised during heat treatment, they should be observed in the ^{31}P MAS NMR study described in the next section.

7.2.3.2 ^{31}P MAS NMR

Table 7.03a *Deconvolution of ^{31}P MAS NMR spectra of glass-ceramics derived from NASIGLAS*

Sample	$P(Q^0)_{Na}$-i			$P(Q^0)_{Na}$-ii			$P(Q^0)_{Na,Zr}$			$P(Q^0)_{3Zr}$		
	δ ±0.5 ppm	W ±0.5 ppm	A ±3.0 %	δ ±0.5 ppm	W ±0.5 ppm	A ±3.0 %	δ ±0.5 ppm	W ±0.5 ppm	A ±3.0 %	δ ±0.5 ppm	W ±0.5 ppm	A ±3.0 %
Gcn2a	14.9	3.3	50	13.8	1.2	21	7.6	4.4	17	-	-	
Gcn2b	14.2	2.6	58	13.2	1.0	32	6.5	3.7	26	-	-	-
Gcn3	13.0	3.1	72	-	-	-	4.9	3.2	13	-	-	-
Gcn4	13.3	3.8	31	-	-	-	5.7	3.9	39	-12.0	4.8	9

Table 7.03b *Spectra parameters of phosphate species of the glassy phase observed in glass-ceramics derived from NASIGLAS.*

Sample	Residual glass $-P(Q^0)_{Na,Zr}$			Residual glass $-P(Q^1)_{Na}$		
	δ (±0.5 ppm)	W (±0.5 ppm)	A (±3 %)	δ (±0.5 ppm)	W (±0.5 ppm)	A (±3 %)
Gcn2a	-	-	-	3.9	9.4	12
Gcn2b	-	-	-	-	-	-
Gcn3	9.74	17.5	15	-	-	-
Gcn4	8.3	17.7	21	-	-	-

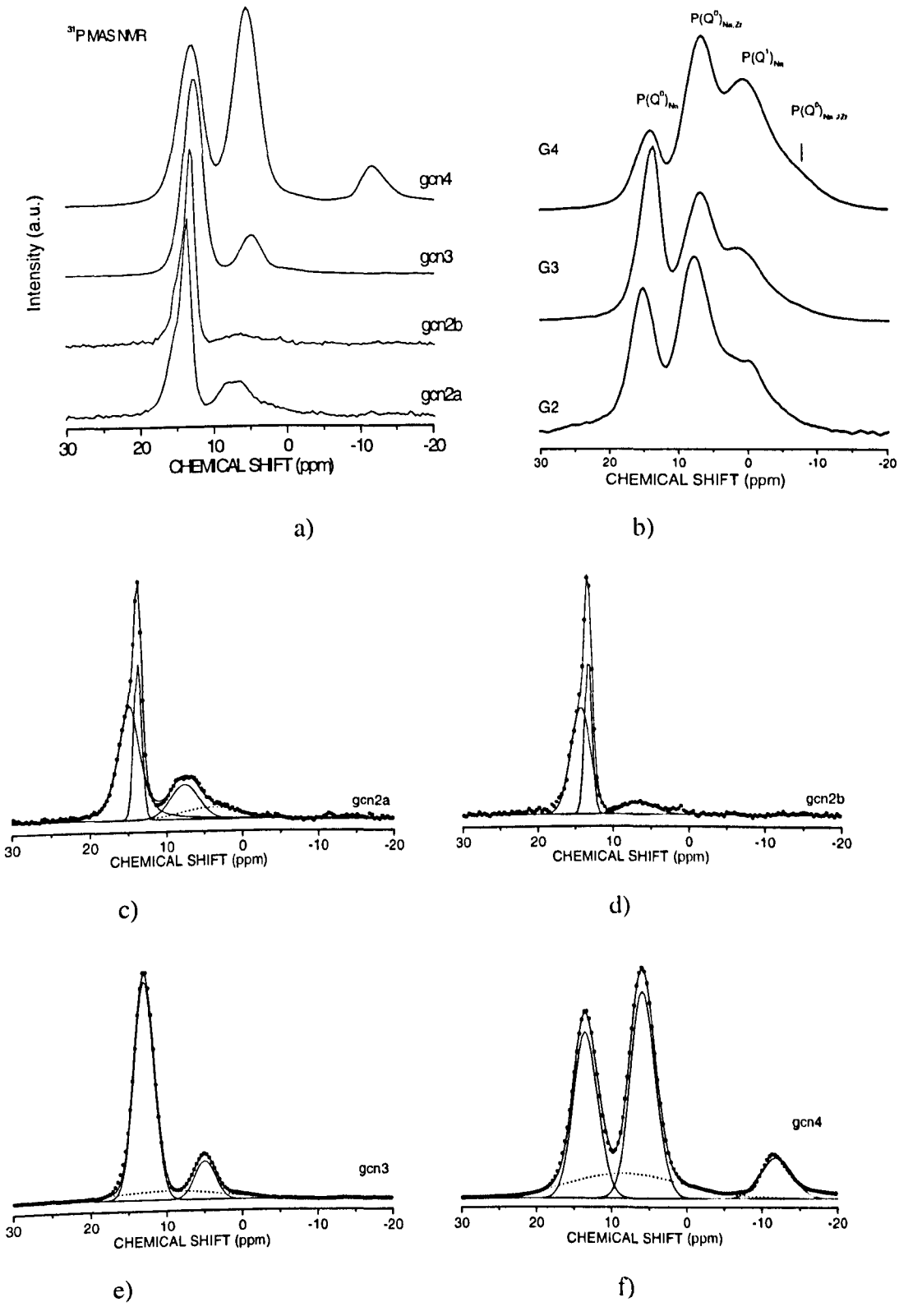

Figure 7.03 a) *^{31}P MAS NMR spectra of glass-ceramic samples comparing with b) the spectra of the parent glasses, c) -e) their best Gaussian fits, dots are the experimental data, solid lines are the simulation curves and peaks due to residual glasses are shown by dotted lines. The spinning speed is 10 kHz.*

The ^{31}P MAS NMR spectra of the glass-ceramic samples are shown in Fig. 7.03a compared with the spectra of their parent glasses (Fig. 7.03b). The spectra of Gcn2a and Gcn2b are very similar, having two overlapping resonances at around 14 ppm and a broader hump at around 7 ppm. In Gcn3 and Gcn4, there is only one broad peak at 14 ppm and the intensity of the peak at 7 ppm is increased sharply for Gcn4. For Gcn4, there is an additional peak present at −12 ppm. Using a Gaussian fit, all peaks can be determined and their spectral parameters are summarised in Table 7.03a and 7.03b. The resonances due to residual glasses are clearly seen in Gcn2a, Gcn3 and Gcn4.

The results in Table 7.03 suggest that there are five possible phosphate species present in heat-treated glass samples. The peaks at approximately 14 ppm are close to the position for $P(Q^0)_{Na}$ in crystalline Na_3PO_4 [26]. These two $P(Q^0)_{Na}$ species are distinguished by their linewidths, 3.0 ppm and 1.0 ppm. The result may imply that these two $P(Q^0)_{Na}$ species locate in a slightly different environment which probably create a difference in averaged P-O bond length and/or distribution of O-P-O bond angle. However, the narrower peak disappears in Gcn3 and Gcn4. The peak at 7 ppm can be assigned as $P(Q^0)_{Na,Zr}$, i.e. $P(Q^0)$ bonded to two Na^+ and one Zr^{4+}, consistent with the assignment of the corresponding parent glass (Chapter 5). $P(Q^0)_{Na,Zr}$ moves to a lower frequency and increases in concentration as P_2O_5 increases. The ^{31}P MAS NMR spectra of $Na_3Zr_2Si_2PO_{12}$ prepared by the sol-gel method also show a peak at around 5 ppm which can be assigned as the $P(Q^0)$ species having mixed bonds with Na^+ and Zr^{4+} [27]. The resonance at −12 ppm can be assigned as $P(Q^0)_{3Zr}$. This assignment is consistent with the presence in Gcn4 of $Na_{2.5}Zr_2Si_{1.5}P_{1.5}O_{12}$, in which all $[PO_4]$ tetrahedra share corners with $[ZrO_6]$ octahedra. The assignment is also consistent with the reported shifts of the NASICON family, -12 ppm for $Na_3Zr_{1.5}(PO_4)_3$ [22], -12.4 ppm for $Na_3ScZrSiP_2O_{12}$ [28],

-17 ppm for $Na_3Zr_2Si_2PO_{12}$ [27], -25 ppm for $NaZr_2(PO_4)_3$ [22]. It should be noted that $P(Q^0)_{3Zr}$ is the only phosphate species observed in the NASICON compositions [29-32]. It can be seen that, the $P(Q^0)_{3Zr}$ species exhibit high field shift when some $[PO_4]$ tetrahedra are substituted by $[SiO_4]$. This is probably due to reduction of net atomic charge of neighbouring Zr atom by silicon atoms which possesses a weaker electronegativity compared to phosphorus atoms [27]. This is strong evidence that the resonance at –12 ppm is given by the $Na_{2.5}Zr_2Si_{1.5}P_{1.5}O_{12}$ crystal and it confirms the XRD result.

The residual glass present in Gcn2a can be assigned as $P(Q^1)_{Na}$ because the resonance at 3.9 ppm is close to the 2.00 ppm of the $Na_4P_2O_7$ crystal. In Gcn3 and Gcn4, the residual glass shows resonances at 9.7 ppm and 8.3 ppm with a width around 17 ppm. This can be assigned as $P(Q^0)_{Na,Zr}$ which is different from that found in Gcn2.

From the XRD results, there is only one crystalline phase that contains $[PO_4]$ tetrahedra, that is $Na_{2.5}Zr_2Si_{1.5}P_{1.5}O_{12}$. There were also unidentified patterns for Gcn2a, Gcn2b and Gcn3. With the observation of two $P(Q^0)_{Na}$ species and one $P(Q^0)_{Na,Zr}$ by the ^{31}P MAS NMR, it is believed that the unidentified phases are in fact of the phosphate compounds having $P(Q^0)_{Na}$ or $P(Q^0)_{Na,Zr}$ species. For Gcn4, the relative intensity of $P(Q^0)_{3Zr}$ is lower than those of $P(Q^0)_{Na}$ and $P(Q^0)_{Na,Zr}$ but the XRD powder pattern of $Na_{2.5}Zr_2Si_{1.5}P_{1.5}O_{12}$ is clearly seen and identified. While, the pattern of Na_3PO_4 is not pronounced. Thus, the strongest peaks of Na_3PO_4 may be obscured by peaks of other crystalline phases.

7.2.3.3 ^{23}Na MAS NMR

The ^{23}Na MAS NMR spectra of glass-ceramic samples are shown in Fig. 7.04. The consistency of results from XRD, ^{29}Si and ^{31}P MAS NMR is useful for analysing the

^{23}Na MAS NMR spectra. There are two Na sites in each of $Na_2ZrSi_2O_7$ [21], $Na_4ZrSi_3O_{10}$ and $Na_{2.5}Zr_2Si_{1.5}P_{1.5}O_{12}$ [29-32, 34-37]. Na_2SiO_3 and Na_3PO_4 should each have only one Na site. Knowing the number of Na sites, quadrupolar parameters can be determined using the Winfit software [38]. Figure 7.04b shows the best simulations of the ^{23}Na MAS NMR spectra and the corresponding quadrupolar parameters are reported in Table 7.04b and 7.04c. ^{23}Na resonances at –2.3 ppm and ~2.0 ppm with intensity ratio 1:1 are assigned to Parakeldyshite ($Na_2ZrSi_2O_7$) and the parameters are compared with literature [21].

Table 7.04a *Comparison of the quadrupolar parameters of $Na_2ZrSi_2O_7$ with ref. [21].*

Na Site	δ_{iso} (ppm)		C_Q (MHz)		η		Intensity (%)	
1	0.0	***-2.3***	1.5	***1.5***	1.0	***0.68***	50	***50***
2	2.0	***2.0***	2.8	***2.8***	0.85	***0.85***	50	***50***

Note: the experimental data of this study are shown by bold numbers.

Table 7.04b *Chemical shift and area of ^{23}Na MAS NMR spectra of glass-ceramic samples derived from NASIGLAS.*

Sample	$Na_2ZrSi_2O_7$		Na_2SiO_3		NC*		Na_3PO_4		Res. Glass	
	δ ±0.3 ppm	A ±3.0 %	δ ±0.3 ppm	A ±3.0 %	δ ±0.3 ppm	A ±3.0 %	δ ±0.3 ppm	A ±3.0 %	δ ±0.3 ppm	A ±3.0 %
Gcn1a	-1.9	16	20.7	7			-	-	-16.2	59.4
	3.1	18								
Gcn1b	-3.4	22	20.5	21	-3.5	19	-	-	-23.5	6
	2.4	26			-18.6	4				
Gcn2a	-2.3	26	-	-	-	-	11.9	10	-16.9	40
	1.3	24								
Gcn2b	-2.3	26	-	-	-	-	11.9	10	-18.1	39
	1.2	25								
Gcn3	-2.3	27	-	-	-	-	10.8	13	-19.8	37
	1.9	23								
Gcn4	-2.5	17	-	-	-3.1	27	10.9	8	-35.1	22
	3.0	24			-25.6	3				

*Note: * NC = $Na_4ZrSi_3O_{10}$ for Gcn1b, NC = $Na_{2.5}Zr_2Si_{1.5}P_{1.5}O_{12}$ for GCn4*

It can be seen that the difference in isotropic chemical shift between the two Na sites is 2 ppm for the natural parakeldyshite whereas in glass-ceramic samples it is 4 ppm. The η of Na1 are also different. The difficulty of fitting the complex line may be responsible for that difference.

The δ ^{23}Na observed for Na_2SiO_3 is 20.5 ppm with C_Q = 1.5 MHz and η = 0.65, in good agreement with reports for Na_2SiO_3 crystal [25,39]. The intensity ratio of Na_2SiO_3 in samples Gcn1a and Gcn1b is 1:3 which is consistent with the ^{29}Si MAS NMR results.

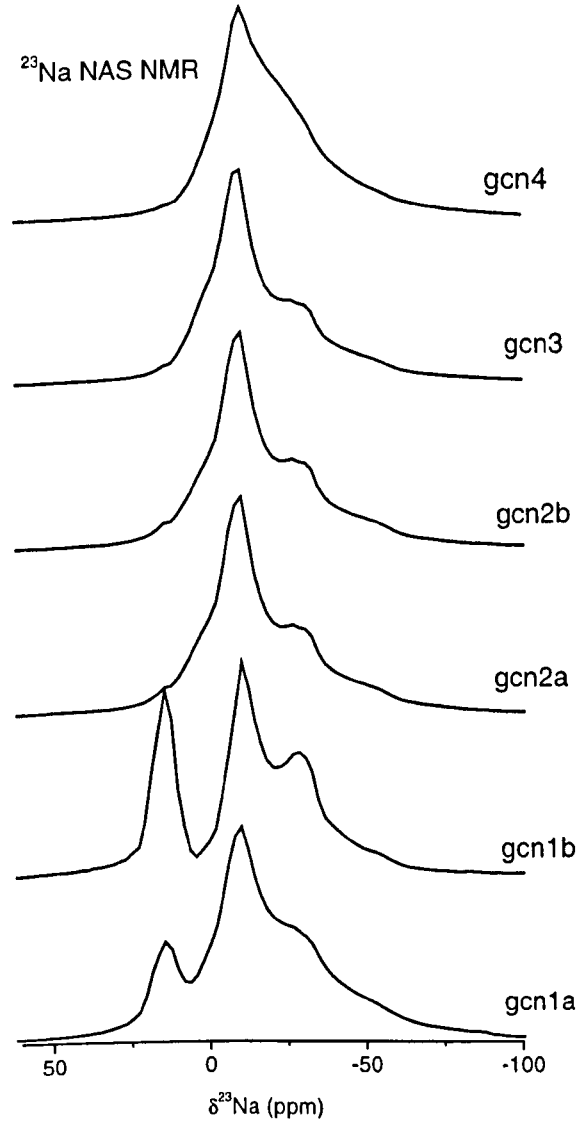

Figure 7.04a *^{23}Na MAS NMR spectra of glass-ceramics derived from NASIGLAS.*

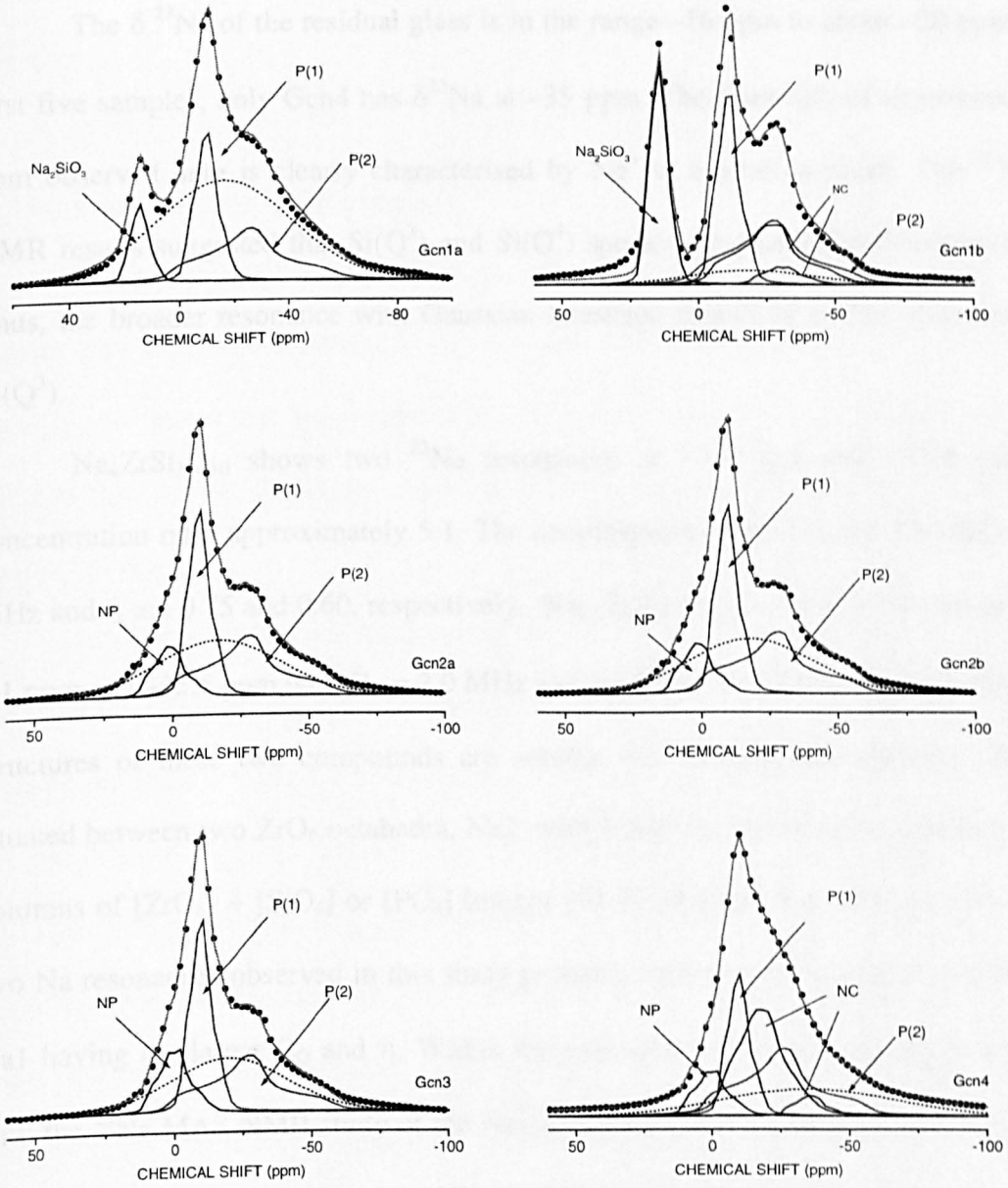

Figure 7.04b *Simulation of ^{23}Na MAS NMR spectra shown in Figure 7.04a . For peak assignments, see text (NP is of Na_3PO_4, P(1) and P(2) are of $Na_2ZrSi_2O_7$).*

Table 7.04c *Quadrupole parameters for ^{23}Na in crystalline phases and residual glass.*

Phase	Quadrupole parameters		
	C_Q (± 0.1MHz)	η (± 0.2)	Width (± 5 ppm)
$Na_2ZrSi_2O_7$	1.5	0.68	
	2.8	0.85	
$Na_4ZrSi_3O_{10}$	2.6	0.75	
	2.0	0.6	
$Na_{2.5}Zr_2Si_{1.5}P_{1.5}O_{12}$	2.0	0.65	
	1.8	0.65	
Na_2SiO_3	1.4	0.65	
Residual glass			52

The δ ^{23}Na of the residual glass is in the range –16 ppm to about –20 ppm for the first five samples, only Gcn4 has $\delta^{23}Na$ at –35 ppm. The linewidth of approximately 52 ppm observed here is clearly characterised by Na^+ in a glass network. The ^{29}Si MAS NMR results suggested that $Si(Q^3)$ and $Si(Q^4)$ species are present in the residual glass. Thus, the broader resonance with Gaussian lineshape should be of Na^+ associated with $Si(Q^3)$.

$Na_4ZrSi_3O_{10}$ shows two ^{23}Na resonances at –3.5 ppm and –18.6 ppm with concentration ratio approximately 5:1. The coupling constants, C_Q, are 2.6 MHz and 2.0 MHz and η are 0.75 and 0.60, respectively. $Na_{2.5}Zr_2Si_{1.5}P_{1.5}O_{12}$ also gives two peaks at –3.1 ppm and –25.6 ppm with C_Q = 2.0 MHz and 1.8 MHz, both have η = 0.65. The crystal structures of these two compounds are similar. Na^+ occupy two different sites; Na1 situated between two ZrO_6 octahedra, Na2, with 8 fold coordination, located between the columns of $[ZrO_6]$ + $[SiO_4]$ or $[PO_4]$ linkage [34-37, 40] (see Fig. 2.01 for details). The two Na resonances observed in this study probably represent those of Na1 and Na2 with Na1 having the larger C_Q and η. Within the experimental error, these are in agreement with the ^{23}Na MAS NMR study of the $Na_{1+x}Zr_2(SiO_4)_x(PO_4)_{3-x}$ compound by Jäger et al. [41] (with x 3.0, Na1 has C_Q = 2.8 MHz, η= 0.84 and Na2 has C_Q = 1.7 MHz, η= 0.53).

The Na^+ of the phosphate complexes are observed as peaks having isotropic chemical shift around 11 ppm with C_Q = 1.8 MHz and η= 0.65. The maximum concentration is found in composition Gcn3 which is consistent with the larger proportion of $P(Q^0)_{Na}$ concentration determined by the ^{31}P MAS NMR study. Compared to sodium orthophosphate, the chemical shifts determined here are similar but the spectral lineshape is different. The spectra are characterised by quadrupolar broadening for Na_3PO_4 in our

glass-ceramic samples and by Lorentzian lineshape for synthesised Na_3PO_4 crystal [42,43].

7.2.3.4 Summary for NMR results

Using solid state MAS NMR to identify the crystalline phases formed in the heat-treated glass samples has proved to be very powerful. It complements XRD which cannot identify substances that are present at very low concentration (i.e. < 5 mol%). With ^{29}Si, ^{31}P and ^{23}Na MAS NMR, the crystalline phases can readily be distinguished from the residual glass.

From this study, heat treatment of four NASIGLAS compositions at six different temperatures yield $Na_2ZrSi_2O_7$ as the major crystalline phase. Na_2SiO_3 and $Na_4ZrSi_3O_{10}$ were found in heat treated G1. $Na_{2.5}Zr_2Si_{2.5}P_{2.5}O_{12}$ was present in heat treated G4, while the Na_3PO_4 was found to crystallise in heat-treated G2, G3 and G4. These results suggest that P_2O_5 acts as a nucleating agent, which is widely found in glass-ceramic preparation [44,45]. The combination of XRD and solid state NMR leads to an unambiguous interpretation of data, especially determination of crystal and glass structures. For example, the structural arrangement of parakeldyshite is justified and confirms the previous proposed model shown by Ferriera et al. [46].

7.2.4 SEM

SEM micrographs of Gcn1a and Gcn1b, prepared by heat treatment of bulk G1, are shown in Fig. 7.05. The microstructures of both samples are similar, consisting of large parakeldyshite crystals and the needle crystals of Na_2SiO_3 (sodium metasilicate). Parakeldyshite crystals show as brighter areas because this is a Zr-rich phase. The needle characteristic of the Na_2SiO_3 crystal is a reflection of its chain structure. In Gcn1a,

Na_2SiO_3 crystals are dispersed around the parakeldyshite crystal. For Gcn1b, the interior microstrucuture is similar to Gcn1a but higher concentration of Na_2SiO_3 crystal is clearly observed at the surface layer (Fig. 7.05ba). This indicates that Na_2SiO_3 surface nucleates and is formed by an increase of crystallisation temperature. The $Na_4ZrSi_3O_{10}$ is not readily discerned because it is present as very small droplets between the parakeldyshite crystals.

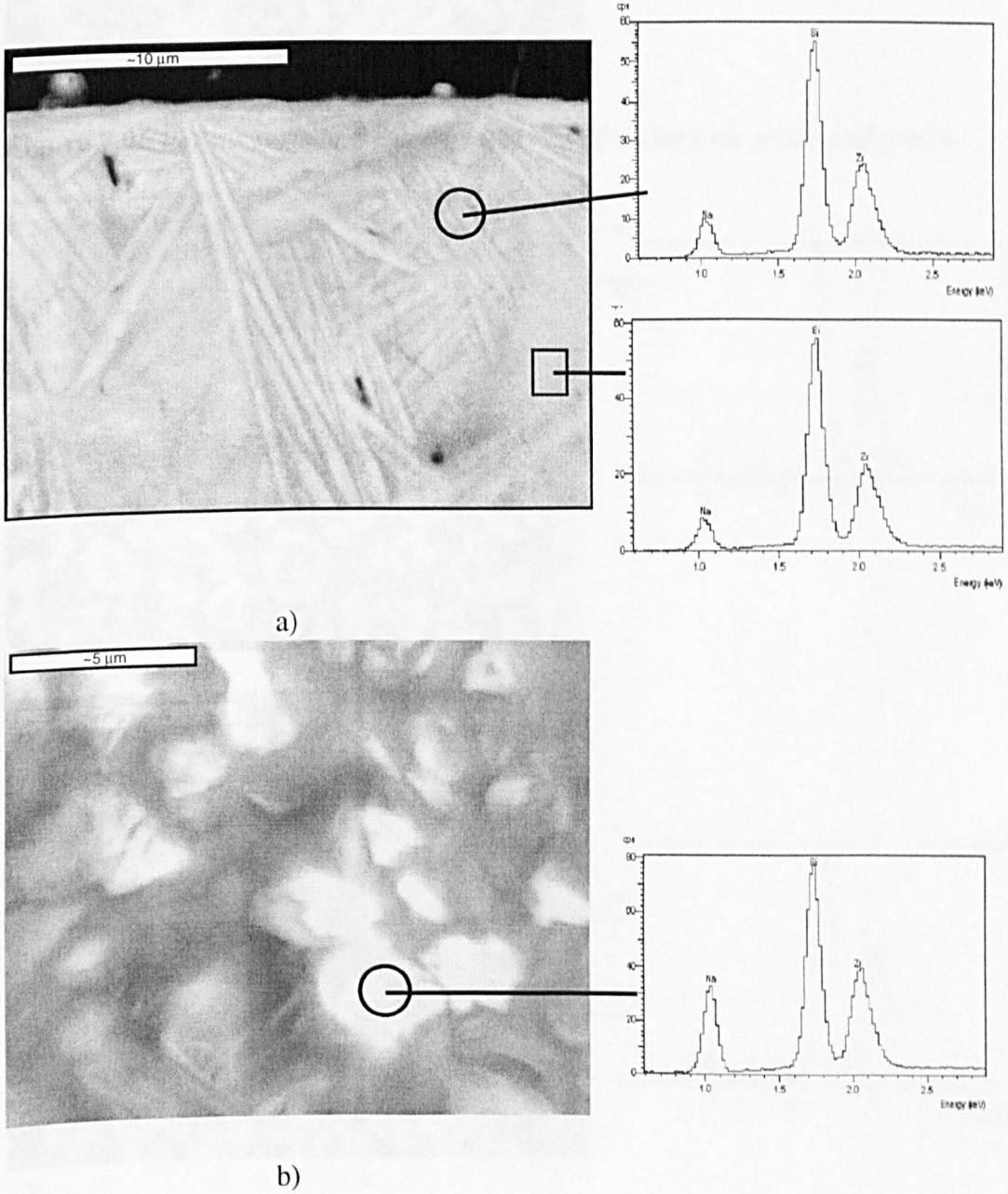

Figure 7.05 *SEM micrograph, a) surface layer of gcn1b and b) internal area of gcn1a, showing large particles of $Na_2ZrSi_2O_7$ and small needle of Na_2SiO_3.*

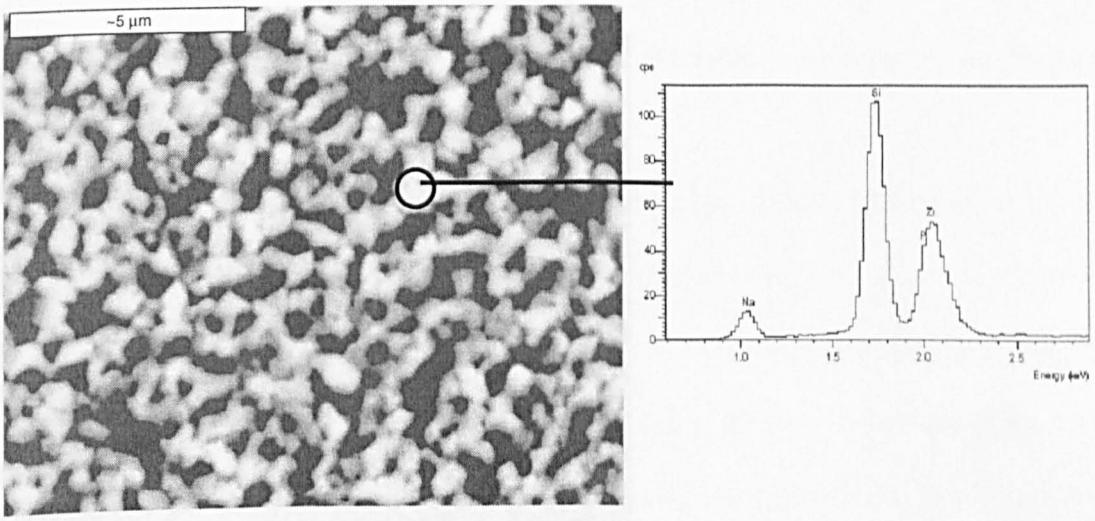

Figure 7.06 *Porous surface created by reaction of water with gcn2a and gcn2b.*

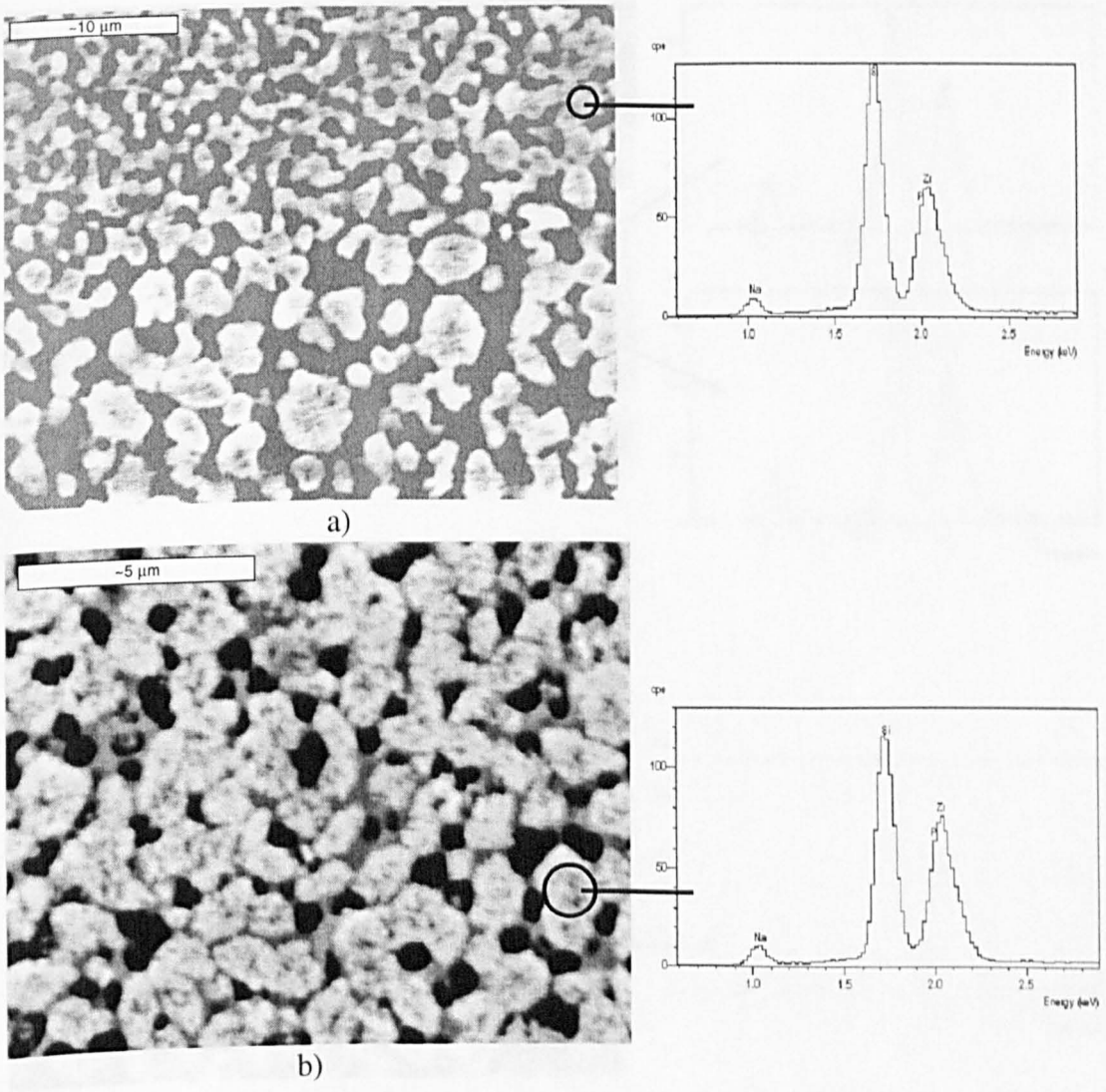

Figure 7.07 *SEM micrograph of gcn3, a) surface layer and b) internal area. White crystals are $Na_2ZrSi_2O_7$ phase and dark area is the glass matrix.*

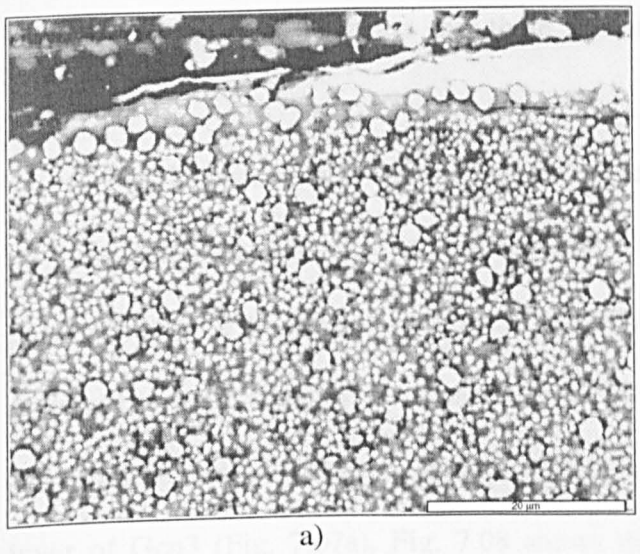

a)

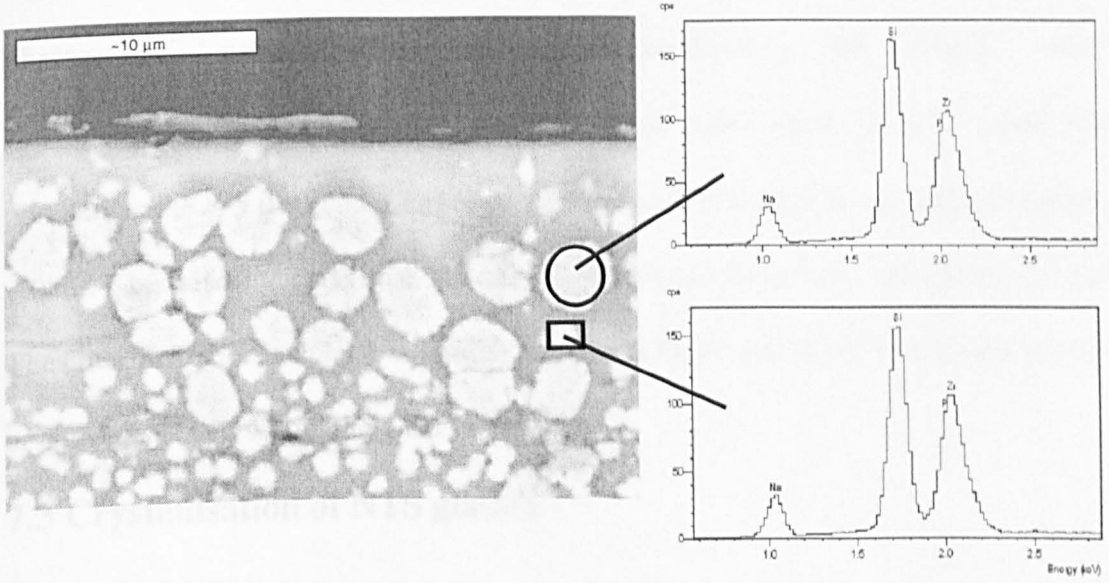

b)

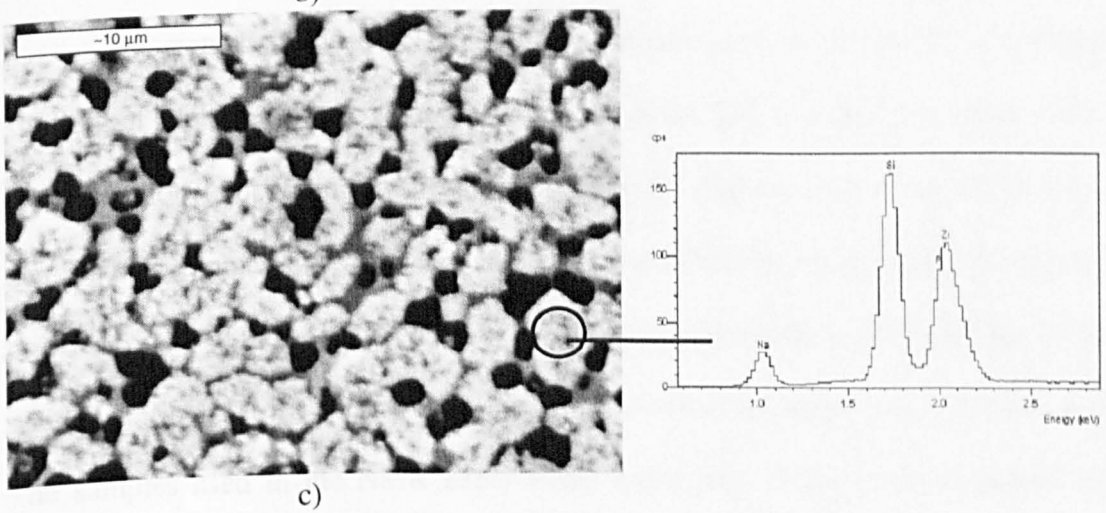

c)

Figure 7.08 *SEM micrograph of gcn4, a) dispersion of $Na_2ZrSi_2O_7$ crystal at the surface layer, b) higher magnification of surface layer and c) the internal area.*

EDX analyses of specific area are shown but the relative sizes of the excitation volume and the crystals means that there is considerable interference from background material.

Fig. 7.06 shows the microstructures of Gcn2a and Gcn2b. During cross-sectioning of these samples, they were in contact with water and result is a porous structure of parakeldyshite with the residual glass partially leached out and appearing as a dark region. The same situation is repeated for Gcn3 (Fig. 7.07), but parakeldyshite shows a larger particle size. However, smaller particle sizes are clearly observed at the surface layer of Gcn3 (Fig. 7.07a). Fig. 7.08 shows the microstructure of Gcn4. Two Zr-rich phases, i.e. parakeldyshite and $Na_{2.5}Zr_2Si_{1.5}P_{1.5}O_{12}$, are clearly observed. $Na_{2.5}Zr_2Si_{1.5}P_{1.5}O_{12}$ has smaller particles sizes (less than 1 μm) compared to parakeldyshite (~5 μm) and a larger concentration is observed at the surface region (Fig. 7.08a). This also indicates that $Na_{2.5}Zr_2Si_{1.5}P_{1.5}O_{12}$ is formed by surface crystallisation. The interior region of Gcn4 is similar to that of Gcn3 and Gcn2 having parakeldyshite crystals dispersed within the glass matrix.

7.3 Crystallisation of NTS glasses

7.3.1 Introduction

The compositions of NTS glasses were detailed in Chapter 6. Crystallisation studies of these glasses were carried out using DTA data. The nucleation and crystallisation temperatures were selected from T_x and Tc shown by Table 6.2a. The heating programmes were the same as for Gcn samples, which was detailed above. Both powder form and bulk specimen NTS glasses were heat treated in a Pt crucible. XRD and solid state MAS NMR were used to identify phases formed in the glass-ceramic products. The samples used in the NMR experiments were those prepared from powder parent glasses.

7.3.2 XRD

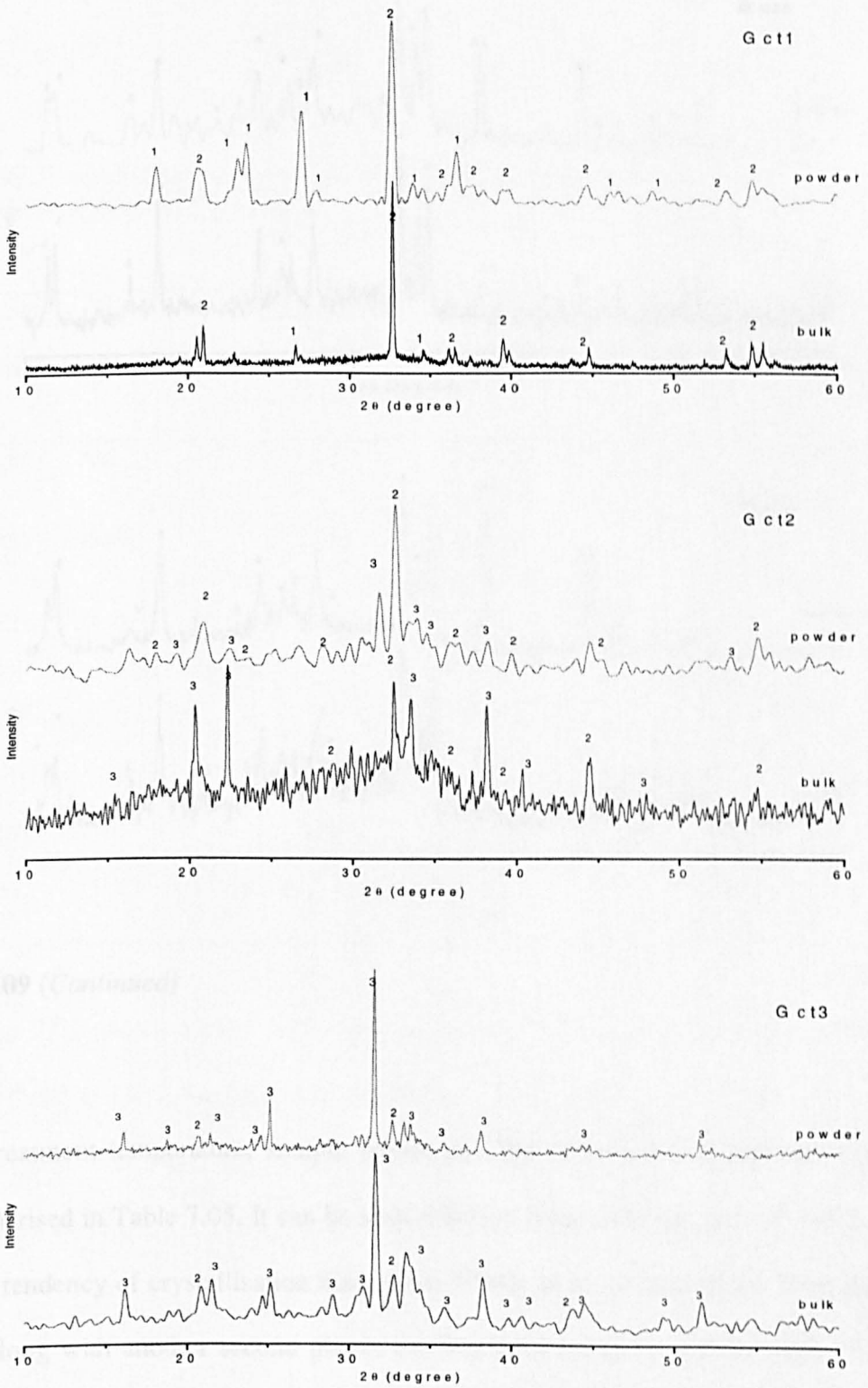

Figure 7.09 *XRD powder patterns of glass-ceramics derived from NTS glasses comparing between samples prepared from powder (top) and bulk specimen (bottom) of parent glasses. There are five identified patterns, 1 = $Na_2Si_2O_5$, 2 = Na_2TiSiO_5, 3 = $Na_2Ti_2Si_2PO_{13}$, 4 = $Na_4TiO(PO_4)_2$ and 5 = $Na_2TiO(Si_4O_{10})$.*

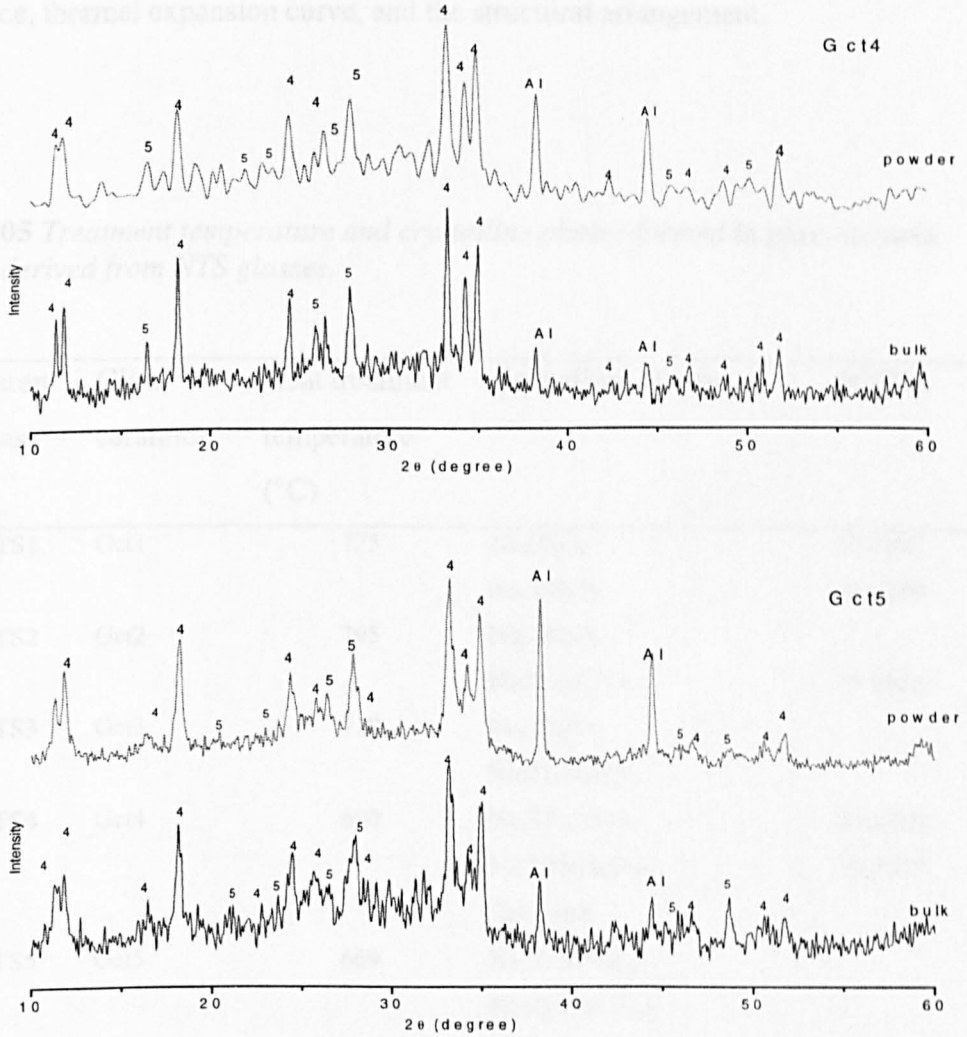

Figure 7.09 (*Continued*)

Treatment temperature, sample names and the corresponding crystalline phases are summarised in Table 7.05. It can be seen that first three samples, Gct1, 2 and 3, show the same tendency of crystallisation having Na_2TiSiO_5 as a common phase. This phase is present along with another second phase, i.e. $Na_2Si_2O_5$ for Gct1 and $Na_2Ti_2Si_2PO_{13}$ for Gct2 and Gct3, respectively. The crystalline phases formed in Gct4 and Gct5 are different from the other three samples, containing two crystalline phases, $Na_4TiO(PO_4)_2$ and $Na_2TiO(Si_4O_{10})$ (narsarsukite mineral), and an unknown minor phase. Results in

Chapter 6 have shown several distinct characteristics of these two compositions, e.g. DTA trace, thermal expansion curve, and the structural arrangement.

Table 7.05 *Treatment temperature and crystalline phases formed in glass-ceramic samples derived from NTS glasses.*

X	Parent glass*	Glass-ceramics	Heat treatment temperature (°C)	Crystalline phases	JCPDS
3.00	NTS1	Gct1	775	$Na_2Si_2O_5$	22-1397
				Na_2TiSiO_5	33-1299
2.75	NTS2	Gct2	795	Na_2TiSiO_5	
				$Na_2Ti_2Si_2PO_{13}$	17-0542
2.50	NTS3	Gct3	710	Na_2TiSiO_5	
				$Na_2Ti_2Si_2PO_{13}$	
2.25	NTS4	Gct4	690	$Na_4TiO(PO_4)_2$	46-0305
				$Na_2TiO(Si_4O_{10})$	33-1297
				Unknown	
2.00	NTS5	Gct5	669	$Na_4TiO(PO_4)_2$	
				$Na_2TiO(Si_4O_{10})$	
				Unknown	

Fig 7.09 shows a clear difference between powder and bulk samples for Gct1, Gct2 and Gct3. In Gct1, the pattern of $Na_2Si_2O_5$ is more visible in powder sample. These results suggest that $Na_2Si_2O_5$ was largely formed by crystallisation at the surface. However, for Gct4 and Gct5, there are no differences between powder and bulk samples.

7.3.3 NMR

7.3.3.1 ^{29}Si MAS NMR

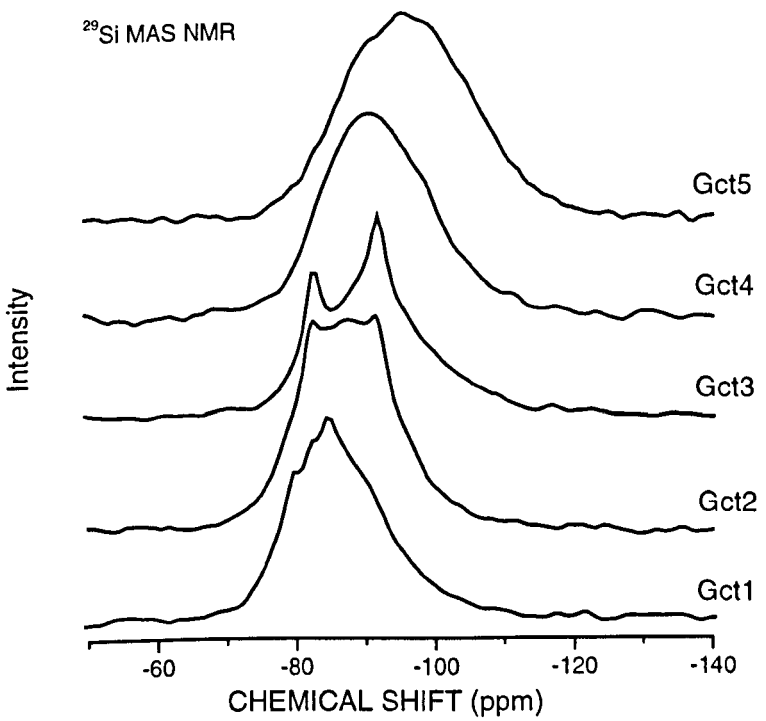

Figure 7.10 *^{29}Si MAS NMR spectra of glass-ceramics derived from NTS glasses.*

The ^{29}Si MAS spectra of Gct samples are shown in Fig. 7.10. The central resonances, due to residual glass, move to lower frequency with decreasing SiO_2 content. The sharp resonances due to crystalline silicate are clearly observable for Gct1, Gct2, and Gct3. For Gct4 and Gct5, the spectra are dominated entirely by the broad resonance of the residual glass. To determine all peaks, Gaussian fitting was used with the constraint of linewidth and chemical shift. The linewidths of crystalline peaks have an upper bound at 5 ppm and of glassy phase have a lower bound at 10 ppm. Minimum chemical shift difference is 1.8 ppm for crystalline and 5 ppm for glassy phase. The deconvolution results are summarised in Table 7.06.

Table 7.06 *^{29}Si MAS NMR spectral parameters of glass-ceramics derived from NTS glasses.*

Sample	Peak description	Isotropic chemical shift ± 0.5 ppm	Linewidth ± 0.5 ppm	Relative area ± 3.0 %
Gct1	Crys	-79.4	2.7	3
	Crys	-82.2	1.5	1
	Crys	-84.5	2.2	2
	ResG	-84.8	14.3	75
		-94.5	20.3	19
Gct2	Crys	-82.2	3.1	4
	Crys	-91.7	2.2	2
	ResG	-87.5	16.7	94
Gct3	Crys	-82.4	2.6	7
	Crys	-91.9	2.7	7
	ResG	-87.5	15.5	66
		-100.6	16.9	20
Gct4	Crys	-98.5	3.2	1
	ResG	-88.9	14.0	59
		-97.2	17.5	40
Gct5	Crys	-95.1	2.6	1
	ResG	-88.1	11.5	12
		-97.7	19.8	87

For Gct1, the peak at –79.4 ppm can be assigned as the Si(Q^0) species of Na_2TiSiO_5 in which all NBO are bonded to Ti^{4+}. This asssignment is in accordance with the chemical shift of $CaTiOSiO_4$ –titanite (-78.5 ppm) [47]. The other two peaks at –82.2 ppm and –84.5 ppm can be assigned as the Si(Q^3) species of the β-$Na_2Si_2O_5$ phase. This assignment is consistent with the observed shift of synthetic β-$Na_2Si_2O_5$ which shows two resonances at –86.7 ppm and –88.6 ppm from inequivalent Si(Q^3) species [48]. The residual glass of Gct1 shows two resonances at –84.8 ppm and –94.5 ppm with linewidth of 14.3 ppm and 20.3 ppm, respectively. These two peaks can assigned as Si(Q^1) and Si(Q^2) which consistent with the observed shift of the parent glass (NTS1). There are two

crystalline phases in Gct2 and Gct3 suggested by XRD and these are seen as two sharp peaks in the ^{29}Si MAS NMR spectra. The first peak is due to the $Si(Q^0)$ species of Na_2TiSiO_5 which show a low frequency shift to –82.2 ppm with slight change of its concentration. The second peak at –91 ppm can be assigned as $Si(Q^2)$ of $Na_5Ti_2Si_2PO_{13}$. This assignment is based on the assumption that there is no linkage between $[SiO_4]$ and $[PO_4]$ tetrahedra and this is close to the reported shift of $Si(Q^2)$ in $Na_2Ti_2Si_2O_9$, i.e. –90 ppm [47]. The residual glass of Gct2 shows only one peak at –87.5 ppm which is due to $Si(Q^1)$.

In Gct4 and Gct5, there is only one crystalline peak at –98.5 ppm and –95.1 ppm, respectively. XRD results suggest that the only crystalline silicate present is $Na_2TiO(Si_4O_{10})$ containing $Si(Q^3)$ species. The shift observed is consistent with that reported for the mineral narsarsukite-$Na_2TiO(Si_4O_{10})$, i.e. –94.2 ppm [47]. The two silicate species in the glassy phase of Gct4 and Gct5 show low frequency shift with decreasing $[SiO_4]$ tetrahedra concentration. It should also be noted that the ^{29}Si shift range observed for both crystalline and glassy phases of sodium titanium silicate compositions in this study are in accordance with the Ti^{4+} being present as $[TiO_6]$ octahedral units [49], except for Na_2TiSiO_5 where Ti^{4+} is five-coordinated (TiO_5) [50].

7.3.3.2 ^{31}P MAS NMR

The ^{31}P MAS NMR spectra of phosphorus containing glass-ceramic samples are shown in Fig. 7.11. The spectra of Gct2 and Gct3 are similar, with two sharp resonances observable at around 7 ppm. The spectra of Gct4 and Gct5 are also similar with broad resonances at more negative chemical shift compared to Gct2 and Gct3. The Gaussian fit results are reported in Table 7.07

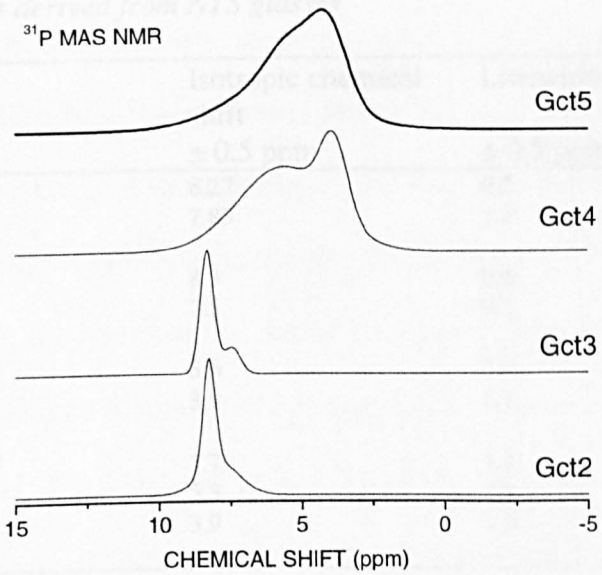

a)

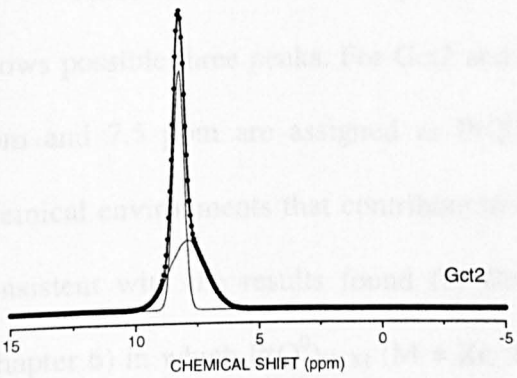

b)

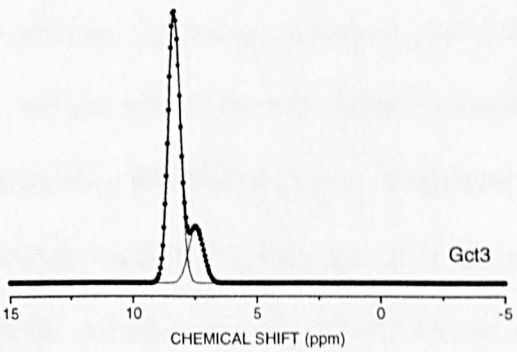

c)

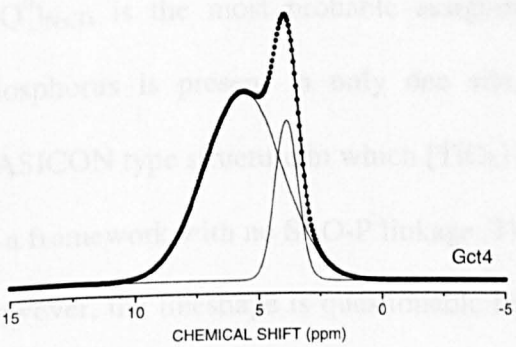

d)

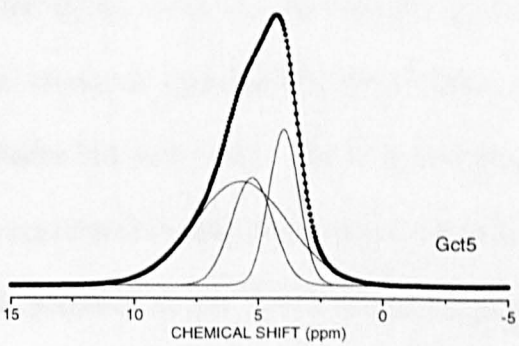

e)

Figure 7.11 *a) ^{31}P MAS NMR spectra of glass-ceramic samples derived from NTS glasses and b)-e) show best fit of the spectra, dots are the experimental data and solid lines are the simulation curves.*

Table 7.07 *Spectral parameters from deconvolution of ^{31}P MAS NMR spectra of glass-ceramics derived from NTS glasses.*

Sample	Isotropic chemical shift ± 0.5 ppm	Linewidth ± 0.5 ppm	Relative area ± 3.0 %
Gct2	8.27	0.5	51
	7.89	1.7	49
Gct3	8.3	0.6	80
	7.5	0.7	20
Gct4	5.6	3.7	80
	3.9	1.1	20
Gct5	5.7	4.5	52
	5.3	1.9	22
	3.9	1.5	26

There are two resonance peaks for the first three samples but the last one (Gct5) shows possible three peaks. For Gct2 and Gct3, the two resonances at approximately 8.3 ppm and 7.5 ppm are assigned as $P(Q^0)_{Na,Ti}$ species which occupy slightly different chemical environments that contribute to the difference in linewidth. This assignment is consistent with the results found for Gcn samples (section 7.2.3.2) and NTS glasses (chapter 6) in which $P(Q^0)_{Na,M}$ (M = Zr, Ti) are the dominate species. The XRD results suggest that Gct2 and Gct3 contain $Na_5Ti_2Si_2PO_{13}$ as the crystalline phosphate. Hence, $P(Q^0)_{Na,Ti}$ is the most probable assignment for $[PO_4]$ units in $Na_5Ti_2Si_2PO_{13}$ where phosphorus is present in only one site. The chemical composition also suggests a NASICON type structure in which $[TiO_6]$ octahedra link with $[SiO_4]$ and $[PO_4]$ tetrahedra as a framework with no Si-O-P linkage. This is confirmed by the observed chemical shift. However, the lineshape is questionable because presence of two peaks at approximately the same chemical shifts but slightly different linewidths. These results may reflect the dynamic (resonating) structural arrangement of $P(Q^0)_{Na,Ti}$ in which rotation of the terminal bond P=O may occur on a time scale observable by ^{31}P MAS NMR [51].

In Gct4 and Gct5, there is also one crystalline phosphate identified by XRD, $Na_4TiO(PO_4)_2$. Therefore, the resonance at 5.6 ppm is believed to be of $P(Q^0)_{Na,Ti}$ species of $Na_4TiO(PO_4)_2$. The narrower peak at 3.9 ppm is probably of the unknown crystalline phase present in XRD patterns. This observed chemical shift is in range of $P(Q^0)_{Na,Ti}$ species but also close to that of $P(Q^1)_{Na}$ (2.0 ppm). Thus, the assignment of this peak is not clear. Two resonances due to inequivalent phosphate species can be also found in another sodium titanium orthophosphate compound, e.g. $Na_5Ti(PO_4)_3$ (0.5 ppm and –5.0 ppm) [51]. The additional peak at 5.3 ppm of Gct5 cannot be identified but is believed to be $P(Q^0)_{Na,Ti}$ species in a sodium titanium orthophosphate compounds.

7.3.3.3 ^{23}Na MAS NMR

The ^{23}Na MAS NMR spectra of Gct samples are shown in Fig 7.12. Three different spectral lineshapes are observed; 1) quadrupolar broadened, with small effect from residual glass for Gct1, 2) larger effect from residual glass for Gct2 and Gct3 and 3) asymmetric Lorentzian lineshape for Gct4 and Gct5. Quadrupolar parameters of these spectra cannot be determined easily because of the large contribution of residual glass to a broader lineshape. However, the spectrum of Gct1 is possible to fit. The results of fit using the Winfit programme are summarised in Table 7.08. The quadrupolar parameters of $Na_2Si_2O_5$ who show two Na sites -consistent with the literature report [48,52]. This consistency allows the parameters of the two Na sites of Na_2TiSiO_5 to be determined. The results suggest the same η, (0.75) for these two sites. For the spectra of Gct2 and Gct3, they are very difficult to fit, even though the total number of Na sites in crystalline phase are known (Both Na_2TiSiO_5 and $Na_2Ti_2Si_2PO_{13}$ have two Na sites). Peaks of crystalline phases are poorly resolved from the broader peak of the residual glass leading to large errors during fitting.

The ^{23}Na MAS NMR spectra of Gct4 and Gct5 are similar, having Lorentzian lineshape. The peak positions are approximately at –17.7 ppm with a width around 23 ppm. This lineshape is from Na^+ in the glassy phase. The resonance peaks of crystalline phases are not observed. This may be due to very low concentration of crystalline phases, as suggested by XRD and ^{29}Si MAS NMR results of these two samples.

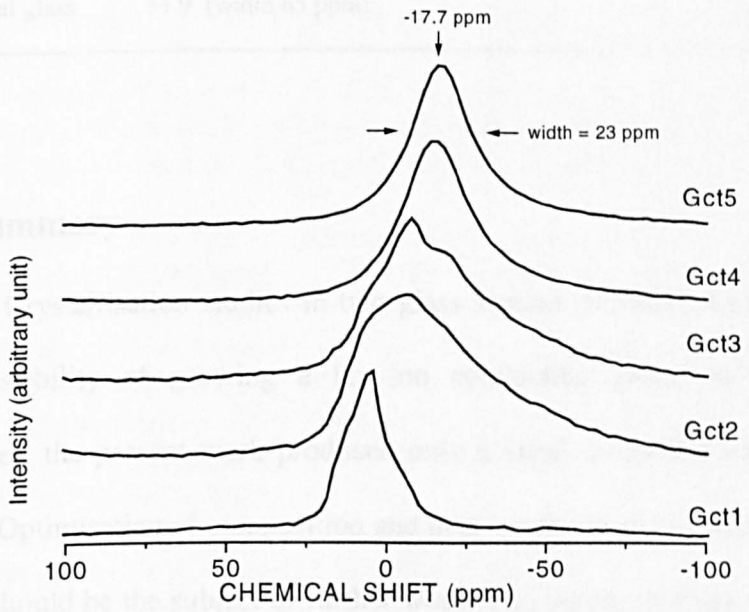

a)

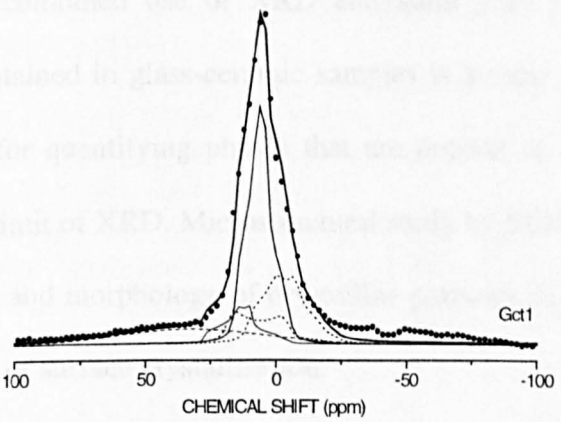

b)

Figure 7.12 *a) ^{23}Na MAS NMR spectra of glass-ceramic derived from NTS glasses, b) simulation of the spectra of Gct1: dot lines represent 2 Na sites in $Na_2Si_2O_5$ and two solid lines are of Na_2TiSiO_5.*

Table 7.08 *^{23}Na quadrupolar parameters determined from ^{23}Na MAS NMR spectra of Gct1.*

Phase	^{23}Na quadrupolar parameters			
	δ_{iso} (± 0.3 ppm)	C_Q (± 0.1MHz)	η (± 0.2)	Area (± 3.0 %)
$Na_2Si_2O_5$	11.9	2.22	0.55	23
	23.9	2.52	0.00	12
Data of $Na_2Si_2O_5$ from ref. [48]	*8.3*	*2.22*	*0.55*	
	20.4	*2.50*	*0.00*	
Na_2TiSiO_5	15.5	1.68	0.75	42
	27.6	2.08	0.75	9
Residual glass	31.9 (width 65 ppm)	-	-	14

7.4 Summary

Crystallisation studies in two glass system, NASIGLAS and NTS glasses, show the possibility of growing a fast-ion conducting phase in glass-ceramic samples. However, the present work produced only a small concentration of fast-ion conducting phase. Optimisation of composition and heat treatment to increase the yield of the desired phase should be the subject of further work. The intensive study of effect of temperature, time and atmosphere during heat treatment are probably the area of interest.

The combined use of XRD and solid state NMR to identify the crystalline phase(s) contained in glass-ceramic samples is a most powerful method. MAS NMR is also useful for quantifying phases that are present at very low relative concentrations, beyond the limit of XRD. Microstructural study by SEM is also useful for visualising the arrangement and morphology of crystalline particles in the glass matrix and determining the presence of surface crystallisation.

References

[1] Yamashita, K., Nojiri, T., Umegaki, T. and Knazawa, T., *Solid State Ionics*. **40/41** (1990), 48.

[2] Yamashita, K., Tanaka, M. and Umegaki, T., *Solid State Ionics.* **58** (1992), 231.
[3] Yamashita, K., Tanaka, M., Kakuta, T. and Matsuda, M., *Journal of Alloys and Compounds.* **193** (1993), 283.
[4] Cho, T., Yamashita, K., Matsuda, M. and Umegaki, T., *Materials Research Bulletin.* **29** (1994), 595.
[5] Yamashita, K., Kakuga, T., Sakurai, B. and Umegaki, T., *Solid State Ionics.* **86-88** (1996), 585.
[6] Raade, G. and Mladeck, M., *Canadian Mineralogist.* **15** (1977), 102.
[7] Susman, S., Delbecq, C.J. and McMillan, J.A., *Solid State Ionics.* **9&10** (1983), 667.
[8] Von Alpen, U., Bell, M. and Höfer, H.H., *Solid State Ionics.* **7** (1982), 345.
[9] Barth, S., Feltz, A. and Jäger, C., *Solid State Ionics.* **26** (1988), 189.
[10] Clearfield, A., Subramanian, M.A., Rodulf, P.R. and Moini, A., *Solid State Ionics* **18&19** (1986), 13.
[11] Goodenough, J.B., Hong, H.Y-P. and Kafalas, J.A., *Materials Research Bulletin.* **11**, no. 2 (1976), 203.
[12] Ramasesha, S.K. and Jacob, K.T., *Materials Letters.* **7**, no.1,2 (1988), 61.
[13] Bogusz, W., Krok, F. and Piszczatowski., *Solid State Ionics.* **119** (1999), 165.
[14] Bortun, A.I., Bortun, L.N. and Clearfield, A., *Chemistry of Materials.* **9** (1997), 1854.
[15] McDonals, W.S. and Cruickshank, D.W., *Acta Crystallographica.* **22** (1967), 37.
[16] Wakasugi, T., Burgner, L.L. and Weinberg, M.C., *Journal of Non-Crystalline Solids.* **244** (1999), 63.
[17] Wakasugi, T. and Ota, R., *Journal of Non-Crystalline Solids.* **274** (2000), 175.
[18] Novaes de Oliveira, A.P., Corradi, A.B., Barbieri, L., Leonelli, C. and Manfredini, T., *Thermochimica Acta.* **286** (1996), 375.
[19] Denry, I.L., Lejus, A.M., Théry, J. and Masse, M., *Materials Research Bulletin.* **34**, no. 10/11 (1999), 1615.
[20] Grimmer, A.-R., Mägi, M., Hähnert, M., Stade, H., Samoson, A., Wieker, W. and Lippmaa, E., *Physics and Chemistry of Glasses.* **25**, no.4 (1984), 105.
[21] Bastow, T.J, Hobday, M.E., Smith, M.E. and Whitfield., H.J., *Solid State Nuclear Magnetic Resonance.* **5** (1996), 293.
[22] Jäger, C., Scheler, G., Sternberg, U., Barth, S. and Feltz, A., *Chemical Physics Letters.* **147**, no. 1 (1988), 49.
[23] Tran Qui, D., Capponi, J.J., Joubert, J.C. and Shannon, R.D., *Journal of Solid State Chemistry.* **39** (1981), 219.
[24] Kuriakose, A.K., Wheat, T.A., Ahmad, A. amd Dirocco, J., *Journal of the American Ceramics Society.* **67** no. 3 (1984), 179.
[25] Dupree, R., Holland, D., McMillan, P.W. and Pettifer, R.F., *Journal of Non-Crystalline Solids.* **68** (1984), 399.
[26] Mudrakovskii, I.L., Shmachkova, V.P., Kotsarenko, N.S. and Mattikhin, V.M., *Journal of Physics and Chemistry of Solids.* **47**, no.4 (1986), 335.
[27] Choy, J-H, Han, Y-S, Kim, Y-H and Suh, K-S., *Japanese Journal of Applied Physics.* **32** (1993), 1154.
[28] Subramanian, M.A., Rudolf, P.R. and Clearfield, A., *Journal of Solid State Chemistry.* **60**, no.2 (1985), 172.
[29] Clearfield, A., Jerus, P. and Cotman, R.N., *Solid State Ionics.* **5** (1981), 301.
[30] Kohler, H. and Schulz, H., *Materials Research Bulletin.* **20** (1985), 1461.
[31] Kohler, H. and Schulz, H., *Materials Research Bulletin.* **21** (1986), 23.
[32] Hazen, R.M., Finger, L.W., Agrawal, D.K., McKinstry, H.A. and Perrotta, A.J., *Journal of Materials Research.* **2** no. 3 (1987), 329.

[33] Kohler, H., Schulz, H. and Melnikov, O., *Materials Research Bulletin.* **18** (1985), 1143.
[34] Tran Qui, D., Capponi, J.J., Gondrand, M., Saïb, M., Joubert, J.C. and Shannon, R.D., *Solid State Ionics.* **3&4** (1981), 219.
[35] Didishim, J.-J., Prince, E. and Wuensch, B.J., *Solid State Ionics.* **18&19** (1986), 944.
[36] Boilot, J.P., Collin, G., Colomban, Ph., *Materials Research Bulletin.* **22** (1987), 669.
[37] Ivanov-Schitz, A.K. and Bykov, A.B., *Solid State Ionics.* **100** (1997), 153.
[38] Massiot, D., Thiele, H., and Germanus, A., *"WinFit - a Windows-based program for lineshape analysis " Bruker Report.* **140**, (1994), 43.
[39] Clark, T.M., Grandinetti, P.J., Florian, P. and Stebbins, J.F., *Journal of Physical Chemistry.* **B 105** (2001), 12257.
[40] Von Alpen, U., Bell, M.F. and Höfer, H.H., *Solid State Ionics.* **3-4** (1981), 215.
[41] Jäger, C., Barth, S. and Feltz, A., *Chemical Physics Letters.* **154** no.1 (1989), 45.
[42] Witschas, M. and Eckert, H., *Journal of Physical Chemistry.* **A 103** (1999), 10764.
[43] Witschas, M. and Eckert, H., Freiheit, H., Putnis, A, Korus, G. and Jansen, M., *Journal of Physical Chemistry.* **A 105** (2001), 6808.
[44] McMillan, P.W., *Glass-Ceramics.* London; Academic Press, 1964.
[45] Novaes de Oliviera, A.P. and Manfredini, T., *Journal of Materials Science.* **36** (2001), 2581.
[46] Ferreira, P., Ferreira, A., Raoch, J. and Soares, M.R., *Chemistry of Materials.* **13** (2001), 355.
[47] Labouriau, A., Highley, T.J. and Earl, W.L., *Journal of Physical Chemistry.* **B 102** (1998), 2897.
[48] Heidemann, D., Hübert, C., Schwieger, W., Grabner, P., Bergk, K.-H. and Sarv, P., *Zeitschrift für anorganische und allgemeine Chemie.* **617** (1992), 169.
[49] Liu, Y., Du, H., Xiao, F.-S., Zhu, G. and Pang, W., *Chemistry of Materials.* **12** (2000), 665.
[50] Peng, G.-W., Chen, S-K. and Liu, H.-S., *Applied Spectroscopy.* **49** no.11 (1995), 1646.
[51] Sobha, K. and Rao, J., *Journal of Solid State Chemistry.* **121** (1996), 197.
[52] Tossell, J.A., *Physics and Chemistry of Minerals.* **27** (1999), 70.

CHAPTER 8

Mixed-Ionic Electronic Conductors

8.1 Introduction

In practice, the electrolyte layer of the solid state pH sensor has to be a mixed-ionic electronic conductor because charge transport for the whole system must be reversible. To convert a normal ionic conducting glass to be mixed-ionic electronic conductor, impurity species that supply electrons are introduced. In this work, NASIGLAS and NTS glass are doped with 1 mol% and 2 mol% of Fe_2O_3. This attempt is based on the assumption that the redox reaction between Fe^{3+} and Fe^{2+} is the key role of supplying electronic conduction. Therefore, the redox equilibrium is studied.

8.2 NASIGLAS with Fe_2O_3 dopant

Mössbauer spectroscopy was used to study the effect of NASIGLAS compositions on the relative concentration of Fe^{3+} and Fe^{2+} at two different doping levels: 1 and 2 mol% Fe_2O_3. The Mössbauer spectra of NASIGLAS containing 1 mol% (DG series) and 2 mol% Fe_2O_3 (NG series) taken at room temperature are shown in Fig. 8.01 and 8.02, respectively. The results of spectral analysis are summarised in Table 8.01. It can be seen that all spectra show two doublets due to the presence of Fe^{2+} at the isomer shift close to 1.0 $mm.s^{-1}$ with quadrupole splitting 2.0 $mm.s^{-1}$ and Fe^{3+} at the isomer shift approximately 0.3 $mm.s^{-1}$ with quadrupole splitting 0.8 $mm.s^{-1}$. These assignments are consistent with previous reports for iron containing silicate glasses [1,2]. The isomer shift results suggest that Fe^{3+} is in tetrahedral coordination consistent with the reported shift range for this coordination, i.e. 0.20-0.32 $mm.s^{-1}$ [3]. The observed shift range for Fe^{2+}

(0.80-0.99) also suggests a tetrahedral coordination. However, the observed shift for NASIGLAS containing 2 mol% Fe_2O_3 moves toward the shift range of Fe^{2+} in octahedral coordination, i.e. 1.05-1.10 $mm.s^{-1}$ [3]. This may indicate that with increasing Fe_2O_3 content, a fraction of Fe^{2+} changes to octahedral coordination. Changing coordination in Fe^{3+} is not pronounced even though the isomer shift is clearly increased with decreasing Fe_2O_3 content but still in the range of tetrahedral coordination. Joseph and Pye [4] also suggested that there is no coordination change for $Fe^{3+}/[\Sigma Fe] > 0.5$ and this is consistent with the present result.

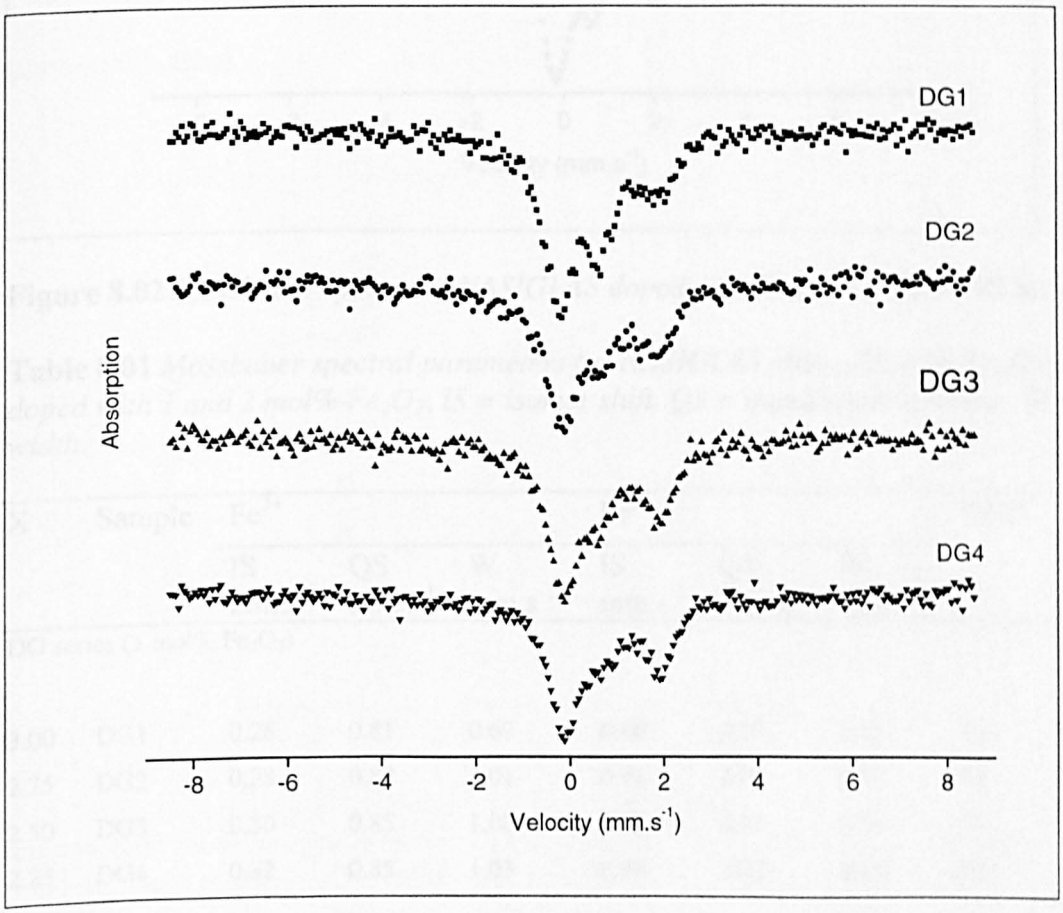

Figure 8.01 *Mössbauer spectra of NASIGLAS doped with 1 mol% Fe_2O_3* (DG series).

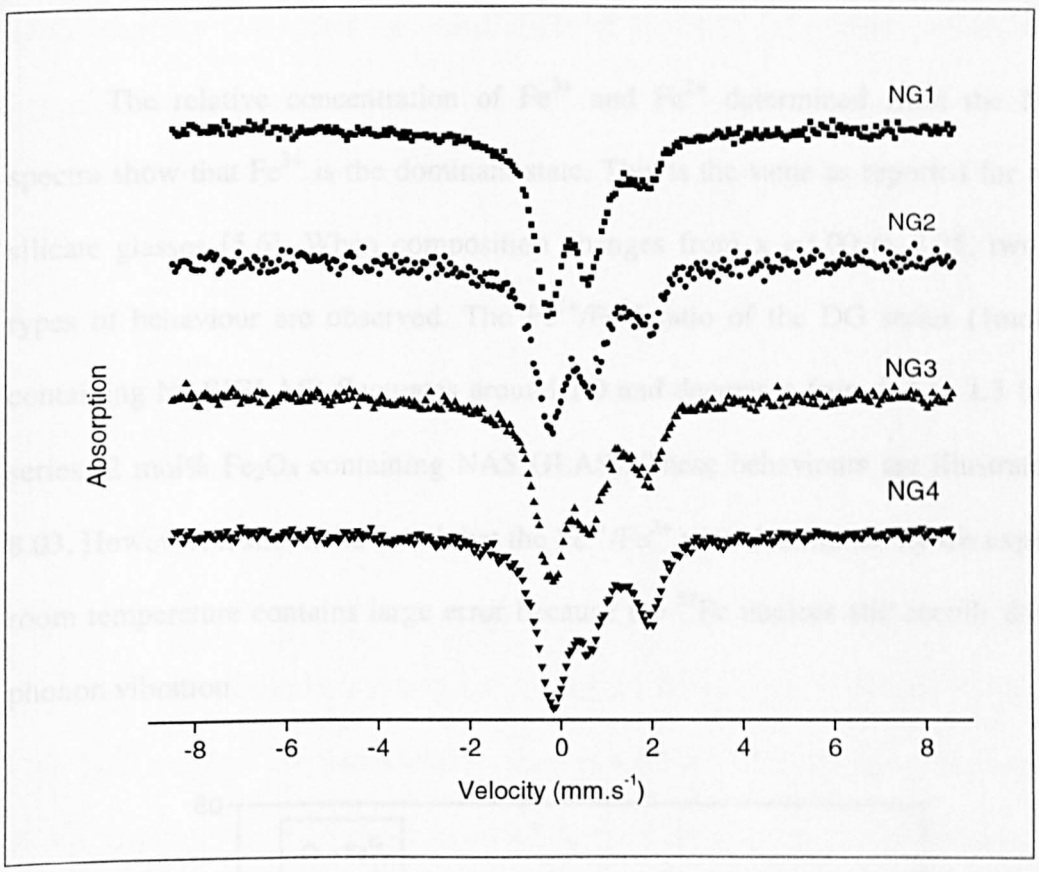

Figure 8.02 *Mössbauer spectra of NASIGLAS doped with 2 mol% Fe_2O_3* (NG series).

Table 8.01 *Mössbauer spectral parameters for NASIGLAS ($Na_{1+x}Zr_{2-x/3}Si_xP_{3-x}O_{12-2x/3}$) doped with 1 and 2 mol% Fe_2O_3, IS = isomer shift, QS = quadrupole splitting, W = line width.*

X	Sample	Fe^{3+}			Fe^{2+}			$\%Fe^{3+}$	$\%Fe^{2+}$
		IS $mm.s^{-1}$	QS $mm.s^{-1}$	W $mm.s^{-1}$	IS $mm.s^{-1}$	QS $mm.s^{-1}$	W $mm.s^{-1}$		
DG series (1 mol% Fe_2O_3)									
3.00	DG1	0.28	0.81	0.60	0.80	2.13	1.13	48	52
2.75	DG2	0.28	0.89	1.01	0.91	2.04	0.80	53	47
2.50	DG3	0.30	0.85	1.00	0.97	2.04	0.66	58	42
2.25	DG4	0.32	0.85	1.03	0.98	2.02	0.65	52	48
NG series (2 mol% Fe_2O_3)									
3.00	NG1	0.26	0.89	0.71	0.84	2.17	0.86	70	30
2.75	NG2	0.27	0.94	0.82	0.93	2.06	0.66	67	33
2.50	NG3	0.26	0.94	0.78	0.96	2.02	0.69	62	38
2.25	NG4	0.27	0.93	0.80	0.99	2.03	0.65	57	43

The relative concentration of Fe^{3+} and Fe^{2+} determined from the Mössbauer spectra show that Fe^{3+} is the dominant state. This is the same as reported for alkali iron silicate glasses [5,6]. When composition changes from x =3.00 to 2.25, two different types of behaviour are observed. The Fe^{3+}/Fe^{2+} ratio of the DG series (1mol% Fe_2O_3 containing NASIGLAS) fluctuates around 1.0 and decreases from 2.3 to 1.3 for the NG series (2 mol% Fe_2O_3 containing NASIGLAS). These behaviours are illustrated in Fig. 8.03. However, it should be noted that the Fe^{3+}/Fe^{2+} ratio determined by the experiment at room temperature contains large error because the ^{57}Fe nucleus still recoils due to large phonon vibration.

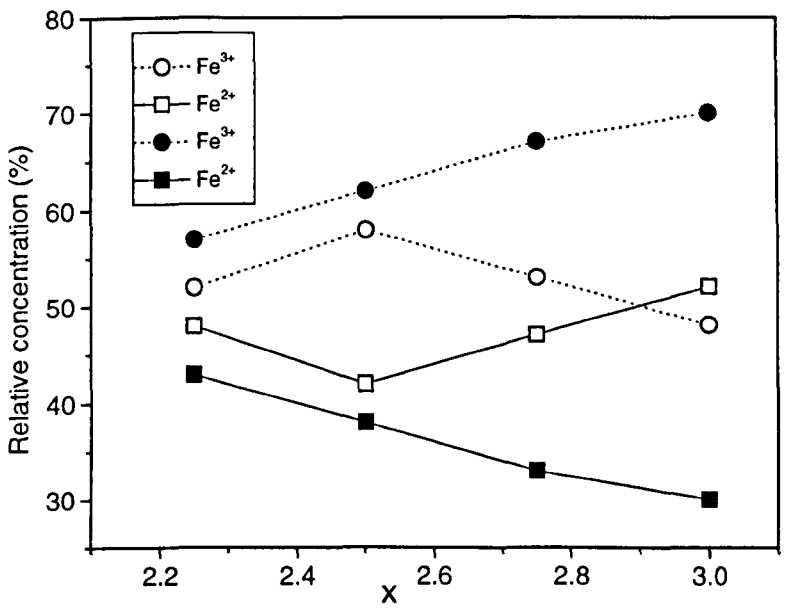

Figure 8.03 *Relative concentration of Fe^{3+} and Fe^{2+} in NASIGLAS doped with 1 (open symbol) and 2 mol% Fe_2O_3 (solid symbol). Note: lines are drawn for guide the eye.*

The redox-equilibria of iron in glass is commonly affected by glass preparation conditions. The types of crucible materials were debated to have considerable effect on the glass melt [7]. Melting conditions such as atmosphere, time, temperature and

quenching rate also effect the redox states of Fe_2O_3 [8-10]. In the present work, such effects were not studied in detail. However, the effect of glass composition is clearly seen to have influence on the redox states and structural role of Fe^{3+} and Fe^{2+}.

8.3 NTS glass with Fe_2O_3 dopant

The Mössbauer spectra of NTS glass with the Fe_2O_3 dopant are shown in Fig. 8.04 and 8.05. These spectra are similar to those of NASIGLAS, consisting of doublets of $Fe^{2+}$and Fe^{3+}. The spectral parameters are summarised in Table 8.02. The isomer shift observed for Fe^{3+} is around 0.3 $mm.s^{-1}$ with QS ~0.85 $mm.s^{-1}$ and for Fe^{2+} is in range 0.90-1.03 $mm.s^{-1}$ with nearly constant QS of 2.1 $mm.s^{-1}$. These results also suggest that both Fe^{3+} and Fe^{2+} are tetrahedrally coordinated. With changing glass compositions and Fe_2O_3 content, there is no pronounced change for IS, QS and linewidth. However, decrease of the Fe^{3+}/Fe^{2+} ratio is observed when x decreases from 3.00 to 2.00. This may indicate that the equilibrium shifts toward Fe^{2+} when Na_2O and SiO_2 content are reduced. Multiple coordination states of Ti^{4+} may also affect the redox couple and make the situation even more complex. In Fe_2O_3 free glass samples, Ti^{4+} was suggested to remain octahedral. For the sample with Fe_2O_3, the structural role of Ti^{4+} may be changed. Since there was no direct investigation on Ti^{4+} for this particular case, there is insufficient information to clarify the influence of Ti^{4+}on the redox equilibria of Fe^{3+}-Fe^{2+}. There is also no direct evidence to determine distribution of iron in the glass network. In some silicate glasses, clustering of iron is detected by Mössbauer spectroscopic studies [11,12]. However, the result may suggest that Fe_2O_3 takes a glass intermediate role and is believed to distribute randomly throughout the glass network.

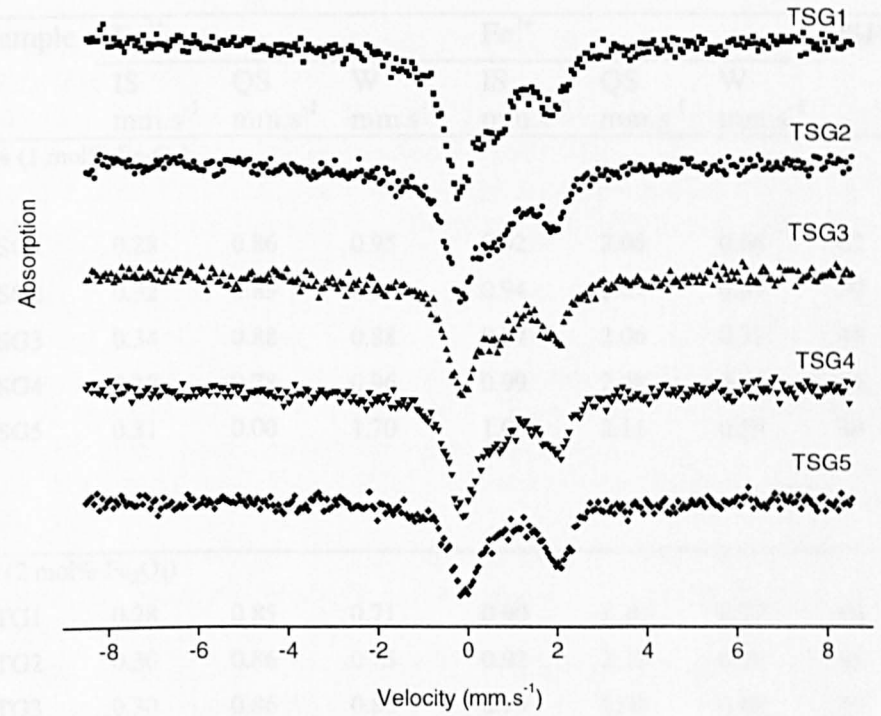

Figure 8.04 *Mössbauer spectra of NTS glass containing 1 mol% Fe_2O_3 (TSG series).*

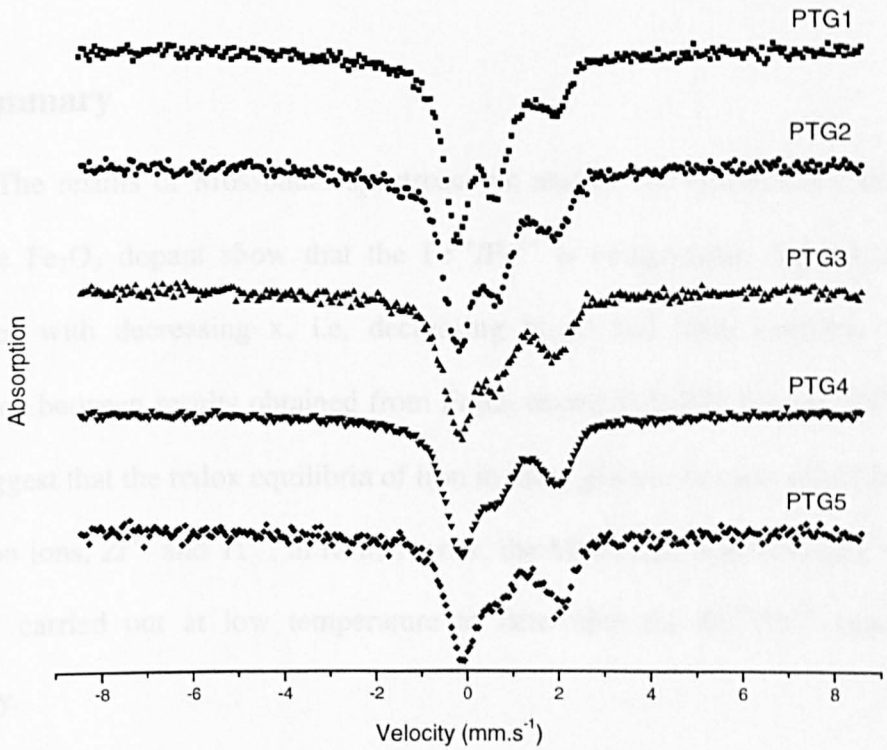

Figure 8.05 *Mössbauer spectra of NTS glass containing 2 mol% Fe_2O_3 (PTG series).*

Table 8.02 *Mössbauer spectral parameters for NTS glass ($Na_{1+x}Ti_{2-x/3}Si_xP_{3-x}O_{12-2x/3}$) with 1 and 2 mol% Fe_2O_3 dopant, IS = isomer shift, QS = quadrupole splitting, W = line width.*

X	Sample	Fe^{3+}			Fe^{2+}			$\%Fe^{3+}$	$\%Fe^{2+}$
		IS $mm.s^{-1}$	QS $mm.s^{-1}$	W $mm.s^{-1}$	IS $mm.s^{-1}$	QS $mm.s^{-1}$	W $mm.s^{-1}$		
TSG series (1 mol% Fe_2O_3)									
3.00	TSG1	0.28	0.86	0.95	0.92	2.06	0.66	62	38
2.75	TSG2	0.32	0.85	0.99	0.94	2.07	0.67	59	41
2.50	TSG3	0.34	0.88	0.88	0.97	2.06	0.72	48	52
2.25	TSG4	0.30	0.78	0.96	0.99	2.08	0.66	46	54
2.00	TSG5	0.31	0.00	1.70	1.03	2.11	0.59	44	56
NG series (2 mol% Fe_2O_3)									
3.00	PTG1	0.28	0.85	0.71	0.90	2.10	0.77	68	32
2.75	PTG2	0.30	0.86	0.75	0.92	2.12	0.70	65	35
2.50	PTG3	0.30	0.86	0.83	0.95	2.08	0.68	59	41
2.25	PTG4	0.32	0.83	0.87	0.99	2.10	0.68	56	44
2.00	PTG5	0.37	0.82	0.83	1.02	2.10	0.68	45	55

8.4 Summary

The results of Mössbauer spectroscopic studies for NASIGLAS and NTS glass with the Fe_2O_3 dopant show that the Fe^{3+}/Fe^{2+} is composition dependent. This ratio decreases with decreasing x, i.e. decreasing Na_2O and SiO_2 contents. There is no difference between results obtained from Fe_2O_3 doped NASIGLAS and NTS glass. This may suggest that the redox equilibria of iron in these glasses has less effect from the other transition ions, Zr^{4+} and Ti^{4+}. In further work, the Mössbauer spectroscopic measurement may be carried out at low temperature to determine the Fe^{3+}/Fe^{2+} ratio with more accuracy.

References

[1] Gosselin, J.P., Shimony, U., Grodzins, L. and Cooper, A.R., *Physics and Chemistry of Glasses.* **8** (1967), 56.

[2] Williams, K.F.E., Johnson, C.E. and Thomas, M.F., *Journal of Non-Crystalline Solids.* **226** (1998), 19.

[3] Johnson, J.A., Johnson, C.E., Holland, D., Mekki, A., Appleyard, P. and Thomas, M.F., *Journal of Non-Crystalline Solids.* **246** (1999), 104.

[4] Joseph, I. And Pye, L.D., *"Mössbauer Spectroscopy in Glasses" in Experimental Techniques of Glass Science.* C.J. Simmons and O.H. El-Bayoumi (Eds.). Ohio: The American Ceramics Society, 1993.

[5] Holland, D., Mekki, A., Gee, I.A., McConville,C.F., Johnson, J.A., Johnson, C.E., Appleyard, P. and Thomas, M., *Journal of Non-Crystalline Solids.* **253** (1999), 192.

[6] Burkhard, D.J.M., *Physics and Chemistry of Glasses.* **38** (1967), 317.

[7] Paul, A. and Douglas, R.W. *Physics and Chemistry of Glasses.* **6** (1965), 207.

[8] Dingwell, D.B., *American Mineralogist.* **76** (1991), 1560.

[9] Kress, V.C. and Carmichael, I.S.E., *Contributions to Mineralogy and Petrology.* **108** (1991), 82.

[10] Hahanshai, S. and Wright, S., *ISIJ International.* **33** no.1 (1993), 195.

[11] Hayashi, M., Susa, M., Noda, S. and Nagata, K., *Journal of Applied Physics.* **80** no.12 (1996), 6906.

[12] Bingham, P.A., Parker, J.M., Searle, T., Williams, J.M. and Fyles, K., *Journal of Non-Crystalline Solids.* **253** (1999), 203.

CHAPTER 9

Ionic Conductivity Measurement

9.1 Introduction

Ionic transport processes in fast-ion conducting glasses have been a subject of deep scientific interest for more than three decades. These are especially the studies of structural and composition dependence of ionic conductivity. Ionic conduction in glassy material is typically due to hopping of the mobile ions, which mostly occupy the network modifying sites. The most common mobile species are the alkali, alkaline earth and silver cations. Fluoride glasses can also exhibit high ionic conductivity of fluoride anions which occupy network former sites [1,2]. Varieties of glass compositions that contain one of these mobile ions can be prepared and these are detailed in the review of Tuller et al. [3]. However, desirable ionic conductivity is found only over a certain range of composition. The important aspect of ionic conductivity measurement is to understand the conduction mechanism of the mobile species which is very important for practical purposes, such as fast-ion conducting glasses for pH sensors. In practice, the complex structure of glasses leads to a complicated transport process and perfect description of ionic conduction mechanisms is difficult to obtain. However, using a simplified approach, conduction behaviour of glasses can be presented by a simple model [4].

In this chapter NASIGLAS and NTS glasses and the related glass-ceramic samples are subjected to ionic conductivity measurement using the ac technique. The fundamentals of the technique and experimental details have been given in chapter 4. Two analytical methods (conductivity spectrum and complex plane impedance plots) are used to determined the dc conductivity of glass and glass-ceramic samples produced in

this work. The ionic conductivity measurements for NASIGLAS samples were carried out using the *Solartron* impedance analyser which is a facility in the Department of Chemistry, University of Aberdeen. NTS glass samples were measured using the *HP 925A* low frequency impedance analyser in the Department of Physics, University of Warwick. The impedance analysers were equipped with home-built two probe jigs (Fig. 4.18) capable of operating over the temperature range from room temperature to around 500 °C.

9.2 Ionic conductivity of NASIGLAS

9.2.1 Conductivity spectrum

The variation of ac conductivity of NASIGLAS with frequency over the range 1 – 10^6 Hz and with temperature over the range 100 °C-300 °C (373-573 K) are shown in Fig. 9.01. At high temperature, electrode polarisation at low frequency is clearly seen from the spectra of G1, G2 and G3. The electrode polarisation is not pronounced for the spectra of G4. The dc conductivity plateaux are clearly observed in the intermediate frequency region (approximately 10^2-10^5 Hz). Steady increase of ac conductivity in the high frequency regions is also clearly seen. To a good approximation, these conductivity spectra obey the *power law* proposed by Jonscher [5]. However, at lower temperature, the additional narrower conductivity plateaux are observed for the spectra of G2 and G3. This is the response from two mobile species in these particular samples. This behaviour is not observed for the spectra of G1 and G4.

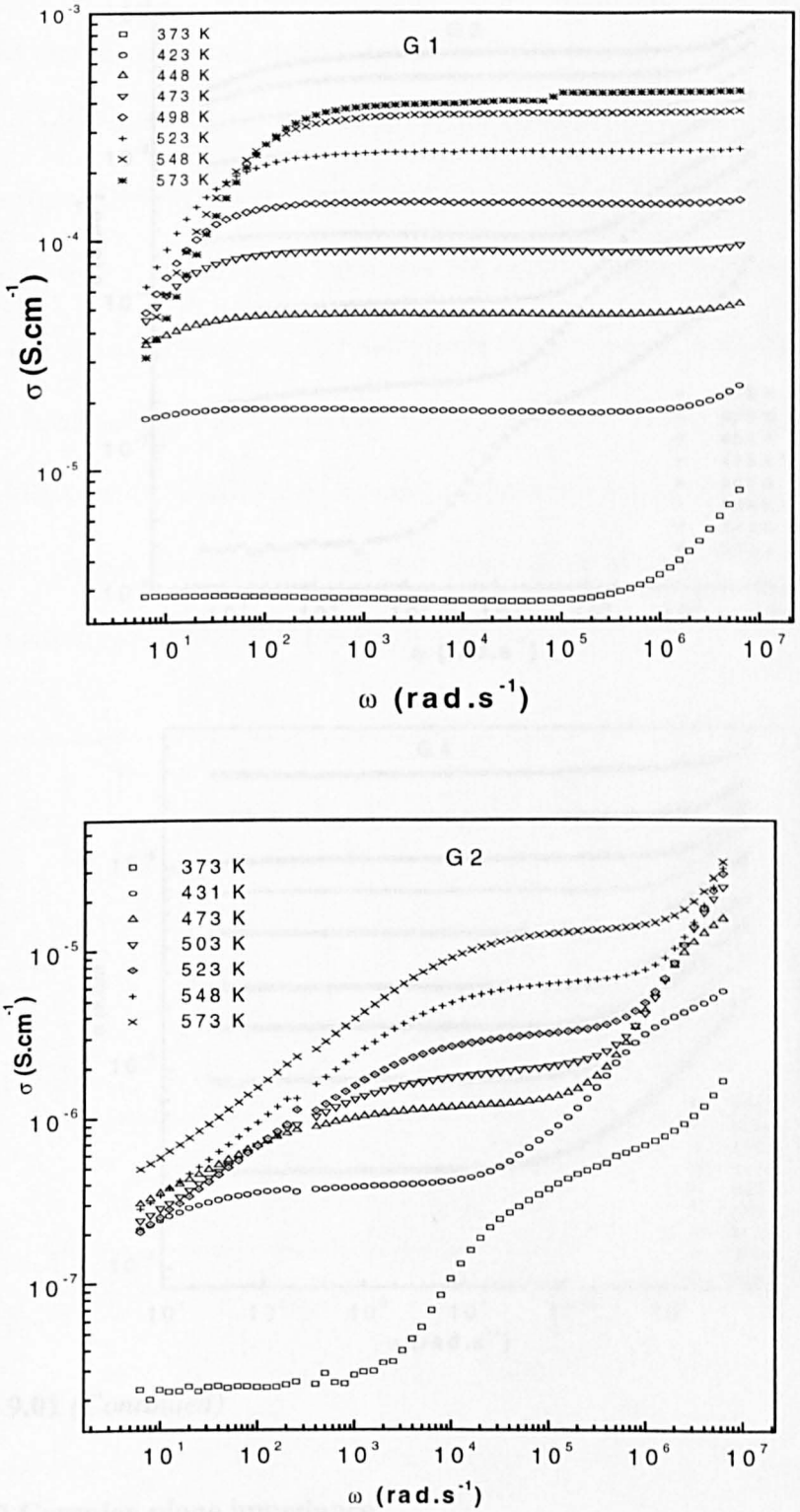

Figure 9.01 *Typical variation of ac conductivity with frequency over the temperature range 273-573 K for NASIGLAS.*

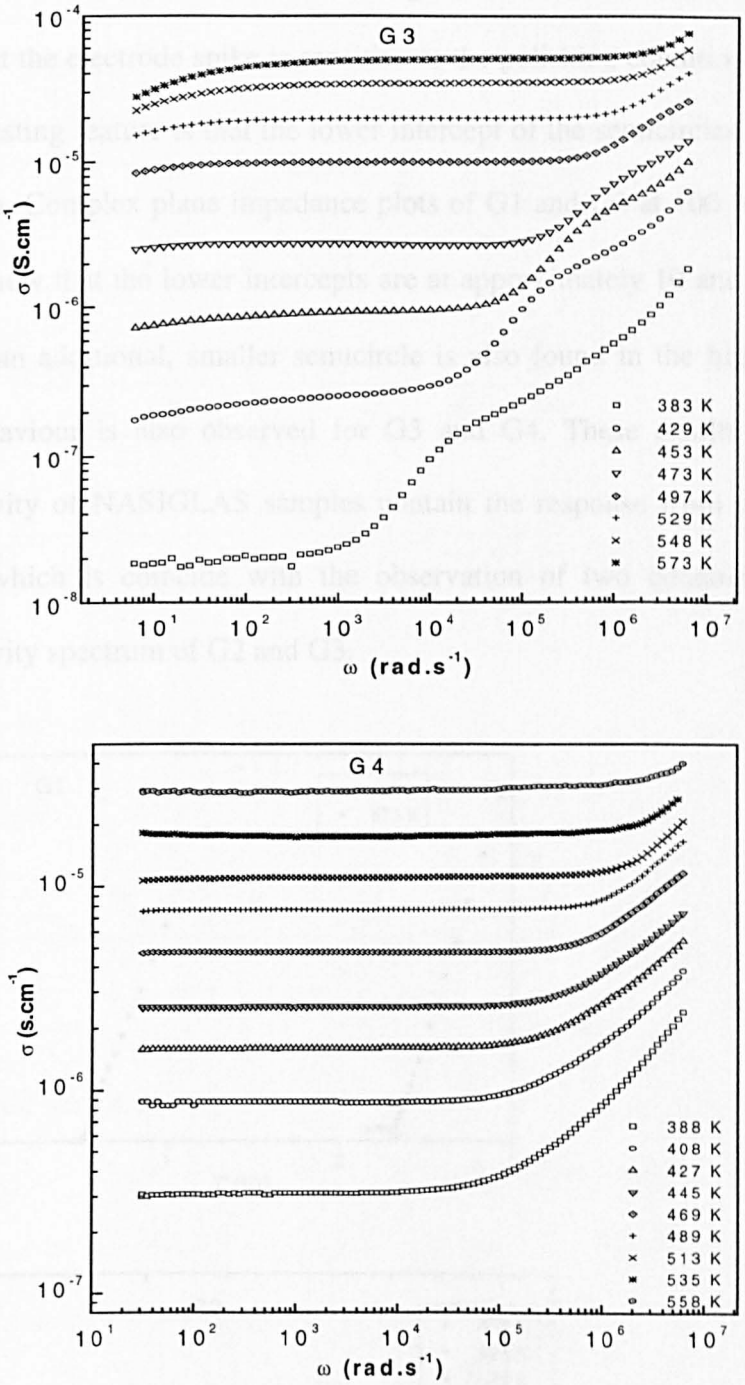

Fig. 9.01 *(Continued)*

9.2.2 Complex plane impedance

The complex plane impedance plots are shown in Fig 9.02. The plots are clearly characterised by a semicircle centred below the Z′ axis at high frequency and the spike of electrode polarisation at lower frequency. G1 shows only the electrode spike at the high

temperature which is an indication of high ionic conduction. However, it should also be noted that the electrode spike is sensitive to the polishing condition of pellet surfaces [6]. An interesting feature is that the lower intercept of the semicircles does not pass through the origin. Complex plane impedance plots of G1 and G2 at 100 °C (373 K) in Fig 9.03 clearly show that the lower intercepts are at approximately 10 and 700 kΩ, respectively. For G2, an additional, smaller semicircle is also found in the higher frequency region. This behaviour is also observed for G3 and G4. These results may suggest that ac conductivity of NASIGLAS samples contain the response from more than one mobile species which is coincide with the observation of two conductivity plateaux in the conductivity spectrum of G2 and G3.

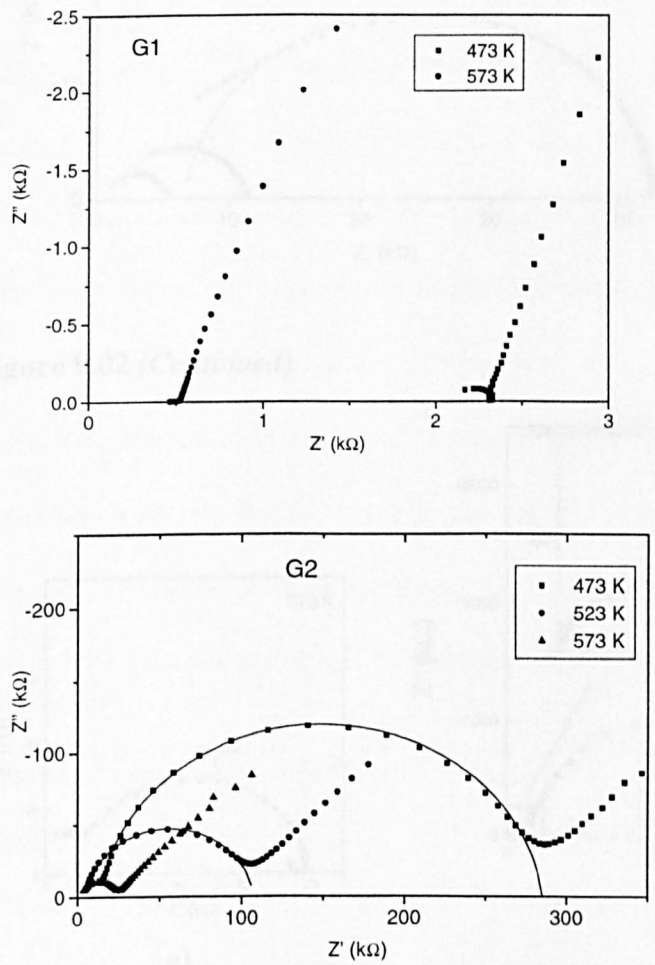

Figure 9.02 *Complex plane impedance plots for four NASIGLAS samples at temperatures 473, 523 and 573 K.*

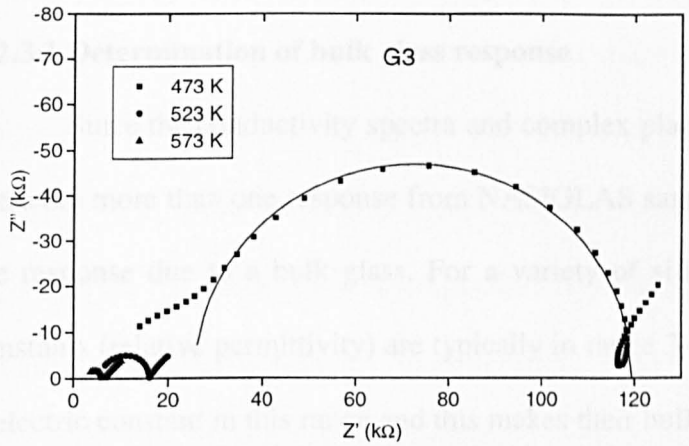

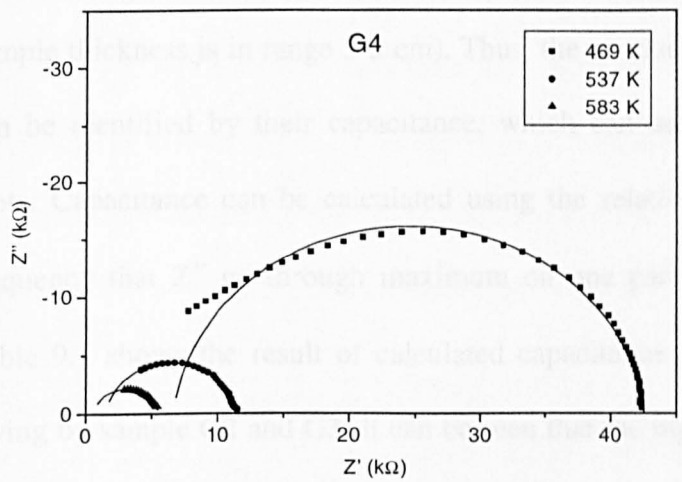

Figure 9.02 *(Continued)*

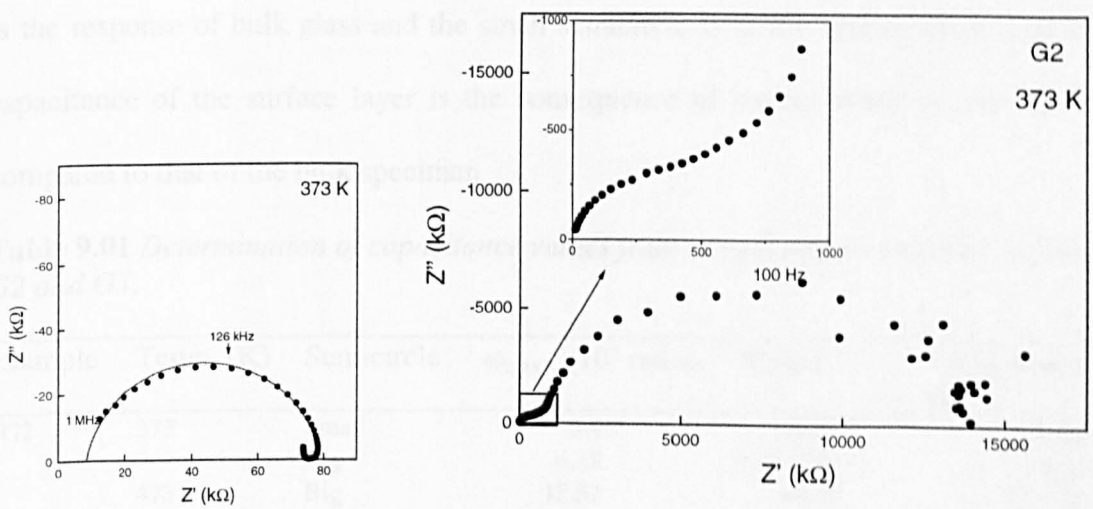

a) b)

Figure 9.03 *Complex plane impedance plots of a) G1 and b) G2 showing additional small semicircle at the lower intercept.*

9.2.3 Conductivity data analysis

9.2.3.1 Determination of bulk glass response

Since the conductivity spectra and complex plane impedance plots suggested that there are more than one response from NASIGLAS samples. Therefore, we must identify the response due to a bulk glass. For a variety of silicate based-glasses, the dielectric constants (relative permittivity) are typically in range 3-10. NASIGLAS should also have dielectric constant in this range and this makes their bulk specimen to have capacitance in order of pF for the cell dimension selected in this work (i.e. the ratio of electrode area and sample thickness is in range 3-5 cm). Thus, the conductivity response of the bulk glasses can be identified by their capacitance, which can be determined from complex plane plots. Capacitance can be calculated using the relation $\omega_{max}CR = 1$, where ω_{max} is the frequency that Z″ go through maximum on one particular semicircle (see sec. 4.6.3). Table 9.1 shows the result of calculated capacitance for the big and small semicircles giving by sample G2 and G3. It can be seen that the big semicircle which locate at lower frequency range give capacitance in order of pF, while the small semicircle show a larger capacitance as high as two order of magnitude. This is clearly seen that the big semicircle is the response of bulk glass and the small semicircle is of the surface layer. The higher capacitance of the surface layer is the consequence of having much smaller thickness compared to that of the bulk specimen.

Table 9.01 *Determination of capacitance values from complex plane impedance plots of G2 and G3.*

Sample	Temp. (K)	Semicircle	ω_{max} ($\times 10^4$ rad.s)	R (kΩ)	Capacitance (F)
G2	373	Small	9.96	1,000.00	1.00×10^{-11}
		Big	6.28	42,833.90	3.72×10^{-13}
	473	Big	12.53	88.80	8.99×10^{-11}
	523	Big	34.24	35.24	8.29×10^{-11}
	573	Big	157.83	7.85	8.07×10^{-11}
G3	383	Small	0.08	1.60	7.81×10^{-7}
		Big	9.42	1,6316.00	6.51×10^{-13}

9.2.3.2 Conductivity spectrum analysis

To determine dc conductivity, σ_{dc}, the spectra were fitted using the relation in equation 4.27, i.e. $\sigma_{ac}(\omega) = \sigma(0) + A\omega^s$ (here, $\sigma(0) \equiv \sigma_{dc}$). The results of the fit are summarised in Table 9.02. In this case, σ_{dc} is of lower frequency plateau. This can be seen that the σ_{dc} values show a temperature dependence. In contrast, parameter A and s are temperature independent. A fluctuates and s values are approximately constant at 1.0. The results also suggest that the conductivity spectra can be fitted to the power law only over a certain temperature range where the conductivity plateaux and rising curve are well-defined. At the temperature difference from the report in Table 9.02, the fit results contain large errors. This may be due to insufficient frequency range, which cannot give well-defined conductivity spectra for the whole range of temperatures.

Table 9.02 *Parameters of conductivity spectra of NASIGLAS determined by fitting a power law.*

Sample	Temperature (±2 K)	σ_{dc} (±0.1 ×10^{-5} S.cm^{-1})	A (± 0.5×10^{-13})	Exponent, s (±0.2)
G1	373	0.3	8.6	1.0
	423	1.8	6.8	1.0
	448	4.7	7.7	1.0
	473	8.9	7.5	1.0
	498	14.5	3.5	1.0
	523	24.4	8.9	1.0
G2	458	0.1	0.3	1.0
	473	0.1	1.2	1.0
	503	0.2	1.2	1.2
	523	0.3	0.1	1.4
G3	453	0.1	9.9	1.1
	473	0.3	5.0	1.3
	497	1.0	5.4	1.1
	529	1.9	4.2	1.1
	548	3.4	5.4	1.3
	573	5.1	4.8	1.4
G4	427	0.2	230	0.8
	445	0.3	124	0.8
	469	0.5	22	0.9
	489	0.7	1.5	1.1
	513	1.0	0.1	1.4
	535	1.8	0.2	1.3

Almond et al. [7] suggested that A is a temperature dependent parameter but this is not observed in the present study. Within the experimental error, exponent s seems to agree very well with the theoretical argument that $0 < s < 1$ [8,9]. However, some authors [10] suggested that s is not obvious verified by a simple power law for good ionic conductors and data from a wider temperature range is needed.

9.2.3.3 Complex plane impedance analysis

Complex plane impedance plots of all samples suggest that the possible representative equivalent circuit is the parallel combination of resistance R and capacitance C in series with the two electrode capacitances, C_e (Fig 9.04). In this case, R is the resistance of bulk glass and can be determined by finding the high intercept of semicircle. To do this, the built-in fitting function of the *Origin software* was employed. The results of dc conductivity converted from R are shown by the Arrhenius plots in Fig. 9.05. The σ_{dc} at 300 °C (573 K) and the activation energies of ionic conduction calculated from the slopes of the Arrhenius plots are reported in Table 9.03. It can be seen that G1 has the highest ionic conductivity (41.6×10^{-5} S.cm^{-1}) and this is only one order lower than that of crystalline $Na_4ZrSi_3O_{10}$, i.e. 4×10^{-3} S.cm^{-1} [11]. The activation energy goes through a maximum at G3 which bears no systematic relation to the Na^+ concentration. This is surprising in view of the ^{23}Na NMR result (section 5.2.6.3) which implies greater Na^+ motion but it should be noted that NMR only measures local motion.

A comparison between σ_{dc} obtained from conductivity spectrum analysis and complex plane impedance shows good agreement within the experimental error. The data for 473 K are shown in Tables 9.02 and 9.03, respectively. This proves that these two analytical methods can be substituted for one another if one has low reliability due to insufficient data range.

Table 9.03 *Ionic conductivity of Na^+ in NASIGLAS and associated activation energies (E_a).*

Sample	Conductivity (σ) at indicated temperature ($\times 10^{-5}$ S.cm^{-1})		E_a (kJ/mol)
	473 K	573 K	
G1	8.7 ± 0.2	41.6 ± 0.1	43 ± 2.6
G2	0.2 ± 0.1	1.3 ± 0.4	52 ± 3.4
G3	0.3± 0.1	5.1 ± 0.2	79 ± 3.1
G4	0.5 ± 0.1	3.0 ± 0.1	50 ± 2.8

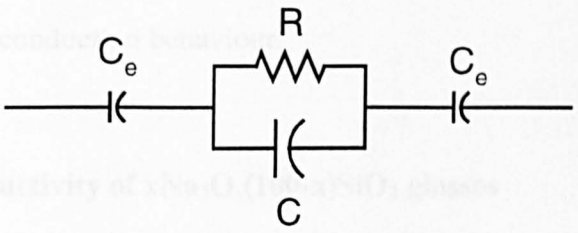

Figure 9.04 *Equivalent circuit representing ionic conduction behaviour of NASIGLAS. R, C are the resistance and capacitance of bulk glass and C_e is the electrode capacitance.*

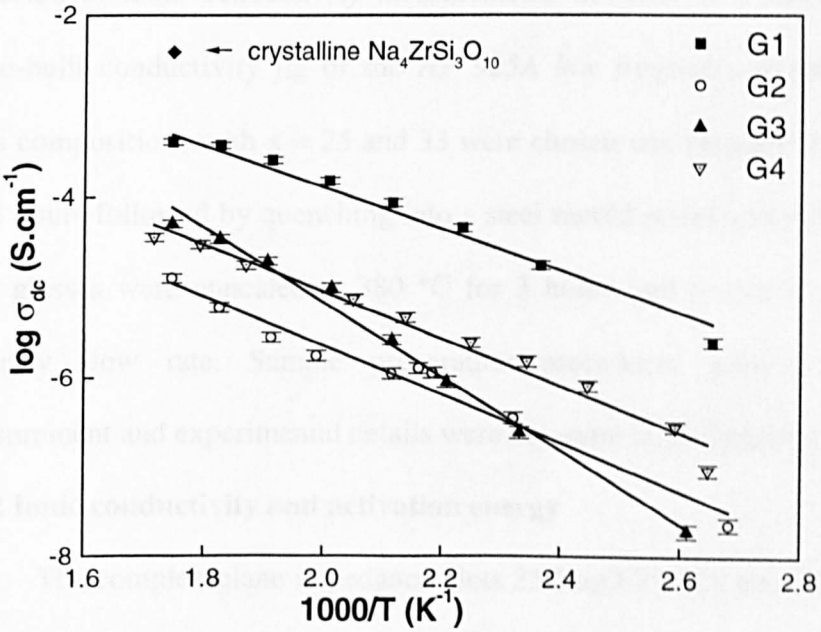

Figure 9.05 *Arrhenius plots of NASIGLAS samples, σ_{dc} were determined from complex plane impedance and the errors of log σ_{dc} are approximately ±1.*

The ionic conductivity of NASIGLAS is in reasonable agreement with the dynamic structure model [12], which suggested a higher conductivity at higher modifier content. Departure from this model occurs only with the anomalous behaviour of G3. It is also noted that the P_2O_5 content in NASIGLAS may contribute to the dc conductivity of Na^+. The influence on the ionic conductivity of Na^+ of a different network former other than silica was demonstrated by Hsieh et al. [13]. Since all Na^+ are bonded to non-bridging oxygens of the glass network, the interaction of Na^+ with the network and adjacent Na^+ is the important factor in ionic transport in glasses and this is debated by Kahnt [14]. The complex composition and structural arrangement of NASIGLAS leads to complex ionic conduction behaviour.

9.3 Ionic conductivity of $xNa_2O.(100-x)SiO_2$ glasses

9.3.1 Introduction

The binary sodium silicate glasses, $xNa_2O.(100-x)SiO_2$, were prepared and subjected to ionic conductivity measurements in order to determine the reliability of home-built conductivity jig of the *HP 925A low frequency impedance analyser*. Two glass compositions with x = 25 and 33 were chosen and prepared by melting at 1400 °C for 3 hours followed by quenching into a steel mould under atmosphere of static air. The bulk glasses were annealed at 380 °C for 3 hours and cooled to room temperature at arbitrary slow rate. Sample preparation procedures prior to ionic conductivity measurement and experimental details were the same as for NASIGLAS.

9.3.2 Ionic conductivity and activation energy

The complex plane impedance plots $25.Na_2O.75SiO_2$ and $33Na_2O.67SiO_2$ glasses are shown in Fig. 9.06 and the corresponding Arrhenius plots are shown in Fig 9.07. The

ionic resistivity of these two samples and the activation energy of Na^+ are reported in Table 9.04a. The reference data from ref. [15] are summarised in Table 9.04b.

Table 9.04a *Experimental data of $25Na_2O.75SiO_2$ and $33Na_2O.67SiO_2$ glasses.*

Sample	Log σ (S.cm^{-1}), (± 5%)			E_a (± 0.05 eV)
	100 °C	200 °C	300 °C	
$25Na_2O.75SiO_2$	-6.93	-4.96	-4.32	0.69
$33Na_2O.67SiO_2$	-5.56	-4.43	-3.42	0.43

Table 9.04b *Referenced data of binary sodium silicate glasses (Na_2O-SiO_2) extracted from ref.* [15].

Na_2O (mol%)	Log σ (S.cm^{-1}), (± 5%)			E_a (± 0.05 eV)
	100 °C	200 °C	300 °C	
24.8	-7.468	-5.45	-4.14	
25.8	-7.36	-5.38	-4.10	
32.2	-6.43	-4.62	-3.47	
33.3	-5.06 (150 °C)		-3.34	
24				0.725
26				0.710
33				0.615

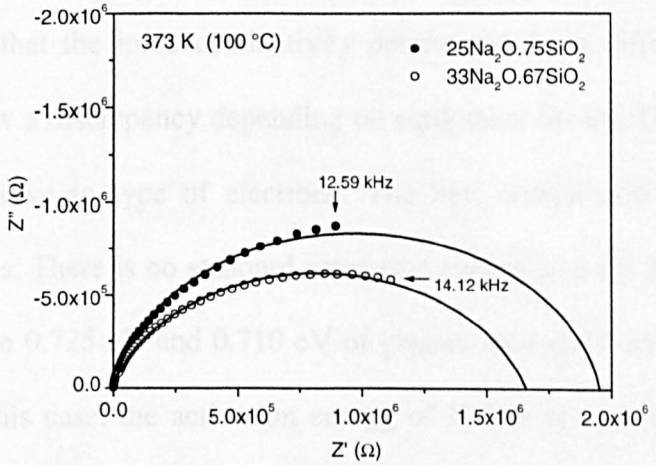

Figure 9.06 *Complex plane impedance plots of $25Na_2O.75SiO_2$ and $33Na_2O.67SiO_2$ glasses at 100 °C.*

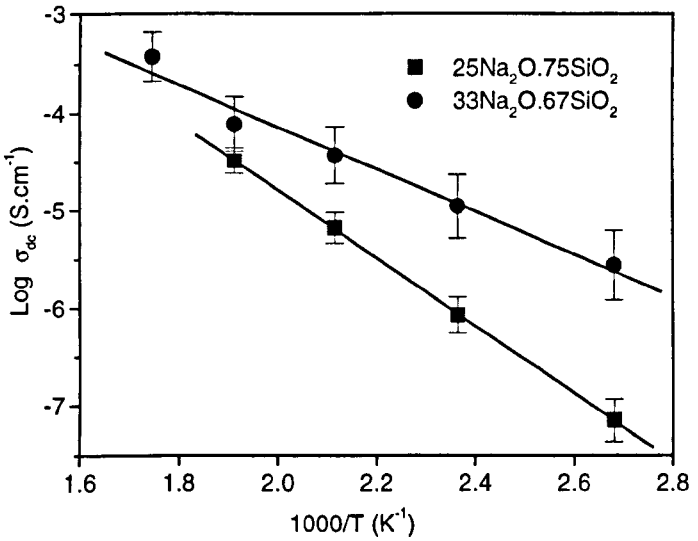

Figure 9.07 *The Arrhenius plots of binary sodium silicate glasses, $xNa_2O.(100-x)SiO_2$, prepared in the present work.*

It can be seen that the conductivities of these two standard compositions determined by the present work are in good agreement with the reference data. There seem to follow conduction behaviour of this glass system, i.e. the higher Na_2O content is the is higher conductivity. At 100 °C, the conductivity of $25Na_2O.75SiO_2$ is also close to the report for $Na_2O.3SiO_2$ glass, which is approximately -7.04 $S.cm^{-1}$ [16]. However, it should be noted that the ionic conductivity determined from different sources can be different and show a discrepancy depending on equipment set up. The ionic conductivity data is also sensitive to type of electrode. The best comparison should be from the activation energies. There is no standard activation energy data for $25Na_2O.75SiO_2$ but it should be between 0.725 eV and 0.710 eV of glasses having 24 and 26 mol% of Na_2O, respectively (in this case, the activation energy of Na^+ is almost linearly dependent on Na^+ concentration). This is in good agreement with the data determined from the present work (0.69 eV). The larger difference in activation energy is observed for $33Na_2O.67SiO_2$, where the present work shows lower activation energy, i.e. 0.43 eV, compared to the 0.615 eV of the reference. The lower conductivity (higher resistivity) at

the higher temperature may be responsible for the discrepancy. This result may suggest that there is a large electrode polarisation effect in this sample where Na^+ is saturated at the surface layer, leading to a lower ionic conductivity for the bulk glass. It is clearly seen that electrode polarisation is sensitive to Na^+ concentration. In conclusion, good agreement is found for the $25Na_2O.75SiO_2$ composition but less for the $33Na_2O.67SiO_2$ glass composition.

9.4 Ionic conductivity of NTS glass

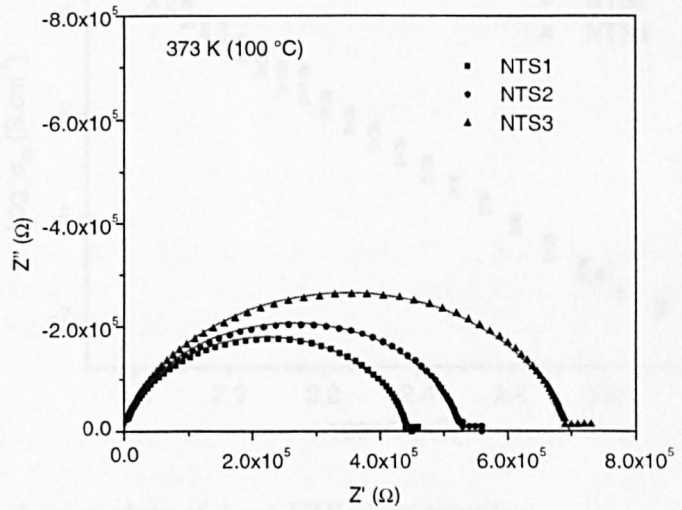

a)

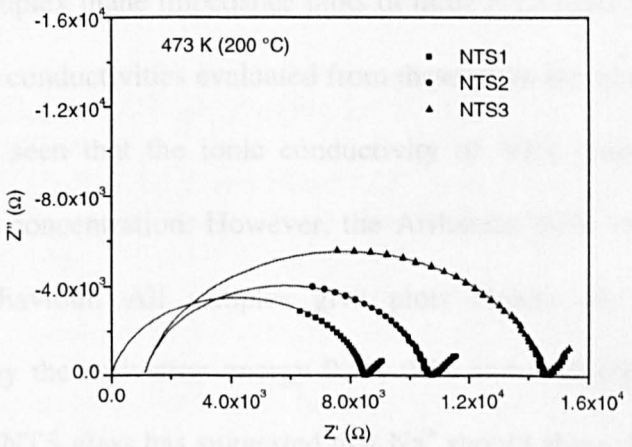

b)

Figure 9.08 *Complex plane impedance plots of NTS glass samples at a) 100 °C and b) 200 °C.*

Table 9.05 *Conductivity of NTS glass samples at 100 °C and 200 °C and activation energy of Na^+.*

Sample	Dc conductivity ($S.cm^{-1}$), ± 5%		E_a (± 0.05 eV)
	100 °C	200 °C	
NTS1	5.68×10^{-7}	2.99×10^{-5}	0.57
NTS2	4.68×10^{-7}	2.35×10^{-5}	0.58
NTS3	3.72×10^{-7}	1.77×10^{-5}	0.58

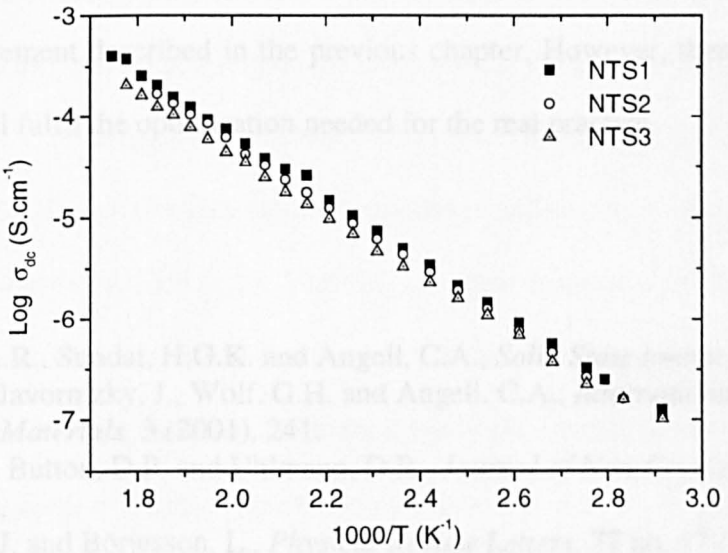

Figure 9.09 *Arrhenius plots of three NTS glass samples.*

The complex plane impedance plots of three NTS glass samples are shown in Fig 9.08. The ionic conductivities evaluated from these plots are summarised in Table 9.05. It can be clearly seen that the ionic conductivity of NTS glass samples increases with increasing Na^+ concentration. However, the Arrhenius plots in Fig. 9.09 show unusual conduction behaviour. All samples give plots almost the same straight line and characterised by the activation energy 0.57, 0.58 and 0.58 eV, respectively. Structural information of NTS glass has suggested that Na^+ should show different activation energy for the different samples. This may imply that the conductivity response from bulk glass

is heavily affected by another component. The factor that manifests the real response of bulk glass is not clear. This may be the effect from the sample handling, preparation conditions, or the components of conductivity jig.

9.5 Summary

At 300 °C, Fast-ion conducting glasses prepared in this work have shown their ionic conductivities in range 10^{-5}-10^{-4} S.cm^{-1}. This conductivity range agrees very well with the requirement described in the previous chapter. However, there will be relevant studies that will fulfil the optimisation needed for the real practice.

References

[1] Kulkari, A.R., Sundat, H.G.K. and Angell, C.A., *Solid State Ionics.* **24** (1987), 253.
[2] Jacob, S., Javornizky, J., Wolf. G.H. and Angell. C.A., *International Journal of Inorganic Materials.* **3** (2001), 241.
[3] Tuller, H., Button, D.P. and Uhlmann, D.R., *Journal of Non-Crystalline Solids.* **40** (1980), 93.
[4] Swenson, J. and Börjesson, L., *Physical Review Letters.* **77** no. 17 (1996), 3569.
[5] Jonscher, A.K. *Nature.* **267** (1977), 673.
[6] Bruce, P.G. and West, A.R., *Journal of the Electrochemical Society.* **130** no.3 (1983), 662.
[7] Almond, D.P., Duncan, G.K. and West, A.R., *Solid State Ionics.* **8** (1983), 159.
[8] Lee, W.K., Lim, B.S., Liu, J.F. and Nowick, A.S. *Solid State Ionics.* **53-56** (1992), 831.
[9] Hsieh, C.H. and Jain, H. *Journal of Non-Crystalline Solids.* **203** (1996), 293.
[10] Henn, F., Giuntini, J.C. and Zanchetta, J.V., *Journal of Non-Crystalline Solids.* **131-133** (1991), 1084.
[11] Von Alpen, U., Bell, M.F. and Höfer, H.H., *Solid State Ionics.* **7** (1982), 345.
[12] Roling, B., Meyer, M., Bunde, A. and Funke, K., *Journal of Non-Crystalline Solids.* **226** (1998), 138.
[13] Hsieh, C.H. and Jain, H., *Journal of Non-Crystalline Solids.* **183** (1995), 1.
[14] Kahnt, H., *Journal of Non-Crystalline Solids.* **203** (1996), 225.
[15] Mazurin, O.V., Streltsina, M.V. and Shvaiko-Shaikovskaya, T.P., *"Hand Book of Glass Data" in Physical Science Data 15.* The Netherlands: Elsevier, 1987.
[16] Provenzano, V., Boesch, L.P., Moynihan. C.T. and Macedo, P.B., *Journal of the American Ceramics Society.* **55**, no.10 (1972), 492.

CHAPTER 10

Conclusions and Future Work

10.1 NASIGLAS ($Na_{1+x}Zr_{2-x/3}Si_xP_{3-x}O_{2-x/3}$)

Glass in this system can be prepared via the melt quenching method with a certain range of x. When x decreases below 2.5, low solubility of ZrO_2 content can be observed as trace amounts of residue. However, the XRD study confirms that all glass samples obtained from these compositions are amorphous. DTA results show that high melting temperature is required and the glass transition temperature is in range 650-730 °C. Crystallisation of NASIGLAS is complex yielding several crystalline phases formed in the temperature range 720-920 °C. Density and thermal expansion coefficient vary non-systematically with the composition. ZrO_2 content is believed to control these two physical properties.

The short range structural arrangement of NASIGLAS can be determined successfully using multi-nuclear solid state NMR techniques. Unambiguous information is obtained from ^{31}P MAS NMR. Phosphate tetrahedra are associated with Zr^{4+} and Na^+ giving five different species of $P(Q^0)$ and $P(Q^1)$. There is no observation of $[PO_4]$ - $[SiO_4]$ linkage. This may indicate that $[PO_4]$ do not participate in the silicate network and $[ZrO_6]$ octahedra are the intermediate units locating between those two tetrahedra. The ^{29}Si MAS NMR spectra are not clearly resolved leading to difficulty of $[SiO_4]$ species determination. However, the observed chemical shift range and its composition suggest that the most probable silicate species are $Si(Q^1)$ and $Si(Q^2)$. The concentration ratios of these two species are composition dependent. ^{23}Na NMR shows the anomalous response of composition x = 2.50. This may suggest that there is phase separation present and it is also consistent with the ^{31}P MAS NMR study.

Crystallisation study of NASIGLAS shows that crystalline $Na_2ZrSi_2O_7$ is the predominant phase. The minority crystalline phases are Na_2SiO_3, $Na_4ZrSi_3O_{10}$ and $Na_{2.5}Zr_2Si_{1.5}P_{1.5}O_{12}$. These results suggest that the crystalline fast-ion conducting phases can be grown by heat treatment process but they are only present at low concentration.

Ionic conductivity of NASIGLAS shows a composition dependence. The higher concentration of Na^+ has the higher ionic conductivity.

10.2 NTS glass ($Na_{1+x}Ti_{2-x/3}Si_xP_{3-x}O_{12-2x/3}$)

NTS glass can be prepared more easily than NASIGLAS and no trace amount of crystal is observed. Higher solubility of TiO_2 also provides a higher fluidity melt, which is a good glass forming melt. Highly glass stability of this system is seen from the DTA results which show low crystallisation. All glass compositions of this system exhibit viscous flow before reaching the crystallisation stage. This effect also leads to a lower glass transition range compared to NASIGLAS. Density and thermal expansion coefficient of NTS glass are independent from changing composition. However, TiO_2 content is believed to responsible for the control of physical properties of glass.

The structural arrangement of NTS glass is very dependent on composition. The same results as NASIGLAS are found for the ^{31}P MAS NMR study. There are also five different phosphate species observed in NTS glass. A higher proportion of phosphate species is $P(Q^0)$, while $P(Q^1)$ increases with increasing P_2O_5 content. $Si(Q^1)$ and $Si(Q^2)$ are also expected to exist in NTS glass although the ^{29}Si MAS NMR spectra seem to be poorly resolved.

Crystallisation studies of NTS glass do not yield a fast-ion conducting phase. The XRD results show complex patterns of crystalline phases formed during heat treatment. Viscous flow is observed as deformation of the bulk specimen. The concentrations of

crystalline phases are also very small. This may be due to insufficient time at the crystallisation temperature.

Though NTS glass samples can be prepared more easily, they exhibit a lower ionic conductivity if compared to NASIGLAS at equivalent Na^+ concentration. There is still no clear conclusion about the reliability of the conductivity jig, further tests and improvements may be needed.

10.3 Future work

Future work may be based on two mainly themes: 1) further investigation on glass composition and related properties and 2) electrochemical cell study using fast-ion conducting glass produced in this work. Relation between glass composition and ionic conductivity may be optimised by further investigation of the NASIGLAS related composition. Thus, extensive structural and ionic conduction study may be required.

To produce a desirable mixed ionic-electronic conductor for solid state pH sensor, further work may focus on the conduction mechanism and preparation method. Understanding interfacial effects between joined materials is also important.